DOCTOR OF PHILOSOPHY

Wind turbine operation in icing conditions

Stoyanov, Dimitar

Award date:
2021

Awarding institution:
Coventry University

Wind Turbine Operation in Icing Conditions

By

Dimitar Borisov Stoyanov

PhD

June 2020

Wind Turbine Operation in Icing Conditions

By

Dimitar Borisov Stoyanov

June 2020

A thesis submitted in partial fulfilment of the University's requirements for the Degree of Doctor of Philosophy

Certificate of Ethical Approval

Applicant:

Dimitar Stoyanov

Project Title:

Wind Turbine Operation in Icing Conditions

This is to certify that the above named applicant has completed the Coventry University Ethical Approval process and their project has been confirmed and approved as Low Risk

Date of approval:

31 July 2020

Project Reference Number:

P109417

Summary

Wind turbine operation in icing conditions has been researched for the last 30 years because of the impact of icing on both wind projects' profitability and financial viability for wind sites, which offer abundance of wind kinetic energy. Much work has been published on modelling ice induced energy losses and quantifying the impact of icing on the overall performance of wind turbines. However, these findings have not led to universally integrated solutions and approaches to adapt wind turbines to different icing events by advanced operational strategies.

This project used the numerical modelling approach for wind turbines subjected to icing to investigate how wind turbine performance in icing conditions can be improved through the design of different ice mitigation operational strategies. Icing events with variable duration, wind speed, ambient temperature and icing parameters were defined to obtain expected energy losses and ice mass accumulation for evaluating different operational strategies for ice mitigation. Wind tunnel experimental measurements were conducted to facilitate the comparison of XFoil and Fluent for estimating aerodynamic degradation and quantifying the sensitivity of predicted energy losses to aerodynamic modelling tools. For preliminary studies and conceptual design of operational strategies it was concluded that XFoil can be used for a range of icing events. Thus, it was used in combination with lewINT ice accretion code and blade element momentum method to demonstrate a novel approach for selecting the best operational strategy or set of strategies to achieve maximum energy generation during periods of icing.

Derating by tip-speed ratio modification during icing was investigated with a focus on its application and advantages. Thus, unlike other studies, a systematic method for choosing modified tip-speed ratio values was developed based on the installed electrical generator and energy payback time scheme. The strategy was found extremely favourable for short and extreme icing events with reduction of icing losses up to 23 %, and accumulated ice mass up to 30 %. The method for comparison outlined in this project allowed derating to be compared against other operational strategies. It was established that for longer and milder icing events the design strategy should be maintained. Non-optimised anti-icing systems was found to be a preferred operational strategy for ambient temperatures above -5 ºC providing the cost of the system was no higher than 2 % of the turbine's capital cost and there were more than 43 short extreme or 26 long mild icing event occurrences per year. For the selected icing events, the operational shutdown strategy was not found to be a viable option. The presented method allows for the comparison of other ice mitigation strategies providing their cost for implementation and operation can be incorporated into the viability and performance analysis.

The work covered in this project proposed a more holistic approach on studying ice mitigation strategies, which would facilitate integrated solutions and higher fidelity studies to develop novel ice mitigation techniques or advance current solutions. Further development of the presented methods would be needed to transfer the results that can be obtained from this analysis from preliminary conceptual design stage to prototype and test stages. However, this is one of the first studies to attempt advancing and designing different operational strategies together to achieve more effective adaption of wind turbines in cold climates.

Acknowledgements

As most things in life, this work would not be possible without the support and the advice of others.

I would like to thank to my supervisory team for their guidance, help and mostly patience. My gratitude goes to my director of studies Dr. Jonathan Nixon who would always find time for discussion and listen to all my ideas and worries about my work, while being supportive and providing insightful guidance. I would like to thank especially to my second supervisor Dr. Hamid Sarlak who would always give me great advice on modelling and improving the quality of my work. In addition, his immense support helped me to not only present well my work in the Winterwind conference in Sweden, but also to have some fun and relaxed time. I would like to thank my third supervisor Prof. Mike Blundell who would always provide support if I asked and for his advice in the very beginning of this project to just enjoy and tell a story with my work that would be worth the time of the reader and would contribute to the common knowledge in the field.

I would like to acknowledge the support, which I received from the technical staff of Coventry University, especially Simon, Luke, Chris and Alex who would always crack some jokes, while I was asking them for help. In addition, I would like to thank the Fluids and Complex System research centre for the support and the opportunity to go and present my work in Sweden. Many thanks to all Coventry University staff members who supported me in any way and also my MSc supervisor Dr. Humberto Medina who would always be happy to advise me on any aspect of my journey as a PhD candidate.

I simply cannot not thank to my PhD peers Abhi, Dhila, Thasos, Panos, Sussie, Chijioke who with we had some good time and laughs in our office. I would like to thank to my friends Marco, Gianluca and Sam who I spent a wonderful time with and especially with Marco who is a very dear friend to me and wonderful housemate.

Last but not least, I would like to express my gratitude to my family and my parents who would support me for every decision that I have made. I am where I am because of the love and support of my parents and family.

Table of Contents

1 Introduction 22
1.1 Background 22
1.2 Thesis outline: 26
2 Literature Review 28
2.1 Cold Climates: Icing Types and Ice Accretion Theory 28
2.1.1 Icing Types 28
2.1.2 Ice Accretion Theory 31
2.2 Aerofoils and iced shapes 33
2.2.1 Aerofoils 33
2.2.2 Ice Shapes 37
2.3 Wind Turbines Operation in CCs 40
2.3.1 Non-iced rotor 40
2.3.2 Iced rotor 42
2.3.3 Wind turbine performance modelling in CCs 43
2.3.4 Operation in icing conditions 52
2.3.5 Ice mitigation strategies 54
3 Methods and Materials 59
3.1 Overview of methodology 59
3.1.1 Wind turbine performance modelling 59
3.1.2 Ice losses and aerodynamic modelling 60
3.1.3 Ice mitigation operational strategies 60
3.1.4 Numerical setup 61
3.2 Icing events 62
3.3 Models 63
3.3.1 Wind turbine model 63
3.3.2 Wind turbine blade model and ice mass calculation 65
3.3.3 Ice accretion modelling – lewINT 66
3.3.4 Power output modelling – BEM theory 67
3.3.5 Numerical setup for aerodynamic characteristics modelling – XFoil and Fluent 69

3.4 Experimental setup 75
3.4.1 Apparatus 76
3.4.2 Working Section 76
3.4.3 Limitations 77
3.5 Test and Method 78
3.6 Summary 80
4 Aerodynamic Degradation Modelling 81
4.1 Results 81
4.1.1 Pre-tests 81
4.1.2 Ice shapes testing 85
4.2 Discussion 96
4.3 Conclusion 98
4.4 Summary 99
5 Design and Implementation of Derating 100
5.1 Method 100
5.1.1 Operational Strategy 100
5.1.2 Energy payback time 101
5.2 Results and Discussion 102
5.2.1 Results 102
5.3 Discussion and Further Work 113
5.4 Conclusion 114
5.5 Summary 114
6 Wind Turbine Adaptation to Icing 116
6.1 Methodology 116
6.1.1 Icing conditions and ice mass calculation 116
6.1.2 Anti-icing power estimation 117
6.1.3 Evaluation of ice mitigation strategies 118
6.2 Results and discussion 121
6.2.1 Variation in wind speed and meteorological conditions 125
6.3 Discussion and Further Work 128
6.4 Conclusion 129

6.5 Summary 130
7 Conclusion 130
7.1 Research questions 130
7.1.1 What is the uncertainty in predicting aerodynamic degradation due to icing when using low computationally intensive tools? 130
7.1.2 How can a wind turbine operational strategy be designed to improve wind turbine output during icing conditions without the installation of additional systems? 131
7.1.3 How can alternative ice mitigation strategies be evaluated and selected to improve wind turbine adaptation to cold climates? 133
7.2 Aim of the project: To improve wind turbine performance in cold climates through advancements in implementation, comparison and selection of ice mitigation operational strategies. 134
7.3 Future Work 134
Appendices 137
Appendix 1 137
Appendix 2 140
Buoyancy 140
Solid blockage 140
Wake blockage 140
Streamline curvature alteration 141
Two-dimensional corrections 141
Appendix 3 142
Appendix 4 144
Appendix 5 145
References: 153

List of Figure:

Figure 1: Cumulative wind energy capacity between 2001 and 2018 (GWEC, 2019: 28) 23
Figure 2: Icing map of Europe based on data obtained from 120 meteorological stations for in-cloud icing leading to rime ice formation (Tammelin, B. et al. 2000: p. 10) 28
Figure 3: Ice accretion type transition during an atmospheric icing on a structure as a function of the ambient temperature and the wind speed. Data based most likely on standard rotation cylinder as included in ISO standard for atmospheric icing on structures, (ESA 2001: p. 7)..... 30
Figure 4: Transition from glaze to rime along the blade of a wind turbine as a function of the ambient temperature and the liquid water content (Lamraoui et al. 2014: p. 42). For each graph, the region on the left depicts when glaze ice would form, while the region on the right shows when rime icing would occur. 30
Figure 5: Water droplets dynamics about an aerofoil section and all modes of water capture and release from the surface (Battisti 2015a) 32
Figure 6: Modes of heat transfer occurring during icing of aerofoils (Messinger 1953)..... 33
Figure 7: Schematics of the NACA 23012 aerofoil showing its geometrical features such as normalised camber (h/c), normalised thickness (t/c), chord (c), leading edge (LE), trailing edge (TE), Suction Side, Pressure side notation and the two-dimensional definition of the aeorfoil contour using coordinate points with x and y coordinates. 34
Figure 8: Integrated aerodynamic force (R), and its components (L and D), applied at the pressure centre of the aerofoil (x_P) as a result of the incmoing flow with velocity (V_∞) and angle of attack (α). 35
Figure 9: Aerodynamic characteristics (i.e. C_L and C_D) of an aerofoil as a function of the angle of attack (α) and denoting the points of minimum drag, maximum achievable lift coefficient prior to stall and the linear region of the lift curve, defined its slope ($\delta CL/\delta$). 35
Figure 10: Laminar, transition and turbulent regions for an aerofoil and its developnig boundary layer from impingement on the leading edge to the trailiing edge. Boundary layer schematised for visualisation purposes only (Agrawal and Platzer 2018: p. 150). 36
Figure 11: Types of aerofoil stall and the variation of the lift coefficient for each type as a function of the angle of attack (Agrawal and Platzer 2018) 37
Figure 12: Roughness ice shape on the leading edge of an aerofoil with the three distinctive zones, which usually are observed – smooth, roughness and feathers (Bragg, Broeren and Blumenthal 2005) 38
Figure 13: Double horn ice shape, formed at the leading edge with upper horn defined by its angle of inclination, height and location at the upper surface of the aerofoil s/c 38
Figure 14: Typical stream-wise (rime) ice shape with conformal geometry to the aerofoil leading edge..... 39
Figure 15: Spanwise-ridge icing shape on the upper surface of the aerofoil, defined by its location s/c, height and shape (Bragg, Broeren and Blumenthal 2005) 39
Figure 17: Drawing of a typical utility-scale wind turbine (a) and its power output as function of the operational wind velocity (b)..... 40

Figure 18: Power coefficinet of a wind turbines as a function of the tip-speed ratio (λ) (Hansen 2008) 41
Figure 19: Blade forces and moments for a upwind two-bladed wind turbine (Hansen 2008) ... 42
Figure 20: The wind turbine blade area, where the most icing occurs for wind turbine blades due to combination of operational and geometrical parameters leading to relatively high ice accretion rate. 43
Figure 21: Distribution of the tangential force, F_T, which integrated gives the torque of a wind turbine blade for an iced and non-iced case, along the blade radius, R. The figure is shown for illustrative purposes only. 43
Figure 22: Iced and non-iced torque speed curves and the change of the optimal rotational speed for iced case. With no additional design procedures the torque controller would prescribe RPM_1 for the new iced aerodynamic model, which would have an optimal rotational speed of RPM_2 (Homola, Matthew 2005, Zanon, Gennaro and Kuhnelt 2018) 52
Figure 23: Outline of the applied numerical modelling approach in this study..... 62
Figure 24: Discretised NREL 5 MW blade and the selected 2D sections for ice accretion analysis..... 65
Figure 25: Velocity triangle (a) and aerodynamic forces distribution (b) on an arbitrary aerofoil on a wind turbine rotor blade, (Hansen 2008: 47-48)..... 68
Figure 26: Aerofoil surface of NACA 64-618 aerofoil as used in XFoil for aerodynamic analysis. 70
Figure 27: Power coefficient (a) and power output (b) data comparison between XFoil with the current setup and documented data from the NREL reference report (Jonkman et al. 2009).... 71
Figure 28: Domain and mesh topology used in this thesis 73
Figure 29: Mesh dependency study based on lift and drag forces convergence for an angle of attack of 4.5° and wind speed (V) of 10 ms^{-1}. 74
Figure 30: Representative convergence criteria graph for the current CFD numerical setup, showing the absolute residuals after solving the continuity equation (continuity), the velocity in x (x-velocity) and y (y-velocity) direction, the turbulence kinetic energy (k) and the specific turbulent dissipation rate (omega); which are all outputs from the k-w STT model. 75
Figure 31: AF100 sub-sonic wind tunnel used to conduct the experiments and its constituting parts(TecQuipment 2013). 76
Figure 32a-b: Wind tunnel working section with mounted test article (a) and the schematics of the working section displaying the arrangement of the pitot tubes and method of taking wake measurements for drag calculations (b) (TecQuipment 2013)..... 78
Figure 33a-b: Lift (a) and Drag (b) coefficients against the angle of attack for the NACA 0012 aerofoil at Re of 194022, whereas Sandia experimental data is obtained for Re of 360 000. Fit1 corresponds to the measurements taken for this study, while fit2 corresponds to the Sandia Laboratory results..... 82

Figure 34: Comparison of the measured lift curve against Hudecz curve and three computational results - obtained with XFoil, CFD with smooth surface and CFD with rough surface of the aerfoils, respectively 83
Figure 35a-c: Ice shapes generated with lewINT for 1-hour icing event A at 0.25, 0.5 and 1.0 hours, (a), (b), and (c), respectively; and tested in the low speed wind tunnel at Re of 165 000. 86
Figure 36a-b: Experimental coefficients of lift (C_L) and drag (C_D) for the NACA 64-618 aerofoil, at the D section of the NREL 5 MW wind turbine blade, for the operational conditions (AoA = 4.52 °, V = 10 ms^{-1}, V_{REL} = 40.4 ms^{-1}) defined by icing event A105 (LWC = 0.5x10^{-4} kgm^{-1}, MVD = 25x10^{-6} m, T_{AMB} = 268.15 K, t_{ICING} = 360 s). 87
Figure 37a-b: Simulated lift coefficient for 1-hour degradation; at 4.5 ° angle of attack; for A105; as predicted by Fluent k-w SST model (a) and XFoil (b) 88
Figure 38: NACA 64-618 aerofoil lift curve after 1-hour icing event (A105) as obtained experimentally, with XFoil and with Fluent for Re of 165 000 88
Figure 39a-d: Ice shapes generated with lewINT for icing event C105 during operating the NREL 5 MW wind turbine at TSR of 7.5 after 0.5 h of icing (a) and 1 h of icing (b); and operating at TSR of 5 after 0.5h (c) and 1h (d) of icing 90
Figure 40a-b: Experimental C_L (a) and C_D (b) coefficient, measured for ice shapes produced during derating from TSR 7.5 to TSR 5 and sampled at 0.5 and 1h after the start of the icing event defined by A105. 91
Figure 41a-b: Simulated lift coefficient data for ice shapes obtained at two different tip-speed-ratios, at the 0.5h and 1h during 1-hour icing event. The performance is evaluated by the means of eperimental measuremnts (a), XFoil predictions (b) and Fluent k-w SST predictions (c). The Differences for the three methods are examined for clean aerofoil and ice shape that was obtained at the end of the event (d). 92
Figure 42a-b: Simulated lift curves with XFoil (a) and Fluent (b) for 1-hour glaze icing event at time intervals of 0.25, 0.5 and 1.0 hours. 93
Figure 43a-b: Simulated drag curves with XFoil (a) and Fluent (b) for 1-hour glaze icing event at time intervals of 0.25, 0.5 and 1.0 hours. 94
Figure 44a-b: XFoil (a) and Fluent k-w SST (b) predictions for operational Re number of the NACA 64-618 aerofoil when TSR is changed from 7.5 to 5 during icing for 1-hour icing event (A105) 95
Figure 45a-b: XFoil (a) and Fluent k-w SST (b) results for the changes in the drag curves of the NACA 64-618 aerofoil as section D of the NREL 5 MW wind turbine, for ice shapes obtained at 0.5 and 1.0 hours in an extreme one-hour icing event, when the operational Re is 6×10^6 96
Figure 46a-b: NREL 5 MW refrence wind turbine TSR operational limits defined by the limiting rotational speeds of the electrical generator (a) and how the power coefficent varies at different TSR (b). 101
Figure 47a-b: Power output (a) and cumulative energy (b) during and after an icing event for a wind turbine operating with a reference (TSR_R) or modified (TSR_M) tip-speed ratio strategy. . 102

Figure 48a-f: Wind turbine power coefficient degradation and total ice mass accumulation per blade during events A1010 (a), A105 (b), A710 (c), A75 (d), A510 (e) and A55 (f). 104
Figure 49a-f: Ice shapes on Section D for event cases A1010 (a), A105 (b), A710 (c), A75(d), A510 (e) and A55 (f). 105
Figure 50a-f: Power characteristics of modified tip-speed ratio values after icing events A1010 (a), A105 (b), A710 (c), A75(d), A510 (e) and A55 (f). 106
Figure 51a-f: Energy payback time for different tip-speed ratio after icing (TSRAI) values for events A1010 (a), A105 (b), A710 (c), A75(d), A510 (e) and A55 (f). 107
Figure 52a-h: Wind turbine Cp deteoration and ice accumulation per blade during events B1010 (a), B710 (c), B75 (e), B510 (g) and ice shapes on section D at the end of events B1010 (b), B710 (d), B75 (f), B510 (h). 109
Figure 53a-d: Power characteristics of modified tip-speed ratio values after icing events B1010 (a), B710 (b), B75(c) and B510 (d) 110
Figure 54a-d: Energy payback time for different tip-speed ratio after icing (TSR_{AI}) values for events B1010 (a), B710 (b), B75(c) and B510 (d). 111
Figure 55a-d: Wind turbine Cp deteoration and ice accumulation per blade during events C1010 (a) and C105 (c) and ice shapes on section D at the end of events C1010 (b) and C710 (d). . 112
Figure 56a-b: Power characteristics of modified tip-speed ratio values after icing events C1010 (a) and C105 (b). 112
Figure 57a-b: Energy payback time for different tip-speed ratio after icing (TSR_{AI}) values for events C1010 (a) and C105 (b). 113
Figure 58: a-b AIS for full surface (a) and impingement zone (b) protection. 117
Figure 59: An example integration limit for estimating the required power for supplying the needed heat flux for anti-icing, when different protection areas are considered. 118
Figure 60:: Instantaneous power output for a 5 MW wind turbine before, during and after a 1-hour icing event for different operational strategies in a 24-hour operational period. 119
Figure 61a-d: Energy payback time (t_{EPB}) for ambient temperatures (T_{AMB}) of -30 °C (a), -20 °C (b), -10 °C (c) and -5 °C (d) 122
Figure 62: Ice mass accumulation on the wind turbine rotor during an extreme icing event and its variation for TSR_{DI} 5 to 7.5 (b) 123
Figure 63: Performance graph indicating the variation in net daily energy loss for ambient temperatures ranging from -30 to -5 °C when derating, AIS and shutdown ice mitigation strategies are utilised. 123
Figure 64a-b: Number of icing days per year, which are required for the AIS Area 1 (a) and AIS Area 2 (b), at surface temperatures of 5°C, to be a viable solution, given the expected daily energy losses for other ice mitigation operational strategies 125
Figure 65 a-d: Daily energy loss (a and c) and total ice mass (b and d) for a 1-hour long icing event at a wind speed of 7 ms^{-1} (a-b) and a milder 4-hour long icing event at a wind speed of 10 ms^{-1} (c-d). 127

Figure 66a-b: Number of icing days per year, which are required for the AIS Area 1 (a) and AIS Area 2 (b), at a surface temperature of 5 °C, to be a viable solution, given the expected daily energy losses for other operational strategies; the wind speed is 7 ms-1 127
Figure 67a-b: Number of icing days per year, which are required for the AIS Area 1 (a) and AIS Area 2 (b), at a surface temperature of 5 °C, to be a viable solution, given the expected daily energy losses for the other operational strategies; the wind speed is 10 ms^{-1} 128

Appendices

Figure A1. 1: The wall treatment of the aerofoil at the leading edge with prism layers transitioning to the triangles 137
Figure A1. 2: The wall treatment of the aerofoil at the trailing edge with prism layers transitioning to the triangular main mesh 138
Figure A1. 3: Y+ value for distribution resulting from setting the first prism layer height to 3×10^{-7}, the growth rate to 2 and the total number of layers to 15. 138
Figure A1. 5: Representative convergence criteria graph for the current CFD numerical setup, showing the absolute residuals after solving the continuity equation (continuity), the velocity in x (x-velocity) and y (y-velocity) direction, the turbulence kinetic energy (k) and the specific turbulent dissipation rate (omega); which are all outputs from the k-w STT model. 139
No table of figures entries found.

Figure A3. 1: The conical stylus used to perform the measurements with cone radius of 60 ° and tip radius of 0.002 mm 142
Figure A3. 2: Surface roughness profile on the chosen patch from the leading edge of the printed aerofoil 143

Figure A4. 1a-d: Pressure coefficient distribution at time intervals of 0 (a), 0.25 (b), 0.50 (b) and 1.0 (d) hours during one-hour extreme icing event for NACA 64-618 aerofoil, simulated at Re of 6×10^{6} with XFoil and Fluent k-w SST turbulence model for angle of attack of 4.5 ° 144
Figure A4. 2a-b: Pressure coefficients for the iced NACA 64-618 aerofoil at section D, for angle of attack of 4.5°, after 0.5 (a) and 1.0 (b) hours of icing at reduced tip speed ratio of 5.0 and Re of 6×10^{6} 145

Figure A5. 1: Ice shapes formed at four different sections along the NREL 5 MW wind turbine blade at the end of icing event A1010. 146
Figure A5. 2: Ice shapes formed at four different sections along the NREL 5 MW wind turbine blade at the end of icing event A105 147
Figure A5. 3: Ice shapes formed at four different sections along the NREL 5 MW wind turbine blade at the end of icing event A710 147
Figure A5. 4: Ice shapes formed at four different sections along the NREL 5 MW wind turbine blade at the end of icing event A75 148

Figure A5. 5: Ice shapes formed at four different sections along the NREL 5 MW wind turbine blade at the end of icing event A510 148
Figure A5. 6: Ice shapes formed at four different sections along the NREL 5 MW wind turbine blade at the end of icing event A55 149
Figure A5. 7: Ice shapes formed at four different sections along the NREL 5 MW wind turbine blade at the end of icing event B1010 149
Figure A5. 8: Ice shapes formed at four different sections along the NREL 5 MW wind turbine blade at the end of icing event B710 150
Figure A5. 9: Ice shapes formed at four different sections along the NREL 5 MW wind turbine blade at the end of icing event B75 150
Figure A5. 10: Ice shapes formed at four different sections along the NREL 5 MW wind turbine blade at the end of icing event B510 151
Figure A5. 11: Ice shapes formed at four different sections along the NREL 5 MW wind turbine blade at the end of icing event C1010 151
Figure A5. 12: Ice shapes formed at four different sections along the NREL 5 MW wind turbine blade at the end of icing event C105 152

List of Tables:

Table 1: Definition of icing events A, B and C, at different wind speeds (V) and temperature (T). 63
Table 2: NREL 5 MW wind turbine blade aerodynamic properties as defined in (Jonkman et al. 2009: p. 7) 64
Table 3: Average values of mesh skewness, orthogonal quality and aspect ratio indicating the overall mesh quality. 74
Table 4: The solver and discretization setup used in Fluent 19.0 to design the CFD numerical analysis for this research 74
Table 5 Clean aerofoil CL and CD at 4.5° angle of attack as measured in the open circuit low-speed Coventry University wind tunnel, the DTU subsonic wind tunnel from Hudecz (Hudecz 2014), predicted by XFoil, Fluent with k-w SST model for smooth and rough surface 85
Table 6: Lift coefficient 1-hour degradation; at 4.5 ° angle of attack; for C105; as modelled using the experimental setup and as predicted by XFoil and Fluent k-w SST numerical tools 89
Table 7: Drag coefficient values obtained with the wake measurement method for angle of attack of 4.52 °, Re of 130 000 and two ice shapes generated for two different TSR settings... 91
Table 8: The lift coefficient of NACA 64-618 aerofoil for Re of 130 000 and four ice shapes, which was obtain by three different methods for performance evaluation. 92
Table 9 : Lift coefficient degradation for ice shapes obtained after 0.25, 0.50 and 1.0 hours of icing, as predicted by XFoil and the k-w SST turbulence model 94
Table 10: C_D of NACA 64-618 as Section D of the NREL 5 MW wind turbine blade, at an angle of attack of 4.5 °, for ice shapes obtained at 0., 0.25, 0.5 and 1.0 hours during an extreme one-hour icing, as predicted by XFoil and Fluent k-w SST for Re of 6×10^6 94
Table 11: The lift coefficient of NACA 64-618 aerofoil at angle of attack of 4.5 °, for Re of $6x10^{-6}$, when ice shapes, at Section D of the wind turbine blade, reduce due to changing the operational TSR from 7.5 to 6.5 during an extreme one-hour icing event 95
Table 12: C_D of NACA 64-618 as Section D of the NREL 5 MW wind turbine blade, at an angle of attack of 4.5 °, for ice shapes obtained at 0.5 and 1.0 hours, while derating the wind turbine from TSR of 7.5 to 5 during an extreme one-hour icing, as predicted by XFoil and Fluent k-w SST for Re of 6×10^6 96

Appendices

Table A3. 1: Measured parameters 143
Table A3. 2: Surface roughness analysis parameters 143

Nomenclature

Variables

A	Area	(m^2)
A1	Cost to use anti-icings	(£)
a	Axial induction factor	(-)
a′	Tangential induction factor	(-)
B	Number of blades	(-)
B1	Financial losses due to icing	(£)
C	Coefficient	(-)
c	Aerofoil chord length	(m)
c_e	Price of electricity	(p/kWh)
Cp	Power coefficient	(-)
D	Drag force	(-)
F	Force	(N)
E	Energy	(MWh)
g	gravitational acceleration	(ms^{-2})
h	Hour	(3600s)
I	Initial investment	(£)
i	Section counter	(-)
k	thermal conductivity	($Wm^{-1}{}^{o}K$)
L	Lift force	(N)
LWC	Liquid water content	(kgm^{-3})
M	Mass	(kg)
$\dot{m}$	Mass Flux	($kgm^{-2}s^{-1}$)
MVD	Median volume diameter	(m)
N	Number of icing days	(day)
n	normal vector	(-)
P	Power	(W)
P_W	Wind power	(W)
q, q”	Heat flux density	(kWm^{-2})
R	Radius	(m)
r	Blade radius	(m)
S	Surface area	(m)
s	Relative coordinate	(m)
s’	Integration limit	(-)
r	Blade radius	(m)
T	Temperature	(°C)
t	Time	(h)
V	Wind speed	(ms^{-1})

Greek

α	Angle of attack	(º)
β	Collection efficiency	(-)
γ	slip angle	(º)
θ	pitch angle	(º)
λ	Tip-speed ratio	(?)
ξ	Source strength	(?)
ρ	Air density	(kgm^{-3})
σ	solidity	(-)
ς	Dipole strength	(?)
Φ	Velocity potential	(?)
ϕ	inflow angle	(º)
ψ	Direction vector	(-)
ω	Rotor Rotational Speed	($rads^{-1}$)

Subscripts

A, B, C, D	Blade section location
24	24 hours
AI	After icing
DI	During icing
d	Drag
drp	Water Droplet property
CAPEX	Capital cost
EPB	Energy payback
e	Evaporation
f	Freezing
ICE	Property of ice
im	Impingement
ke	Kinetic heating
l	lift
lat	Latent heating
M	Modified operational strategy
N	Normal direction
nc	net convective heat
O&M	Operations and maintenance cost
R	Reference operational strategy
S	Operational shutdown
Surf	Surface
sens	Sensible heating
sh	Shedding

st	Standing
T	Tangential direction
rb	Run-back from\to other area
rel	Relative to the blade
req	Required

Acronyms

AIS	Anti-icing system
AoA	Angle of attack
BEMT	Blade element momentum theory
CC	Cold climate
DU	Delft University of Technology
NACA	National Advisory Committee for Aeronautics
NREL	National Renewable Energy Laboratory
TSR	Tip-speed ratio

1 Introduction

1.1 Background

Renewables have become a significant part of the global energy mix with increasing share every year and growing to over 33% of the global electricity generation capacity in 2018 (REN21, 2019: p. 29). The net annual energy additions between 2014 and 2018 increased from 50% to 65%, with yearly investments in the sector over USD 230 billion. In 2018, 18.9% of the EU gross consumed energy was generated by renewables (Eurostat 2020); for Austria, Sweden and Denmark, three fifths of the total consumed energy was generated mainly from hydro and wind power.

For the past 15 years, wind energy has always been the biggest contributor to the global energy mix among modern renewables (*i.e.* solar, wind, ocean, CSP and geothermal energy), as reported by REN21. Although currently it is the second in terms of newly installed renewable energy sources, power generation cost from wind is projected to remain the most cost-effective option for newly installed power plants in comparison to solar, coal and gas (BP 2017c: 42). In 2018, the total installed capacity of 591 GW was reached, marking a yearly growth of 9% (GWEC, 2019: p. 22) and accounting for 5.5% of the global electricity energy production (REN21, 2019: p. 30-32). Over the last 18 years the cumulative growth of the wind energy sector has been steady, as shown in Figure 1. The major share of wind energy is installed onshore, as the share of offshore installations in the end of 2018 came to 4% of the total installed production capacity.

The identification of suitable wind site locations is one of the main objectives during wind farm development. The requirements include steady and relatively high average wind speeds, road access, power line connections and clearance above ambient vegetation and orographic objects. Most of the requirements are typically addressed with the choice of a geographical location and relevant consideration can be made during the design phase of wind projects to account for variations. However, wind speed steadiness cannot be ensured because of its hourly, daily and yearly variation. Wind turbines are designed to operate in different regimes so that optimal energy convergence can be achieved for each wind speed. This is realised by installing various instrumentation units to monitor environmental parameter, which are then used by wind turbine controllers to adjust the operational parameters of the wind turbine so that optimal or near optimal power performance is ensured.

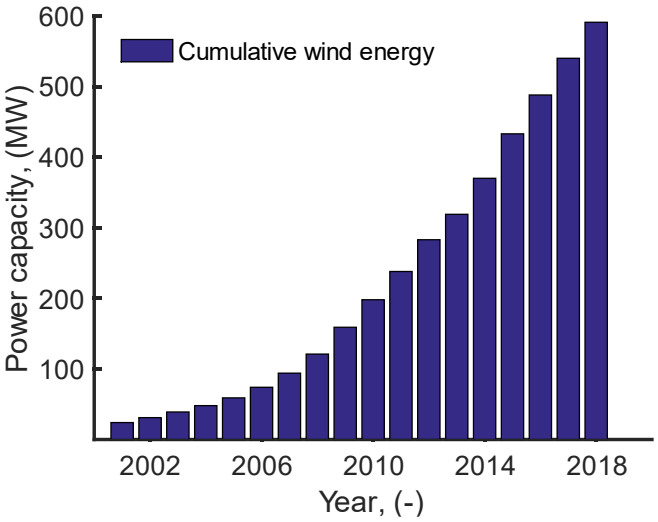

Figure 1: Cumulative wind energy capacity between 2001 and 2018 (GWEC, 2019: 28)

The importance of optimal wind turbine operation is mostly pronounced for locations, which provide extremely favourable conditions for wind energy generation, but their climate imposes challenges upon exploitation. Non-conventional wind turbine such as Cold Climates, where frequent atmospheric icing and/or temperatures below the operational limits of wind turbines exist (Bredesen *et al.* 2017: p. 12)(Bredesen et al. 2017: p. 12) are characterised with increased wind resources, but their hostile climate leads to wind turbines operating in extreme environmental conditions, (Battisti, 2015: p. 1-3). It has been reported that more than 10% energy from wind can be generated in cold climate (CC) sites due to increased air density and favourable wind speed vertical gradient (Fortin *et al.*, 2005: p.1). This highlights the importance of CC potential wind sites and the interest in exploiting them. According to latest reports approximately 25% of the total installed wind capacity operates in cold climate conditions and it has been forecasted that this proportion is going to remain the same for newly developed wind farms (Karlsson 2017: p. 17).

Cold climates are characterised as areas, where either icing occurs on regular basis (Icing Climate) or wind turbines operate in low temperatures outside their design operational limits (Low Temperature Climate) (IEA, 2017). Additional features of CCs include prolonged period of the year with ambient temperatures below 0 ºC, clouding in the proximity of the ground, average elevation of 700 – 800 a.m.s.l., complex terrains, high turbulence and extreme gusts (Battisti 2015: p. 2). Operating wind turbines in such conditions is challenging because of the detrimental impact that ice build-up has on power performance, safety and maintenance (Laakso et. al 2010, Bredesen *et al.*2017). Ice induced energy losses can exceed 20% of the annual energy production (AEP) depending on geographical location and wind turbine size (Bredesen *et al.*2017, Tammelin *et al.*2000). For wind turbines in close proximity to roads and populated areas, ice throw presents a significant safety concern, as ice can shed and fall from wind turbine rotors for up to a few hundred meters, creating concerns for cars, buildings and

human beings (Sarlak and Sørensen 2015). Additional structural loads and low temperatures lead to prolonged and expensive maintenance (Barrin-Gould *et al.*2010).

The greatest impact that icing has on wind farms is the reduction of power output, which directly influences negatively the viability of a project and the investment flow related to it, (Krenn *et al.* 2016: 7). The return of the initial investments is crucial for the future of potential wind farms, which makes the preliminary assessment of a wind site and the expected power output a prime concern, (Homola, Matthew 2005: 6). Operating wind turbines in CCs and the associated risks with ice occurrence have been recognised as an engineering challenge since 1980 (Mortimer 1980). A great body of work has been generated since then, dealing with understanding the ice formation process and its impact on wind turbine power performance and longevity (WECO, VTT, TASK 19). The main body of research on wind turbine icing has been done on developing recommended practices for operation, aerodynamics of iced aerofoils, ice accretion models, ice throw models, statistical and numerical models for predicting and estimating ice losses, but few have looked at ice mitigation techniques and their integration into operational strategies.

To adapt wind turbines for the harsh environment in cold climates, various ice mitigation techniques have been researched and developed. Mainly operational shutdown and thermal anti/de-icing systems have been used, as the former being more intuitive approach, while the latter has been used successfully to mitigate in-flight icing on airplanes. Passive approaches such as black paint, flexible/modified blades, water repellent coatings and chemical de-icing have been considered as options to tackle icing, but commercially available solutions are yet to be established. The viability of each ice mitigation techniques varies with location, machine scale and icing conditions, which makes it challenging for wind turbine operators and manufacturers to adequately adapt wind turbines to icing conditions. This challenge can be addressed by designing effective operational strategies for icing conditions, which would ensure optimal operation. The need for new methods and techniques, which enables the evaluation and comparison of different ice mitigation operational strategies was also recognised by Fakorede *et al.*2016 and Laakso *et al.*2005. More efficient approaches to operate wind turbines in icing conditions would greatly facilitate the exploitation of current and future wind sites in CCs (Cattin 2012: p. 23, Bredesen *et al.*2017: p. 3-6).

This project set out to provide solutions for reducing the investment risk related to wind energy generation in cold climates. The aim of the project was to improve wind turbines performance in cold climates through advancements in the implementation, comparison and selection of ice mitigation operational strategies. This will enable wind turbine operators to reduce the uncertainties in energy generation due to icing by choosing an optimal operational strategy or a set of strategies for a wind site location of interest. Moreover, approaching the problem of wind turbine operation in icing conditions by using such analysis would promote more holistic and functional studies for the future with a focus on the smart and efficient exploitation of cold climate wind sites.

The research questions, which follow from the project aim are:

1. What is the uncertainty in predicting aerodynamic degradation due to icing when using low computationally intensive tools?

2. How can a wind turbine operational strategy be designed to improve wind turbine output during icing conditions without the installation of additional systems?

3. How can alternative ice mitigation strategies be evaluated and selected to improve wind turbine adaptation to cold climates?

The project's objectives that are aligned with the aim and the research questions were chosen as follows:

- Choose a representative horizontal-axis utility scale wind turbine to be used as a reference wind turbine for ice accretion, aerodynamic and power output analyses
- Define icing conditions and events that can be used to obtain representative ice shapes for a typical utility scale wind turbine to model the detrimental impact on the aerodynamic efficiency and power output from ice build-up
- Estimate the expected ice induced energy losses for the chosen icing conditions
- Determine the difference in predicted losses when using XFoil, Fluent and experimental data
- Set out a method for the systematic implementation of derating
- Model the changes in the performance of the wind turbine when different ice mitigation techniques are incorporated and define when each is a preferred option for operation
- Provide suggestions on the use of the considered ice mitigation strategies and how their viability would change for different operational, financial and environmental conditions.

1.2 Thesis outline:

This chapter has shown that wind energy is one of the most established branches in the renewable sector for electricity generation and it can be further developed by utilising wind site in Cold Climates. The potential of utilising Cold Climates siting where the adverse impact of icing needs to be addressed was also outlined. The need for developing improved operational strategies to reduce energy losses was identified. The chapter defines the aim, objectives and the research question, which tend to investigate improved techniques and methods for ensuring optimal wind turbine adaptation to Cold Climates and maximum energy yield.

In chapter two, background information is provided on ice formation types and the general ice shapes that are of practical interest. A brief overview of aerofoil and wind turbine performance for conventional operational conditions is included with focus on the relevant performance characteristics that are used to model wind turbine operation in icing conditions. The quasi-3D numerical modelling approach was found as the only suitable method for investigating operational strategies with the capability of modelling and analysing all icing and operational parameters. The need to develop a design procedure for power optimisation strategies realised with operational tip-speed ratio modification was identified. In addition, a particular gap was found for tools enabling the comparison and selection of operational strategies ensuring optimal wind turbine performance for different icing conditions. The literature review showed that tip-speed ratio modification and anti-icing are two promising ice mitigation strategies that could be used to develop and demonstrate methods for selection and evaluation of operational strategies.

The overall methodology that was followed to design and advance current ice mitigation operational strategies for improved wind turbine performance in icing conditions is outlined in chapter 3. The experimental and numerical methods used for modelling the wind turbine performance and the design parameters for the design methods developed in this thesis are presented and explained.

In chapter 4, the experimental design used to measure the lift and drag characteristics of 3D printed aerofoils is described. Measured and numerical results are analysed for 7 different icing shapes for a Reynolds number of about 160 000. The variation in estimated icing losses due to the choice of a simulation tool was obtained by simulating the same ice shapes of operational Reynold number with XFoil and Ansys Fluent. The percentage difference that can be expected when using a low computationally intensive tool as XFoil is defined in comparison to the results that can be obtained with a CFD tool.

The fifth chapter studies the potential implementation of alternative tip-speed ratio operational strategy for derating to mitigate the icing losses. A systematic approach was developed for the choice of tip-speed ratio value during and after icing. It is based on the rotational speed of the shaft of the fitted electrical generator and the estimated payback time to recover the lost energy

from intentional tip-speed ratio reduction during icing. The results from the study are presented, which are then used to identify in what conditions the operational strategy would be preferred for ice mitigation.

In the sixth chapter, a method based on ice-induced energy losses, ice mass and viability of implementing anti-icing has been outlined to evaluate and compare different ice mitigation operational strategies. The method was demonstrated for three icing events and considering a 24-hour period of operation for the analysed wind turbine. The results, which showed how the viability of three ice mitigation operational systems change depending on the icing and operational parameters are presented. When each operational strategy would be a preferred choice for ice mitigation was specified based on the obtained data.

The last chapter summarises the findings of the current project and to what extent the research questions defined in the beginning have been addressed. How the current methodology can be further developed and what future topics would be beneficial for future research is also covered.

2 Literature Review

2.1 Cold Climates: Icing Types and Ice Accretion Theory

2.1.1 Icing Types

The most affected wind installation sites from icing are situated in North America and Europe, where wind power operating in CCs has been predicted to reach 114.4 GW by the end of 2020, which makes it the biggest market for “non-standard” wind turbine sites exploitation (Lehtomaki *et al.* 2018: p. 9). Icing can be an issue for large areas in Europe and its intensity increases with altitude and latitude, as shown by Figure 2. Mountainous and coastal areas are shown to be the most affected, with icing frequency of more than 15 days per year, which is caused by air with increased humidity. This is due to warm maritime air being cooled down when moving from areas with low elevation to areas with high elevation (*i.e.* mountains) and increased wind velocities due to funnelling in mountain passes (ESA 2001: p. 9-10). The combination of increased humidity and low temperatures creates favourable conditions for ice formation.

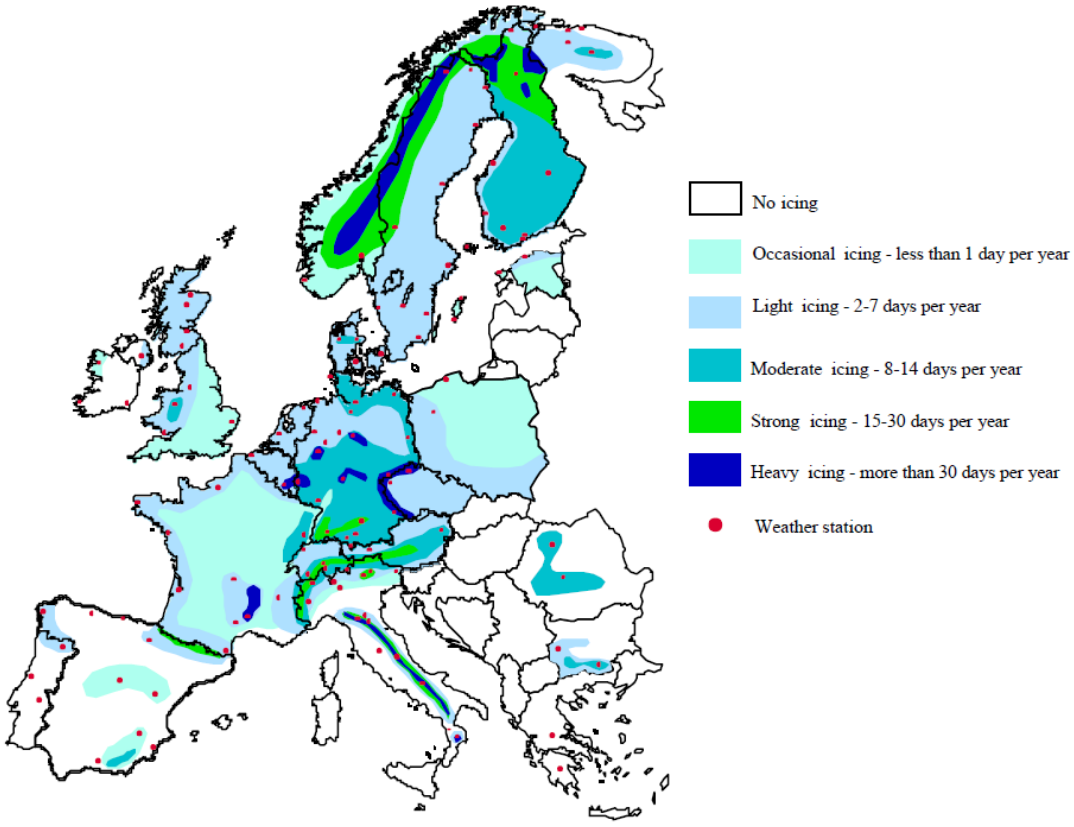

Figure 2: Icing map of Europe based on data obtained from 120 meteorological stations for in-cloud icing leading to rime ice formation (Tammelin, B. et al. 2000: p. 10)

Atmospheric icing on structures can be formed by either precipitation or in-cloud icing (ESA 2001: p. 6). Precipitation icing occurs, when freezing rain or snow sticks to the surface of a

structure and subsequently freezes, which can result in an ice formation with high adhesion strength (Dalili, Edrisy and Carriveau 2007: p. 431). For wind turbine applications, in-cloud icing has been identified as the most severe icing phenomenon and unlike precipitation icing, it is challenging to forecast and icing rate data is either not observed or measured (Tammelin, B. *et al.* 2000: p. 8-10). In-cloud icing occurs when supercooled water droplets exist in a cloud with extremely low temperature (Parent and Ilinca 2011: p. 2-3). When the height of a structure is higher than the cloud base-height, supercooled water droplets impact its surface and subsequently freeze. This is a common issue currently for utility-scale wind turbines, as rotor blades can easily be subjected to this sort of icing due to their elevation above ground level, and especially for wind turbines located in hilly regions.

Based on the properties of the formed deposition, glaze and rime ice types can be identified. Glaze icing forms during wet in-cloud icing events, which are characterised by medium to large LWC and droplet diameters. Such events are common for ambient temperatures above -10 ºC and as very little oxygen is entrapped in the ice, it appears transparent and its adhesion force to the iced surface is strong. For lower LWC, droplet diameters and ambient temperatures, rime icing forms, which can be either with strong (hard rime) or weak (soft rime) adhesion force to the iced surface. When the ambient temperatures are extremely low and only small supercooled water droplets are present, the resultant ice has white colour due to the higher amount of entrapped oxygen. It should be noted that often the ambient conditions fluctuate and depending on the combination of the different parameters a mixed type of icing can form, which possesses some of the features of both rime and glaze. However, for engineering purposes, typically only rime and glaze icing conditions are used to define an icing event. The main difference between the two types of icing are the resultant ice shapes that form depending on the type of structure and the density of the deposition. Glaze ice has usually higher density (900 kgm^{-1}) than rime ice (200-900 kgm^{-1}).

The formation of ice is a result of the combination of many parameters – wind speed, ambient temperature, liquid water content in the air (LWC), diameter of droplets, structure dimensions, icing duration, local topographical features and humidity. The rate of ice accumulation of a structure is proportional to the LWC and is a function of the cube of the droplets' velocity. For wind turbines, the icing process is more dynamic leading to more accumulated ice than structures with no moving part such as guy wires, meteorological masts and buildings, as wind turbine blades see higher relative wind speeds. Figure 3 and Figure 4 depict how the transition limits between rime and glaze can change based on conditions (*i.e.* operational and environmental) or blade location, respectively. It should be noted that for each graph the parameters that have not been defined are fixed. The variables, which affect the icing process have a wide range of variation and it is difficult to standardise icing or define strict limits, which show when to expect a certain type of icing.

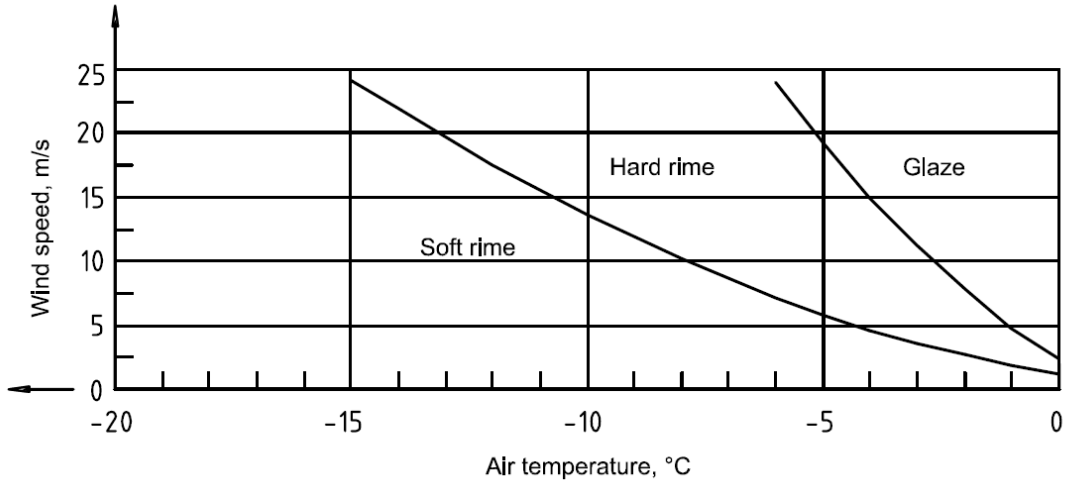

Figure 3: Ice accretion type transition during an atmospheric icing on a structure as a function of the ambient temperature and the wind speed. Data based most likely on standard rotation cylinder as included in ISO standard for atmospheric icing on structures, (ESA 2001: p. 7)

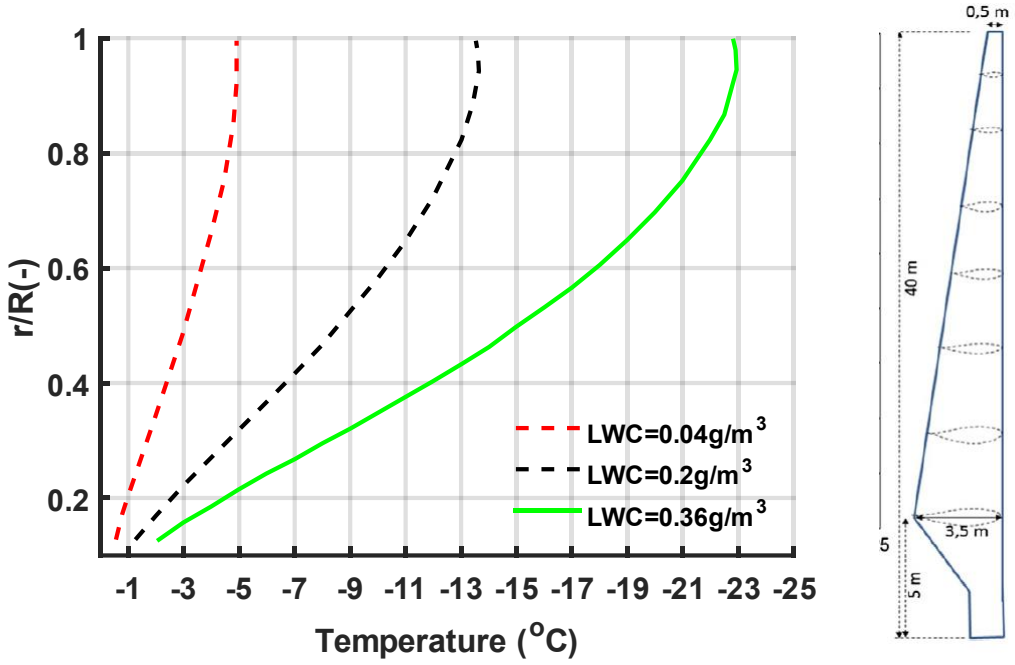

Figure 4: Transition from glaze to rime along the blade of a wind turbine as a function of the ambient temperature and the liquid water content (Lamraoui *et al.* 2014: p. 42)*. For each graph, the region on the left depicts when glaze ice would form, while the region on the right shows when rime icing would occur.*

Most commercial wind turbine blades are designed as lift generating devices, which are constituted of aerodynamically shaped streamline cross sections (aerofoil sections). The aerodynamic efficiency of aerofoils is mostly a property of their shape. When ice deposits on the aerofoil surface, the aerodynamic efficiency deteriorates. This is generally well known from previous research on aircraft icing (Bragg, Broeren and Blumenthal 2005, Laakso *et al.* 2010, Tammelin, B. *et al.* 2000, Tammelin, Bengt and Seifret 2001), and many studies are now focusing on the implications for the wind energy industry. Rime and glaze icing types are defined based on the physical properties of the ice accretion, which does not indicate clearly

what the geometrical changes of the aerofoils will be and how these changes will affect the final aerodynamic performance/efficiency. Therefore, the ice accretion process needs to be defined considering the mechanisms of its formation and final shape rather its final physical properties only.

2.1.2 Ice Accretion Theory

The final ice build-up shape on a wind turbine blade varies widely with the possible combinations of weather and operational parameters. Depending on the ambient conditions, dry and wet ice growth can be observed. Dry growth occurs when all of the entrapped supercooled water droplets freeze upon impact with the aerofoil surface, which often leads to ice formation conformal to its shape, and typically has the properties of rime. Wet growth is characterised by both ice and water presence on the aerofoil surface. As only a part of the impinged water freezes upon impact, water film, rivulets and beads can be observed during wet ice growth with ice properties typical for glaze. When the water freezes, more complex ice shapes are formed as water flows on an already formed ice layer driven by surface tension, wind shear and aerodynamic forces. Additional challenge to the definition of icing is the fact that dry growth can transition to wet growth due to the temperature gradients in the ice and water layers and the ambient conditions, (Myers 2001). Moreover, ice layers are often not homogenous, and their physical properties (*i.e.* density, strength, surface strength) can vary in the same formation, which is important for ice shedding (WECO).

The final shape on a wind turbine blade can only be determined through modelling, which includes all processes that lead to ice build-up. As stated in (Battisti 2015a), ice shapes are a result of: the meteorological processes leading to the generation of liquid water in the air; mechanical processes associated with the dynamics of the water droplets in the carrying flow and the impinged water on the blade's surface; thermodynamic processes, which characterise the build-up of ice layers; processes related to ice shedding, which are governed by the properties of the ice formation, centrifugal forces, vibrational forces and ambient conditions. Different models have been developed to study and predict the processes, which affect icing. Previous research has focused mostly on the processes, which look at the formation of icing layers on the aerofoil surfaces rather than on modelling meteorological processes typically needed to obtain input parameters for ice accretion models. Often the weather parameters (LWC, droplet diameters, ambient temperature, humidity and wind speed) are taken as constants during ice accretion analyses. However, to evaluate the potential icing impact for a wind site over long period of time, weather research models are used (Lehtomaki *et al.* 2018: p. 18-20).

Ice accretion models are based on determining how much water is collected by the geometry under consideration (body wetness) and what part of it freezes. For aerofoils, the body wetness depends on the quantity of water in the air (LWC), the moment of inertia of droplets (function of velocity and droplet diameter) and the frontal area of the body, which is perpendicular to the

direction of the incoming flow. The water droplets tend to reach the surface of aerofoils when their moment of inertia is high (larger diameters and high velocity) and the aerofoil chord lengths are relatively small. Upon impingement, water can freeze immediately, freeze after a certain period of time, shed or evaporate as displayed on Figure 5. The dynamics of water droplets before and after hitting the aerofoil's surface is typically modelled by droplet trajectories calculation and mass balance, respectively. The single parameter, which have been introduced to characterise how much of the incoming water reaches the aerofoil is called the collection efficiency. It is defined either locally (local collection efficiency, β) or as an absolute value (total collection efficiency, E). The modelling of the parameter can be done empirically (Finstad, Lozowski and Gates 1986), by integrating droplet trajectories using the Langrangian method (Brahimi, Chocron and Paraschivoiu 1998, Fortin, Perron and Ilinca 2007, Makkonen *et al.* 2001) or by applying the Euler method (Kinzel, Sarofeen and Noack 2010). The empirical formulation has been used in most first-generation ice accretion codes and it is based on the experimentally obtained values for a stationary or rotational cylinder. The Langrangian method is implemented in most of the established ice accretion codes such as LEWICE, TURBICE, CANICE, *etc.* The Euler method has been used recently for models, which make use of CFD packages and programming environments. It has been used in FENSAP-ICE, which is considered as a new generation ice accretion code, because the icing physics is modelled using partial differential equations rather than empirical formulations.

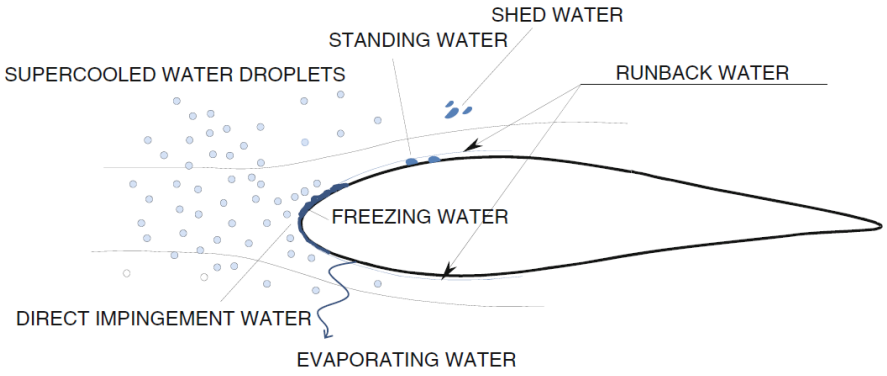

Figure 5: Water droplets dynamics about an aerofoil section and all modes of water capture and release from the surface (Battisti 2015a)

The amount of freezing water is determined by a thermodynamic analysis, which is applied at the surface, subjected to icing. Different modes of heat transfer are taking place on the surface of an aerofoil during icing. The challenges associated with determining them are mostly with the time-dependant nature of the ice build-up and the associated changes, which arise when considering the wide variability of the parameters that affect the icing process. All ice accretion models use an energy balance approach for determining how the ice layers will grow. Messinger (1953) introduced the idea of freezing fraction (f). For rime ice, f equals 1, which denotes that all of the entrapped water freezes, while for glaze the values of f range between 0 and 1. Similar approach was incorporated in the Makkonen's model (Makkonen and AUTTI

1991, Makkonen 2000), which applies an energy balance analysis to determine a parameter named ice accretion efficiency, which also takes values between 0 and 1 depending on how much water transitions to ice. The energy balance that is typically incorporated in ice accretion models is shown on Figure 6. The modes of heat transfer either add or extract energy at the ice-water region. Convection, sublimation (evaporation for warm ambient temperatures) and conduction cool down the surface and promote higher rates of ice formation, while viscous heating, kinetic heating by incoming droplet and heat of fusion add energy to the surface. Among all, the major drivers of the energy balance are convection and sublimation modes of transfer energy, as reported in (Battisti 2015b, Makkonen *et al.* 2001). When all modes of energy are determined, the amount of water, which freezes on the surface can be estimated. Then, the results are used to obtain ice thickness, which modifies the aerofoil's contour, leading to changes to all the parameters that define icing.

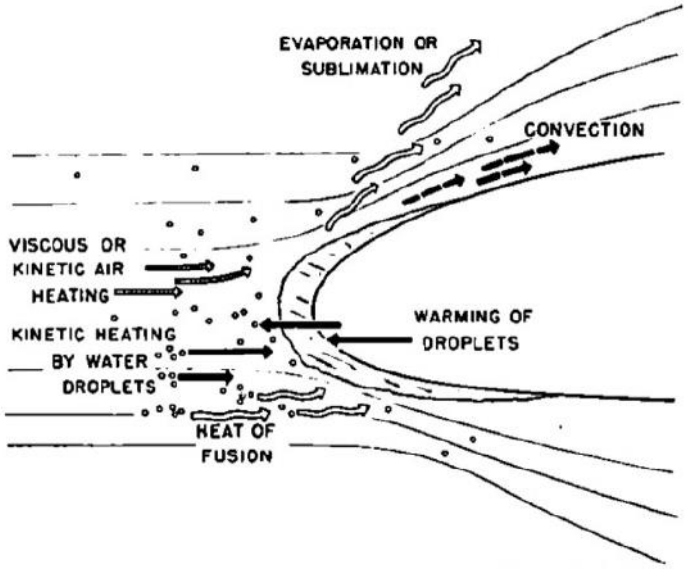

Figure 6: Modes of heat transfer occurring during icing of aerofoils (Messinger 1953)

2.2 Aerofoils and iced shapes

2.2.1 Aerofoils

Aerofoils are cross-sections of aerodynamically shaped geometries such as wind turbine blades and aircraft wings. Their aerodynamic properties are driven by their shape and geometrical features. For some conditions, the aerodynamic characteristics of blades and wings can be simply predicted from the known characteristics of their constituting aerofoils (Abbot and Doenhhoff, 1959: p. 2). For sub-sonic applications, aerofoils have rounded frontal area (leading edge), curved upper (suction side) and lower surfaces (pressure side) and slightly rounded, sharp or blunt end (leading edge) as shown on Figure 7. The shape of an aerofoil is defined by

2D coordinates (x, y), its camber (h/c) and thickness (t/c) distribution along the aerofoil's length. The distance between the leading edge (LE) and the trailing edge (TE) of aerofoils is called the aerofoil's chord, *c*, which is a main parameter for defining the aerofoil's scale and it is extensively used for non-dimensional expression of operational parameters. Experimentally, it has been established that there is a difference in the local static pressure and velocity distribution on the upper and the lower surfaces of the aerofoil. The local static pressure on the upper surface of aerofoils is lower than the static pressure of the carrying flow, while the opposite effect is observed on the aerofoil's lower surface.

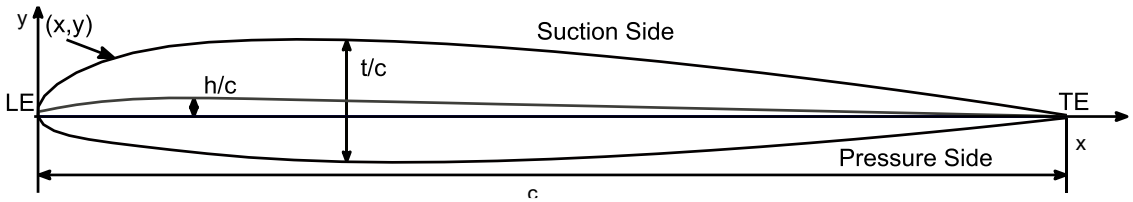

Figure 7: Schematics of the NACA 23012 aerofoil showing its geometrical features such as normalised camber (h/c), normalised thickness (t/c), chord (c), leading edge (LE), trailing edge (TE), Suction Side, Pressure side notation and the two-dimensional definition of the aeorfoil contour using coordinate points with x and y coordinates.

Due to the differences in the pressure distribution on the upper and the lower surface, a resultant force, R (N), acting on the aerofoil is generated, as shown on Figure 8. The component of the force, which is perpendicular to the direction of the airflow velocity is called lifting force, L (N), while the component of the force acting in streamwise direction but against the direction of motion of the aerofoil is called drag, D (N). Due to the pressure distribution around the aerofoil a pitching moment is generated, which tends to increase the angle at which the aerofoil is positioned (angle of attack/ α (º)) in reference to the velocity vector of the carrying flow, V_∞ (ms^{-1}). Lift and drag forces can be calculated by knowing the density of the flow, its velocity and the chord of the aerofoil as shown by Eq. 1 and Eq. 2. The performance of aerofoils is usually examined by studying the changes of the lift (C_L) and drag (C_D) coefficients with respect to the angle of attack as shown on Figure 9. There is a range of angles of attack, where C_L increases linearly ($\delta C_L/\delta\alpha = const$) and C_D is very low. This denotes that the flow is attached to the aerofoil surface. With the increase of the angle of attack, the drag increases as the flow starts separting from the aerofoils surface. C_L increases to a maximum value $C_{L,MAX}$, before the crticial angle of attack is reached. After this point the flow separates at the leading edge (*i.e.* stall), which is denoted by the reduction of the lift coefficient and the rapid increase in the drag coefficient.

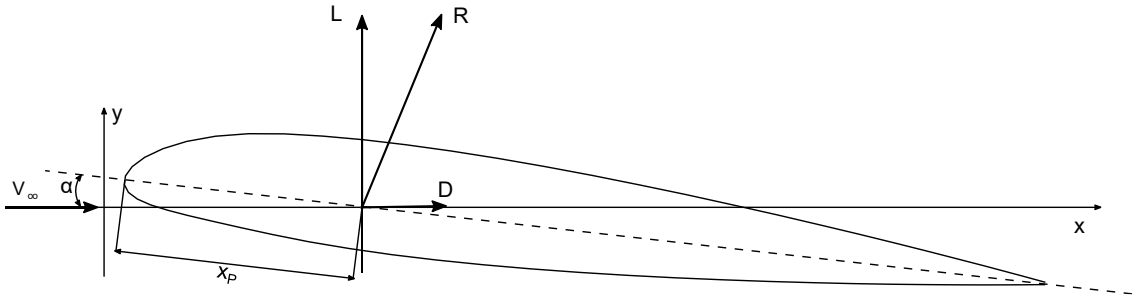

Figure 8: Integrated aerodynamic force (R), and its components (L and D), applied at the pressure centre of the aerofoil (x_P) as a result of the incmoing flow with velocity (V_∞) and angle of attack (α).

$$L = 0.5 C_L \rho V_\infty^2 c \quad (1)$$

$$D = 0.5 C_D \rho V_\infty^2 c \quad (2)$$

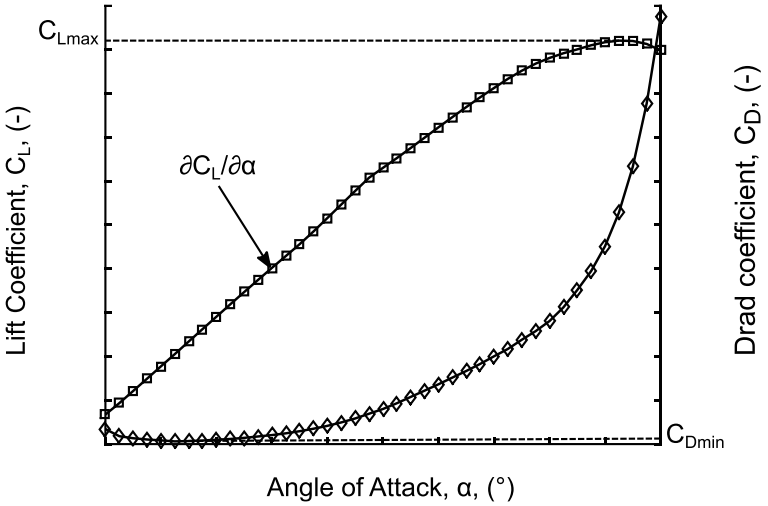

Figure 9: Aerodynamic characteristics (i.e. C_L and C_D) of an aerofoil as a function of the angle of attack (α) and denoting the points of minimum drag, maximum achievable lift coefficient prior to stall and the linear region of the lift curve, defined its slope ($\delta C_L/\delta$).

The total lift and drag forces are a function of the aerofoil's geometry and the flow conditions. They are a result of pressure and viscous (friction) forces. The pressure forces act on the aerofoil due to the interaction between the aerofoil and the carrying flow and they mainly affect the lift force, while the viscous forces act in an extremely thin region next to the aerofoil's surface (wall), called a boundary layer (BL) and they mostly affect the drag force when attached. The boundary layer is a result of the interaction between the aerofoil's surface and the airflow molecules. Its thickness and type of flow regimes affect the aerofoil's aerodynamic properties. The thickness of the boundary layer is defined by the relative velocity profile to the wall, which changes from 0, at the wall, to approximately the velocity of the ambient flow, at the maximum thickness of BL. The type of flow in the BL affects the aerodynamic characteristics of aerofoils.

The flow regimes in the boundary layer can be laminar and turbulent. The aerodynamic properties of aerofoils are determined by the location of transition between the two types, Figure

10. The laminar flow is characterised by the orderly development of the flow from the leading edge to some point (usually a region but often approximated with a point), where it transitions from laminar to turbulent. The turbulent boundary layer is characterised by chaotic movement of the flow molecules and mixing of the different layers. Laminar boundary layers lead to smaller resultant drag but are more susceptible to separation when angles of attack increase. The turbulent boundary layer is less susceptible to separation because of the higher stream-wise velocities and more momentum transferred from the edge of the boundary layer by vortical structures called eddies. However, due to the higher velocity gradient in a direction normal to the surface of the aerofoil, higher shear stresses occur in the vicinity of the aerofoil's surface, leading to higher drag values than the laminar case.

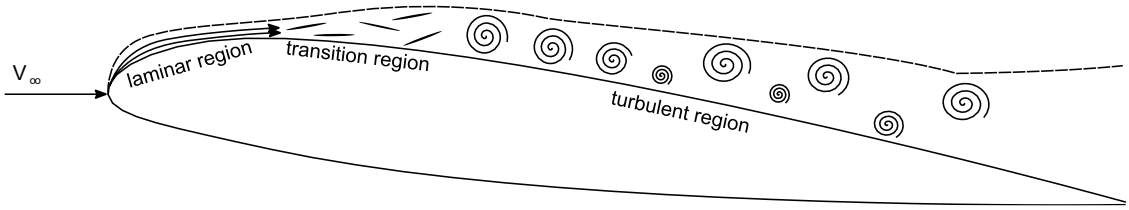

Figure 10: Laminar, transition and turbulent regions for an aerofoil and its developnig boundary layer from impingement on the leading edge to the trailiing edge. Boundary layer schematised for visualisation purposes only (Agrawal and Platzer 2018: p. 150).

The lift coefficients shown on Figure 9 are for cases when the flow is attached to the aerofoil surface (*i.e.* the boundary layer is wrapped around the aerofoil surface). When the adverse pressure gradients exist ahead of the development of the boundary flow, a reverse flow, leading to separation occurs, which is typically called stall. Few types of stall exist as shown on Figure 11: leading edge stall leading to either long or short bubble separation, and trailing edge separation, which could happen with or without the presence of fluctuating and bursting separation bubble. There have been reported cases when mixed separation occurs (Agrawal and Platzer 2018: p. 173).

The aerofoil's characteristics are often studied using non-dimensional parameters or also known as similarity parameters. Reynold's number (Re) and Mach number (M) are two dynamic parameters for similarity used by designers to define flow conditions and aerofoil operational states, which are the same for scaled and full-scale models. Re is the ratio of inertial forces to viscous forces, Eq. 3), and for wings and wind turbine blades is usually in order of millions. The M number is the ratio of local airflow velocity to the speed of sound, V_C (ms^{-1}), for set ambient temperature and pressure of the ambient air, Eq. 4. M numbers for wind turbines and aircraft wings for general and commercial aviation are mostly below 0.35, which has been established as the region where a simplified aerodynamic theory can be used to predict the performance of wings and wind turbine blades without considering the compressibility of the air.

$$Re = \rho V_{\infty} c/\nu \quad (3)$$

$$M = V_\infty / V_c \quad (4)$$

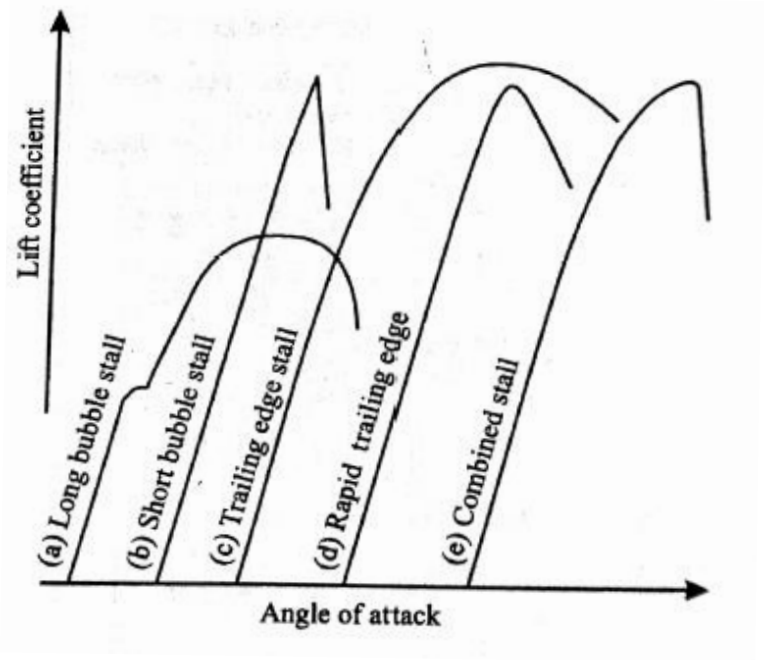

Figure 11: Types of aerofoil stall and the variation of the lift coefficient for each type as a function of the angle of attack (Agrawal and Platzer 2018)

2.2.2 Ice Shapes

Although no official characterisation has been established for icing shapes, previous research, which was based on the review of a vast experimental data on icing for aerofoil, has defined four main types of icing shapes – roughness (Figure 12), horn (Figure 13), stream-wise (Figure 14) and span-wise icing (Figure 15). In most of the cases, the icing leads to reduction in the maximum lift coefficient, increase in the drag due to earlier transition of the boundary layer or separation, reduction of the critical angle of attack and changes in the types of stall of the aerofoil.

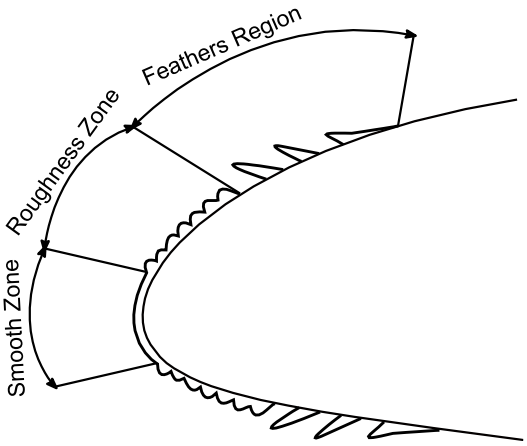

Figure 12: Roughness ice shape on the leading edge of an aerofoil with the three distinctive zones, which usually are observed – smooth, roughness and feathers (Bragg, Broeren and Blumenthal 2005)

Roughness typically occurs during the onset of icing and its impact on the aerodynamic performance is a function of the roughness height of the individual beads and its roughness density. The greater the height of individual beads, the bigger the influence on the aerodynamic performance. The roughness density affects the aerodynamic performance when it is less than 30%. Roughness ice causes a premature transition of the boundary layer, which affect the lift and the drag. Typical reduction of the lift and increase of the drag can range between 10 – 40% and 50 – 200%, respectively. In addition, roughness ice type can change the stall characteristics of an aerofoil from trailing edge stall to leading edge stall.

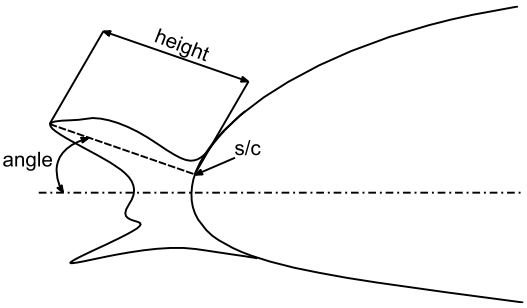

Figure 13: Double horn ice shape, formed at the leading edge with upper horn defined by its angle of inclination, height and location at the upper surface of the aerofoil s/c

When the ice formation occurs for temperatures typical for glaze icing or during icing events with large droplet diameters, horn icing occurs. It is characterised by highly irregular shapes, which have either one or two horns, or dendritic type of protrusion. It greatly affects the aerodynamic performance of aerofoils due to the formation of large separation bubble behind the horn-like protrusions, which leads to temporal variation of the lift and drag. It has been reported that the shape and the roughness of the horn icing deposition have smaller effect on lift and drag than the height of the horn, its angle of orientation and its position along the surface of the aerofoil (Bragg, Broeren and Blumenthal 2005). Typical reduction of the lift for horn icing is between 5 – 85%, while the drag can increase up to 800%.

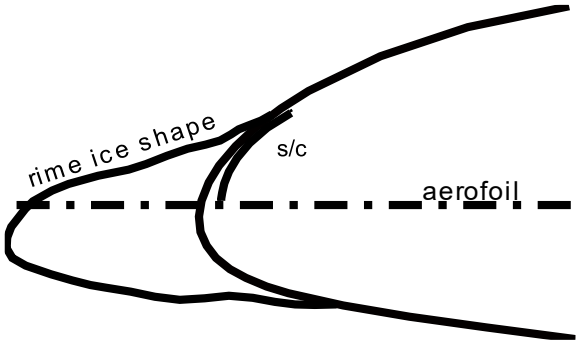

Figure 14: Typical stream-wise (rime) ice shape with conformal geometry to the aerofoil leading edge

Streamwise icing occurs during rime icing conditions when the impinged water freezes upon impact. Thus, the final shapes are usually conformal to the geometry for low angles of attack. The impact on the aerodynamic performance is less abrupt than horn icing, as usually the separation bubble does not form, or it is much smaller than for horn icing. It has been reported that in some cases streamwise ice formation can act as a leading edge slat, which increases the maximum lift coefficient. The reduction in lift for streamwise icing is between 5 – 10%, while the drag increase can be up to 300%. The length of the protrusion does not have significant influence on the generated aerodynamic forces; however, the roughness of the shape affects them and especially the drag.

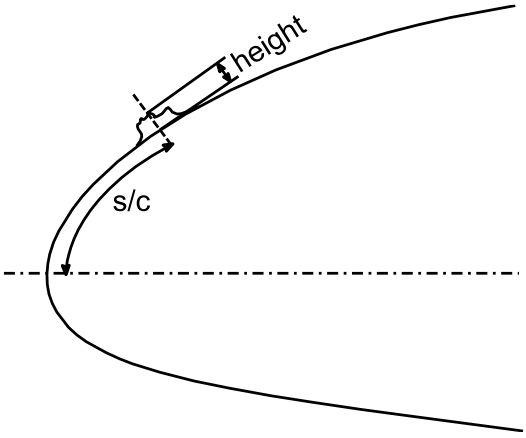

Figure 15: Spanwise-ridge icing shape on the upper surface of the aerofoil, defined by its location s/c, height and shape (Bragg, Broeren and Blumenthal 2005)

Spanwise ridge icing is typical for run-back ice accretion and when de-icing system is used. It acts as flow obstacle, which leads to separation both upstream and downstream of the location of formation. It greatly disturbs the flow and leads to significant aerodynamic degradation. The important parameters defining it are its location downstream of the leading edge, its shape and height. Some aerofoils can be affected to a lesser degree from this type of icing, which would depend on the location of the ice formation and the location of the minimum pressure peak of the aerofoil. Typical lift reduction is between 10 – 80%, while drag can increase by a factor of 2.3. For wind turbines, this type of icing has not been investigated extensively and the probability of it happening is related to the design of an anti/de-icing heating systems.

Aerofoil performance varies when Re is ranged from low to high values. The performance of iced aerofoil does not change significantly for horn-like shapes but has been reported to be of significance for roughness type of icing, as the separation point for the flow is not fixed. When iced aerofoils are studied for a wide range of Re, the performance of the clean aerofoil for the same range of Re should be available, as it has been shown that the degradation for the same aerofoil at low Re is different for high Re (Lynch and Khodadoust 2001)

2.3 Wind Turbines Operation in CCs

2.3.1 Non-iced rotor

Contemporary utility-scale wind turbines are typically designed as three-bladed, horizontal-axis machines, which convert wind kinetic energy to electrical energy as shown on Figure 16a. They are constructed by erecting the blades, which are fixed to a rotor hub that house the electrical generator, on a tower providing enough clearance from the ground and ambient vegetation so that the incoming wind flow is not disturbed. The generated power output depends on the efficiency of the wind turbine blades and the site-specific parameters, such as wind velocity and orographic features contributing to its unsteadiness. The direct power output of a wind turbine, P (W), is proportional to its conversion efficiency, C_p (-), the density of the air, ρ (kgm^{-3}), the square of its rotor diameter, D (m), and the cube of the wind velocity, V (ms^{-1}), as shown by Eq. 5 (Jha, A. R., Jha and Jha 2010: p. 86). As wind turbines operate in a given range of wind speeds, it is important to define their power curve, Figure 16b. The power curve shows how the power output of wind turbines vary with wind speeds, which is then used to estimate expected annual energy production (AEP) (Hansen 2008: p. 55-62). However, this requires a prior knowledge of the wind speed frequency distribution and the availability of the wind turbine.

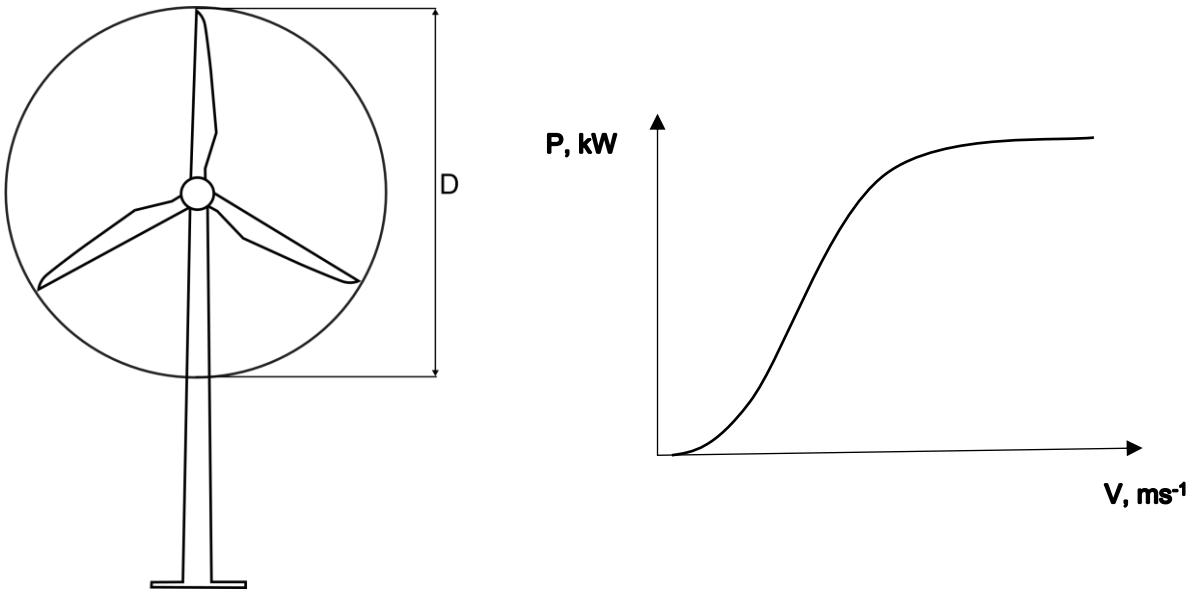

Figure 16: Drawing of a typical utility-scale wind turbine (a) and its power output as function of the operational wind velocity (b)

$$P = 0.5C_p\rho\pi(0.5D)^2V^3 \quad (5)$$

The conversion efficiency of the wind turbine or its power coefficient (*i.e.* C_P) shows how much of the kinetic energy that is contained in the wind can be converted to electrical energy. The maximum theoretical value was calculated to be 0.593, which was derived for an ideal, frictionless flow and an energy converter Betz (1919). For actual wind turbines, this coefficient is reduced due to various losses related to aerodynamic and geometrical features of the rotors and mechanical losses from the coupling of the rotor and the electrical generator shafts. The highest conversion efficiency for a given wind turbine design ($C_{P,\,max}$) is achieved for a particular tip-speed ratio value (TSR or λ), as shown in Figure 17. The tip-speed ratio parameter is the ratio between the blade tip speed and the incoming wind speed to the rotor. It is used to identify the reference rotation speed of the blades, for which the highest conversion efficiency can be achieved ($C_{P,\,max}$) (Spera 1994: p. 285 - 286).

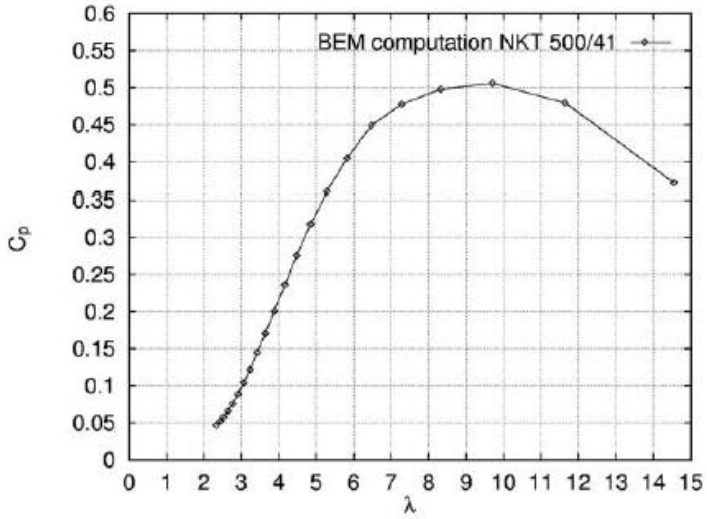

Figure 17: Power coefficinet of a wind turbines as a function of the tip-speed ratio (λ) (Hansen 2008)

Wind turbine blades are subjected to tangential and axial forces, which are distributed along their length (see Figure 18). They are obtained when the generated lift and drag forces distribution is known and projected onto the rotor plane. Thus, the total tangential force produces torque, which rotates the shaft of the rotor, while the total axial force produces negative thrust (Glauert 1983: p. 206 - 207), which loads the wind turbine structure. When the mechanical losses in the drivetrain (rotor and electrical generator shaft) are not accounted, the power output of the wind turbine is proportional to the total torque, τ (Nm) and the rotational speed, Ω (s^{-1}) of the rotor shaft, Eq. 6.

$$P = \tau\Omega \quad (6)$$

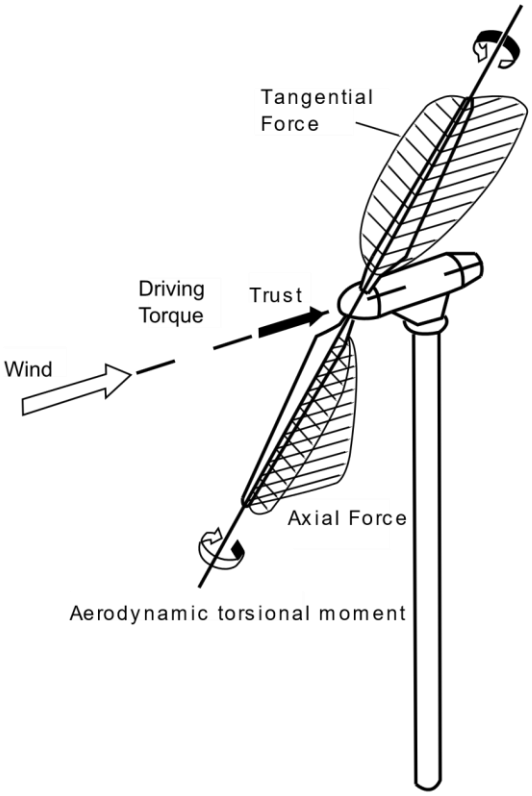

Figure 18: Blade forces and moments for a upwind two-bladed wind turbine (Hansen 2008)

The direct relation between torque and power output highlights the importance of the aerodynamic efficiency of wind turbine blades, which is a function of the characteristics of the aerofoil sections and the wind turbine wake. The wind turbine wake is known to be the vortical structures after the wind turbine rotor, which are a result of the generation of lift and the rotation of the blade. The combined effect of the vortices affects the axial and the tangential velocities seen by the blade. They can be determined by different models, the most used of which is the Blade Element Momentum theory, detailed later in Section 3.3.4.

2.3.2 Iced rotor

A significant amount of research has been carried out on how ice forms on wind turbines (Etemaddar, Hansen and Mo 2012, Tammelin, B. *et al.* 2000), impacts power output (Bredesen *et al.* 2017, Davis *et al.* 2014, Tammelin, Bengt and Seifret 2001) and affects structural robustness (Etemaddar, Hansen and Mo 2012, Hu *et al.* 2017). Thus, it has been established how much more severe icing is for longer icing events, larger water droplet sizes and liquid water contents, smaller blade section chord lengths and higher wind speeds. In addition, it is known that ice thickness increases approximately linearly from the root to the tip of the blade when considering a 2D analysis and not accounting for ice shedding (Hu *et al.* 2017). From here, it can be deduced that the most sensitive section of the blade to icing is the region

of maximum torque production and the blade span between half span (0.5R) and full span (R), Figure 19.

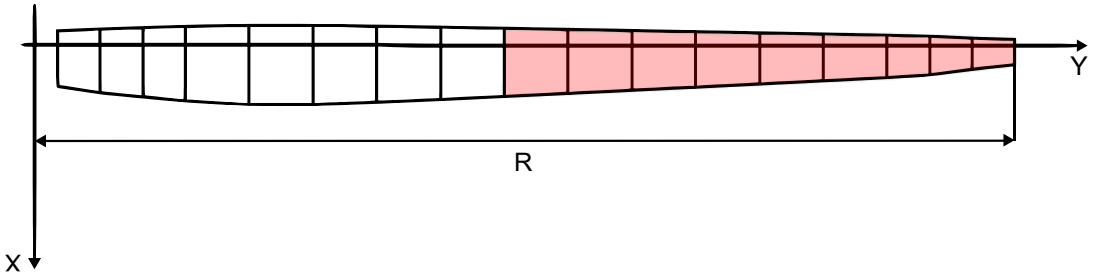

Figure 19: The wind turbine blade area, where the most icing occurs for wind turbine blades due to combination of operational and geometrical parameters leading to relatively high ice accretion rate.

Wind turbine power is proportional to the amount of produced torque (Eq. 6), which is a function of the aerodynamic efficiency of the blade and the magnitude of the produced tangential force, F_T (N). Thus, when ice starts building-up on the blade surface, it reduces the amount of produced torque, leading to reduced power output. On Figure 20 is shown how the severity of the reduction depends on the degree of aerodynamic degradation of the blade, which is a function of the ice formation type, as shown in the previous subsections. Maximum ice thickness, blade ice thickness distribution and power output degradation are the most common parameters used to evaluate the detrimental effects of icing deposition on wind turbine rotors.

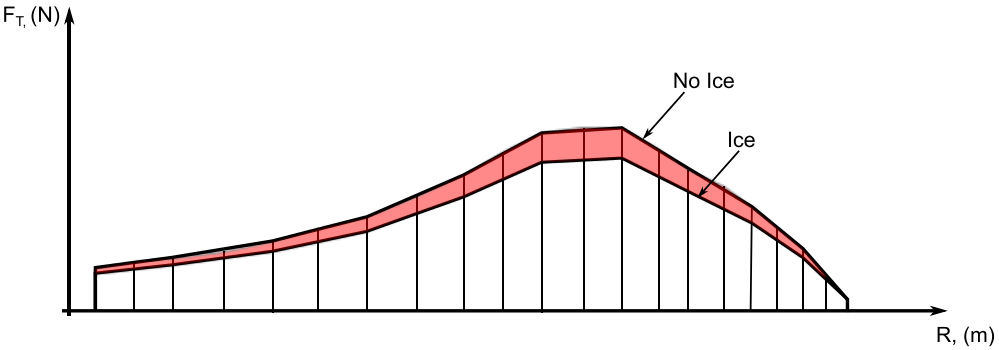

Figure 20: Distribution of the tangentia force, F_T, which integrated gives the torque of a wind turbine blade for an iced and non-iced case, along the blade radius, R. The figure is shown for illustrative purposes only.

2.3.3 Wind turbine performance modelling in CCs

This section reviews current wind turbine performance modelling approaches. The operation of wind turbines cannot be analysed without modelling its performance, which enables the determination of power losses and the design of ice mitigation techniques. Numerical and experimental modelling approaches are reviewed, which are typically used to investigate and understand how icing affects energy generation. Each approach provides different type of data and can be tailored depending on the purpose of the analysis.

2.3.3.1 Numerical and statistical

Wind turbine power performance is usually studied by modelling 2D ice shapes along the length of wind turbine blades to determine the degradation of the aerodynamic characteristics of the iced aerofoils, which is then used to obtain the reduced power output. Although ice formations have 3D geometrical characteristics, this approach provides a quasi-3D solution and has been widely used in the research community. Most of the research work that has been focused on wind turbine performance losses in cold climates used a methodology, which comprised of the modelling of ice shapes for selected conditions, evaluating the degradation of the aerodynamic efficiency of the newly formed iced geometry and recalculating the power output of a studied wind turbine. Studies differ on the choice of specific tools that could be used during the different stages of the methodology. Exception from the general approach are the research efforts, which make use of statistical models that were developed using actual production data (Karlsson, Turkia and Wallenius 2013). Another approach is combining statistical data and a simple numerical ice accretion model to predict expected ice losses (Davis *et al.* 2014, Soderberg *et al.* 2020).

Statistical modelling approach for evaluating and predicting wind turbine performance in icing conditions is advantageous when wind farms and large periods of operation need to be considered. Soderberg *et al.(2020)* showed that good correlation between simulated and field operational data can be obtained by using statistical models. The accuracy of statistical models would depend on the size and quality of the data, which is used to realise them. Large amount of data is usually required to reduce the uncertainty between estimated and forecasted losses (Davis *et al.* 2014: p. 126). Simplified approaches to account for ice induced losses can be used, as in (Byrkjedal 2009), where fixed values were used to filter out icing events and estimate ice induced power losses. However, the author reported that the losses can be underestimated, and better actual modelling of the icing rate would be required to improve the capabilities of the approach. Statistical models for evaluating ice induced power losses do not provide transparency on the actual physics of icing and the relation among parameters could not be established once training algorithms are used. In addition, as this approach requires a large dataset of production data, its application strictly remains for organisations, which directly collaborate with operators and manufacturers making the data proprietary. Thus, it is challenging for independent research groups to apply this approach until public data is available for everyone to use.

In contrast to a statistical modelling approach, numerical modelling provides higher fidelity when modelling the physics of ice formation; and the relation among all parameters that affect the ice formation can be examined (Etemaddar, Hansen and Mo 2012). Historically, this is the first and most used approach to study ice accretion on aerofoils. Before 1990, most of the research work on numerical ice accretion was focused for application in the aircraft industry. Numerical ice accretion codes such as LEWICE, TRAJICE2, ONERA (Wright, William, B., Gent and Guffond

1997),CANICE (Chocron, Brahimi and Paraschivoiu 1996, Gouttebroze, Saeed and Paraschivoiu 2000) and FENSAP-ICE (Habashi, Morency and Beaugendre 2001) were developed to simulate ice shapes. The similarities between the codes are that they all were based on the method of predicting ice accretion, which was presented in 2.1.2 and they all used Messinger thermodynamic model (Messinger 1953). The differences between the models were mainly on some of the methods used to calculate certain variables (Wright, William, B., Gent and Guffond 1997: p. 3-5). It should be noted that ice accretion codes depend on the adequate prediction of the parameters affecting the icing process, which means that results can vary depending on what models are used during the calculation routines. However, this provides an opportunity for models to be varied, improved and studied more in-detail. Furthermore, regardless of the used models, an experienced ice accretion modeller can greatly improve the accuracy of a model during simulation setup (Wright, William, B., Gent and Guffond 1997: p. 14).

Ice accretion codes are the basis of numerical models aimed at modelling the performance of wind turbines operating in CCs using the quasi-3D approach. Makkonen and Autiti (1991) first related the established ice accretion modelling approach to wind turbine applications. However, it was not until Chocron *et al.* (1996) and Brahimi *et al.* (1998), when most likely for the first time an ice accretion code was integrated in performance modelling tool. The authors modified CANICE code by including aerodynamics evaluation and performance capabilities to the code. It should be noted that the aerodynamic model was an empirical formulation developed by Gray (1964). Similar approach was adopted by Tammelin *et al.*(2001), but instead of using an empirical model, a limited database of ice shapes was obtained, and then used to develop a simplified aerodynamic model for extrapolating ice losses to an arbitrary aerofoil. Brillembourg (2013) applied similar method to study whether modified operational parameters could minimise power losses due to icing. Correlating expected ice losses for an arbitrary aerofoil from an existing database is applicable if the icing conditions and the aerofoil scale for the studied aerofoils are similar to the aerofoils and shapes included in the database. As ice events and wind turbines blade aerofoils vary, this approach provides acceptable results for limited cases.

A more holistic approach is to use separate models for each stage of the performance modelling (*i.e.* ice accretion, aerodynamic performance evaluation and power performance estimation). Dimitrova *et al.*(2011) developed a numerical tool (PROICET) designed to evaluate wind turbine annual energy production during icing. The aim of the study was to provide an alternative to the cost demanding approaches for evaluating the icing impact on future wind farm site such as wind tunnels and field testing. The model was created by using three different pieces of software – ice accretion one (CIRALIMA), virtual wind tunnel one (XFOIL) and wind turbine performance one (PROPID). Yirtici *et al.*(2019) used XFoil for obtaining the aerodynamic characteristics of iced aerofoils, but unlike Dimitrova *et al.*(2011), an in-house ice accretion code was used. Homola (2012) used similar approach to model the performance of the NREL 5 MW wind turbine, but used FENSAP-ICE and Fluent for ice accretion and aerodynamics modelling,

respectively. Zanon *et al.*(2018) developed a model integrating all modules in one framework, which was capable of simulating the transient nature of the icing process. The majority of the studies used a power prediction model based on the blade element momentum theory, as it provides acceptable results for not heavily loaded rotors. All studies identified the sensitive of the numerical results to the choice of aerodynamic models and emphasized on the lack of field data for validation.

2.3.3.2 Computational fluid dynamics (CFD) analysis – aerodynamics characteristics modelling

Wind power performance modelling using blade element momentum theory requires accurate aerodynamic data to provide results with a small uncertainty margin. XFoil and Reynold-Averaged Navier Stokes modelling are two approaches, which are typically used for computational aerodynamic analysis of non-iced (Herbert-Acero et al. 2015, Morgado et al. 2016, Munduate and Ferrer 2009) and iced (Brillembourg 2013, Dimitrova, Mariya, Ramdenee and Ilinca 2011, Homola, Matthew et al. 2010, Villalpando, Reggio and Ilinca 2012) aerofoils. A major difference between these approaches is the computational intensity. XFoil is relatively fast, but it is limited due to the theory used for its mathematical formulation. In contrast, RANS modelling takes longer to setup and run, but can be used to model various flow conditions at a greater fidelity. In this subsection, the two approaches were reviewed in the context of external flow field modelling around iced and non-iced aerofoils for wind turbine power performance modelling.

RANS modelling approach provides numerical solutions of the Navier-Stokes equations by representing the properties of a flow as the sum of an average value and fluctuations (Wilcox 2006: p. 33). Subsequently, turbulence models are needed to provide closure for the numerical solutions. The models consist of a varying number of equations, which model additional flow quantities so that the unknown momentum fluxes resulting from the averaging process can be found (Wilcox 2006: p. 33). After a mathematically and physically converged solutions is achieved, all flow quantities are known at the discretized points of a computational domain.

XFoil was developed for subcritical aerofoil design and analysis and it is used to analyse, modify and blend aerofoils (Drela 1989). It is a two-dimensional tool, which incorporates the integral boundary layer equations in the viscous boundary layer and potential flow equations in the outer inviscid region about an aerofoil; the two regions are coupled using a viscous-inviscid interaction scheme. The code is capable to capture a viscous pressure distribution, limited trailing edge separation and laminar separation bubbles (Morgado *et al.* 2016: p. 210).

The governing physics, which helps to determine the aerodynamic performance of aerofoils was briefly covered in section 2.2. Lift and drag forces can be predicted accurately if the properties of the boundary layer are known. For this purpose, the transition point (region) of the boundary

layer from laminar to turbulent and the shear stresses near the surface are the two main parameters required to estimate the aerodynamic characteristics of aerofoils. The boundary layer properties become even more important when ice is present on the surface of the aerofoils, as forced transition can occur and depending on the ice shape geometry a large separation bubble can form with time-dependant nature (section 2.2). Thus, the aerodynamic characteristics of the aerofoil can vary in time, even if the properties of the carrying flow remain constant during the analysis (Andy et al. 2011:p. 336-343).

Modelling the complex physics of iced shapes can be achieved with unsteady numerical solvers and computational tools, which provide detailed solutions of the flow. However, this requires high computational power and sometimes extremely fine tuning of the computational setup. For engineering applications RANS and XFoil are used to obtain numerical solutions for preliminary design of blades, operational strategies and anti/de-icing systems (Brillembourg 2013, Etemaddar, Hansen and Mo 2012, Zanon, Gennaro and Kuhnelt 2018). Thus, steady state analysis can be applied for the development of fast engineering computational tools, which model icing, aerodynamics and power output for wind turbines.

Among the RANS-based models, the k-w SST model is most frequently used to analyse lift and drag forces of iced aerofoils (Hudecz 2014, Villalpando, Reggio and Ilinca 2016, Zanon, Gennaro and Kuhnelt 2018), because it is capable of capturing laminar to turbulent boundary layer transition. The model combines the numerical stability and modelling capabilities of the k-w model of Wilcox and the capabilities of k-ε model for modelling free shear flow (Menter 1994). The two-equation model is capable of both accurately predicting pressure-induced separation and the resulting viscous-inviscid interaction (Menter 1994), which are both important for obtaining aerodynamic characteristics over a wide range of Re numbers and when separated flows form.

Herbert-Acero *et al. (*2015) compared the transition SST k-w and XFoil to 11 fluid flow models to provide an extended assessment for the two-dimension steady-state aerodynamic characteristics of the NACA 4412 aerofoil. The authors stressed importance of capturing the onset of flow transition and the accurate prediction of the flow field in the vicinity of the aerofoil. Transition SST k-w and XFoil models were found to predict drag with good agreement with the experimental data; with XFoil providing better modelling of the friction and pressure components of the drag. However, the models overpredicted the lift coefficients, which highlighted their limitations. XFoil models the boundary layer without the ability to account for rotational effects and flow detachment conditions, while the transition SST k-w model was found to need further improvement in its capability to model the laminar-to-turbulent flow transition in the outer layers of the boundary layer.

Both RANS-based models and XFoil have been reported to be capable of modelling aerodynamic performance of clean aerofoils (Coder and Maughmer 2014, Morgado et al. 2016),

providing the simulation conditions do not exceed their modelling capabilities (Herbert-Acero et al. 2015, Munduate and Ferrer 2009). Ferrer and Munduate (2009) showed the importance of incorporating corrections to the SST k-w model so that roughness on the NREL S814 aerofoil can be simulated. The authors reported XFoil to be performing as good as any full turbulent model for modelling aerodynamic polars, but with significant underprediction of the drag value. This can be attributed to the natural difficulties with modelling roughness and that additionally tailored models were used for the SST k-w model (Munduate and Ferrer 2009: p. 9).

The importance of adequate modelling of transition and separation phenomena becomes more important when considering the modelling of iced aerofoils aerodynamics (Villalpando, Reggio and Ilinca 2012) and wind turbine performance (Etemaddar, Hansen and Mo 2012, Homola, Matthew 2005). Zanon, Gennaro and Kühnelt (2018) developed a RANS-based modelling framework for the transient simulation of a utility-scale wind turbine under icing conditions, which also studied the power output response of a utility-scale wind turbine to different rotational speed controls. However, the simulation of an 8-hours icing event with fixed operational and weather conditions took two weeks with the use of a cluster machine, which indicates the balance that will be needed between modelling fidelity and needed computational resources for practical applications(personal communication with A. Zannon), which underlines the computational requirements when RANS-based analysis framework is used for wind turbine performance modelling. For this reason, XFoil was preferred for the development of fast design and evaluation engineering tools in (Brillembourg 2013, Dimitrova, Mariya, Ramdenee and Ilinca 2011).

The balance that will be needed for future analysis tools between accuracy and computation suggest that both XFoil and RANS modelling are going to be used for future research. However, currently no direct comparison has been performed on their suitability in modelling iced induced power losses and operational strategies design, and therefore this is an area requiring further research.

2.3.3.3 Experimental studies on wind turbine performance

Studying the effect of ice deposition on aerofoil performance has been a topic of research for applications in the aircraft industry for decades. A large body of experimental work has been carried out, which helped defining main ice shape geometry features and their influence on the generation of lift and drag. Lynch and Khodadoust (Lynch and Khodadoust 2001) complied a large dataset of experimental results and managed to establish provisional ranges for possible losses of maximum achievable C_L (C_{Lmax}), reduction in stall angle and increased minimum parasite drag (C_{Dmin}). It was reported that C_{Lmax} reduction can vary from 3 to 80%, while C_{Dmin} can increase up to 10 times its initial value; the stall angle can reduce by up to 13 °. This depends on the type of icing (geometry, location, height), aerofoil geometry (thickness, type of loading, chamber) and flow conditions (Re, Mach) (Lee and Bragg 2003, Lynch and Khodadoust 2001). Experimental work on classifying ice shapes and better document their influence on the aerofoil performance is still an active topic of research (Andy *et al.* 2011, Han, Y. and Palacios 2012, Pouryoussefi *et al.* 2016). The two main methods used for that are field and wind tunnel testing.

A limited number of studies have conducted field experiments to investigate and quantify the ice induced reduction of wind turbine power performance. Rong *et al.*(1991) conveyed a field experiment on a 40 kW wind turbine using a mounted spray system, placed in front of the wind turbine. The icing conditions defined by the ambient temperature (-3 °) and the wind speed (7 ms^{-1}) corresponded to glaze ice type. Complete loss of power output was measured after 40 minutes of operation and the final ice shapes at tip of the blade was recorded showing geometry conformal to the leading edge with icicle formation on the lower surface of the blade section. Barber *et al.*(2011) conducted a pre-site tests in the Swiss Alps of a 600 kW wind turbine, equipped with hot air heating system. Although the focus of the study was not the ice impact on the performance of the wind turbine, it was reported that 1600 icing events were registered for 3 months leading to 109 hours of downtime. The estimated annual energy losses due to icing were reported to be 10.8 MWh, which was 1.4% in total. Dierer *et al.*(2011) studied the performance of two 2 MW wind turbines in Northern Switzerland to test the forecasting capabilities of a weather research forecasting (WRF) model, coupled with an icing algorithm for structures. The annual energy losses that were reported for the tested period (2009-2010) accounted to 10% of the annual energy yield from the wind turbines on the studied site, which were reduced to 3.5% when blade heating was used to mitigate the icing. Shu *et al.*(2018) studied the impact of icing on the wind turbines operational control parameters (pitch angle, rotor speed and power) for a 300 kW wind turbine in natural icing conditions. Image processing was used to quantify the ice thickness and identify icing events durations as in (Barber, Chokani and Abhari 2011, Dierer, Oechslin and Cattin 2011). Maximum ice thickness of 86 mm was reported for 1 hour of operation of the wind turbine at ambient temperature of -0.8 °C and wind speed of 10.5 ms^{-1}. The power of the wind turbine was measured to drop from the designed value of 300 kW to approximately 25 kW, marking a significant degradation.

The limitation of the reviewed field tests is that icing parameters, such as LWC, MVD, humidity, cloud base height and dew point, have not been systematically measured and defined. This stems from the nature of the studies and their focus on quantifying the ice induced energy losses simply by measuring the power output, which helps understanding the general impact that the icing could have but did not provide enough data for modelling purposes. In addition, the icing parameters required to model the icing phenomena were both hard and expensive to measure. Until the availability of real-time measurements with LIDAR systems and their implementation in integrated systems, the best option remains on-site measuring masts and correlation with data from nearby airports and meteorological stations. Nonetheless, the covered studies provided an essential in-sight to the icing problem and its detrimental effect on the performance of both small- and large-scale wind turbines. However, future studies would require more scrutinised measuring of the icing parameters and the resultant ice shapes and their features.

Another experimental approach to study the icing phenomena is the use of wind tunnels, which can be either climatic or conventional. The climatic wind tunnels provide a controlled icing environment to simulate ice build-up on test models (Hochart, Fortin and Perron 2007, Hudecz 2014), while the conventional wind tunnels require the manufacturing of ice shapes to obtain the aerodynamic properties of tested models (Lee and Bragg 2003, Manshadi and Esfeh 2016, Seifert and Richert 1997). In climatic wind tunnels, scaling icing parameters is an issue, as the parameters of similarity Re, M and Weber numbers need to be chosen such that the resultant energy balance on the surface of the tested aerofoil leads to comparable ice formation process (Lynch and Khodadoust 2001). However, this would require detailed analysis and cautious selection of testing parameters (Re, M, Weber number, LWC, MVD, icing exposure time). As climatic wind tunnels require much energy to operate and are not standard testing equipment, conventional wind tunnels are usually chosen.

To carry out research using conventional wind tunnels, ice shapes are manufactured and placed on clean aerofoils and testing procedures are carried out. Ice shapes are usually manufactured by casting of actual ice formations on blades (Seifert and Richert 1997), 3D printing (Hudecz 2014), artificial roughness or wooden simplified shapes (Lee and Bragg 2003). Most of the studies investigate glaze and rime icing conditions and their effect on the aerodynamics of various aerofoils with the implications on the wind turbine power output (Hochart, Fortin and Perron 2007, Jasinski *et al.* 1998, Seifert and Richert 1997), while few recent studies looked at the visualisation of the flow over the iced surface and its better quantification (Manshadi and Esfeh 2016). Drag increase and lift reduction was reported by the majority of the studies with glaze icing incurring the highest aerodynamic degradation. It has been shown that drag can increase up to 4 times (Hochart, Fortin and Perron 2007), while lift can reduce up to 80% from its clean value. Typically, the results of the tests are used to provide provisional estimation of the expected ice induced icing losses or simply study the aerodynamic degradation of the aerofoils.

Moulding actual ice shapes from wind turbine blades (Seifert and Richert 1997) or simulating ice shapes in icing research wind tunnels (IRTs) (Hudecz 2014) are expensive methods for manufacturing test articles for wind tunnel measurements. In addition, only few facilities in the world have IRTs, which can be used for high fidelity testing of ice shapes, providing accurate scaling of the icing parameters is ensured. The most inexpensive method is to manufacture test articles either from foam cutting, 3D printing or wood. In addition, the results obtained by using the latter methods can be directly compared to simulation results, as in both cases it is challenging to account for the actual roughness of the ice shapes.

2.3.4 Operation in icing conditions

Large-scale horizontal wind turbines are usually equipped with variable speed and pitch controllers to operate at their optimal energy conversion rate. However, it has been noted by previous researchers that often the control sequences that are used by the turbine controller do not account for wind turbine rotor contamination. In this case, the aerodynamic model of the rotor changes (Blasco, Palacios and Schmitz 2016) and the controllers set wind turbines to operate in sub-optimal way (Homola, Matthew C. *et al.* 2012). This is visualised by the torque-speed controller curve in Figure 21, where the solid line shows the designed torque-speed curve, while the dashed line denotes the altered curve due to icing. Few methods have been proposed to tackle the issue, including adjusting the controller to track the altered torque-speed curve, maximum point tracking and enforcing optimal tip speed ratio. None have been tested in the field or have received additional investigation. Controllers either alter the rotational speed of the rotor or adjust the angle of attack of the blades. This provides means of some control over the ice accumulation rate, as the relative velocity to the blade and the catching efficiency can be both influenced. Thus, by applying additional control strategies during icing, different outcomes can be achieved. There is a particular need to search for more efficient approaches to operate wind turbines in icing conditions (Cattin 2012). An efficient wind turbine operational strategy can minimise annual power losses, prevent structural damage and reduce wind turbine downtime.

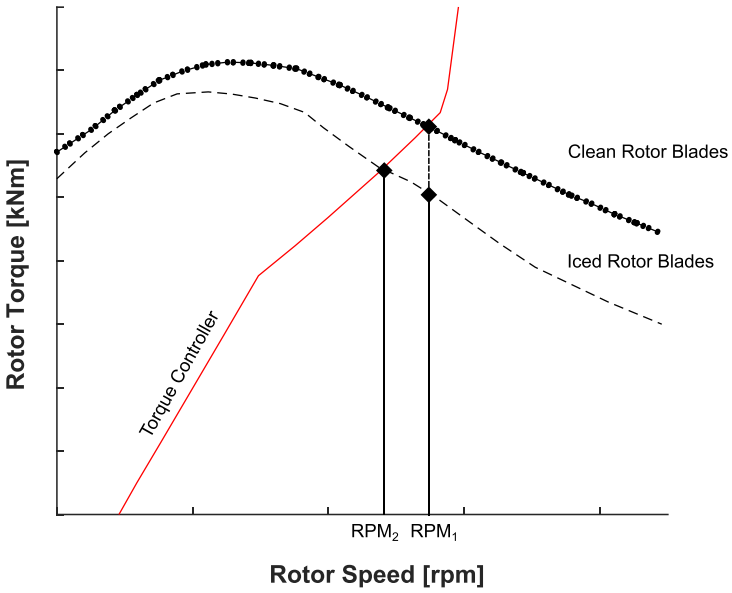

Figure 21: Iced and non-iced torque speed curves and the change of the optimal rotational speed for iced case. With no additional design procedures the torque controller would prescribe RPM_1 for the new iced aerodynamic model, which would have an optimal rotational speed of RPM_2 (Homola, Matthew 2005, Zanon, Gennaro and Kuhnelt 2018)

Limited research is available on ice mitigation strategies based on rotational speed and pitch control, referred in the literature as power optimisation techniques during icing (Lehtomaki *et al.* 2018: p. 43-44). Blasco *et al.*(2016) showed that for an icing case leading to 15% lift reduction

and 127% drag increase with mean power loss of 28%, a modified pitch control could recover the power output to the baseline value for wind speed higher than 15 ms^{-1}. The alteration resulted in increased rated wind speed and unchanged ice induced power losses of 19.8% for wind speeds below 15 ms^{-1}. The results were obtained for casted ice shapes and indicated how the power performance could be recovered, but it did not provide solution for lower wind speeds. By using casted ice shapes, the opportunity to apply different pitch control during icing to influence the ice accumulation rate was not realised. Nonetheless, the results indicated that for small rough ice shapes, at high wind speeds, the baseline wind turbine performance could be recovered by modified control. The work of Brillembourg (2013) and Jha *et al.*(2012) was aimed at developing a fast engineering tool for wind turbine analysis in icing conditions. Although the focus of the study was on the engineering tool, the operation of different wind turbines during icing was tested for modified rotational speeds and pitch angles. It was shown that the final ice-induced energy losses could be influenced and, in some cases, reduced by 2 to 3 times. However, the authors found it difficult to generalise the findings due to the limitations of their study but concluded that pitch control “hardly alleviates the adverse effect in performance degradation”. As the modifications of the rotational speed and pitch were made simultaneously, the reported improvement in the performance can be attributed solely to the changes in the rotational speed of the wind turbine rotor.

Homola *et al.*(2012) and Zanon *et al.*(2018) investigated the operation of the National Renewable Energy Laboratory (NREL) 5 MW reference wind turbine in icing conditions. Both studies analysed the performance of the wind turbine considering the torque-speed curve and the torque-speed controller. Homola *et al.*(2012) simulated the iced performance of the wind turbine after a one-hour long icing event, operating the wind turbine either by adapting the torque-speed controller to the iced-torques-speed curve or by modifying the controller to maintain the TSR at its design value. When examining the wind turbine power curve for the iced blade and bypassing the controller, a 10% higher achievable power output for velocities between 7 ms^{-1} and 13 ms^{-1} was reported, while slightly higher power losses were seen for wind speeds between 3 ms^{-1} and 6 ms^{-1}. As the study focused on a single icing condition, the authors highlighted the need for further analysis of more severe icing cases. In addition, this approach, as in (Blasco, Palacios and Schmitz 2016), did not account for the possibility to influence the icing process during operation. Moreover, post-icing event, when the ice shapes were present and no further ice shape changes occurred, operating at higher tip-speed ratios only changed the Re number over the iced blade and the angle of attack. Thus, the increase that was reported in that study, could mostly be attributed to the overall increase of the performance of the iced blade due to the Re number, which is typically seen for clean blades. Zanon *et al.*(2018) proposed a numerical modelling method to account for the transient nature of the icing phenomena. The interaction between ice accretion and wind turbine performance was exclusively the focus of the work. The model was used to study how the wind turbine performance would change when the rotational speed of the rotor was used as a control parameter. The results showed how the ice-induced losses could be reduced by modifying the

TSR during an icing event and 6% higher power output could be obtained post-icing event. Reduced ice induced power losses does not necessarily mean improved overall energy yield, as the reduction of the TSR leads to intentional energy losses.

By reducing the TSR during an icing event to minimise ice build-up, the reference TSR could be restored once an icing event ends to improve performance (Brillembourg 2013). However, the reference TSR may no longer be the best post-icing event operational strategy due to ice remaining on the blades and changes in the aerodynamic behaviour. To determine if gains in energy generation can actually be achieved, a turbine's performance needs to be analysed throughout and immediately after an icing event. This approach could also be used to implement an operational strategy to both reduce ice build-up during an event and maximise post-icing event power output. Moreover, a method for comparing and evaluating different TSR operational strategies is needed and the performance analysis needs to be applied for a wide range of different icing conditions, as previous studies have done it for limited range of icing conditions. In addition, it has not been investigated how to implement the operational strategy in systematic way and evaluate its effectiveness.

2.3.5 Ice mitigation strategies

Control systems for icing conditions are actively used to adapt wind turbines for operation during icing. Wind turbine controllers can change operational parameters (*i.e.* TSR and pitch), activate an ice protection system, curtail production or stop operation, as a part of the wind turbine operation in icing mode (IOM) (Lehtomaki *et al.* 2018: p. 43-48). Modifying operational parameters has not been adopted for ice mitigation by manufacturers and there is only one indication of similar control strategy used by General Electric (GE) (GE Renewable Energy 2013, Lehtomaki *et al.* 2018: p. 44), which is not publicly available and there are no details on its implementation and effectiveness. The ice mitigation approaches, which are reported to be widely used are either operational shutdown or a combination of monitoring and ice protection systems (Fakorede, Feger *et al.* 2016: p. 670, Lehtomaki *et al.* 2018: p. 47-48, Parent and Ilinca 2011: p. 93); various ice protection techniques are possible for blade protection.

Ice prevention systems based on mechanical principals or changing the surface properties of blades are pneumatic boots, electro-impulsive/expulsive system, black paint, chemical and protective coatings (Dalili, Edrisy and Carriveau 2007: p. 432-433, Fakorede, Feger *et al.* 2016: p. 665-667, Parent and Ilinca 2011: p. 93-95). Pneumatic boots have been widely used in the aircraft industry, but noise, intensive maintenance and design difficulties have prevented it of being actively implemented for wind turbine applications. Electro-impulsive/expulsive systems have not been used for wind turbine application yet but are thought to be a promising technology due to being inexpensive, energy efficient, easily automated, environmentally friendly and do not interfere with Hertz transmission. The only concern at this stage is that the expulsion of ice can be a safety risk. Black paint has been reported to be effective for light icing conditions. It is provided as an ice mitigation strategy by only a few manufacturers, as it is not

effective during in-cloud icing and at night. Chemical treatment is used for aircraft on ground level and it is meant to protect the aircraft until the energy regulation on board allows for ice protection systems to be activated if needed. For wind turbines, this strategy requires, manpower and chemicals are pollutant, which makes it unsuitable for ice mitigation. Protective coatings have been reported to be effective against icing with making the surface of the rotor blade ice phobic. Parent and Illinca (2011) have concluded that protection from icing with only coatings is unrealistic. The protective layers are not 100% ice phobic and degrade by becoming porous, which diminishes their effect and can even lead to ice imbalances on the blades. However, it has been reported that protective coatings can reduce the required power for heating by up to 90% for electrothermal ice protection technologies, (Gao *et al.* 2019: p. 943).

Electrothermal ice protection system are realised by applying heat to the surface of the blade and are currently the most used type of ice protection systems (Dalili, Edrisy and Carriveau 2007: p. 432, Fortin and Perron 2009: p. 18, Laakso *et al.* 2010: p. 1). Historically, much experience of such systems has been gained from their application in the aircraft industry. For wind turbine applications, the heat to the surface from electrothermal ice protection systems is supplied from microwave radiation, hot-air circulation or heat resistance mats (Fakorede, Feger *et al.* 2016: p. 667-669, Madi *et al.* 2019: p. 275-277). Microwave systems have been researched, but not implemented on actual wind turbines. The technology most likely will be developed in the future, as it has been found to be energy efficient with the possibility for ensuring an even surface heat distribution and lighting strike protection. Challenges with the systems effectiveness for some icing conditions and its sensitivity to the blade design need to be addressed as well (Madi *et al.* 2019: p. 276-277).

Hot-air and heat resistance systems are the two most common technologies, which manufacturers and independent companies are developing. Most of the manufacturers currently rely on systems based on hot-air technology (Lehtomaki et al. 2018: p. 47-48) . This is most likely driven from the fact that the system has a good historical track record and the main wind turbine platform for the past 10 years have been wind turbines with rated power between 2 MW and 3.5 MW. As wind turbine size increases, most likely this technology will be used on smaller wind turbines, as its thermal efficiency and response time are generally low and reduces even more for longer and bigger wind turbine blade (Fakorede, Feger *et al.* 2016: p. 668). The fact that the heating source is located in the root of the blade and the highest requirement for heating is at the blade tip region limits the application of the system as well (Laakso *et al.* 2010: p. 10, Madi *et al.* 2019: p. 276). Moreover, independent ice protection systems providers mainly develop systems currently based on the heating resistance technology, as seen from the review in (Lehtomaki *et al.* 2018: p. 47-48).

Electrothermal heating resistance systems are realised with the installation of heating mats either mounted on the blade surface or embedded in the layers of the blade composite structure (Fakorede, Ibrahim *et al.* 2016: p. 668-669). This approach is effectively being used in the aircraft industry and has been tested for more than a decade on wind turbines in Finland. It has

nearly 100% thermal efficiency due to the direct heating of the surface and could be designed to heat the blade almost isothermally (Laakso *et al.* 2010: p. 10). The main disadvantage of the technology is that it could require a lot of power to operate. However, it has been reported that the energy consumption could vary from 1% to 10% of the annual energy production depending on the icing climate and the size of the wind turbine (Fakorede, Ibrahim *et al.* 2016: p. 673, Parent and Ilinca 2011: p. 94). Field data showed that an electrothermal heat resistance system in Sweden and Finland did not exceed 6% of the turbine's rated power and 3% of the gross production (Peltola *et al.* 1999, Tammelin, B. *et al.* 2000). Initial concerns on susceptibility to lighting strikes, mechanical durability issues and electrical connection quality have been raised, but field experience has shown no problems regarding the concerns (Laakso and Peltola 2005). Disadvantages of the system can be the possibility of high maintenance costs for replacing failed heaters and increased surface roughness for heating mats, which are not embedded in the composite structure of the blade.

There are two main types of thermal icing protection systems: protecting the blade surface to prevent ice deposits (anti-icing) and removing deposited ice by minimising its adhesive force with the protected surface (de-icing) (Laakso and Peltola 2005, Parent and Ilinca 2011). A significant disadvantage with both technologies is the required power to operate them and failure of heating elements can lead to structural damage and rotor imbalance. The low thermal efficiency of hot-air systems makes them unsuitable for anti-icing technologies and it is typically used for de-icing. During de-icing with hot-air systems, wind turbines are often stopped for the procedure to take place (Begin-Drolet et al. 2020: p. 9, Fakorede, Feger et al. 2016: p. 670). This could lead to multiple stops for a given time period and energy is both lost from stopping and using the ice protection system. As de-icing allows for an ice layer to form before activation, the technology depends on the magnitude of the aerodynamic and centrifugal forces to remove it, which in some operational conditions might be insufficient. Electrothermal de-icing technology can address some of the limitation of hot-air systems.

Most of the wind turbine manufacturers have implemented different de-icing technologies as an ice protection approach (Fakorede, Feger *et al.* 2016: p. 669-670), which has been shown to require less energy than anti-icing. However, the anti-icing approach for ice mitigation can keep the blade surface free of ice for extremely low temperatures, provide isothermal heating, ensure operation during icing events and systems are not constrained by the length of the blade (Laakso and Peltola 2005). The only drawback of anti-icing is that it can require a lot of power to keep the blade free of ice. This can be addressed with improved control system and design layout (Fortin and Perron 2009: p. 22). It is known that anti-icing technology can both operate in evaporative and running wet regimes. Thus, heating the protected surface to either evaporate all of the impinged water or ensure all impinged water is in liquid phase and no ice forms (Wright, William 2008). Wind turbine operators such as Nordex, have recently presented that their anti-icing system is effective and provides even heating along the protected areas on their blades (Sachse 2020). For anti-icing system, the control strategy and design are as challenging

as for de-icing systems and in future both technologies probably will be employed for effective ice mitigation. Moreover, much development will be required as current systems are relatively new (Lehtomaki *et al.* 2018: p. 47-48) and ice monitoring and protection system integration is possible for only a few technologies (Madi *et al.* 2019: p. 280).

Research on wind turbine and anti/de-icing techniques is very limited, with studies focusing on the review of current technologies (Dalili, Edrisy and Carriveau 2007, Fakorede, Feger *et al.* 2016, Laakso *et al.* 2010, Parent and Ilinca 2011), modelling of the process to establish methods for analysis (Fakorede, Ibrahim *et al.* 2016, Raj and Myong 2016, Suke 2014) and quantification of needed power to achieve protection for chosen icing conditions (Battisti *et al.* 2007, Fakorede, Ibrahim *et al.* 2016, Reid *et al.* 2013, Shu *et al.* 2017, Villalpando, Reggio and Ilinca 2016). Estimating the needed power for operation in different conditions is a priority to enable the viability of thermal systems to be established.

Fakorede *et al.*(2016) conducted an experimental analysis on a NACA 0012 aerofoil section to measure the magnitude of the heat flux, which was required to keep the surface at 5 ºC for varying ambient temperature and liquid water content in the air. By using linear fitting, the authors extrapolated the results for a number of wind turbines. It was concluded that anti-icing would require too much energy to protect a wind turbine economically. The results were obtained for non-scaled icing conditions and the heaters were placed on the surface of the blade, which most likely contributed to an early development of turbulent boundary layer and increased surface roughness. This could have led to the measuring of increased heat fluxes. In addition, the liquid water content values were chosen to be typical for extreme icing events and freezing rain. Battisti *et al.*(2007) numerically has shown that the required power for anti-icing becomes a lower percentage of the rated power output with the increasing of wind turbine size. The author stressed on the fact that anti-icing power could initially be estimated to be high, but only a detailed analysis considering the actual design, ambient conditions and control strategies should be used to evaluate whether the system would be beneficial and financially viable. Reid *et al.*(2013) showed that an optimal design for anti-icing can be obtained by dividing the systems in sections and varying the power for each element. It is important to identify the conditions when an ice protection system would be a viable option. It has been shown that the viability of thermal ice protection systems depends on the frequency of icing and the price of electricity (Battisti 2015b: p. 106-109, Peltola *et al.* 1999: p. 1037) . Currently, there are no proven and reliable solutions for ice mitigation (Fakorede, Feger *et al.* 2016: p. 674)*;* further research and development to address the challenges of implementing ice protection have become an urgent requirement for manufactures and operators (Baring-Gould *et al.* 2010, Cattin 2012).

Most of the current technologies are on prototype level and much more development will be needed to optimise their performance and implement them in integrated systems. Furthermore, the efficiency of ice protection techniques depends on the specifics of the icing climate and the design parameters of wind turbines. Thus, it is necessary to establish new methods and

techniques to compare and evaluate different ice mitigation strategies, enabling the choice of an optimal ice mitigation approach or set of approaches for a selected wind turbine and location.

3 Methods and Materials

This project promotes an improved energy generation from wind during icing conditions by answering research questions on aerodynamic degradation modelling and designing operational strategies. The current chapter provides an overview and justification of the project's methodology designed to answer the research questions set out in Chapter 1. Experimental and numerical approaches were used to address the aerodynamic degradation modelling aspect of this project, while the investigation on designing and improving wind turbine ice mitigation operational strategies was completed using only numerical simulations. How icing events, ice accretion and wind turbine performance were modelled is explained in this chapter. The experimental setup and specific ice shapes for determining degraded aerodynamic performance and expected modelling uncertainties when using low computationally intensive tools are further detailed in Chapter 4. The methods for designing and comparing operational strategies for ice mitigation are outlined in Chapter 5 and Chapter 6, respectively.

3.1 Overview of methodology

3.1.1 Wind turbine performance modelling

To enable the analysis of ice mitigation operational strategies, the quasi-3D numerical approach was utilised for wind turbine performance modelling. By using the approach, the wind turbine performance can be modelled and the relation between all icing and operational parameters can be investigated. Modelling wind turbine performance using this numerical approach has four distinctive/fundamental stages:

1. Definition of environmental parameters, which are essential for predicting the formation of icing – wind velocity, liquid water content (LWC), median volume diameter (MVD) and ambient temperature.
2. Provided the selected wind turbine geometry and operational conditions are known, generation of 2D ice shapes, which modify the wind turbine blades geometry.
3. Evaluation of aerodynamic degradation (*i.e.* reduction in C_L and increase in C_D), which is caused by the presence of ice on the wind turbine rotor blades.
4. Estimating power output losses by comparing the power output of the selected wind turbine with and without ice deposition for the modelled conditions (environmental and operational).

For each stage, different models and approximations can be applied. In the current methodology, the environmental parameters were chosen to be representative of typical in-cloud icing events as discussed in section 3.2 instead of using numerical weather prediction models or weather research forecasting models. The defined icing events (see section 3.2) were used to analyse different ice mitigation strategies and identify the design constraints, which should be considered for real applications. This ensured that the analysis is focused on the investigated operational strategies and their ice mitigation effectiveness rather than simply predicting the wind turbine performance for specific locations.

To define representative geometrical and operational features for a typical utility-scale horizontal-axis wind turbine, the NREL 5 MW reference wind turbine (Jonkman *et al.* 2009) was selected. Its geometrical and operational parameters were used to obtain 2D ice shapes along the wind turbine blade for the defined icing events. The 2D ice shapes were generated with lewINT (Wright, William 2008) ice accretion tool, while relative blade velocity, blade angle of attack, aerodynamic characteristics and wind power output were obtained with Qblade (Marten and Wendler 2013). Qblade is the only open source blade design software, which provides all modelling tools to analyse and design the performance of a wind turbine. XFoil (Drela 1989) and blade element momentum theory (BEMT) (Hansen 2008) are both implemented in the software for the aerodynamic and power analysis, respectively. In addition, extrapolation schemes, which are typically needed after the aerodynamic analysis are readily available in the software. Both XFoil and BEMT have been widely used for conceptual analysis and design of aerofoils and wind turbine blades, which makes them a suitable choice for the purposes of the current thesis.

3.1.2 Ice losses and aerodynamic modelling

BEMT is known to predict wind turbine power output with great confidence when the aerodynamic characteristics of the wind turbine blade are estimated accurately. Typically, XFoil and Fluent are used to obtain aerodynamic characteristics of aerofoils. It is of practical importance to identify whether and when low computational tools can be used for preliminary performance analysis of wind turbines during icing and what the variation in the estimated icing losses could be when using different methods.

XFoil and Fluent were used to analyse the aerodynamic performance of ice shapes obtained during different rotational speeds of the wind turbine rotor. The obtained results were compared with experimental data generated in the Coventry University open circuit sub-sonic wind tunnel. This comparison was used in the current methodology to define by how much the predicted icing losses could vary depending on the chosen simulation tool. It is of practical importance due to the significant difference in their running time. XFoil provides extremely fast results but its accuracy reduces for abrupt geometries because of the incorporated panel method routine in its algorithm. Fluent can provide better accuracy and consistency of the results but both the setup of the simulation environment and the time required for calculations is much larger. The experimental setup and the results from the analysis are presented in Chapter 4.

3.1.3 Ice mitigation operational strategies

Previous research has established that the relative velocity and the angle of attack of the wind turbine blade govern to great extent the ice accretion process and the expected ice shapes (Etemaddar, Hansen and Mo 2012). In section 2.3.4 was concluded that rotational speed modification of the rotor could be an effective ice mitigation strategy, but previous research did not elaborate on methods to systematically design and evaluate such strategies. Previous studies tended to choose arbitrary values for modifying the rotational speed and did not provided methods for systematic implementation of the strategy. Thus, by addressing the second research question posed in Chapter 1, a novel systematic method for modifying the

rotational speed of the rotor was proposed. By using the operational TSR as a design parameter, a range of possible operational tip-speed-ratios was defined. The range depends on the minimum and maximum speeds of rotation of the fitted electrical generator in the wind turbine nacelle. The best tip-speed-ratio setting during icing was determined by developing an estimated payback time approach, which accounted for the loss of power that was sustained during the intentional reduction of the rotational speed. Further details on the design approach and the implementation of the strategy are provided in Chapter 4.

To adapt wind turbines to CCs, not only various operational strategies and ice protection systems would be needed, but effective methods for their optimal implementation and evaluation will be required. This is suggested from the wide variety of solutions that can be implemented and the natural wide variation of icing conditions. The merits of each possible operational strategy can be determined for typical icing events, durations and ranges of environmental and operational parameters. By identifying the operational limits of each ice mitigation technique, the most preferable technique or set of techniques can be found. Such comparisons would also aid the process of further development of the techniques and would promote more holistic studies of the icing process on wind turbines. To demonstrate the advantages of having such method, this project compared derating by tip-speed-ratio modifications with alternative anti-icing and operational shutdown. The method was based on ice induced energy losses over a period of operation of the wind turbine and accumulated ice mass, which are typically investigated when studying ice accretion on wind turbines. Anti-icing was modelled based on the heat fluxes needed to keep the surface of the blade at a prescribed temperature, for a wide range of conditions. Moreover, the number of annual icing days required for anti-icing system viability were also modelled by estimating financial breakeven points and considering system cost. The method is outline and detailed in Chapter 5.

3.1.4 Numerical setup

The numerical setup that was used to model the power performance and investigate the design and implementation of different ice mitigation strategies is shown in Figure 22. The ice accretion was modelled for a set of conditions defined by the selected icing events and operational regimes. Each icing event was defined by its duration, ambient temperature, wind speed, LWC and MVD, while the blade section relative velocity and angle of attack were obtained from the BEMT analysis and the chosen operational regime. During ice accretion modelling, ice shapes corresponding to the expected blade geometry alteration were obtained. In addition, the power demand required to realise anti-icing was also calculated for two different layouts. Once the altered geometry was obtained, XFoil was applied to obtain the aerodynamic characteristics of the iced shapes. The power output for an iced wind turbine rotor was estimated with the application of BEMT. This approach is similar to modelling software tools found in the literature, but unlike other studies, the application is focuses on advancing the design of ice mitigation operational strategies rather than simply modelling expected icing losses and ice mass.

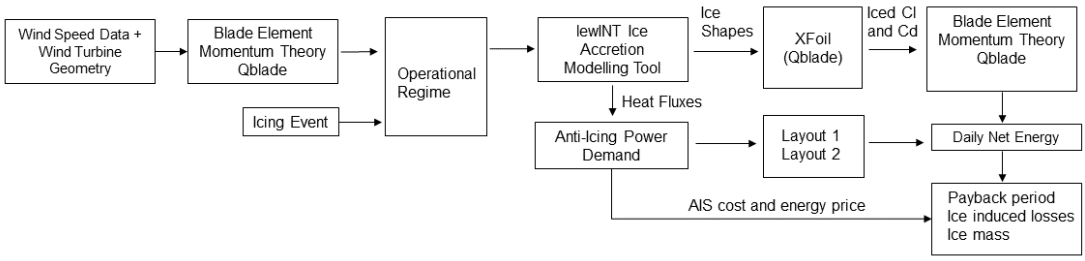

Figure 22: Outline of the applied numerical modelling approach in this study

The outlined approach capabilities depend on the used models and the way how their input-output connections are realised. The chosen setup was balanced between computational intensity and modelling accuracy. Instead of implementing higher fidelity modelling tools such as the 3D ice accretion modelling tool FENSAP-ICE and aerodynamic analyses with CFD models, more established tools and methods with lower computational intensity were chosen.

3.2 Icing events

To study wind turbine performance during different in-cloud icing events, encompassing rime, mixed and glaze icing conditions, a number of icing events were defined based on published experimental (Poots 1996) and field data (Cober, Isaac and Strapp 1994, Pederson *et al.* 2018). The different ice modelling parameters that need to be considered include liquid water content (LWC), median volume diameter (MVD) and icing event duration (t_{Event}). Each parameter can vary widely for different locations and especially for different orographic features. In-cloud icing conditions are mostly pronounced in hilly and mountainous terrains, where wind turbine blades can reach the low-level cloud base (300-1200m) during winter months (Cober, Isaac and Strapp 1994). A typical MVD for in-cloud icing is 20×10^{-6}m (Poots 1996), but it can range from 10-35×10^{-6}m (Cober, Isaac and Strapp 1994). The LWC is normally 3×10^{-4} kg.m^{-3} (Poots 1996), and ranges from 0.4-5×10^{-4}kg.m^{-3} (Cober, Isaac and Strapp 1994, Lamraoui *et al.* 2014). Ice events tend to be shorter for larger liquid water contents and droplet sizes (Lamraoui *et al.* 2014, Lewis 1947) and typical durations range from 20 min to 48 hours, while in some cases up to several weeks (Lamraoui *et al.* 2014).

During an icing event, wind speed (V) and ambient temperature (T) significantly influence the type of ice being accreted. Thus, three icing events (defining LWC, MVD and duration) are chosen along with different wind speeds and ambient temperatures that are most likely to occur. The icing events are based on environmental parameters typical for relatively short icing events (Stoyanov and Nixon 2020). Although icing conditions vary with location and in time, energy yield losses and operational strategy performance are often studied by using fixed operational and meteorological conditions, as seen in (Etemaddar, Hansen and Mo 2012, Homola, Matthew C. et al. 2012, Zanon, Gennaro and Kuhnelt 2018). Table 1 shows icing event A (LWC of 5×10^{-4} kgm^{-3} and MVD of 25×10^{-6} m), B (LWC of 3×10^{-4} kgm^{-3} and MVD of 20×10^{-6} m) and C (LWC of 0.4×10^{-4} kgm^{-3} and MVD of $12\text{x}10^{-6}$ m), which are modelled at different temperatures (-5 °C and -10 °C), wind speeds (5, 7 and 10 ms^{-1}) and duration (1 hour for Event

A and 4 hours for events B and C) giving a total of 12 different icing cases. Event A represents the harshest conditions, which typically occur for a relatively short duration, and events B and C are mild and light conditions respectively.

Table 1: Definition of icing events A, B and C, at different wind speeds (V) and temperature (T).

Event, V, T	LWC (10^{-4} kgm^{-3})	MVD (μm)	Duration, t_{Event} (s)	V (ms^{-1})	T (°C)
A1010	5	25	1	10	-10
A105	5	25	1	10	-5
A710	5	25	1	7	-10
A75	5	25	1	7	-5
A510	5	25	1	5	-10
A55	5	25	1	5	-5
B1010	3	20	4	10	-10
B710	3	20	4	7	-10
B75	3	20	4	7	-5
B510	3	20	4	5	-10
C105	0.4	12	4	10	-5
C1010	0.4	12	4	10	-10

3.3 Models

3.3.1 Wind turbine model

NREL 5 MW reference wind turbine has been chosen as a model wind turbine for this project, because of its wide recognition in the research community (Homola, Matthew C. *et al.* 2012, Zanon, Gennaro and Kuhnelt 2018). In addition, detailed information about its design features is available (Jonkman *et al.* 2009). The wind turbine has been designed as a representative utility-scale multimegawatt type for in-land and off-shore applications. It has been configured as a 3-bladed upwind wind turbine with variable speed and collective pitch control system. Its operational range is between cut-in speed of 3 ms^{-1} and cut-out speed of 25 ms^{-1}. The rated power output of 5 MW is achieved for a wind speed of 11.4 ms^{-1} and rotational speed of 12.1 RPM, leading to blade tip speed of 80 ms^{-1}. The blade length combined with the hub radius is 63 m, which results in a 12468.98 m^2 of swept area.

The aerodynamic properties of the blade are shown on Table 2, which are defined by the distribution, twist angle, chord and type of blade cross-section (aerofoil). The wind turbine blade consists of two types of cylindrical cross-sections, which connect the blade to the rotor hub with drag coefficients of 0.5 (Cylinder 1) and 0.35 (Cylinder 2). The aerodynamically efficient part of the blade consists of 6 aerofoils from the DU family wind turbine dedicated aerofoils REF and a 6-digit NACA aerofoil with extended laminar flow on the upper surface Table 2.

Table 2: NREL 5 MW wind turbine blade aerodynamic properties as defined in (Jonkman et al. 2009: p. 7)

Mid-Section Location (m)	Section Span (m)	Twist Angle (º)	Aerofoil Chord Length (m)	Aerofoil Type (-)
2.8667	2.7333	13.308	3.542	Cylinder 1
5.6000	2.7333	13.308	3.854	Cylinder 1
8.3333	2.7333	13.308	4.167	Cylinder 2
11.7500	4.1000	13.308	4.557	DU 99-W-405
15.8500	4.1000	11.480	4.652	DU 99-W-350
19.9500	4.1000	10.162	4.458	DU 99-W-350
24.0500	4.1000	9.011	4.249	DU 97-W-300
28.1500	4.1000	7.795	4.007	DU 91-W2-250
32.2500	4.1000	6.544	3.748	DU 91-W2-250
36.3500	4.1000	5.361	3.502	DU 93-W-210
40.4500	4.1000	4.188	3.256	DU 93-W-210
44.5500	4.1000	3.125	3.010	NACA-64618
48.6500	4.1000	2.319	2.764	NACA-64618
52.7500	4.1000	1.526	2.518	NACA-64618
56.1667	2.7333	0.863	2.313	NACA-64618
58.9000	2.7333	0.370	2.086	NACA-64618
61.6333	2.7333	0.106	1.419	NACA-64618

The DU family of aerofoils have been designed to address issues with the thick members of 4- and 6- digits aerofoil, which have been used as thick aerofoil section on the in-boards part of wind turbine blades (Timmer and van Rooij 2003). The DU aerofoils were design as an alternative to the thick NACA aerofoils (maximum relative thickness of above 21 %), which suffered from premature transition and severe performance degradation. Thick aerofoils are used in wind turbine blades for structural considerations. The main design parameter of the family of aerofoils is their low sensitivity to leading edge roughness and contamination. It has been achieved by limiting the maximum lift capacity to a moderate level, by restraining the maximum thickness of the upper surface. To compensate it, aft loading on the lower surface of the aerofoils is applied, which gives the typical S-shape form of the pressure distribution on the lower surface. The DU aerofoils were designed to improve the tendency of the thick NACA aerofoil towards premature transition leading to severe degradation of the performance.

NACA 64-618 belongs to the NACA 6-series family, which have been designed using a desired velocity distribution on the aerofoil surface, which is then used to develop an aerofoil shape through shape factors (ABBOT and VON DOENHOFF 1959: p. 120). The main design parameters for this family of aerofoils was desirable drag (achieved with extended laminar flow

region), critical Mach number and maximum-lift characteristics. They are characterised by a uniform chordwise loading from the leading edge to a certain point, where the load starts decreasing linearly to the trailing edge.

3.3.2 Wind turbine blade model and ice mass calculation

To reduce the number of required simulations for the power output modelled, four sections of the wind turbine blade were modelled to determine the ice accumulation along its length during the icing events. This approach provides a good representation of an iced wind turbine blade and reduces the computational intensity required for further modelling as reported in previous research (Etemaddar, Hansen and Mo 2012, Homola, Matthew C. et al. 2012, Zanon, Gennaro and Kuhnelt 2018). Figure 23 shows the sections, which are considered between the half-span and the full span of the blade: sections A, B, C and D. The distances from the blades centre of rotation are as follows: l1 is 0.52R, l2 is 0.65R, l3 is 0.80R and l4 is 0.94R with R being the blade radius. The hub radius, LH, and blade length, LB, are 1.5 m and 61.5 m, respectively. The aerofoils corresponding to the chosen blade sections are DU 91W225 for Section A, DU 93W21LM for Section B and NACA 64618 for sections C and D.

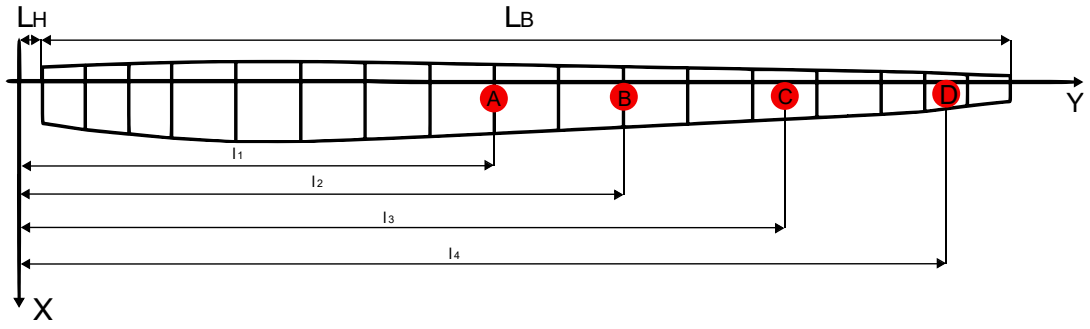

Figure 23: Discretised NREL 5 MW blade and the selected 2D sections for ice accretion analysis.

The ice formation analysis was conducted using the 2D aerofoil sections at each of the four discretised locations. Symmetrical ice deposition across the turbine's three blades was assumed with uniform ice geometry for each iced section. The relative speed to the blade sections was calculated using classic BEMT theory, Eq. (7), where V_{rel} is the relative speed to the blade, V is the wind speed, ω is the rotational speed of the rotor, r is the local blade section radius, and a and a' are the axial and tangential induction factors, respectively. The ice mass is estimated by using the predefined ice density of 917 kg.m^{-3} in LewINT (Wright 2008).

$$V_{rel} = \sqrt{\left(V(1-a)\right)^2 + \left(\omega r(1+a')\right)^2} \tag{7}$$

Ice mass was modelled at different TSR settings. Instead of using the mass of water which freezes on impact with the aerofoil surface as used in (Etemaddar, Hansen and Mo 2012, Hu *et al.* 2017), the total ice mass ($M_{ICE,T}$) was modelled. The total ice mass, $M_{ICE,T}$, is calculated as in Eq. 8, where $A_{ICE,i}$ is the area of the ice shape at each blade section, ΔR_i is the blade section width, ρ_{ICE} is the density of the ice and *i* is the blade section counter. The assumptions made

during the modelling of the ice mass include constant ice density of 917 kgm^{-3} and symmetrical ice deposition on the rotor blades.

$$M_{ICE,T} = (A_{ICE,A}\Delta R_A + A_{ICE,B}\Delta R_B + A_{ICE,C}\Delta R_C + A_{ICE,D}\Delta R_D)\, \rho_{ICE} \quad (8)$$

3.3.3 Ice accretion modelling – lewINT

To simulate ice formation for the events defined in Section 3.2, LewINT® ice accretion software was used as it is the most widely established tool for generating 2D ice shapes on aerofoils and it has been validated extensively for aircraft icing (Wright, William, B. 2005, Wright, William 2008). LewINT® is based on source and dipole singularities superposition panel method to obtain flow velocities, which are used to calculate droplet trajectories, aerofoil surface water fluxes and energy balance for the ice shape calculations.

LewINT is a numerical tool, which simulates ice accretion by following the basic methodology outline in Chapter 2, section 2.1.2. It provides 2D aerofoil section ice shapes and also has the capabilities to simulate anti/de-icing system performance by providing results for the surface temperature of the aerofoil and the temperature in the materials used to make the aerofoil. As stated, the software has four modules for ice accretion simulation.

The carrying flow velocity field, which is used to calculate the droplets velocities and the velocities at the aerofoil surface, is obtained with the means of aerodynamic panel method solver. It is based on solving an equation for the velocity potential Φ, Eq. 9, which is a function of the combined influence of distributed source (ξ) and dipole (ς) basic aerodynamic flow patterns. The potential theory is based on the idea that the velocity at any given point in the domain is a function of its relative position to the superposed flow pattern. The relative position is defined by the distance between the domain point and the source (r, m). The sources act on surface area, S (m) with a unit normal vector n.

$$\Phi = \int \left[\frac{\xi}{r} + \frac{d}{dn}\left(\frac{\varsigma}{r}\right)\right] dS \quad (9)$$

The Langrangian method of particle tracing has been implemented in lewINT to solve the 2D momentum equations for the droplets in order to obtain the collection efficiency (β). The equations are solved for their acceleration in x and y direction, which are $\ddot{x}_p$ (ms^{-2}) and $\ddot{y}_p$ (ms^{-2}), respectively. As per the Newton's second law, the momentum of a droplet (point mass/object) with mass m (kg) is a result from the net force, which acts on it. Eq. 10) and Eq. 11 show how the momentum of the droplet in x and y direction is a function of the lift force (L_{drp}) and drag forces (D_{drp}) acting on the droplet, the gravitational force as function of the gravitational acceleration, g (ms^{-2}) and the angle of slip of the water droplet, γ (º). The angle of attack of the flow (α) is also of significance to the calculation. Eq. 10 and Eq. 11 determine the trajectory of each supercooled droplet used to obtain the aerofoil's collection efficiency, which determines the amount and the limits of the accreted ice. For more detailed explanation on how the modelling parameters affect the overall ice accretion the reader can refer to section 2.1.

$$m\ddot{x_p} = -\overrightarrow{D_{drp}} \cos\gamma - \overrightarrow{L_{drp}} \sin\gamma + mg \sin\alpha \quad (10)$$

$$m\ddot{y_p} = -\overrightarrow{D_{drp}} \sin\gamma + \vec{L}_{drp} \cos\gamma + mg \cos\alpha \quad (11)$$

After determining the body wetness, the mass balance (Eq. 12) on the surface of the aerofoil is calculated for discrete areas on the aerofoil's surface denoted with $S_{current}$ for the area, where the analysis is being conducted at the current step of the calculation and S_{next} denoting the neighbouring area. At each area, the mass fluxes of water, which remains due to impingement ($\dot{m}_{im}$, kgm^{-2}s^{-1}) and run-back from other area ($\dot{m}_{rb_{in}}$, kgm^{-2}s^{-1}), and the mass fluxes of water, which is removed due to evaporation, ṁ$_e$ (kgm^{-2}s^{-1}), freezing, ṁ$_f$ (kgm^{-2}s^{-1}), running-back, $\dot{m}_{rb_{out}}$ (kgm^{-2}s^{-1}), shedding, ṁ$_{sh}$ (kgm^{-2}s^{-1}), and standing, ṁ$_{st}$ (kgm^{-2}s^{-1}), are determined. Once the mass balance is calculated, the quantity is used to conduct the thermodynamic analysis and determine what is the temperature at the surface.

$$\dot{m}_{im} + \dot{m}_{rb_{in}} = \dot{m}_e + \dot{m}_f + \dot{m}_{rb_{out}} \times \frac{\Delta S_{next}}{\Delta S_{current}} + \dot{m}_{sh} + \dot{m}_{st} \quad (12)$$

The mass balance is then used to determine the surface temperature of the aerofoil depending on the energy balance at the surface, which is driven by the different modes of heat exchange by using Eq.13 . The surface temperature, T_{SURF} (ºK), is determined considering the normal direction to the surface with a direction vector ψ and the thermal conductivity of the body in normal direction, k_ψ (Wm^{-1}ºK). The heat balance at the surface is calculated considering the net convective heat loss, q''_{nc} (Wm^{-2}), heat loss from evaporation, q''_{evap} (Wm^{-2}), kinetic heating, q''_{ke} (Wm^{-2}), latent heating from freezing, q''_{lat} (Wm^{-2}), and sensible heat loss/gain, q''_{sens} (Wm^{-2}).

$$-\left(k_\psi \times \frac{dT_{SURF}}{d\phi}\right)_{\psi=0} = q''_{nc} + q''_{evap} - q''_{ke} - q''_{lat} \pm q''_{sens} \quad (13)$$

To model the heat fluxes needed for maintaining a set surface temperature, the anti-icing calculation routine of LewINT was used. Previous research has validated that lewINT provides satisfactory estimations of anti-icing heat fluxes for aircraft cruising operational conditions (Al-Khalil et al. 1997). Although LewINT is designed for aircraft in-cloud icing, the operational range of angles of attack and icing parameters that can be modelled are similar to the icing conditions, which wind turbines experience and the operational conditions of the outer section of the blades. More in-detailed definitions of the used terms and equations can be found in (Wright, William 2008).

3.3.4 Power output modelling – BEM theory

Qblade is utilised for the power performance analysis (Marten and Wendler 2013); it incorporates Blade Element Momentum Theory (BEMT) for power analysis and XFoil (Drela 1989) for the aerodynamic analysis, which utilises vortex and source singularities panel method together with integral boundary layer method. Both methods have been widely used and allow for relatively low computationally intensive simulations to be carried out.

The blade element momentum theory has been derived from applying the actuator disk momentum theory for non-rotating and rotating disk, which shows that the axial and tangential velocities at the disk are modified by the influence of the wake with induction factors *a* and ***a"***. Then the blade element theory is incorporated so that the effect of the induction factors is accounted during the computation of the relative wind speed to the blade's leading edge. The BEM algorithm uses iterative solution to find the induction factors (Marten and Wendler 2013: p. 33), which are then used to obtain the actual lift, drag, thrust and torque forces needed to calculate the power in the rotor shaft from the aerodynamic effects. The detailed derivation can be found in (Hansen 2008, Hau 2013, Spera 1994)

The theory is accurate for incompressible, steady state flows and for well predicted lift and drag characteristics of the aerofoils. The calculation procedures are conducted by discretising the wind turbine blade in elements (annular) with a width of dR. It is then assumed that the distribution of the lift and drag forces is constant along the element and that adjacent elements do not interact with each other. The latter assumption corresponds to a rotor with an infinite number of blades. To correct for the assumptions inherently incorporated from the derivation, various corrections are typically applied to represent closer the actual physics (Hansen 2008: p. 53-55).

At a discrete blade annular element, the arrangements of velocities and forces is as shown by Figure 24. The influence of the induction factors is visualised by the modification of both the axial, V_∞ (ms^{-1}), and the tangential velocities, ωr (ms^{-1}), which contribute to the relative wind speed, V_{rel} (ms^{-1}), at the leading edge of the element. The resolving of the induction factors and the relative velocity allows for the determination of the inflow angle, ϕ (º), which depends on the angle of attack and the pitch angle, θ (º). When, the velocity triangle and the associated angles are known, the lift and drag forces can be computed from the aerofoils' characteristics. Then, the normal force, F_N (N), and the tangential force, F_T (N) can be calculated.

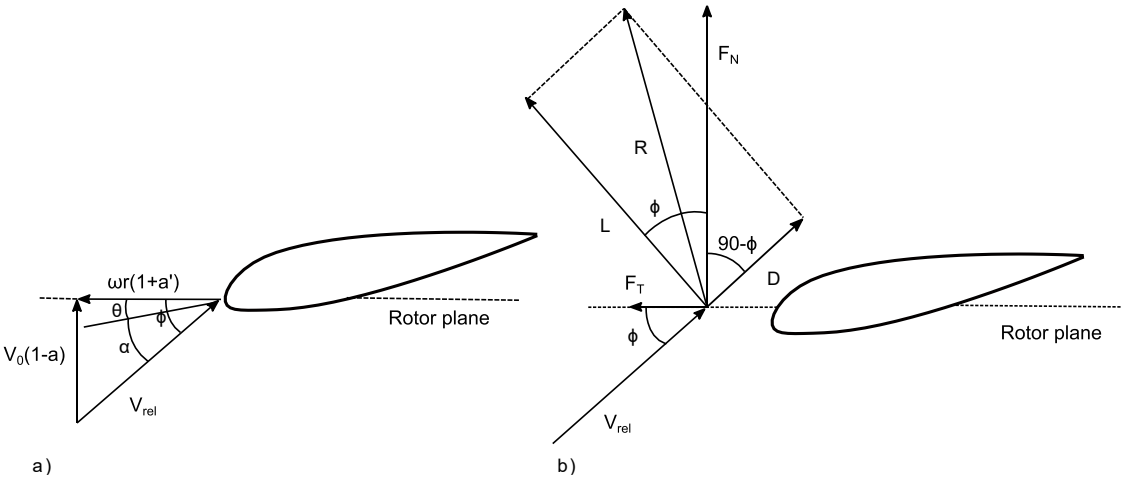

Figure 24: Velocity triangle (a) and aerodynamic forces distribution (b) on an arbitrary aerofoil on a wind turbine rotor blade, (Hansen 2008: 47-48)

The calculation procedures of BEMT start with an initial guess for the induction factors, which can be obtained either by considering typical constant or applying an empirical formula. Then ϕ is calculated from Eq. 14 to find the angle of attack, Eq. 15, which is needed to find the values of the lift and drag coefficients. The coefficients of the normal and tangential forces are then computed by using Eq. 16 and Eq. 17. The calculation routine finishes with the re-computing of the induction factors and accounting for the convergence of the results. The used formulae are depicted by Eq. 18 and Eq. 19, where σ is the local rotor solidity. The solidity σ is a function of the local chord length, c(r) (m), the number of blades, B (-), and the local radius of the element from the rotor hub, r as shown by Eq. 20.

$$\phi = \arctan\frac{(1-a)\times V_0}{(1+a')\times\omega\times r} \tag{14}$$

$$\alpha = \phi - \theta \tag{15}$$

$$C_n = C_l \times cos\phi + C_d \times sin\phi \tag{16}$$

$$C_t = C_l \times sin\phi + C_d \times cos\phi \tag{17}$$

$$a = \frac{1}{\frac{4\times\sin\phi}{\sigma\times C_n}+1} \tag{18}$$

$$a' = \frac{1}{\frac{4\times sin\phi\times cos\phi}{\sigma\times C_t}-1} \tag{19}$$

$$\sigma(r) = \frac{c(r)\times B}{2\times\pi\times r} \tag{20}$$

The power of the rotor is found by integrating the tangential force for one blade, then estimating the torque moment and multiplying with the rotational speed of the rotor and the number of blades.

3.3.5 Numerical setup for aerodynamic characteristics modelling – XFoil and Fluent

XFoil and Ansys Fluent 19.0 were selected to perform an aerodynamic analysis of a clean and iced NACA 64-618 aerofoil, with results compared with experimental data. The simulation flow conditions were selected to correspond to the Re numbers, which were achieved when the experimental data for this research was taken (*i.e* 165 000) and the operational Re of the wind turbine blade section for a wind speed of 10 ms^{-1} (*i.e*. 6 000 000). The aerofoil polars were generated for angles of attack ranging between -10° and 16° and data was generated at every 2° (a 4.5° operational angle of attack was also included). The investigation aimed to quantify the uncertainties that can be expected when low computationally intensive tools are used for

aerodynamic analysis of iced aerofoils. This is particularly needed as aerodynamic performance modelling enables the quantification of ice induced power losses, and the subsequent development of operational strategies for effective wind turbine adaptation to icing conditions.

3.3.5.1 *XFoil*

In this research, the code has been used as implemented in the free licence software Qblade for wind turbine design and analysis. XFoil has been used to obtain the lift and drag curves of both clean and iced aerofoils. It has been chosen due to its wide usage within the research community for fast aerofoil design and analysis (Marten and Wendler 2013, O. Günel, E. Koç and T. Yavuz 2016, Timmer and van Rooij 2003). Moreover, its ability to be embedded in analysis system makes it a good choice for simulation tools analysing the wind turbine power performance for iced conditions leading to relatively small geometrical modifications of the aerofoil (Brillembourg 2013, Dimitrova, Mariya, Ramdenee and Ilinca 2011, Jha, K., Pankaj, Brillembourg and Schmitz 2012, Yirtici, Ozgen and Tuncer 2019).

To use XFoil, the aerofoil was discretised into panels, which depending on the ice shape would vary between 150-250, with typical clustering at the leading edge and the trailing edge, as shown in Figure 25. The variation was needed to prevent the noticeable distortion of the aerofoil geometry for a high number of panels, which led to inability of the calculation routine to continue. Additional optimisation of the panel distribution was not applied and the trailing edge to leading edge density ratio was set to 0.15; the refined area to leading edge panel density ratio was set to 0.2.

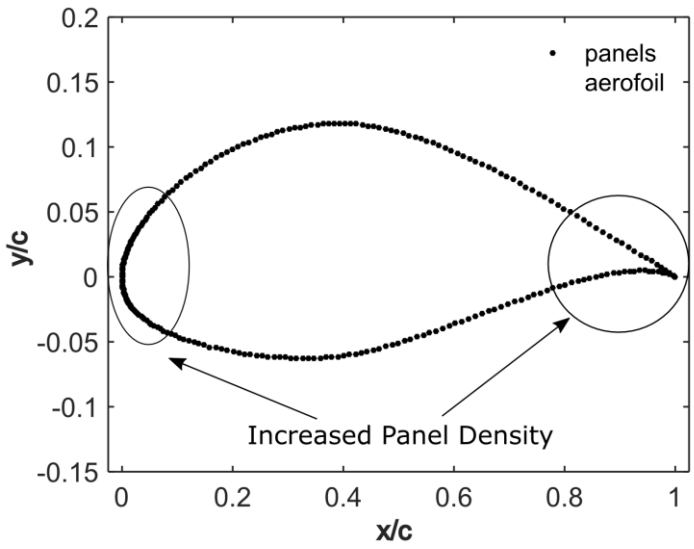

Figure 25: Aerofoil surface of NACA 64-618 aerofoil as used in XFoil for aerodynamic analysis.

In XFoil, the transition of the boundary layer from laminar to turbulent can be modelled either by using a free transition method, e^n method (Marten and Wendler 2013, Morgado *et al.* 2016), or a forced transition method, which can be prescribed at any location on the top and the bottom

surfaces of the aerofoil. In this research, a free transition method was utilised with the critical amplitude (Ncrit) of the most amplified Tollmien-Schlichting waves set to 9 (default value), as forced transition is more suitable for direct comparison with experimental data (*i.e.,* transition locations are known) where the transition location is identified. In other research, regardless whether XFoil was used for clean or iced aerofoil analyses, the free transition method was preferred (Herbert-Acero *et al.* 2015, Morgado et al. 2016, Yirtici, Ozgen and Tuncer 2019). In Figure 26a-b, justification of the current setup of the software is provided, by comparing the power coefficient (Figure 4a) and power output (Figure 4b) data documented in (Jonkman *et al.* 2009) with results obtained by the current setup of XFoil. The data obtained from XFoil was in good agreement with the published data for the NREL 5 MW reference wind turbine. The differences towards the lower tip-speed ratios is seen for the maximum panel number used in this project and is attributed to an excessive number of panels and the lack of fine tuning of the aerodynamic data for the extrapolation scheme. The slight disagreement for tip-speed ratio of above 7.5 is due to the current results being for a constant rotational speed, while the actual design of the wind turbine considered variable rational speed. This can be improved with fine tuning of the aerodynamic data and re-calculating the curves with the designed rotational speed. The power curve estimation for the region of interest of this research (*i.e.* wind speeds between 7 and 10 ms^{-1}) is in excellent agreement with the published power curve for the analysed wind turbine.

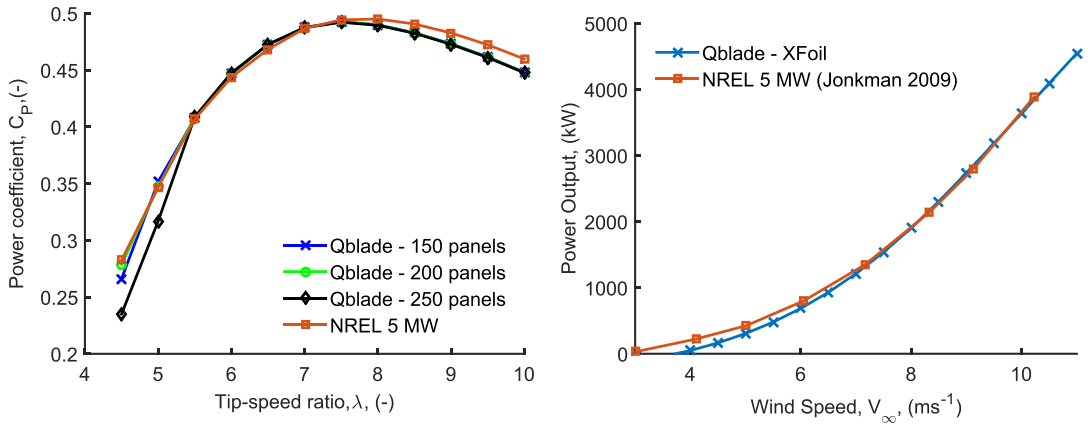

Figure 26: Power coefficient (a) and power output (b) data comparison between XFoil with the current setup and documented data from the NREL reference report (Jonkman et al. 2009)

3.3.5.2 *Computational Fluid Dynamics*

Two-dimensional, incompressible, RANS-based, steady-state simulations were performed to analyse the aerodynamic performance of the NACA 64-618 aerofoil. ANSYS Fluent 19.0 was used for the analysis and turbulence was modelled with the k-w SST model, as formulated in (Menter 1994) and described in (Morgado *et al.* 2016). The model has been widely used within the research community for aerodynamic characteristics of iced aerofoils (Han, W., Kim and Kim 2018, Hudecz 2014, Jin and Virk 2019, Villalpando, Reggio and Ilinca 2012, Zanon, Gennaro and Kuhnelt 2018). In addition, it has been shown that turbulence modelling based on the kw

SST modelling framework can provide numerical results much closer to experimental data than other turbulence models (Herbert-Acero *et al.* 2015).

The numerical setup, which involves the choice of computational domain topology and computational discretization procedures, was based on previous research of iced two-dimensional aerodynamic profiles. In addition, a conservative choice was made to exclude the use of any specialized setup and settings for simulation ease, which will be beneficial for future ice loss prediction tools that would require multiple simulations of various iced profiles. Moreover, the accuracy of the turbulence models is not certain due to the fact that their derivation includes many constants that are specifically tailored for certain flow properties, excluding severe geometry changes and the respective complex flow patterns that can be seen on iced aerofoils. Previous research noted that even for non-iced two-dimensional profiles, turbulence models can benefit from fine tuning of some of the constants used in their formulation (Herbert-Acero et al. 2015: p. 29)

Similar to previous studies, the domain was modelled by using a C-type mesh topology (Herbert-Acero et al. 2015, Villalpando, Reggio and Ilinca 2016, Zanon, Gennaro and Kuhnelt 2018). To ensure that the domain boundaries will not affect the numerical solution, each boundary was placed at 20-chord lengths from the aerofoil geometry as shown on Figure 27. The discretization of the domain was performed with an all triangles method for achieving a best split and to capture the boundary layer, 15 layers for mesh inflation were generated at the aerofoil surface. The first layer was placed at 3×10^{-7} m to ensure a good transition ratio between the inflation layers, and for the main mesh, a growth rate of 2 was set, which resulted in a y+ value of less than 1, removing the need for using wall function technology to model the boundary layer. Additional details about the method of calculating the y+ value and the graphs showing its distribution along the lengths of the aerofoil can be found in Appendix 1.

The global element size of the mesh was chosen to be 0.3 m after a mesh dependency study, which is shown in Figure 28a-b. The resulting mesh consisted of 145 000 elements, which is similar to the mesh size achieved in (Villalpando, Reggio and Ilinca 2012, Zanon, Gennaro and Kuhnelt 2018). Additional settings of the global mesh include a defeaturing size of 3×10^{-6} m, curvature min size of 1×10^{-6} m and curvature normal angle of 9º. The growth rate of the mesh from a minimum size to the boundary edges was set to 1.2. Edge sizing was used to discretise the aerofoil surface and the control cut that was made between the aerofoil's trailing edge and outlet boundary (*i.e.* Figure 27). Sizing of 1×10^{-3} m and 5×10^{-2} m was used for the elements, which discretize the aerofoil's surface and the control cut, respectively. The behaviour of the discretization was set to soft to ensure good transition between mesh elements. The mesh quality is summarized in

To simulate the changing angles of attack the velocity at the inlet of the domain was specified with its components in x and y directions, the inlet boundary condition was set to Velocity-inlet and an absolute reference frame. Initial Gauge Pressure, Turbulence viscosity and Turbulence

Intensity (TI) were set to 0 Pa, 10% and 5%, respectively. Although TI of 5% is a relatively high value for aerofoil analysis, it was seen that the final prediction of the forces was not sensitive to the value of the inlet turbulence intensity. Another reason for keeping a relatively higher percentage is due to the unknown turbulence intensity of the wind tunnel used for aerodynamic analysis. However, it is expected to be above 5% similarly to the experimental setup in (Hudecz 2014).

The outlet and the wall were set to be the default pressure outlet and wall boundary conditions, respectively. The wall did not include slip as the aerofoil was simulated to be stationary and no roughness was added for the main simulation cases.

The solution was achieved by using the numerical setup outline in **Error! Not a valid bookmark self-reference.**. The Semi-Implicit method for Pressure-Linked Equations (SIMPLE) was selected, which is also the default solution method. To discretize the fluid properties terms second order methods were selected for better accuracy. All simulations were started with standard initialization, which used the prescribed flow properties from the intel conditions. The monitoring of the solution was performed with a scaled absolute convergence criterion and all quantities, which are normally reported by the k-w SST model were set to converge when the residuals reach a value of 10^{-5}.

Table 4, where the average mesh quality parameters are shown.

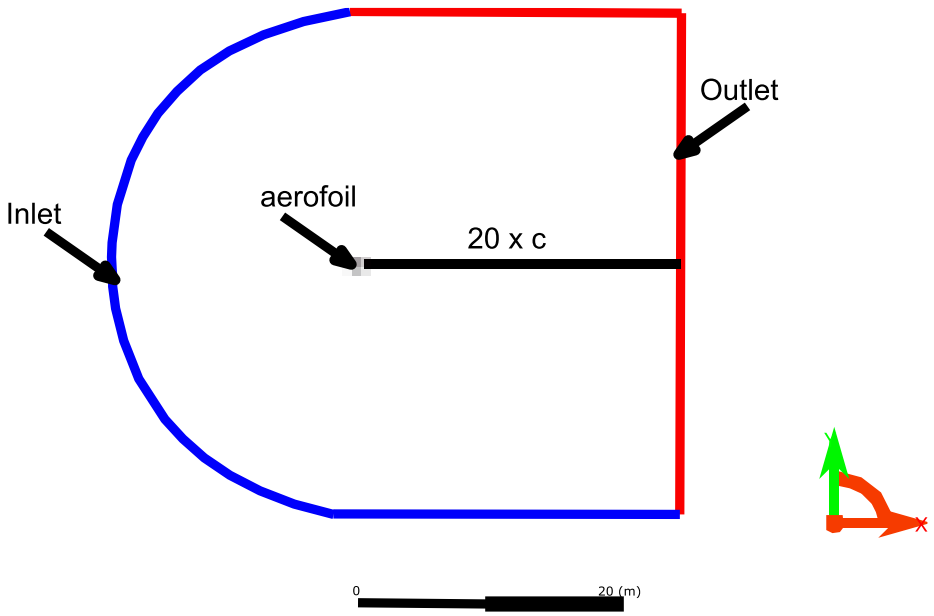

Figure 27: Domain and mesh topology used in this thesis

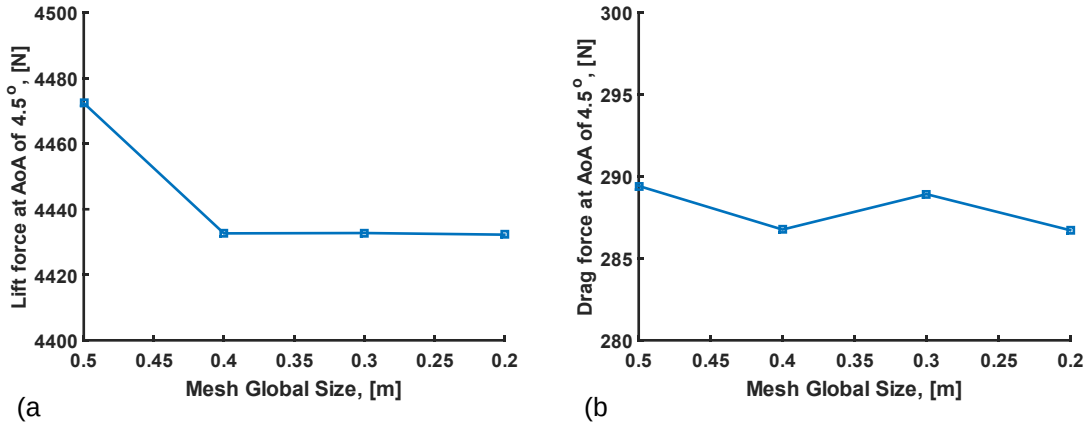

Figure 28: Mesh dependency study based on lift and drag forces convergence for an angle of attack of 4.5° and wind speed (V) of 10 ms^{-1}.

Table 3: Average values of mesh skewness, orthogonal quality and aspect ratio indicating the overall mesh quality.

Parameter	Mean Value
Skewness	0.85
Orthogonal Quality	0.97
Aspect Ratio	0.56

To simulate the changing angles of attack the velocity at the inlet of the domain was specified with its components in x and y directions, the inlet boundary condition was set to Velocity-inlet and an absolute reference frame. Initial Gauge Pressure, Turbulence viscosity and Turbulence Intensity (TI) were set to 0 Pa, 10% and 5%, respectively. Although TI of 5% is a relatively high value for aerofoil analysis, it was seen that the final prediction of the forces was not sensitive to the value of the inlet turbulence intensity. Another reason for keeping a relatively higher percentage is due to the unknown turbulence intensity of the wind tunnel used for aerodynamic analysis. However, it is expected to be above 5% similarly to the experimental setup in (Hudecz 2014).

The outlet and the wall were set to be the default pressure outlet and wall boundary conditions, respectively. The wall did not include slip as the aerofoil was simulated to be stationary and no roughness was added for the main simulation cases.

The solution was achieved by using the numerical setup outline in **Error! Not a valid bookmark self-reference.**. The Semi-Implicit method for Pressure-Linked Equations (SIMPLE) was selected, which is also the default solution method. To discretize the fluid properties terms second order methods were selected for better accuracy. All simulations were started with standard initialization, which used the prescribed flow properties from the intel conditions. The monitoring of the solution was performed with a scaled absolute convergence criterion and all quantities, which are normally reported by the k-w SST model were set to converge when the residuals reach a value of 10^{-5}.

Table 4: The solver and discretization setup used in Fluent 19.0 to design the CFD numerical analysis for this research

Solver	SIMPLE
Spatial Gradient Discretization	Least square method
Pressure Gradient Discretization	Second order
Momentum Discretization	Second order Upwind
Turbulence Kinetic Energy Discretization	Second order Upwind
Specific Dissipation Rate Discretization	Second order Upwind
Initialization	Standard from Inlet

. Figure 29 displays an example of the convergence criteria after 5000 iterations, which indicates that the mesh has some regions, which contribute to higher residuals from the solution of the mass continuity equation. However residual values below 10^{-3} would be considered acceptable when resolving the mass continuity equation, as higher fidelity CFD analysis is out of the scope of the current research. A complete graph of the residuals for an ice-free aerofoil surface can be seen in Appendix 1.

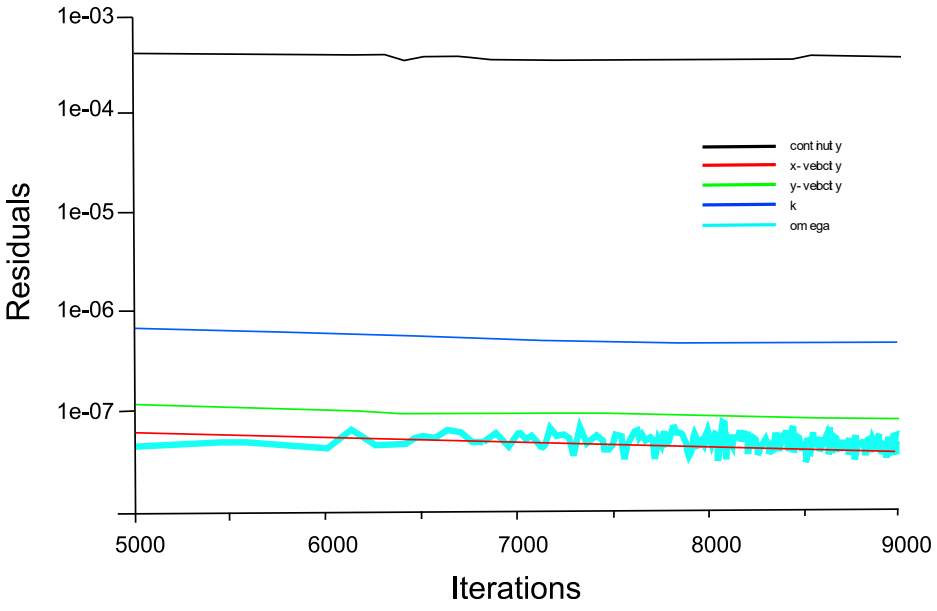

Figure 29: Representative convergence criteria graph for the current CFD numerical setup, showing the absolute residuals after solving the continuity equation (continuity), the velocity in x (x-velocity) and y (y-velocity) direction, the turbulence kinetic energy (k) and the specific turbulent dissipation rate (omega); which are all outputs from the k-w STT model.

3.4 Experimental setup

The experimental study, which was utilised to supplement the analysis in the previous chapter is outlined in this subsection. The experimental design is presented, and it covers details about

the wind tunnel specifications and properties, test pieces design and manufacturing and the testing conditions used for measuring lift and drag forces.

3.4.1 Apparatus

3.4.1.1 Wind Tunnel

The research was carried out in the open circuit subsonic wind tunnel in Coventry University, UK. A schematic of the wind tunnel is shown on Figure 30, where the constituting part of the setup can be examined. The tunnel work section has a rectangular shape and measures 0.6 m in length. Both the width and the height of the working section are 0.305 m. It is equipped with two pitot assemblies and ambient temperature variations between 5 and 40 °C and wind speed of up to 36 ms^{-1} can be simulated. The wind tunnel design does not allow for ambient pressure and density control. The medium used for testing is air and its maximum relative humidity at temperatures of 31 °C is 80%; decreasing linearly to a relative humidity of 50% at 40 °C.

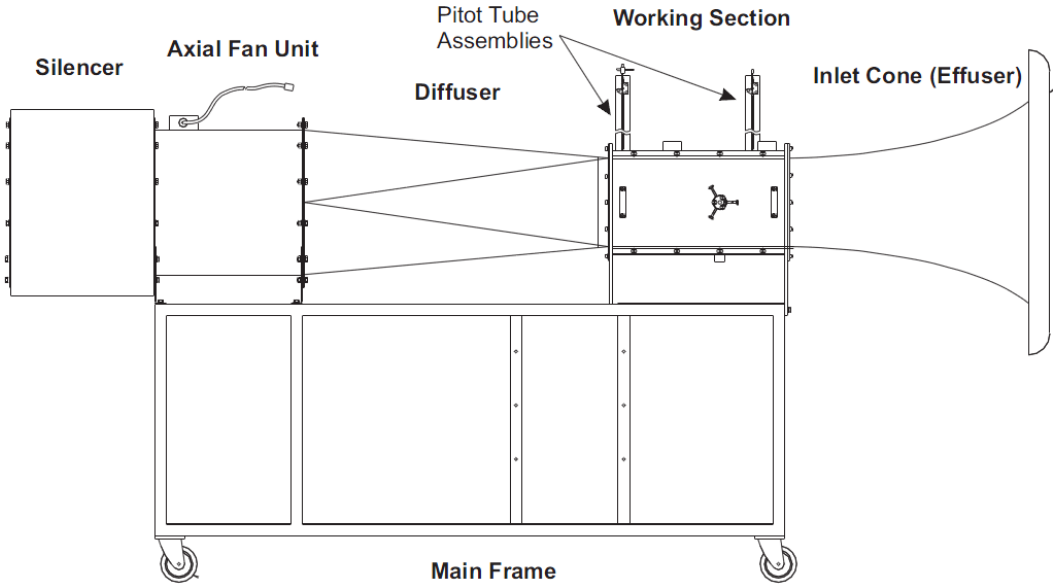

Figure 30: AF100 sub-sonic wind tunnel used to conduct the experiments and its constituting parts(TecQuipment 2013).

3.4.2 Working Section

The working section is equipped with pitot and static-pitot tubes, Figure 31a-b, which both measure the dynamic pressure at prescribed locations. The basic pitot tube receives a feedback for the static pressure in the working section from a wall tapping (Figure 31b), while the pitot-static tube is designed to measure the static pressure without additional feedback. The probes are connected with flexible hoses to the processing unit of the wind tunnel, where the measurements are displayed as pressure difference. The static-pitot tube can be used for wake measurements to obtain the drag of the tested article as shown on Figure 31b, as approximated method to wake rake method.

Test articles are mounted in the working section by means of a stem. The stem is attached to the aerofoil and a three-component balance that is used to measure lift force, drag force and pitching moment. The precision of the three-component balance for measuring forces is +/- 0.2-0.25 N as per AFA3 User Guide (TecQuipment 2013) .

3.4.3 Limitations

The current analysis is limited by the maximum wind speed that could be used during testing and the accuracy of the measuring system. Maximum testing speed of 20 ms^{-1} is allowed due to noise regulation in the testing facility, which limits the maximum Re that can be achieved to 160 000 (for a 0.122 m chord lengths). During testing the NACA 64-618 aerofoil, it was seen that the drag force that is measured for angles of attack around 5° is approximately 0.35 N, while the lift force is approximately 4 N. Thus, considering the precision of the testing equipment, the uncertainties for the drag measurements can be expected to be up to 71%, while for the lift force could be 6.25%. It should be noted that for angles of attack below 3° the drag force is about 0.2 N that would suggest 100% uncertainty value. The temperature of the air was on average of 25 ºC, which was used with a standard atmospheric pressure at sea level (1013×10^5 Pa) to yield the density of the air. Thus, the density of the air varied between 1.18 kgm^{-3} and 1.19 kgm^{-3}.

The turbulent intensity of the wind tunnel is not documented by the manufacturer, but it is expected to be high. Due to the fixing of the testing article to the measuring rod, an opening exists in the test section, providing space for air leakage. This should be taken into consideration when the obtained results are being reviewed in future. The wind tunnel design influences the results and could lead to higher measured separation angles, reduced lift due to air leakages and increased drag, when using the measurement unit

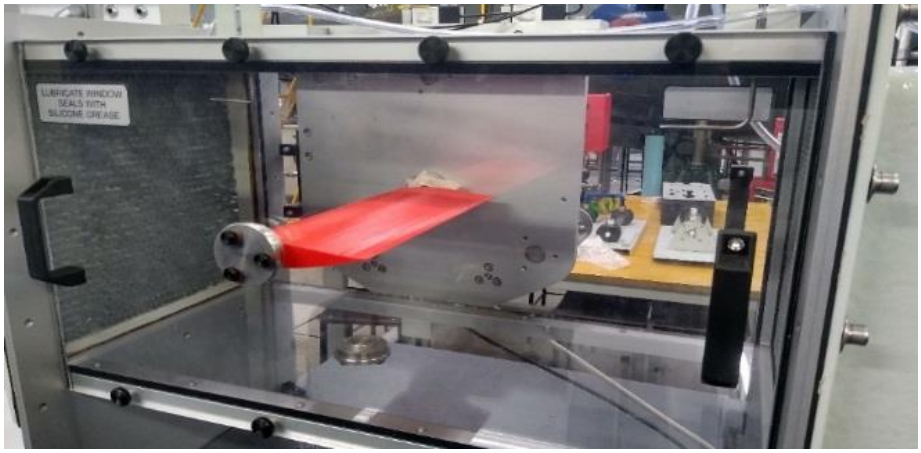

(a

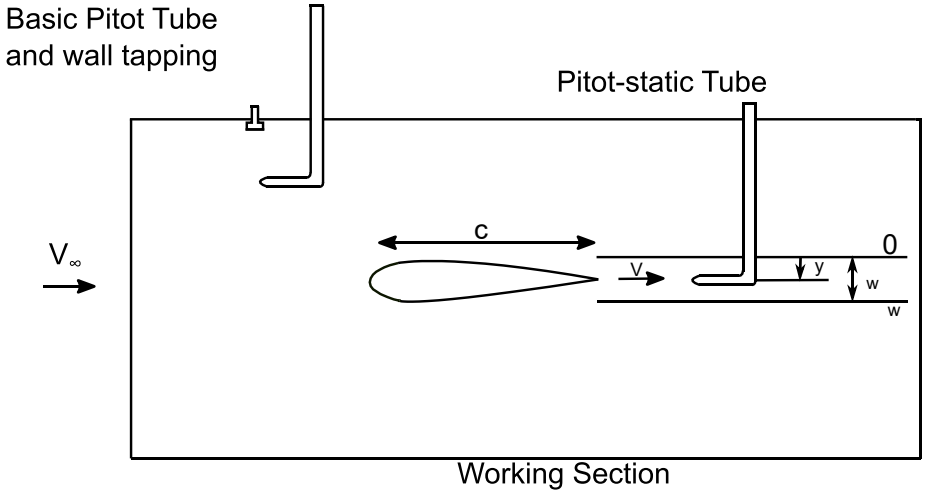

(b

Figure 31a-b: Wind tunnel working section with mounted test article (a) and the schematics of the working section displaying the arrangement of the pitot tubes and method of taking wake measurements for drag calculations (b) (TecQuipment 2013)

3.5 Test and Method

NACA 64-618 and NACA 0012 were tested in the sub-sonic wind tunnel of Coventry University to measure lift and drag forces. To evaluate the experimental design of the used facility, two pre-tests for non-iced aerofoils were conducted to compare lift and drag force data obtained with the current setup against available experimental data in the literature. After the pre-tests, NACA 64-618 was used to measure iced induced aerodynamic degradation for two operational strategies. The aerofoil section was tested for ice shapes, which were obtained for a 1-hour long icing event at discrete times and ice shapes produced during derating of the wind turbine from tip-speed ratio of 7.5 to 5.0 during icing.

The experimental results were used to compare the predictive capabilities of XFoil and Fluent for the Re, which can be achieved in the wind tunnel. This was done to evaluate the predictive

capabilities of the two tools for the flow conditions that can be achieved in the wind tunnel. Although this method allowed for the predictive capabilities of the two tools to be compared, it did not indicate what the implications would be of choosing either of the tools to model the performance of a wind turbine in icing conditions. This was mostly caused by the limitations of the measuring setup. To address this limitation, numerical simulations with XFoil and Fluent were conducted at operational Re for the NREL 5 MW wind turbine.

Overall aerodynamic degradation was quantified by registering reduction of C_L and increase in C_D for an angle of attack of 0 º and angle of attack of maximum C_L. The lift curve slope (*i.e.* $\partial C_L/\partial\alpha$) was also used as an indicator of the lift characteristics of the tested aerofoils. It was implemented by applying a linear fitting to the data points, which were corresponding to the linear region of the lift curve. Lift and drag data for angles of attack of 4.5 º and 8 º was analysed for the corresponding test cases (both experimental and numerical), as these are the operational angles of the wind turbine blade section, when it is operated at TSR of 7.5 and 5, respectively.

The NACA 0012 aerofoil section aspect ratio was 2 with chord length and span of 0.150 m and 0.3 m, respectively. When mounted in the test section of the wind tunnel, 0.025 m gap was present between the vertical walls of the working section and the tips of the aerofoil

NACA 64-618 aerofoil was used to analyse ice shapes for 1-hour long extreme icing event, when the NREL 5 MW wind turbine is operated either at its reference TSR (7.5) or at a modified TSR (5). An extreme icing event was chosen to produce the ice shapes with wind speed of 10 ms^{-1}, LWC of 5×10^{-4} kgm^{-3}, MVD of 25×10^{-6} m and ambient temperature of -10 °C (see Table 1). In total 8 test sections were 3D printed. Four sections were printed to represent the ice shape, which were expected for 1 hour of icing and operating at TSR of 7.5. The test models of NACA 64-618 were printed with a chord length of 0.125 m and a span of 0.303 m. The chord length of 0.125 m was chosen to ensure test section width to chord length ratio of approximately 0.40; the span of the model ensured 0.001 m clearance at each side of the model. However, because of the printing capabilities of the used Ultimaker 2 3D printing facilities, the actual chord length of the printed model was reduced by 2%, resulting in a chord length of 0.1225 m. Surface roughness analysis on a patch at the leading edge showed roughness average, R_a, of 0.0128 µm and mean roughness, R_z, of 0.0714 µm. Additional data on the surface roughness analysis is presented in Appendix 2, which show the surface roughness that was obtained and used for all tested models.

During testing, it was seen that at angles of attack larger than 3 ° upstream disturbance could be seen at the front pitot tube causing between 0.5% and 9.8% reduction in the flow velocity readings in the test section. Thus, a decision was made to reduce the chord length to 0.100 m, but the printed articles were with a final chord length of 0.096 m. As a result, the upstream disturbance was reduced, but only marginally. This could be due to the fact that NACA 64-618 aerofoil is a high-lift aerofoil, which would need a larger test section for testing. As the change

took place after the first set of printed aerofoils was ready (*i.e.* ice shapes for TSR of 7.5), only the ice shapes representing icing for operation at the reduced TSR of 5 had chord lengths of 0.096 m. This did not affect the overall aim of the analysis, as the focus of the measurements was to establish relative degradation of the aerodynamic characteristics. Thus, the percentage change of C_L and C_D was to be measured.

Comparison between rime and glaze icing shapes were performed, as it is a common test case, which can be found in the literature (Appendix 2). The results were used to evaluate what aerodynamic degradation could be registered with the current setup and how it compared with data. The glaze case was chosen to be the ice shapes produced after 1 hour of icing for event A105, while the rime ice case was selected to be represented with the ice shapes, which would be expected after 1 hour of icing for B1010.

3.6 Summary

This chapter provided details on the overall design of the methodology for this research and the specific methods that were used to model the performance of a utility-scale wind turbine in icing conditions and design different operational strategies for ice mitigation. Another focus of the methodology is to compare different computational methods for the aerodynamic analysis, which is needed to evaluate ice induced aerodynamic losses. An experimental study was designed to supplement the comparison analysis and help assessing the expected percentage differences when XFoil and RANS-based modelling approaches are utilised. The results of the are provided in the subsequent chapters.

4 Aerodynamic Degradation Modelling

This chapter set out to investigate the aerodynamic degradation of iced aerofoils, typically used in wind turbine blade design. Experimental and numerical results for different ice shapes are presented to evaluate variations in lift and drag characteristics. Seven ice shapes were generated using LewINT for two different operational strategies. Each ice shape was manufactured and tested in a set of wind tunnel experiments. XFoil and Fluent numerical results were obtained for the same flow conditions that could be achieved in the wind tunnel and flow conditions, which were representative of actual wind turbine during operation. The research went on to examine the differences and similarities in the iced aerofoil performance results, and thus establishing which tools and methods should be adopted further in the thesis.

4.1 Results

The results obtained from the numerical and the experimental analyses are presented and compared in this chapter. Pre-tests evaluating the quality of the experimental design are presented along with the direct comparison of the data obtained with XFoil and Fluent; and lift and drag measurements from the experiments. The chapter concludes with discussion on the implications of using XFoil for aerodynamic modelling within a wind turbine performance modelling framework and the consideration that would be needed for future analysis and studies.

4.1.1 Pre-tests

4.1.1.1 NACA 0012

NACA 0012 was tested at Re of 194 022 and C_L and C_D were measured as shown on Figure 32a-b. For the C_D measurements, both load cell and wake sampling methods were used. The wake sampling method was realised by measuring the pressure deficit behind the tested aerofoil using the static-pitot tube. To minimise the differences between the undertaken method and the established wake rake method, the pressure sampling was done by using small sampling step in vertical direction of 0.002 m. The final results were evaluated against measurements taken in Sandia Laboratory at Re of 360 000 (Sheldahl and Klimas 1981).

.

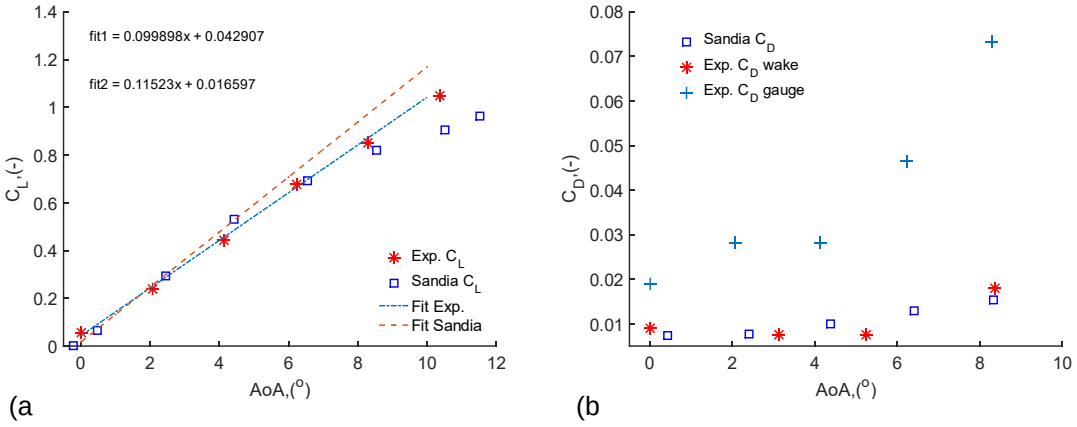

Figure 32a-b: Lift (a) and Drag (b) coefficients against the angle of attack for the NACA 0012 aerofoil at Re of 194 022, whereas Sandia experimental data is obtained for Re of 360 000. Fit1 corresponds to the measurements taken for this study, while fit2 corresponds to the Sandia Laboratory results. Drag measurements from wake deficit method (Exp. C_D wake) and from wind tunnel measuring equipment (Exp. C_D gauge). (b)

A linear fit for angles of attack between 0 ° and 6 ° was used to obtain the lift curve slope for the two C_L experiments, which are displayed on Figure 32a. The measured wind tunnel results were found to be within 13% agreement with the published data. For angles of attack between 2 ° and 10 °, the differences were less than 8%. The greatest percentage difference between measured values was registered for C_L at AoA of 0 °, which for Sandia Laboratory results was 0.017, whereas the current measurements showed 0.042. The 158% difference was attributed to the few data point that were available for the fitting and the fact that the magnitude of the measured values in both cases was in the order of 10^{-2}.

Due to the sensitivity of the load cells, their precision (+/-0.25N) and the magnitude of the measured force (around 0.4 N), the measured C_D data from the load cells showed much higher values than the published results. Better agreement with the available data, was found with C_D measurements, which were completed with the wake sampling method (Figure 32b). As a static-pitot tube was used for taking the measurements the agreement was considered to be sufficient, providing the accuracy of the method was reduced in this case.

Disagreement between the two set of results that have not been reviewed could be attributed to differences in the Re; wind tunnel air leakages and interaction between the working section of the wind tunnel and the model. Taking the measurements manually can introduce some uncertainty as well.

4.1.1.2 NACA 64-618: Clean aerofoil experimental and numerical results

The experimental measurements of C_L and C_D were conducted for Re of approximately 160-000. The lift curve was obtained by a linear fit to the measured data for angles of attack between 0 and 10 °. Drag measurements were taken with the force balance, while wake measurements were conducted only for an angle of attack of 4.5 °, as this is the operational

angle of attack for the test section, when the NREL 5 MW wind turbine is at rated power output. The results were compared against previous experimental measurements obtained for Re of 312 700 (Hudecz 2014). This is the only study in the literature that looked at the aerodynamic performance of the NACA 64-618 for Re lower than 350 000.

The current measurements indicated 13% higher lift curve slope and 36.12% lower $C_{LAoA=0}$ than the reported values (Hudecz 2014), as it can be seen from Figure 33. The differences between the two measurements come from mainly three sources of dissimilarity. The first one is the lower Re number at which the current measurements were taken indicating that the aerofoils were not measured for dynamically similar conditions. The second difference is the application of tunnel corrections, which in this study was done by adding the wake blockage correction, ε_{WB}, using the drag coefficient data sampled with the force balance measuring equipment. This was calculated to introduce up to 3**%** variation in the corrected results for C_L and C_D, when the angle of attack is below 10 º. Another significant influencing source of dissimilarity in the results is the surface treatment of the aerofoil. The reported values in (Hudecz 2014) were for a smooth aerofoil, while the tested aerofoil was 3D printed with some roughness. Previous studies have shown that rough aerofoils perform better at low Re numbers, ensuring smaller overall degradation of Cl, as this minimizes the influence of the laminar separation bubble (Lynch and Khodadoust 2001: p. 680).This can explain the higher lift coefficient slope and the lower lift coefficient value at the 0 ° angle of attack. Further dissimilarities might source from unaccounted air leakage in the work section due to the wind tunnel design and the condition of the sealings.

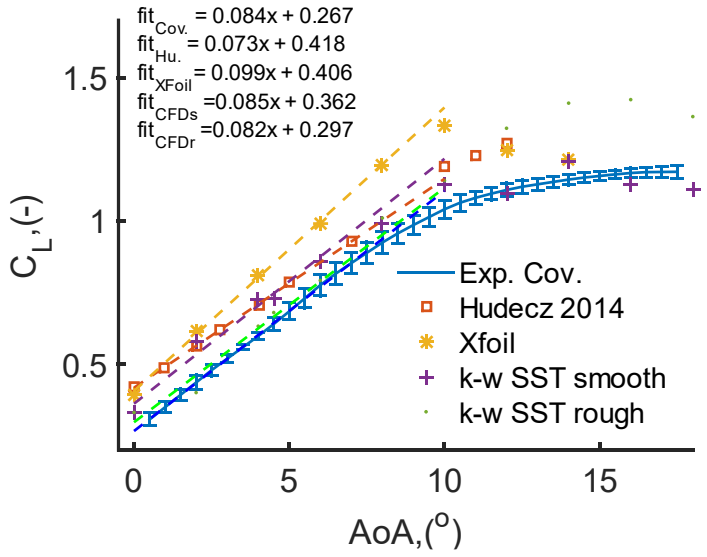

Figure 33: Comparison of the measured lift curve against Hudecz curve and three computational results - obtained with XFoil, CFD with smooth surface and CFD with rough surface of the aerfoils, respectively

The numerical results that were included in the analysis were obtained for smooth aerofoil, as in general it is hard to match the exact roughness for different studies. However, a simulation including roughness consideration was performed using the predictive capabilities of k-w SST

turbulence model. Equivalent sand grain roughness of 120 μm was used, which was based on the measured Ra of the printed model and the approximation scheme developed in (Adams, Grant and Watson 2012), accounting for the differences in the results presented by the authors.

XFoil and Fluent results were found to be closer to the reference experimental data with no surface roughness for an angle of attack is 0 °, with 2.8% and 13.3% difference, respectively. The lift curve slope, which were obtained numerically are both higher than ones measured in the reference study. XFoil and Fluent agreed within 16.5% with each other, while in comparison to the reference data they overpredict the lift curve slope by 35.6% and 16.4%, respectively. It should be noted that the simulated results are closer to the true values of the lift curve slope as it has been shown that the reference experimental data used here underpredicts the lift curve slope of the aerofoil (2014: p. 38).

The argument that the difference between the experimental measurements obtained in the wind tunnel and the reference measurements was due to the surface roughness differences becomes stronger, when the k-w SST model results are studied for smooth and rough surfaces. The simulation results for smooth surface were closer to the reference measurement data, while the ones with roughness added, were closer to the measured data for the rough aerofoil. The agreement was found to be consistent for both C_L at 0 º angle of attack and the lift curve slope. The overall agreement of k-w SST results to the reference and the measured data was estimated to be between 13.33 – 16.44% for the smooth aerofoil and between 2.3 – 11% for the rough aerofoil. To obtain a more detailed understanding of the nature of the difference between the results, the pressure distribution on the surface of the aerofoils needs to be investigated at every angle of attack, the skin friction coefficient and the transition points/regions. Only then it can be concluded with higher degree of certainty why the results differ. In addition, the current analysis is limited as the wind tunnels that were used were not fully documented in terms of the flow quality, which was ensured in their working sections.

The operational angle of attack for the NACA 64-618 aerofoil on the outer blade section of the NREL 5 MW wind turbine is approximately 4.5 ° and C_L and C_D data from both experimental measurements and the simulations is summarised on Table 1. Percentage differences in reference to the experimental values obtained in the Coventry university wind tunnel are presented. The calculated differences correlate with the conclusions, which were drown from the analysis of the lift curves. Thus, C_L data for the operational angle of attack correlate with the value obtained in the reference experimental data within 15.6%, while depending on the numerical tool and setup, the differences between measured and simulated values ranges between 13.04% and 31.3%. The results, which were simulated for rough aerofoil were disregarded, as additional modelling would be needed to obtain conclusive results. Overall the results measured with the current design setup agree within 15.6% to previous studies that can be found in the literature.

Table 5 Clean aerofoil CL and CD at 4.5° angle of attack as measured in the open circuit low-speed Coventry University wind tunnel, the DTU subsonic wind tunnel from Hudecz (Hudecz 2014), predicted by XFoil, Fluent with k-w SST model for smooth and rough surface

Approach	$C_{L4.5}$	$\Delta_{CL4.5}$, %	$C_{D4.5}$	$\Delta_{Cd4.5}$, %
Exp. Cov.	0.64	-	0.0253	-
Hudecz	0.74	-15.6	-	-
XFoil	0.84	-31.3	0.0238	5.9
k-w STT smooth	0.73	-14.1	0.0286	-13.04
k-w SST rough	0.68	-6.3	0.0389	-53.76

4.1.2 Ice shapes testing

4.1.2.1 One-hour long icing event

During icing, ice continuously builds-up from the start of an event until its end, which for wind turbine blades results in the gradual change of their cross-sectional area. On Figure 34a-c, ice shapes for 1-hour long event are shown. The shapes have been obtained for Section D of the NREL 5 MW reference wind turbine blade (see Figure 24) where the relative wind speed to the blade's leading edge is the highest, resulting in high ice accumulation rate. Wind speed of 10 ms^{-1} and TSR of 7.5 were used to estimate the operational angle at the chosen blade section, which was found to be 4.52 º. The weather conditions, defining the icing event parameters, were chosen the same as icing event A105 (*i.e.* LWC of 5 kgm^{-3} and MVD of 25 μm). The ice shapes on Figure 34a-c illustrate how the cross-sectional area of blade section D changed after 0.25, 0.5 and 1.0 hours of icing. Their aerodynamic performance (C_L and C_D) was studied using wind tunnel measurements at Re of 165 000, which were then studied in conjunction to simulation predictions from XFoil and Fluent.

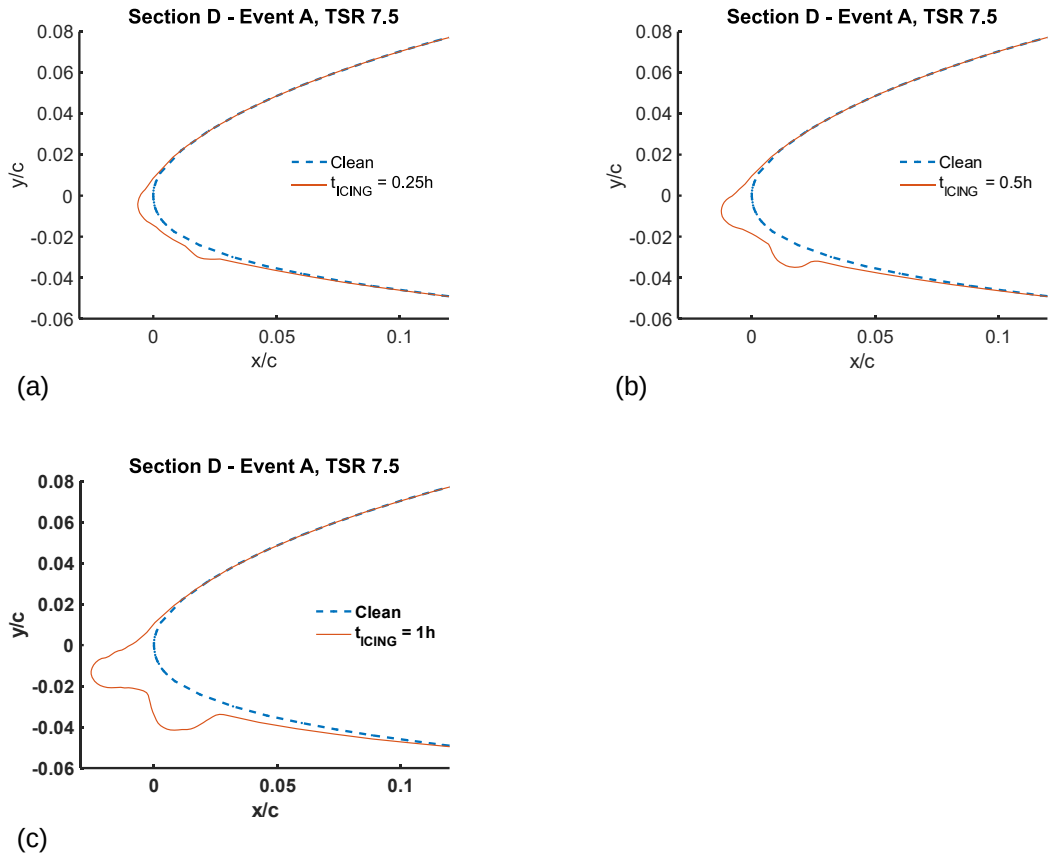

Figure 34a-c: Ice shapes generated with lewINT for 1-hour icing event A at 0.25, 0.5 and 1.0 hours, (a), (b), and (c), respectively; and tested in the low speed wind tunnel at Re of 165 000.

On Figure 35a, the degradation of C_L at each time interval during the icing event can be observed. The lift generation capabilities of the aerofoil decreased with the increasing ice shape area, which is shown by the reduced maximum C_L that can be achieved for each shape and the overall reduction of both the $\partial C_L/\partial \alpha$ slope and the lift coefficient at angle of attack of 0 °. For angles of attack larger than 10 °, the gradual degradation of the performance was more pronounced, as the generated forces in the test section were larger. In addition, the final ice shape geometry is such that it disrupts the suction flow for higher angles of attack due to the direction of the horn-like protrusion. For angles of attack lower than 10 °, it was not possible to obtain a good representation of the gradual degradation of the lift generating capabilities of the aerofoil due to the measuring equipment and setup. Nonetheless, the overall degradation of the performance was measured, which allowed for the subsequent comparison of the results with the numerically obtained ones.

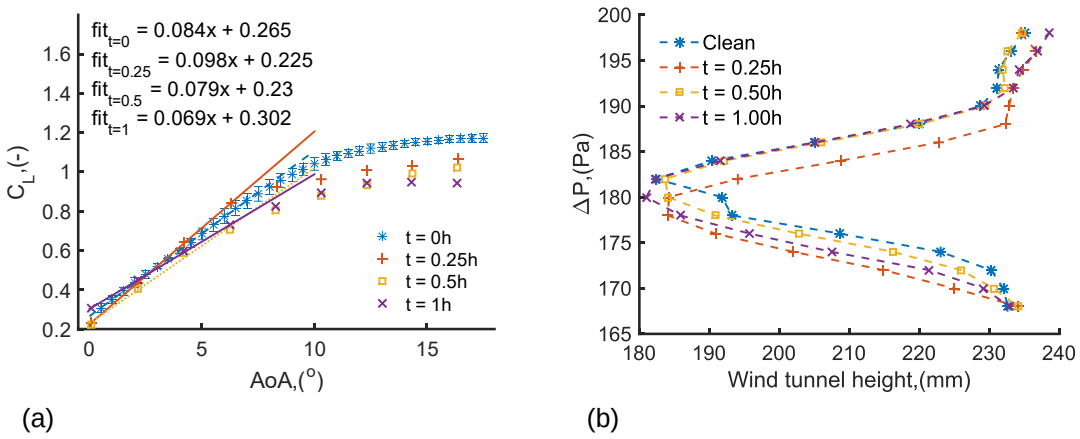

Figure 35a-b: Experimental coefficients of lift (C_L) and the wake deficit ΔP indicating the magnitude of experienced drag for the NACA 64-618 aerofoil, at the D section of the NREL 5 MW wind turbine blade, for the operational conditions (AoA = 4.52 °, V = 10 ms^{-1}, V_{REL} = 40.4 ms^{-1}) defined by icing event A105 (LWC = 0.5x10^{-4} kgm^{-1}, MVD = 25x10^{-6} m, T_{AMB} = 268.15 K, t_{ICING} = 360 s). Axes inverted as sampling method was conducted from top of the wind tunnel working section to its bottom.

To quantify the overall degradation, a linear fit was applied using the data points for the first 4 measurements, which correspond to the linear region of the lift curves. Thus, the overall degradation can be measured even if the lift curve has discontinuity. In this case, the tested models have some roughness and the expected turbulence intensity is high for the current setup, which would prevent or minimise the formation of laminar separation bubble, which is typical for low Re number flows. The overall degradation after 1 hour of icing was found to be approximately 18%, based on the difference in $\partial C_L/\partial\alpha$ for the clean aerofoil and the final ice shapes (*i.e.* Figure 34c).

The wake deficit behind the aerofoils for the shapes is shown on Figure 35b. It can be seen that with the gradual increase of the ice deposition the pressure difference behind the aerofoil increased. The C_D was calculated to change from 0.032 at t_o, it reached 0.036 at $t_{0.25}$ and $t_{0.5}$ and at the end of the event it was 0.047, marking a 46.9% increase. This indicates that the overall degradation of the aerodynamic efficiency of an aerofoil – the ratio of the lift coefficient over the drag coefficient – is more affected by the increase of the drag than the decrease of the lift.

The numerical results obtained with XFoil and Fluent are presented on Figure 36a-b. Both tools show consistent degradation of the lift generation capabilities of the aerofoil at almost every time interval. The presence of a separation bubble is evident from the discontinuity of the lift curves for angles of attack higher than 4°, as for XFoil the resultant degradation and change in the predicted lift curve was found to be more pronounced as shown in Figure 36b. This phenomena was predicted most likely due to the fact that the simulated flow was not with a high turbulence intensity and unlike the experimental results, on Figure 36a-b the discontinuity can be seen. The graphs indicate that higher overall icing losses could be expected in the case when XFoil is utilised for evaluating the aerodynamic performance of an aerofoil.

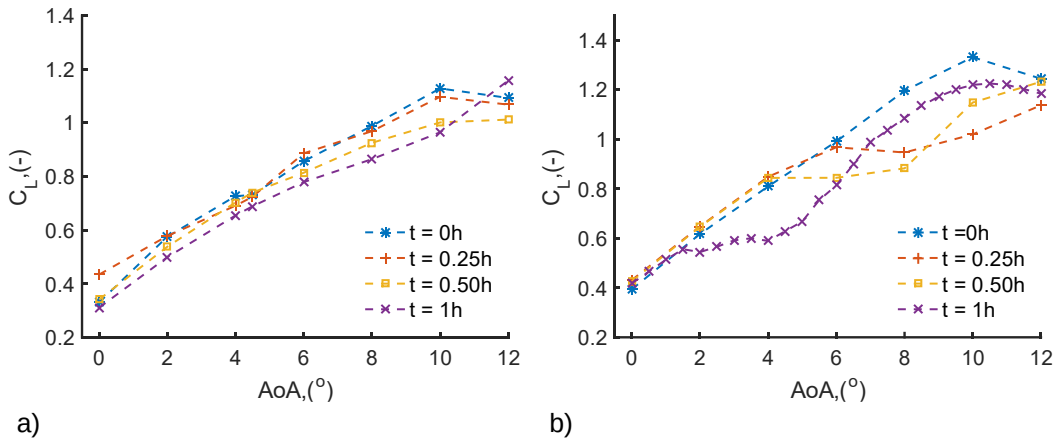

Figure 36a-b: Simulated lift coefficient for 1-hour degradation; at 4.5 ° angle of attack; for A105; as predicted by Fluent k-w SST model (a) and XFoil (b)

Although the three approaches predict differently the overall physics, the lift curves obtained for the ice shape after 1 hour of icing are in good agreement for the operational angles of attack of the 2D blade section (*i.e.* angle of attack of 4.52 °), as shown on Figure 37. Thus, for this case and setup, the dissimilarities in the results from the three approaches are mainly from the obtained values for C_L when the aerofoil is clean. The obtained values of C_L at an angle of attack of 4.5 °, for the three approaches are presented in Table 6. The overall degradation during the icing event was measured to be 3.91%, while the values obtained with the numerical tools were 5.62% and 25% with Fluent and XFoil, respectively. The predicted C_L value for the final shape with XFoil is within 2.3% agreement with the experimental measurements, while Fluent is within 12%. The overall agreement between XFoil and Fluent's, looking at the values for every time step in Table 6, was 9 – 24%.

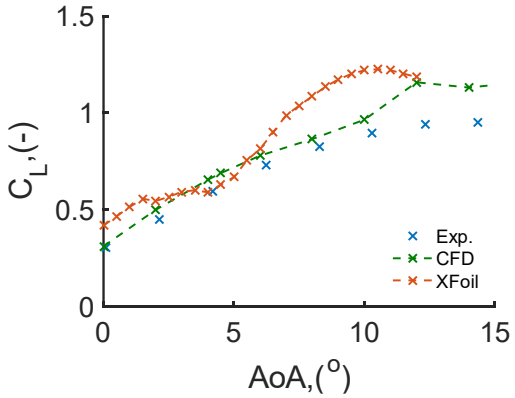

Figure 37: NACA 64-618 aerofoil lift curve after 1-hour icing event (A105) as obtained experimentally, with XFoil and with Fluent for Re of 165 000

Table 6: Lift coefficient 1-hour degradation; at 4.5 ° angle of attack; for C105; as modelled using the experimental setup and as predicted by XFoil and Fluent k-w SST numerical tools

$C_{L4.5°}$	t = 0.00 h	t = 0.25 h	t = 0.50 h	t = 1.00 h	Δt_0-t_1, %
Wind tunnel	0.64 ± 0.071	0.671	0.606	0.615	3.91
XFoil	0.84	0.896	0.859	0.629	25.12
k-w SST	0.73	0.724	0.739	0.689	5.62

4.1.2.2 Ice shapes produced for an alternative operational regime

As it has been suggested that alternative operational regimes can improve the performance of a wind turbine in icing conditions, ice shapes for two operational settings were tested – operating at a reference TSR and operating when utilising derating. Four shapes were generated for the same 1-hour icing event as in 4.1.2.1, at two time intervals (0.5 and 1.0 hours), considering a reference tip-speed ratio of 7.5 and a tip-speed ratio for derating of 5.0. As the relative speed to the NREL 5 MW wind turbine blade changes with the TSR setting, the angle of attack at Section D changes as well and for the reference TSR it is 4.52 °, while for the derating setting it is 8 °.

How the ice shapes would change at Section D of the NREL 5 MW wind turbine blade during 1-hour icing event, when the operational TSR is reduced from 7.5 to 5.0, is displayed on Figure 38a-d. Although the environmental conditions are the same, simply due to the change of the rotational speed and the respective change of the angles of attack, completely different ice shapes were generated. For TSR of 5, the relative flow speed at section D is lower, while the operational angle of attack is higher. Thus, generally smaller ice shape was predicted due to lower ice deposition rate; and only one distinctive horn like protrusion could be seen, as visualised in Figure 38c-d. In reality, due to the higher angle of attack, droplets with smaller diameters and subsequently smaller moment of inertia will not reach the surface of the aerofoil, because of their tendency to follow the flow streamlines, as further detailed in (Battisti 2015a). Thus, less water mass will be collected from the aerofoil and less ice formation will be present on the surface. In contrast, due to the smaller angle of attack when operating at TSR of 7.5, the aerofoil collects more water and more icing can be expected as droplets with smaller moment of inertia can reach the surface. As a result of the non-immediate freezing of the super-cooled droplets and the availability of more latent heat of freezing on the ice/air surface a double horn-like shape forms. The predicted ice shapes with LewINT indicate an icing shapes development corresponding to expected ice shapes that would form in real operational conditions. However, field measurements and testing should be considered for further development of the current analysis so that higher fidelity can be achieved.

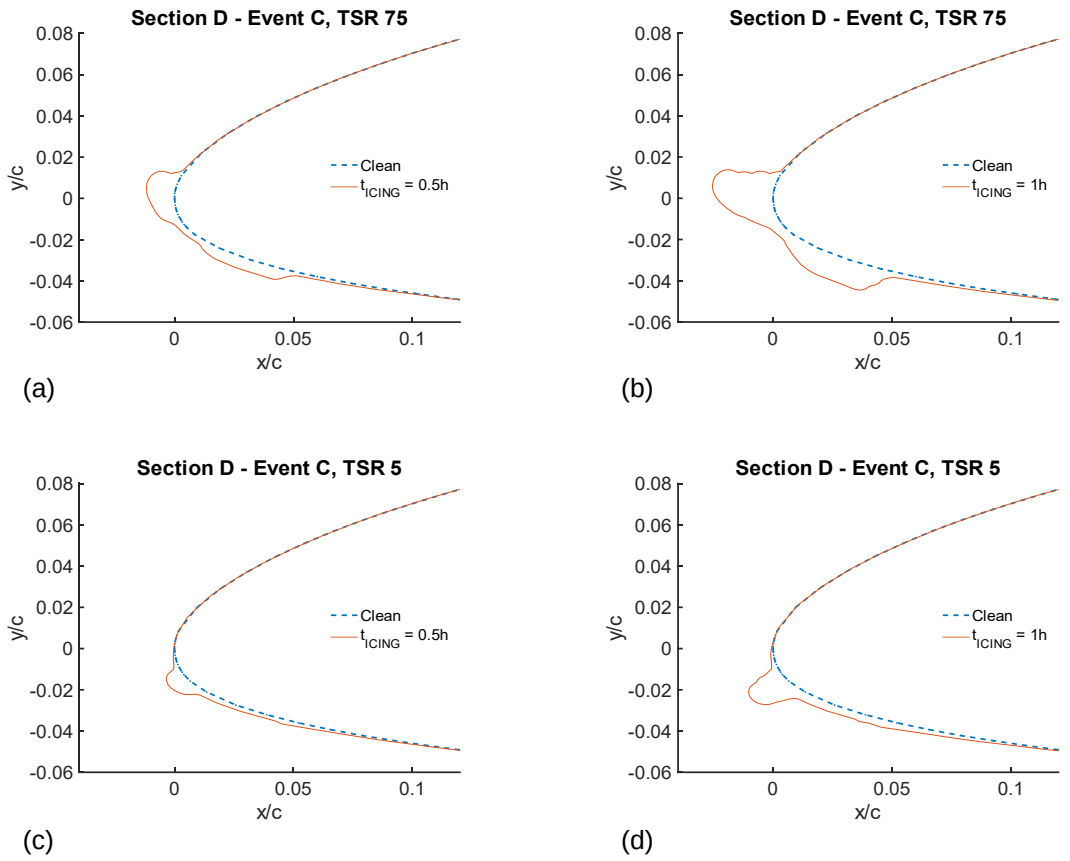

Figure 38a-d: Ice shapes generated with lewINT for icing event C105 during operating the NREL 5 MW wind turbine at TSR of 7.5 after 0.5 h of icing (a) and 1 h of icing (b); and operating at TSR of 5 after 0.5h (c) and 1h (d) of icing

Higher performance reduction is expected for the ice shapes obtained at TST of 7.5 (Figure 38a-b) than shapes obtained during operation at TSR of 5 (Figure 38c-d). Higher disruption of the flow would be seen from the double horn-like protrusions, which would affect the lift generation capabilities of the aerofoil. The smaller ice shapes, which are orientated normal to the suction side of the aerofoil characteristic for the alternative TSR would lead to an overall aerodynamic degradation, but it will be mainly due to increased drag, as the suction side is ice-free.

The variation of the lift and drag for the ice shapes obtained at two different TSR values is shown on Figure 39a-b. The experimental results showed improved performance during the testing of ice shapes corresponding to operation at TSR of 5. This is specifically noticeable for angles of attack higher than 10 °, where the graphs showing the C_L are closer to the clean geometry measurements with higher maximum C_L than the larger shapes from the nominal TSR 7.5 operational condition. Due to the decreased area of the aerofoils from the chord length reduction and the sensitivity of the measuring equipment, similar C_L curves were measured for angles of attack below 10 °. The results for both set of shapes for TSR of 5 and 7.5 at the end of the icing event depicted the degraded performance of the models between the time steps and overall improvement in the performance was indicated at larger angles of attack only.

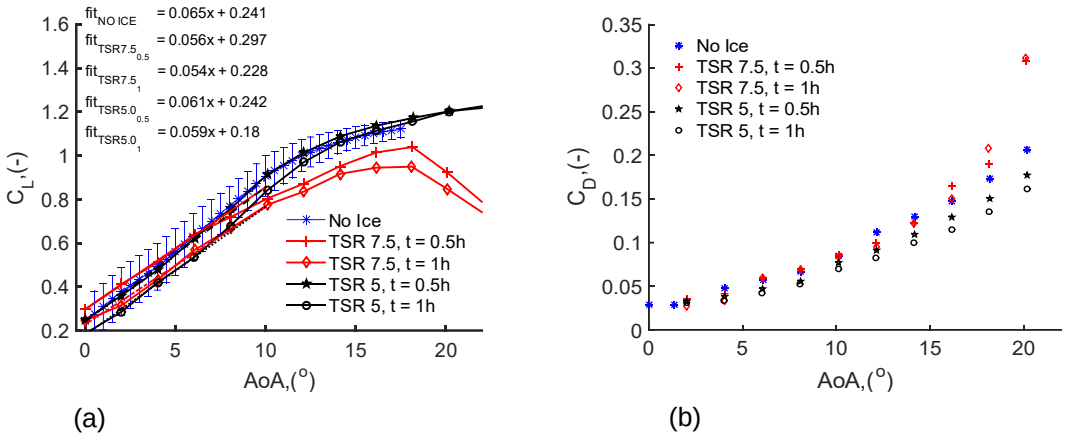

Figure 39a-b: Experimental C_L (a) and C_D (b) coefficient, measured for ice shapes produced during derating from TSR 7.5 to TSR 5 and sampled at 0.5 and 1h after the start of the icing event defined by A105.

Although the measurements did not show improvement of the lift generation properties of the aerofoil for angles of attack between 0 and 10 °, linear fitting to that region could provide an indication for the performance of the aerofoil. The resultant linear fits are shown also on Figure 39a, where the C_L slope can be examined. For both cases and time steps, the slopes are lower than the slope for the non-iced geometry. However, the reduction for the shapes from derating is less. Thus, from indirect method of comparison using the C_L curves slopes and the direct comparison of the graphs for angles of attacks higher than 10 °, the experimental results indicated that overall performance can be improved with alternative TSR settings during operation in icing conditions.

The drag coefficients obtained with the wake measurement method, at half span of the model, for angle of attack of 4.52 ° are summarised in Table 7. The ice shapes obtained for TSR of 5.0 (see Figure 38c-d) showed an overall improvement of the performance of the iced aerofoil. It can be seen that the overall increase of the C_D was reduced from 30.6 to 4.5 %.

Table 7: Drag coefficient values obtained with the wake measurement method for angle of attack of 4.52 °, Re of 130 000 and two ice shapes generated for two different TSR settings.

Time step, h	t = 0	TSR 5, t = 0.5	TSR 5, t = 1.0	TSR 7.5, t = 0.5	TSR 7.5, t = 1.0
$C_{D,4.5}$	0.0268	0.0270	0.0280	0.0266	0.035

The numerical simulations predicted the performance of the iced shapes obtained for derating to be similar to non-iced conditions as shown in Figure 40a-b. This is identifiable for angles of attack between 3 and 6 ° for XFoil and between 5 and 12 ° for Fluent. Overall improvement of the performance was predicted from Fluent, while the results from XFoil are highly affected by the presence of the horn-like protrusions in the ice shapes. Interestingly, the predicted overlapping of the C_L curve by both approaches for low angles of attack is similar to the measured curves. This could be attributed to the flow physics associated at these angles of

attack. However, to understand exactly what causes the measured and predicted behaviour, higher fidelity analysis should be undertaken, which should include higher precision measuring equipment, surface pressure measurements and high-fidelity numerical setup. Additional difficulties for experimental measurements could source from the fact that the NACA 64-618 aerofoil has been designed to be a high-speed aerofoil.

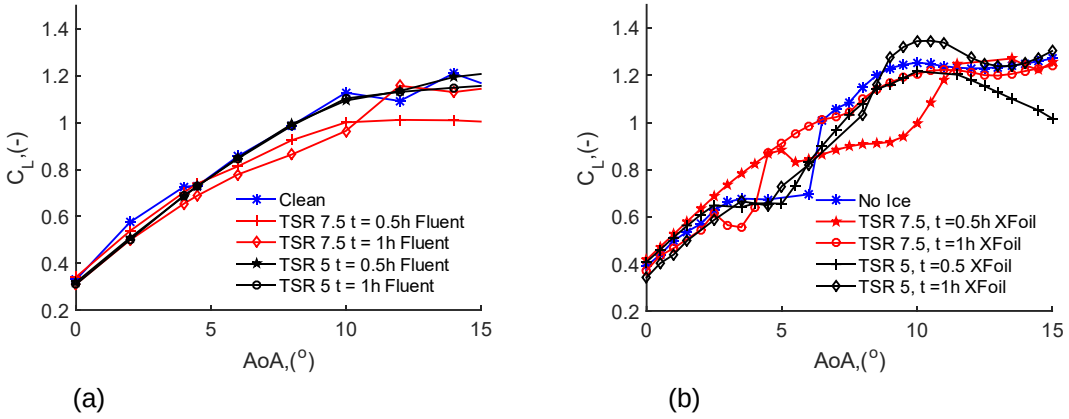

Figure 40a-b: Simulated lift coefficient data for ice shapes obtained at two different tip-speed-ratios, at the 0.5h and 1h during 1-hour icing event. The performance is evaluated by the means of eperimental measuremnts (a), XFoil predictions (b) and Fluent k-w SST predictions (c). The Differences for the three methods are examined for clean aerofoil and ice shape that was obtained at the end of the event (d).

On Table 8 the obtained C_L for angle of attack of 4.5 ° are summarised. The results obtained from Fluent showed improvement of the lift generation properties for the shapes at time step of 1.0 hours. The lift generating properties of the aerofoil were predicted to be 5.4% higher for the ice shape from derating at the end of the event. The results from the other two methods could not be used to convey the analysis, as XFoil has difficulties coping with the abrupt geometry, while the overall 2% improvement of the iced shape from the experimental data is within the uncertainty limits of the experimental measurements, which is 19% for angle of attack of 4.5 º.

Table 8: The lift coefficient of NACA 64-618 aerofoil for Re of 130 000 and four ice shapes, which was obtain by three different methods for performance evaluation.

Approach	Clean	$C_{L,4.5}$ TSR 5 t = 0.5	$C_{L,4.5}$ TSR 5 t = 1	$C_{L,4.5}$ TSR 7.5 t = 0.5	$C_{L,4.5}$ TSR 7.5 t = 1
Exp. Cov	0.525 ± 0.1	0.51	0.47	0.54	0.46
XFoil	0.673	0.657	0.648	0.867	0.873
k-w SST smooth	0.731	0.7285	0.7295	0.74	0.69

4.1.2.3 High Re comparison XFoil and Fluent

XFoil and Fluent were compared in this sub-section as often those tools are utilised for obtaining the aerodynamic performance data for iced aerofoils, which is then used to estimate the power output of a wind turbine in icing conditions. The simulations have been completed for

Re of 6×10^6, as this Re was used to obtain the NACA 64-618 aerofoil polars in the data sheet of NREL 5 MW wind turbine blade (Jonkman *et al.* 2009). It is important to know what predictions can be expected when using different simulation tools, as it affects the extrapolation routines used and eventually the final results. The numerical simulations have been conducted for the ice shapes that were analysed in the previous two sub-sections.

4.1.2.4 1-hour long icing event

Both XFoil and Fluent showed reduced performance over the length of the icing event as shown on Figure 41a-b. XFoil predicted the degradation to be as expected for the angles of attack up to 4 º. In this region, the gradual degradation with the increase of the icing shape was captured. However, for higher angles of attack, the results fluctuated, as it can be seen from Figure 41a. This could be attributed to the more dynamic flow physics that is expected for this region and the fact that the geometry of the ice shape is challenging for XFoil because of the presence of horn-like protrusions. Fluent predicted the degradation to be characterised by reduction in both the maximum achievable C_L and the slope of the lift curve (Figure 41b). For angles of attack below 4 °, the iced curves were predicted to be similar, with differences in the predicted C_L less than 3.5%.

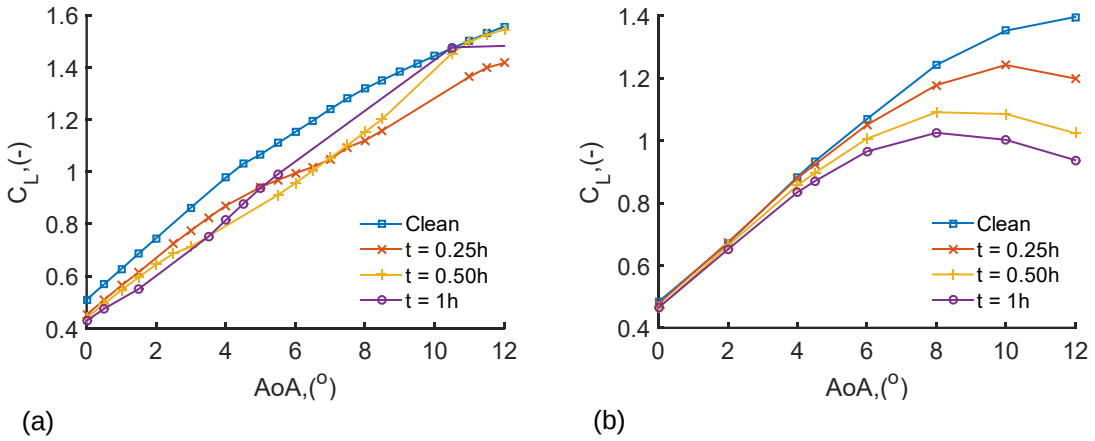

Figure 41a-b: Simulated lift curves with XFoil (a) and Fluent (b) for 1-hour glaze icing event at time intervals of 0.25, 0.5 and 1.0 hours.

XFoil and Fluent are within 10% agreement when predicting the C_L for an angle of attack of 4.5 °, as the biggest difference is during the prediction of the clean aerofoil performance with XFoil predicting higher values as shown on Table 9. This could be attributed to the numerical setup used in Fluent. The pressure coefficient distribution for the two simulation tools show good agreement for the operational angle of attack of the blade section, as shown in Appendix 4.

Table 9 : Lift coefficient degradation for ice shapes obtained after 0.25, 0.50 and 1.0 hours of icing, as predicted by XFoil and the k-w SST turbulence model

$C_{L4.5°}$	t = 0.00h	t = 0.25h	t = 0.50h	t = 1.00h	Δt_0-t_1, %
XFoil	1.03	0.906	0.832	0.877	15
k-w SST	0.934	0.924	0.897	0.840	10
Δ, %	10.3	2	7.3	4.4	

The calculated drag values for both approaches are displayed in Figure 42a-b. The drag increase from the beginning of the event to its end was predicted by both approaches. An interesting observation is that XFoil predicted overall higher degradation for C_D than Fluent (Figure 42b), which was mainly driven from the C_D curves predictions for non-iced surface. From Table 10 can be seen that the higher C_D obtained with Fluent for clean geometry can lead to more than 6 times less icing losses in comparison to XFoil. Except for the clean geometry, the agreement between XFoil and Fluent is within 12 % for the considered ice shapes.

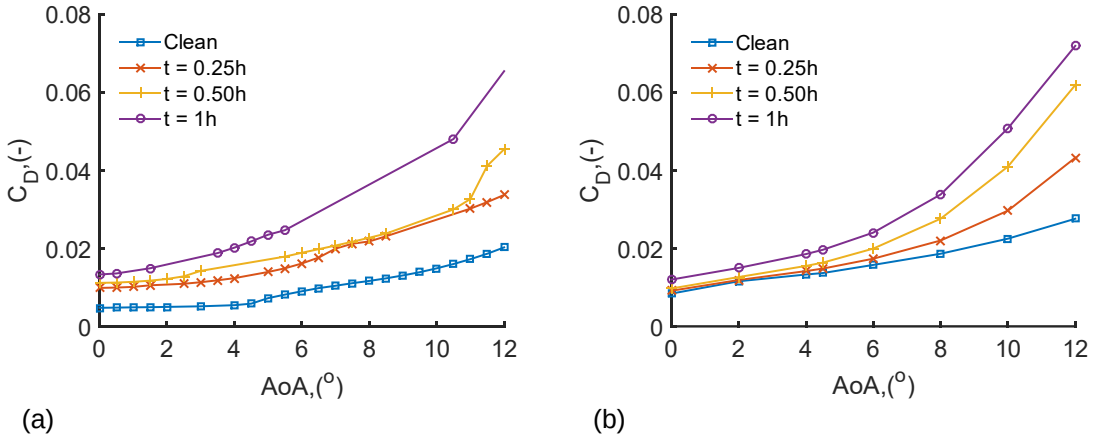

Figure 42a-b: Simulated drag curves with XFoil (a) and Fluent (b) for 1-hour glaze icing event at time intervals of 0.25, 0.5 and 1.0 hours.

Table 10: C_D of NACA 64-618 as Section D of the NREL 5 MW wind turbine blade, at an angle of attack of 4.5 °, for ice shapes obtained at 0., 0.25, 0.5 and 1.0 hours during an extreme one-hour icing, as predicted by XFoil and Fluent k-w SST for Re of 6×10^6

$C_{D4.5°}$	t = 0.00h	t = 0.25h	t = 0.50h	t = 1.00h	Δt_0-t_1, %
XFoil	0.0059	0.0132	0.0165	0.0218	269
k-w SST	0.0137	0.0148	0.0164	0.0196	43
Δ, %	132	12	0.6	9.7	

4.1.2.5 Ice shapes produced for an alternative operational regime

XFoil and Fluent aerodynamic performance predictions at Re of $6x10^6$, for the ice shapes shown on Figure 38a-d, are shown on Figure 43a-b. An overall improvement of the performance was

found, but its magnitude depending on the tool, as indicated by the differences in the C_L curves. The C_L curves predicted with XFoil showed much higher sensitivity to the studied ice shapes than Fluent for angles of attack below the operational (*i.e.* 4.5 °), as depicted on Figure 43a. Nonetheless, XFoil was found capable of predicting improved performance due to the smaller ice shapes. However, it should be noted that reduced accuracy for the overall representation of the computed C_L curves could be expected due to convergence issues for some angles of attack.

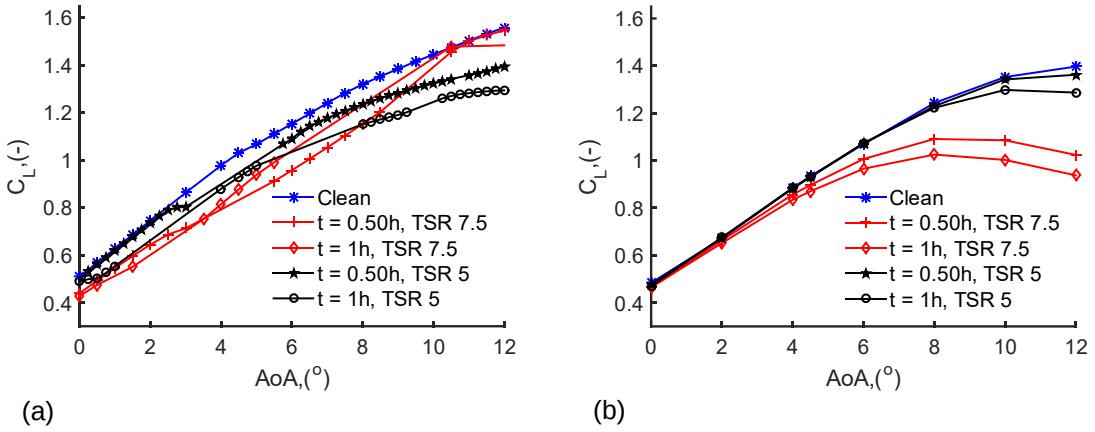

Figure 43a-b: XFoil (a) and Fluent k-w SST (b) predictions for operational Re number of the NACA 64-618 aerofoil when TSR is changed from 7.5 to 5 during icing for 1-hour icing event (A105)

The improved C_L performance, when less ice is accumulated, can be examined for the operational angle of attack at TSR of 7.5 for the section D of the NREL 5 MW wind turbine blade. As shown on Table 11, 5.1% and 9.7% less ice induced losses – represented by C_L reduction - were predicted by XFoil and Fluent, respectively, indicating that reducing the rotational speed of a wind turbine rotor in icing conditions can improve on the overall performance. The two tools were found to agree within 10.3% and also a good agreement for predicted pressure distribution was achieved (Appendix 4). However, due to differences in the predicted values of the C_L for clean aerofoil, XFoil could predict higher degradation.

Table 11: The lift coefficient of NACA 64-618 aerofoil at angle of attack of 4.5 °, for Re of $6x10^{-6}$, when ice shapes, at Section D of the wind turbine blade, reduce due to changing the operational TSR from 7.5 to 6.5 during an extreme one-hour icing event

Approach	XFoil	k-w SST	Δ, %		XFoil	k-w SST	Δ, %
$C_{L,4.5}$ t = 0	1.03	0.934	10.3		1.03	0.934	10.3
$C_{L,4.5}$ TSR 5, t = 0.5	0.947	0.930	1.8	$C_{L,4.5}$ TSR 7.5, t = 0.5	0.832	0.897	7.2
$C_{L,4.5}$ TSR 5, t = 1	0.928	0.931	0.3	$C_{L,4.5}$ TSR 7.5, t = 1	0.877	0.840	4.4
Δt_0-t_1, %	9.9	0.3		Δt_0-t_1, %	15	10	

The C_D performance predicted by the two tools indicates the potential benefits of reducing the rotational speed during icing, as shown on Figure 44a-b. Both XFoil and Fluent predict the C_D curves for the lower TSR to be lower than the curves depicting the C_D performance during

nominal TSR operation. As for the C_L predictions, the main difference between the obtained results is that the performance for clean aerofoil surface was predicted differently with Fluent simulations resulting in higher C_L values.

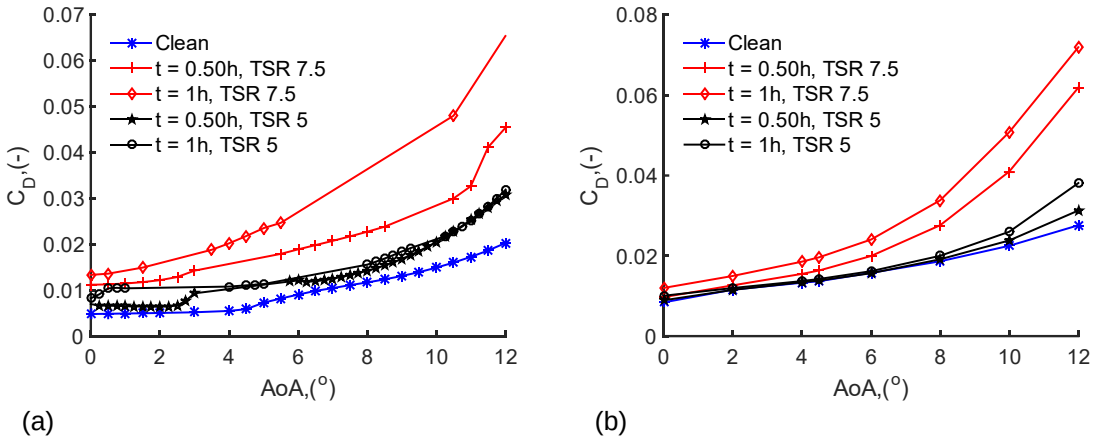

Figure 44a-b: XFoil (a) and Fluent k-w SST (b) results for the changes in the drag curves of the NACA 64-618 aerofoil as section D of the NREL 5 MW wind turbine, for ice shapes obtained at 0.5 and 1.0 hours in an extreme one-hour icing event, when the operational Re is 6×10^6

The reduced ice shapes resulted in improved C_D performance, as the deterioration of the drag was simulated to change from 269 to 88% and from 43 to 3.7% with XFoil and Fluent, respectively (Table 12). Thus, depending on the simulation tool, the C_D degradation would improve by either 3 or 11 times. Overall agreement for the C_D values of the iced aerofoils between XFoil and Fluent was found to be between 0.6 - 30%. This and the difference in the predicted values of the drag for the clean aerofoil surface led to almost 4 times better drag performance predicted by Fluent.

Table 12: C_D of NACA 64-618 as Section D of the NREL 5 MW wind turbine blade, at an angle of attack of 4.5 °, for ice shapes obtained at 0.5 and 1.0 hours, while derating the wind turbine from TSR of 7.5 to 5 during an extreme one-hour icing, as predicted by XFoil and Fluent k-w SST for Re of 6×10^6

Approach	XFoil	k-w SST	Δ, %		XFoil	k-w SST	Δ, %
$C_{D,4.5}$ t = 0	0.0059	0.0137	132		0.0059	0.0137	
$C_{D,4.5}$ TSR 5 t = 0.5	0.0107	0.0139	30	$C_{D,4.5}$ TSR 7.5 t = 0.5	0.0165	0.0164	0.6
$C_{D,4.5}$ TSR 5 t = 1	0.0111	0.0142	30	$C_{D,4.5}$ TSR 7.5 t = 1	0.0218	0.0196	9.7
Δ, %	88	3.7		Δ, %	269	43	

4.2 Discussion

The pre-tests showed that the current measuring setup could be used to obtain aerofoil aerodynamic performance with approximately 13% confidence for the NACA 0012 standard aerofoil section. When measured data for the NACA 64-618 aerofoil was compared to the reference data found in (Hudecz 2014), 13% higher lift curve slope, 36% smaller C_L at angle of attack of 0 º and lower C_{Lmax} were registered. The results were found interesting, as the higher

lift curve slope is closer to the theoretical lift curve of the NACA 64-618 aerofoil in comparison to the reference data in (Hudecz 2014). This suggests that the reduction of the chord length and the increase of the span of the test article were beneficial. The other differences were attributed to dissimilarities in the flow and aerofoil surface quality. Overall, the current setup was found acceptable for the purposes of the study, but future work should include flow quality measurements to document the expected turbulence intensity of the flow and quantify the air leakages and their influence on the measured results. In addition, optimal aspect ratio for the tested articles should also be investigated.

The ice induced aerodynamic degradation of the NACA 64-618 aerofoil for shapes representing 1-hour icing event showed reduction in C_L of 4% and increase in C_D of 47%; the lift curve slope analysis indicated 18% degradation. Hudecz (2014) reported 35%, 46.5% and 25% degradation in C_L for 1-hour glaze, mixed and rime ice events, respectively, while C_D degradation was shown to increase between 4 to 10 times depending on the ice shape type. As these results were measured for actual ice shapes in icing research wind tunnel, the fidelity of the analysis is greater than the current measurements, because it includes automatically the surface roughness effects of the ice shapes. In addition, the measurements were conducted for slightly higher ice deposition rate, resulting in more deposited ice. When the current results were compared to data obtained for similar ice shapes and modelling methods, a better agreement was found. Sandstad (2018: p. 39) measured 3% degradation of C_L for ice shapes with similar thickness. In (Lynch and Khodadoust 2001: p. 725), the C_L reduction was reported to be 5 – 7% for NACA 63_2 – A415 aerofoil. These results indicate how hard it is to achieve similarity for data obtained in different wind tunnels and represent actual ice shapes using 3D printed models. Future research might focus on classifying types of shapes that could be studied using 3D printed models and the utilisation of moulded ice shapes as in (Tammelin, Bengt and Seifret 2001).

XFoil and Fluent predicted 5.6% and 25% C_L degradation for the ice shapes, which represented 1-hour long icing event during the low Re simulations. The predicted values at each time step for both simulations tools agreed within 9-24%. XFoil predicted larger icing losses due to the higher C_L value at 0 º angle of attack for non-iced aerofoil. Both the experimental and Fluent results predicted smaller degradation due to the low value at that angle. This can be further highlighted by the fact that the experimental and XFoil results for C_L at the largest ice shape differed by 2%, while the same difference when accounting Fluent was found to be 8%. It can be suggested that if the tested articles were measured for smooth aerofoil surface and better flow quality, larger degradation could be measured. The same argument could be used for Fluent and if higher quality mesh was used to conduct the simulations. However, both cases would be an interesting topic of research for future projects.

An overall improvement was observed when the ice shapes representing alternative rotational speed during icing were analysed. The experimental measurements showed some improvement in the aerodynamic performance by higher C_{Lmax}, lift curve slope and reduction of

the C_D for the operational angle of attack from 30.6% to 4.5%. For the same conditions, higher C_{Lmax} was predicted by Fluent for the smaller ice shapes. The results obtained with Fluent for operational angles of attack and XFoil did not show the expected aerodynamic behaviour due to their limitations. However, these results were obtained for low Re, which is of little practical interest when modelling wind turbine performance but provide an insight to how the different predictive methods compare with each other. The computational results that were obtained for the operational Re were more conclusive with XFoil predicting reduction in the lift losses from 15% to 9.9% and in the drag losses from 269% to 88%. The results with Fluent showed changes in the C_L degradation from 10% to 0.3% and in the C_D degradation from 43% to 3.7%. Thus overall, improvement in the performance was seen, which provides reasoning for further investigation on the implications of reducing the ice accumulation rate during icing to minimise the icing.

The numerical results in this study compared qualitatively good with the data that can be obtained from the literature. The numerical degradation from both methods showed 10 – 15% reduction in the C_L and 43 to 269% increase in C_D. Only few studies have looked at the isolated aerodynamic characteristics of NACA 64-618 aerofoil and the tested shapes differ from the shapes simulated in the current study. Han, Kim and Kim (2018) reported 15% C_L and 399% C_D degradation for Case 5 of their study, which produced qualitatively comparable ice shapes in terms of ice thickness and orientation of the main protrusion. The increased C_D values are most likely caused by the better mesh and the C_D correction, which were used. Generally, it can be seen that numerical values for an iced shape around the LE, not pointed upwards disrupting the suction flow significantly leads to relatively high reduction of the maximum C_L, but to marginal degradations for angles of attack up to 5 º. This can be seen from (Etemaddar, Hansen and Mo 2012: p. 253, Jin and Virk 2019: p. 126, Sandstad 2018: p. 39, Villalpando, Reggio and Ilinca 2012: p. 42). This can explain the predicted lift degradation of approximately 25% from the numerical studies, which complement the reference wind tunnel results used for comparison here (Hudecz 2014: p. 68).

4.3 Conclusion

Experimental measurements on 3D printed aerofoils can be used for obtaining qualitative differences in the aerodynamic characteristics of different aerofoils. This can be particularly useful for testing ice mitigation by using operational parameters such as angle of attack, rotational speed and pitch angle. In fact, the current results showed that derating by using rotational speed modifications leads to overall improvement in the aerodynamic performance. However, low Re and surface treatment are limitations, which need to be addressed with appropriate test articles design. Better quantification of the characteristics can be achieved with moulds of actual ice shapes or ice shapes obtained in ice research wind tunnel.

XFoil and Fluent were found to be in 9-24% agreement for the low Re studies and in 0.6-30% agreement for high Re studies, when comparing predicted values for angles of attack expected

at the outermost section of a utility-scale wind turbine blade. XFoil tends to predict higher overall aerodynamic losses. However, the differences between XFoil and Fluent can be reduced with finer mesh and ice shapes, which do not lead to the formation of abrupt horn-like protrusions. High quality mesh for the application of Fluent should be a priority for future studies investigating icing, while XFoil should be applied with smoothing algorithms for abrupt ice shapes and modellers need to account for the fact that discontinuities can be found in predicted lift curves from failed convergence. Research is needed to tailor both methods for icing applications; however, XFoil remains an ideal tool for preliminary design results and fast engineering computational codes, while Fluent can provide higher fidelity analysis on the expense of higher computational cost and complex setup.

4.4 Summary

This chapter investigated the aerodynamic degradation of the NACA 64-618 aerofoil for ice shapes that were simulated with LewINT for 1-hour extreme icing event, when the NREL 5 MW wind turbine was operated with two different operational strategies. Experimental and numerical analysis was applied to evaluate the aerodynamic degradation. The purpose of the study was to identify how the overall ice induced aerodynamic degradation varies when different evaluation tools are used, which is of importance when ice mitigation operational strategies are being designed. XFoil and Fluent were used to generate the numerical results and were compared for low and high Re. The high Re data was chosen to be representative for the operational conditions of the NREL 5 MW wind turbine, while the low Re data provided numerical data for comparison against experimental measurements. XFoil and Fluent evaluation results for C_L and C_D were found to agree within 30%. In addition, when using XFoil it was found that higher overall ice induced losses might be predicted and the results were sensitive to the abruptness of the ice shapes. Nonetheless, due to its fast-computational capabilities and the relatively good agreement with higher fidelity numerical tools, XFoil could be used for designing ice mitigation operational strategies, as usually many ice shapes need to be analysed when modelling the temporal wind turbine performance in icing conditions. In addition, it is suitable for scenario-based analysis, which would not require extremely long ice events to be studied.

5 Design and Implementation of Derating

This chapter aims to establish a method for evaluating different operational strategies based on tip-speed ratio modifications made both during and after an icing event. This is achieved by introducing the concept of an energy payback time, which is based on the time taken for an alternative TSR strategy to start producing more energy than the reference operational regime after the end of an icing event. By considering a wide range of different icing events, wind speeds and ambient temperatures, the study sets out to determine when an alternative operational strategy should be used to reduce ice build-up during an icing event and increase energy yield once an event ends.

5.1 Method

Three typical icing events are considered to evaluate a number of different operational strategies based on varying tip-speed ratios. Furthermore, each event is tested for three different wind speeds (5, 7 and 10ms^{-1}) and two ambient temperatures (-5 and -10 °C).

5.1.1 Operational Strategy

The control parameter used in this study is TSR and its setting during (TSR_{DI}) and after (TSR_{AI}) an icing event. The TSR changes can be implemented by either prescribing constant TSR during the event or by adapting the torque-speed controller to the iced torque-speed curve (Zanon, Gennaro and Kuhnelt 2018). In this work, steady state simulation of the icing process and the aerodynamic effects is considered, similarly to previous research (RW.ERROR - Unable to find reference:71, Hu *et al.* 2017). It is assumed that the TSR during icing will remain constant as the icing durations in the current study are short enough and the natural degradation of the TSR will be small [19]. The possible TSR values that can be set are chosen according to the rated (maximum) rotational speed (seldom synchronous and asynchronous generators are operated above their rated speed) and the minimum rotational speed, required for energy generation. Considering the NREL 5 MW generator (Jonkman *et al.* 2009) with a minimum RPM of 670 and maximum of 1173.7RPM, the possible TSR limits (TSR_{Min} and TSR_{Max}) for operation can be determined (see Figure 45). The reference TSR design strategy is shown by TSR_R and Figure 45b shows how the coefficient of power (*Cp*) varies at different TSR settings for a non-iced blade. During an icing event, it is assumed that the controller will allow intentional energy yield reduction by reducing the tip-speed ratio, thereby reducing ice accretion and enabling an improved *Cp* to be obtained once the event finishes (Etemaddar, Hansen and Mo 2012).

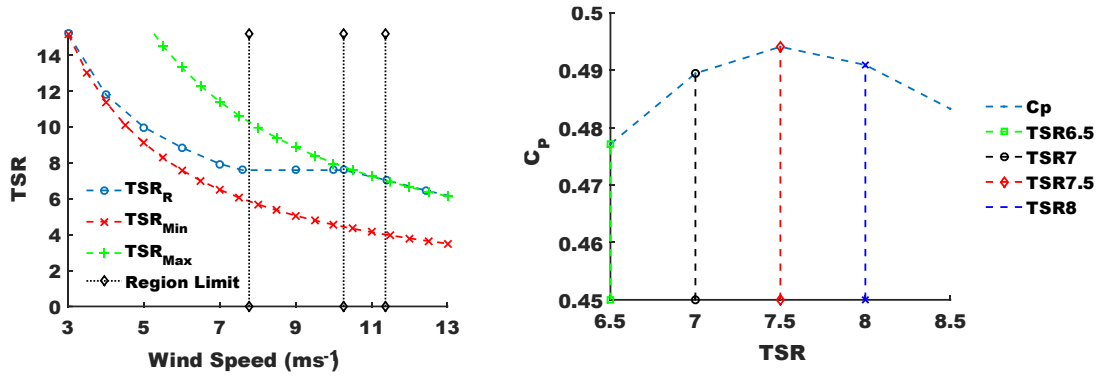

(a) (b)

Figure 45a-b: NREL 5 MW refrence wind turbine TSR operational limits defined by the limiting rotational speeds of the electrical generator (a) and how the power coefficent varies at different TSR (b).

5.1.2 Energy payback time

The energy payback time, t_{EPB}, defines how long it will take an alternative modified operational strategy (TSR_M) to start producing more power than the turbine's reference strategy (TSR_R). Figure 46a depicts the reduction of the instantaneous power output during an icing event by operating with an alternative TSR_{DI}, and the potential for improving performance at the end of an icing event by increasing the TSR_{AI} due to less accreted ice and better power characteristics. To compare a modified and reference operational strategies, the cumulative energy harvested during and after an event needs to be determined (see Figure 46b). The cumulative energy produced during icing, E_{DI}, is found from the available power in the wind, P_w, and the power coefficient, Cp, which varies throughout the duration of the icing event and depends on the chosen TSR (Eq. 21). P_W is defined by the air density, ρ, wind speed, V, and wind turbine blade radius, R (Eq. 22).

$$P_W = 0.5\rho V^3 \pi R^2 \tag{21}$$

$$E_{DI} = \int P_w Cp_{(TSR,t)} dt \tag{22}$$

The assumption is made that for a short period (<48 hours) after the end of an icing event, no significant ice melting or shedding will occur. This assumption is based on the consideration of winter anticyclone weather conditions with low temperatures and wind speeds that could span up to a week or more after an in-cloud icing event (Chen *et al.* 2014). The coefficient of power will remain constant, if the assumption is made that the iced blade geometry will not change significantly soon after the end of an icing event. Thus, the cumulative net energy output will be linear as Cp defines the rate of energy yield. The energy produced after an icing event by the reference ($E_{AI,R}$) and modified ($E_{AI,M}$) operational strategies can be represented by equations *Eq.* 23 and *Eq.* 24, respectively. The rate of cumulative energy after the icing event is calculated in addition to the total energy produced during the icing event (E_{DI}); $E_{DI,R}$ and $E_{DI,M}$ are

respectively the cumulative energy produced during the icing event for the reference and modified operational strategies. The time taken for the modified strategy to payback the lost energy during icing is determined when $E_{AI,R}$ equals $E_{AI,M}$; making t_{EPB} the subject of the equation results in *Eq.* 25. When estimating t_{EPB}, it should be noted that the results are only an indication for the potential effectiveness of an alternative strategy and extremely large values would suggest that alternative solutions to the TSR strategy should be considered and melting and shedding would need to be taken into account to obtain more accurate t_{EPB} values.

$$E_{AI,R} = P_W C_{p(TSR_{AI,R})} t_{EPB} + E_{DI,R} \tag{23}$$

$$E_{AI,M} = P_W C_{p(TSR_{AI,M})}\, t_{EPB} + E_{DI,M} \tag{24}$$

$$t_{EPB} = \left(E_{DI,R} - E_{DI,M}\right) / \left[P_w \left(Cp_{(TSR_{AI,M})} - Cp_{(TSR_{AI,R})}\right)\right] \tag{25}$$

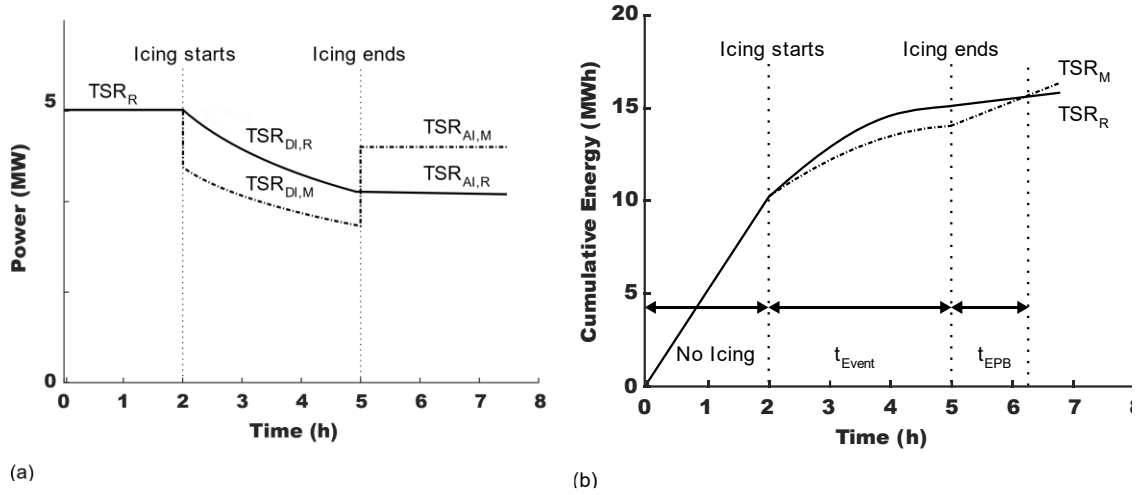

Figure 46a-b: Instantaneous power output (a) and cumulative energy (b) during and after an icing event for a wind turbine operating with a reference (TSR_R) or a modified (TSR_M) tip-speed ratio strategy.

5.2 Results and Discussion

5.2.1 Results

For each icing condition, *Cp* degradation, ice accumulation, final ice shapes for section D, ice induced power losses, rotor power characteristics, *Cp*(t), at the end of the event and energy payback times are presented in this section. In total 1176 ice shapes were generated for all icing events, with 180 ice shapes per timestep being analysed. Ice mass and *Cp* degradation were estimated considering all 1176 ice shapes, while the power characteristics and t_{EPB} were

analysed investigating the ice shapes at the end of the icing events. All final ice shapes at the modelled blade locations are provided in Appendix 4, while in this section only the most heavily iced blade location has been presented (section D). Ice-induced power losses and total harvested energy before and after an event, considering all modelled blade sections, were the main parameters used for the comparison of alternative TSR_{DI} and TSR_{AI} strategies. Ice mass for each strategy on a single blade is shown, but aeroelastic effects and component loads are beyond the scope of this work as for similar icing conditions it has been shown that the effects on the structural loading from additional ice mass are minimal (Etemaddar, Hansen and Mo 2012, Hu *et al.* 2017).

5.2.1.1 Event A

Event A has been simulated for wind speeds of 10, 7 and 5 ms^{-1} and ambient temperatures of -10 and -5°C, resulting in 6 cases – A1010; A105; A710; A75; A510 and A55. E.g. A1010 represents the LWC, MVD and duration defined by Event A in Table 1, occurring with a wind speed of 10 ms^{-1} and an ambient temperature of -10°C.

The deteoration of *Cp* for the whole simulated wind turbine rotor and the ice mass accumulation for each blade for all cases of Event A are presented on Figure 47a-f. Alternative viable operational TSRs of 6.5 to 8 for wind speeds of 10 and 7 ms^{-1} (Figure 47a-d) and TSRs of 9 to 10 for wind speed of 5 ms^{-1} (Figure 47e-f) are shown. TSR values greater than TSR_R for a wind speed of 5 ms^{-1} are not considered for the analysis, as it would result in a high V_{rel} and ice build-up (see Figure 45a). As the ice accumulation rate is a function of the blade's relative velocity (Battisti 2015a, Etemaddar, Hansen and Mo 2012), less ice deposition is apparent when the ambient temperature increases and both the wind speed and the TSR decrease (see Figure 47). The highest amount of accreted ice per blade is 11.5 kg for case A1010; the least is 4 kg for case A55. As the type of ice being formed can change from one type to another for the same icing case (rime to glaze) and it can vary along the blade of utility scale wind turbines, the power convergence efficiency does not degrade linearly. Depending on the type of accreted ice and the disturbance of the flow over the blade, the *Cp* decreases either gradually (A1010, A710 and A510) or more sharply (A105, A75 and A55).

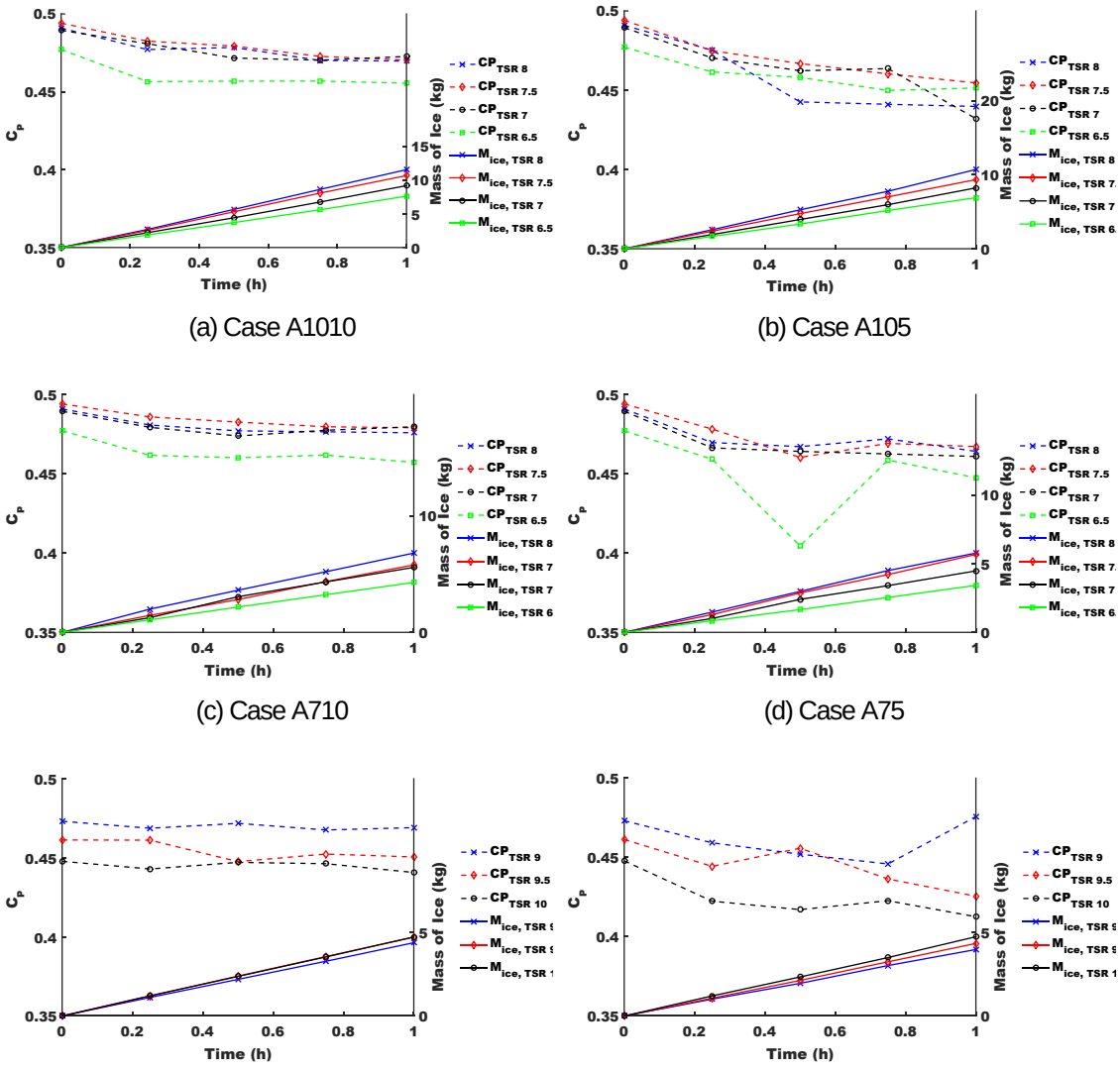

(a) Case A1010 (b) Case A105

(c) Case A710 (d) Case A75

(e) Case A510 (f) Case A55

Figure 47a-f: Wind turbine power coefficient degradation and total ice mass accumulation per blade during events A1010 (a), A105 (b), A710 (c), A75 (d), A510 (e) and A55 (f).

Final ice shapes for blade Section D are displayed on Figure 48a-f. The ice shapes for A105, A75 and A55 are typical for glaze icing conditions. They are characterised by having a less conformal geometry to the aerofoil contour and the presence of one or two horns (Poots 1996). The shapes for A510 are typical for rime ice cases as they are more conformal to the aerofoil geometry. Higher energy losses are expected for glaze and mixed icing conditions (Etemaddar, Hansen and Mo 2012). As these shapes produce more complex wall bounded flow, the aerodynamic uncertainties from the simulations tend to be higher, which is represented by the greater *Cp* fluctuations obtained for events A105, A75 and A55 (Figure 47b, d and f). Higher fidelity analyses over a smaller range of time steps are needed to further investigate these specific flow features and fluctuations in the results. For cases A1010, A710 (Figure 47a and c) the ice shapes are representative for mix-type icing, being conformal to the aerofoil contour at first (rime) and subsequently forming horn-like protrusions. The flatter *Cp* profiles for Events A1010, A710 and A510 (Figure 47a, c and e) are attributed to ice forming normal to the leading

edge or on the pressure side of the aerofoil causing less aerodynamic disturbance (Bragg, Broeren and Blumenthal 2005) (see Figure 48a,c and e).

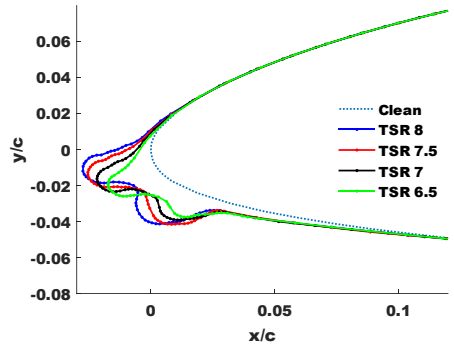

(a) Case A1010

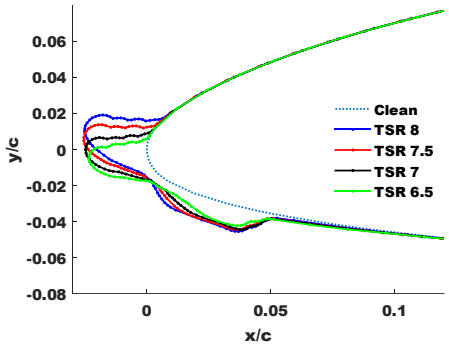

(b) Case A105

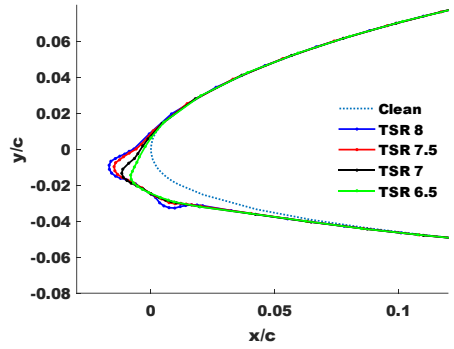

(c) Case A710

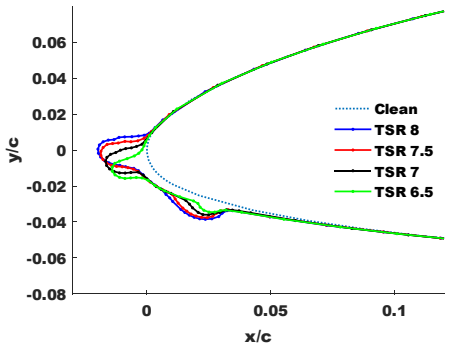

(d) Case A75

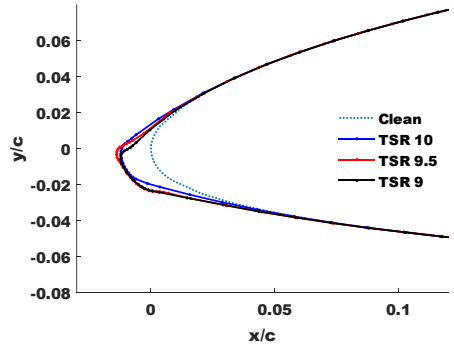

(e) Case A510

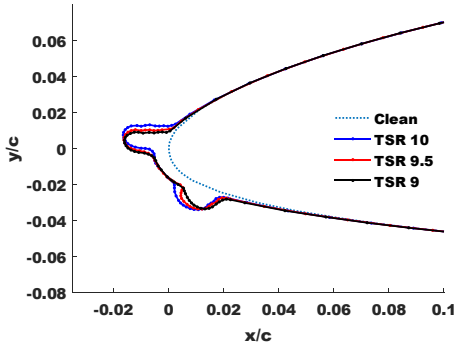

(f) Case A55

Figure 48a-f: Ice shapes on Section D for event cases A1010 (a), A105 (b), A710 (c), A75(d), A510 (e) and A55 (f).

Figure 49a-f reveals how setting different TSR values can be used to minimise power losses during icing and maximise performance after an icing event ends. Specifically, the results show the power coefficients of the iced wind turbine at the end of the icing events for different TSR_{DI} values, and subsequent power coefficients that can be obtained with a new TSR_{AI} value. As expected, the minimum TSR_{DI} typically provides the best possible post-icing performance, due

to less ice having deposited on the rotor blades. The exception is case A710, where the differences between alternative TSRs are negligible due to the relatively small accumulation of ice. For example, Figure 49d shows that the turbine could be slowed down to a TSR_{DI} of 6.5 with TSR_{AI} increased to 8 to achieve a power coefficient of over 0.475. These results also highlight how significant the degradation of *Cp* can be for the TSR_R value of 7.5 (Figure 49a-d) and that restoring TSR_{AI} to 7.5 would improve the power performance after icing in events A1010 and A105. To maximise the power output and minimise the icing losses for a wind speed of 5 ms^{-1}, both TSR_{DI} and TSR_{AI} should be 9 as it provides higher *Cp* at lower rotor rotational speeds due to the negative curve slope of the graph, but the viability of this depends on the coupled electrical generator.

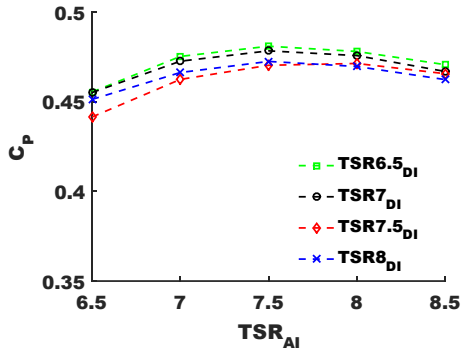

(a) Case A1010

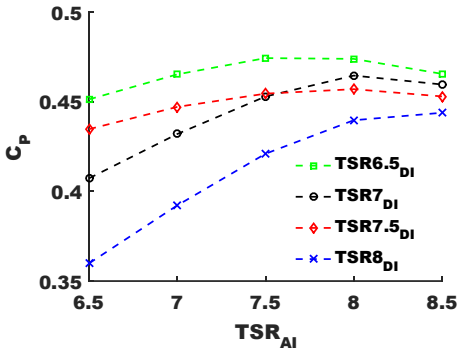

(b) Case A105

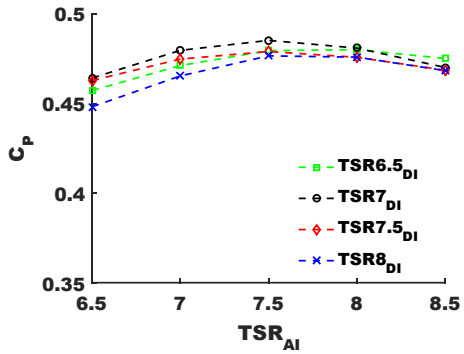

(c) Case A710

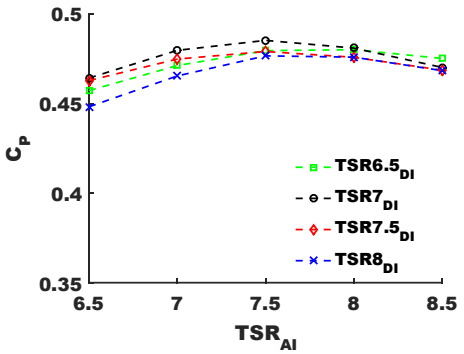

(d) Case A75

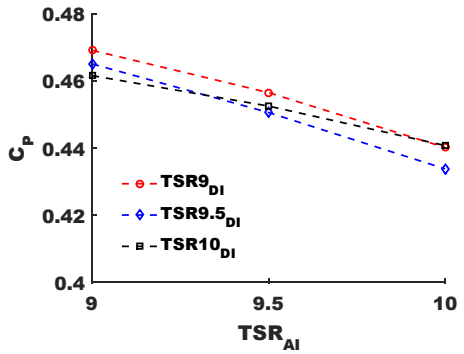

(e) Case A510

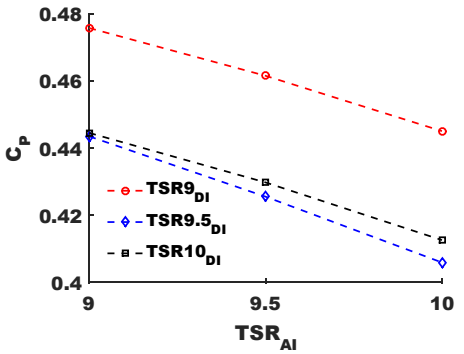

(f) Case A55

Figure 49a-f: Power characteristics of modified tip-speed ratio values after icing events A1010 (a), A105 (b), A710 (c), A75(d), A510 (e) and A55 (f).

The time it would take to replace the lost energy for reducing the TSR during the icing event, t_{EPB}, is shown for Event A on Figure 50a-f. It is noticeable how sensitive t_{EPB} is to variations in wind speed, ambient temperature and TSR operational regime. For Event A at wind speeds of 7 and 10ms^{-1} (Figure 50a-f), the most beneficial TSR_{DI} is 7 with TSR_{AI} set to either 7.5 or 8, which provides energy payback times of around 0.5-2.5 hours. Interestingly, if the TSR_{AI} was to be restored to the turbines reference speed (TSR_R) of 7.5 after event A105, the only TSR_{DI} and resulting characteristics that could replace the lost energy would be $TSR6.5_{DI}$. For event cases A510 and A55, *Cp* is improved for a reduced TSR value both during and after the icing events, so there is no energy payback, and this suggests that the reference design strategy could be improved for non-icing conditions. As a result, the energy payback time appears negative in Figure 50e and Figure 50f.

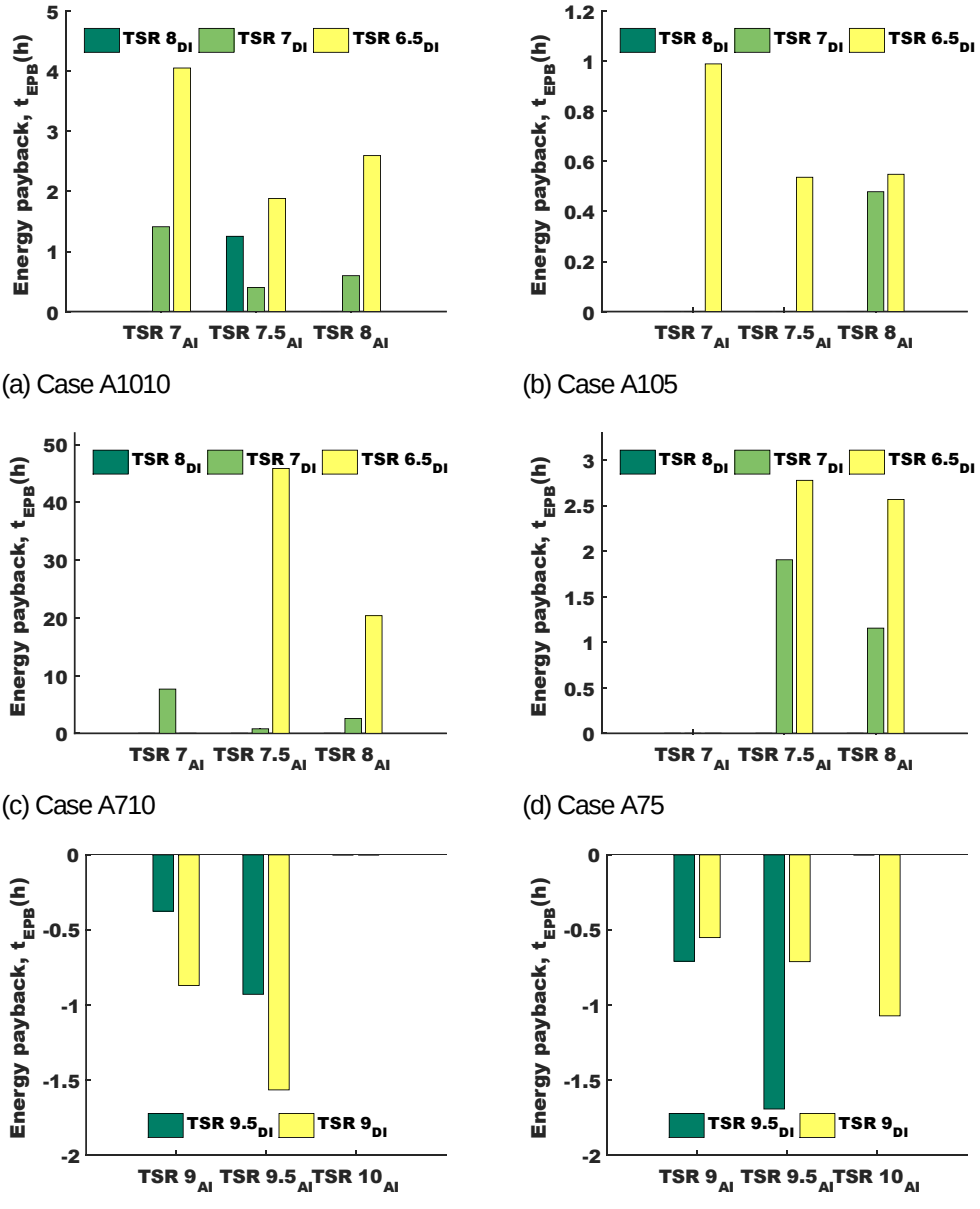

(a) Case A1010

(b) Case A105

(c) Case A710

(d) Case A75

(e) Case A510

(f) Case A55

Figure 50a-f: Energy payback time for different tip-speed ratio after icing (TSRAI) values for events A1010 (a), A105 (b), A710 (c), A75(d), A510 (e) and A55 (f).

5.2.1.2 Event B

In comparison to Event A, the *Cp* degradation for all Event B cases is more gradual due to a reduced ice accretion rate and more conformal ice shapes to the blade geometry (see Figure 51a-h). The sudden Cp drop for B710 and B75 during the first hour of icing is an interesting observation and can be attributed to the way the ice shapes form during the event. As the ice shapes are representative for rime and mixed-type icing, they are conformal to the clean geometry until the thermodynamic equilibrium changes on the air-ice boundary. It is apparent that before the thermodynamic equilibrium changes, the rime shapes during the first hour of icing are characterised by greater leading edge curvature slopes than the ice shapes at the end of the event. Due to the nature of the panel method algorithm, greater curvature slopes lead to reduced accuracy of the analysis. The aerodynamic uncertainties for B710 and B510 indicate ice shapes with increased curvature slopes near the leading edge region occurring during the 3rd hour of icing. This highlights the need for a greater fidelity aerodynamic analysis of such conditions.

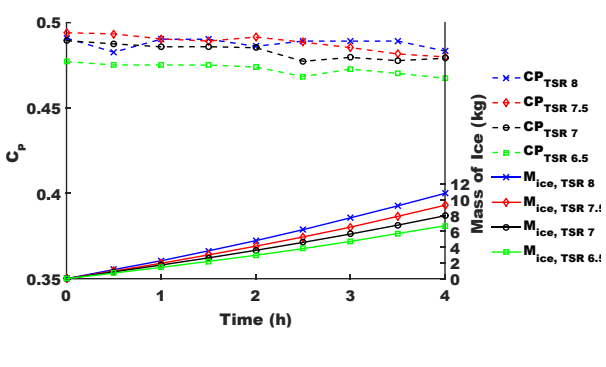

(a) case B1010

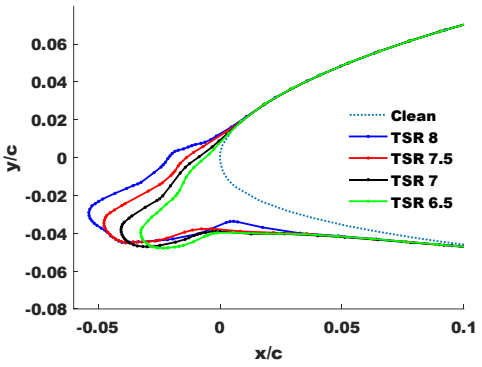

(b) case B1010

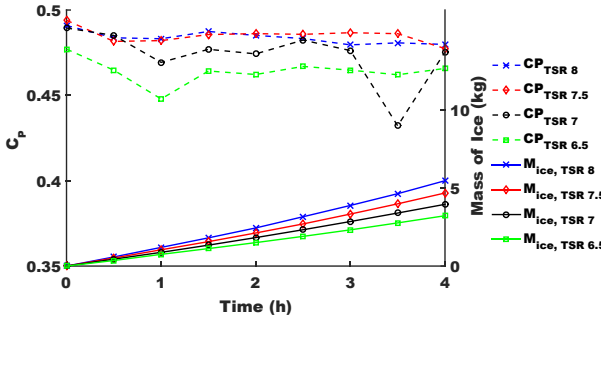

(c) Case B710

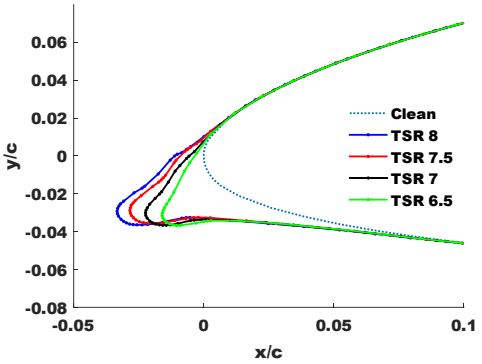

(d) Case B710

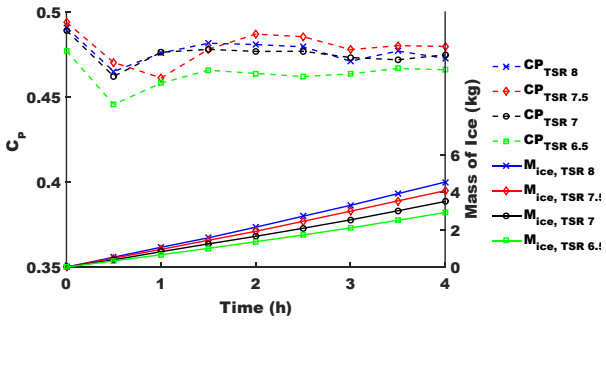

(e) Case B75

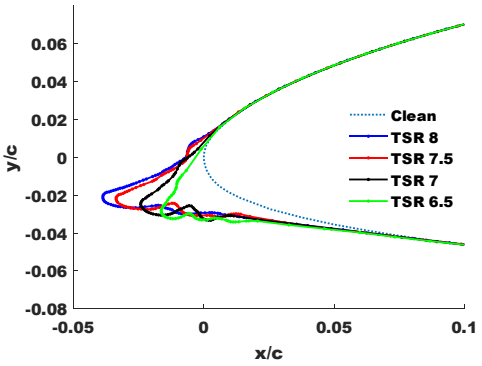

(f) Case B75

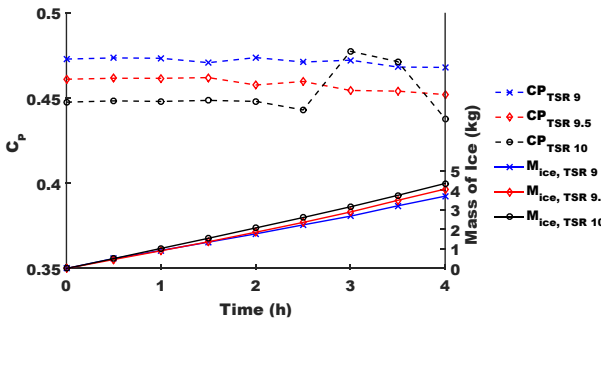

(g) Case B510

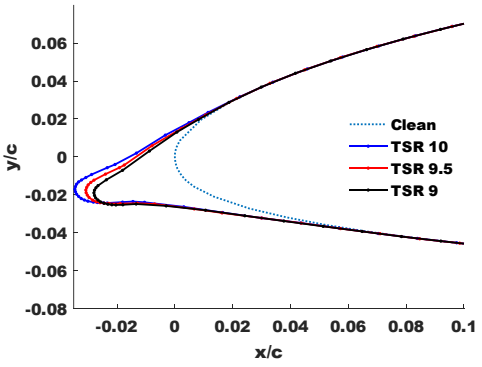

(h) Case B510

Figure 51a-h: Wind turbine Cp deterioration and ice accumulation per blade during events B1010 (a), B710 (c), B75 (e), B510 (g) and ice shapes on section D at the end of events B1010 (b), B710 (d), B75 (f), B510 (h).

The TSR_{AI} power characteristics for shapes produced during Event B cases are not particularly sensitive to changes in TSR_{DI}. Figure 52a-d shows that only minimal performance improvements can be achieved after icing by slowing the rotor down during the icing event. Unlike for Event A, only event B75 results in a TSR_{DI} of 7 being the preferred option for post-icing operation. Similarly, the minimum TSR_{DI} for event B510 provides the most favourable power characteristics after icing. The maximum TSR_{DI} of 8 indicated as the best option for B1010 is likely due to the discrepancies of the aerodynamic analysis and the negligible differences in the aerodynamic performance of the produced ice shapes under these conditions and TSR_{DI} values.

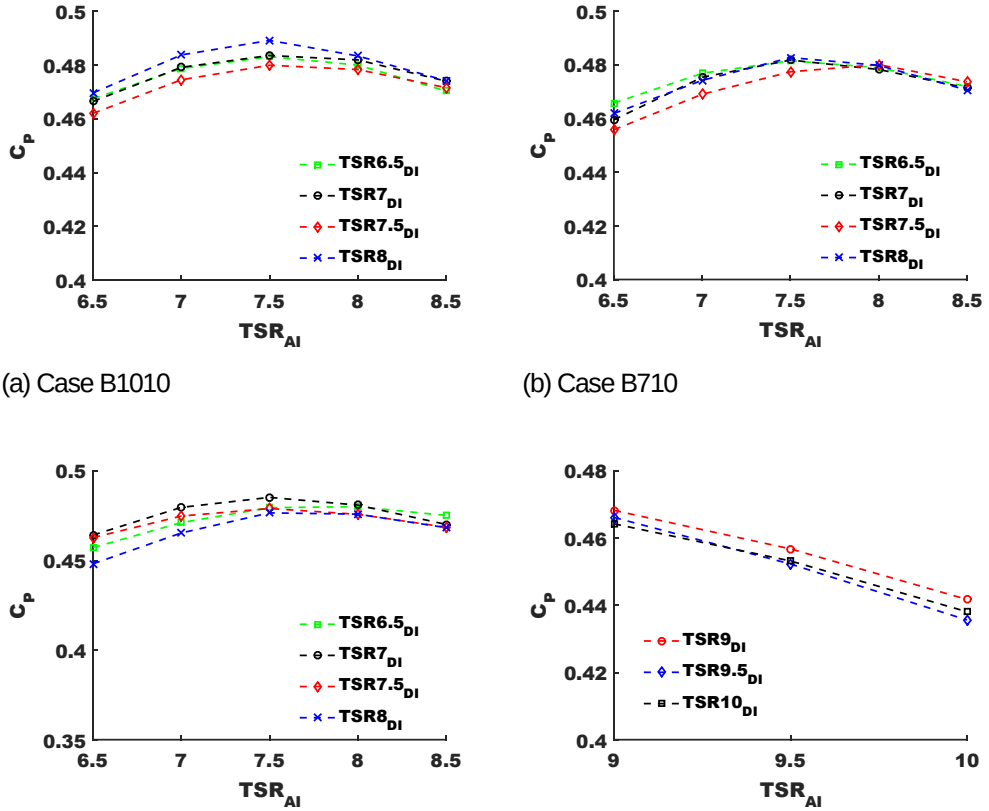

(a) Case B1010 (b) Case B710

(c) Case B75 (d) Case B510

Figure 52a-d: Power characteristics of modified tip-speed ratio values after icing events B1010 (a), B710 (b), B75(c) and B510 (d)

The minimal performance improvement observed from reducing the TSR_{DI} indicates that the energy payback time will be long or unachievable for icing event similar to event B. Reducing to a TSR_{DI} of 7 and increasing to a TSR_{AI} of 7.5 would have a long energy recovery time of 6h for B1010, 11.5h for B710 and 8.5h for B75. For $TSR6.5_{DI}$ this would increase to 19.5h, 21.3h and 16h for events B1010, B710 and B75, respectively. For some TSRs, t_{EPB} can reach extreme values (48-200h), which indicates that alternative ice mitigation approach should be considered or, if the power losses are too high, complete shutdown would be advisable. With a TSR_{DI} of 7.5 and 8 having very similar performance profiles for event B1010 and B710 (Figure 52a-b) and TSR_{DI} of 8 slightly underperforming on average–but having a higher *Cp* at the end of the icing

event (see Figure 51a and Figure 52c)–the short energy payback time indicated for TSR_{DI} of 8 on Figure 53a-b should be neglected. During B510, the modified TSR strategies (TSR_{DI} of 9 and TSR_{DI} of 9.5) provide higher energy yield and less ice-build up than operating at TSR_R resulting in a negative energy payback time.

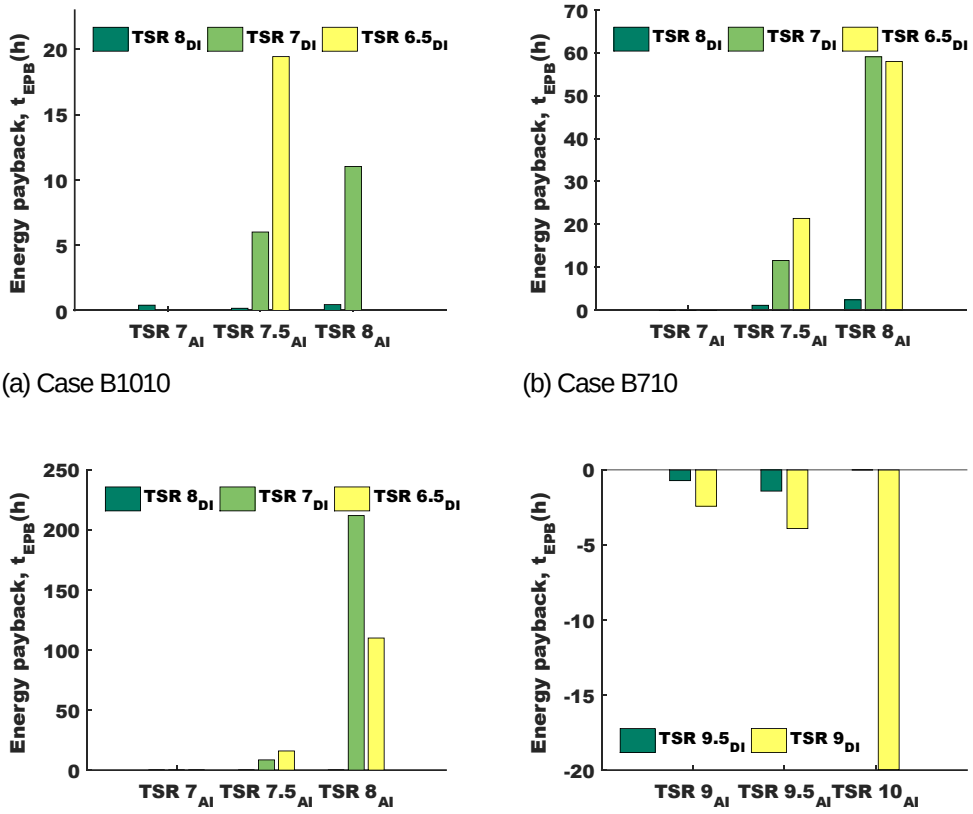

(a) Case B1010

(b) Case B710

(c) Case B75

(d) Case B510

Figure 53a-d: Energy payback time for different tip-speed ratio after icing (TSR_{AI}) values for events B1010 (a), B710 (b), B75(c) and B510 (d).

5.2.1.3 Event C

Among Events A, B and C, Event C is characterised by having the lowest values for LWC and MVD and ice accretion rates. With Event C being simulated for a wind speed of 10 ms^{-1} and ambient temperatures of -5 and -10 °C, two cases are presented: C1010 and C105. Due to small ice build-up and shapes (approximately 0.15 to 0.4 kg for different TSR_{DI} values), the power losses are no greater than 1% over the duration of the 4-hour icing events. In addition, the ice shapes are located on the pressure side of the leading edge of the blade (see Figure 54), leading to increased drag but minimal changes in lift (Bragg, Broeren and Blumenthal 2005).

From the energy payback time analysis, it can be concluded that the best option for operation for event C is to maintain operation at the reference TSR_R (*i.e.* 7.5). Energy payback time for all alternative operational strategies is relatively high for Event C, as there are minimal changes in *Cp* for different TSR_{DI} values (Figure 55a-b) and the ice deposition is low. For instance, by

setting the TSR_{DI} to 7 and then operating at a TSR of 7.5 the energy recovery time would be either 24h (A105) or 14h (A1010) (see Figure 56a-b).

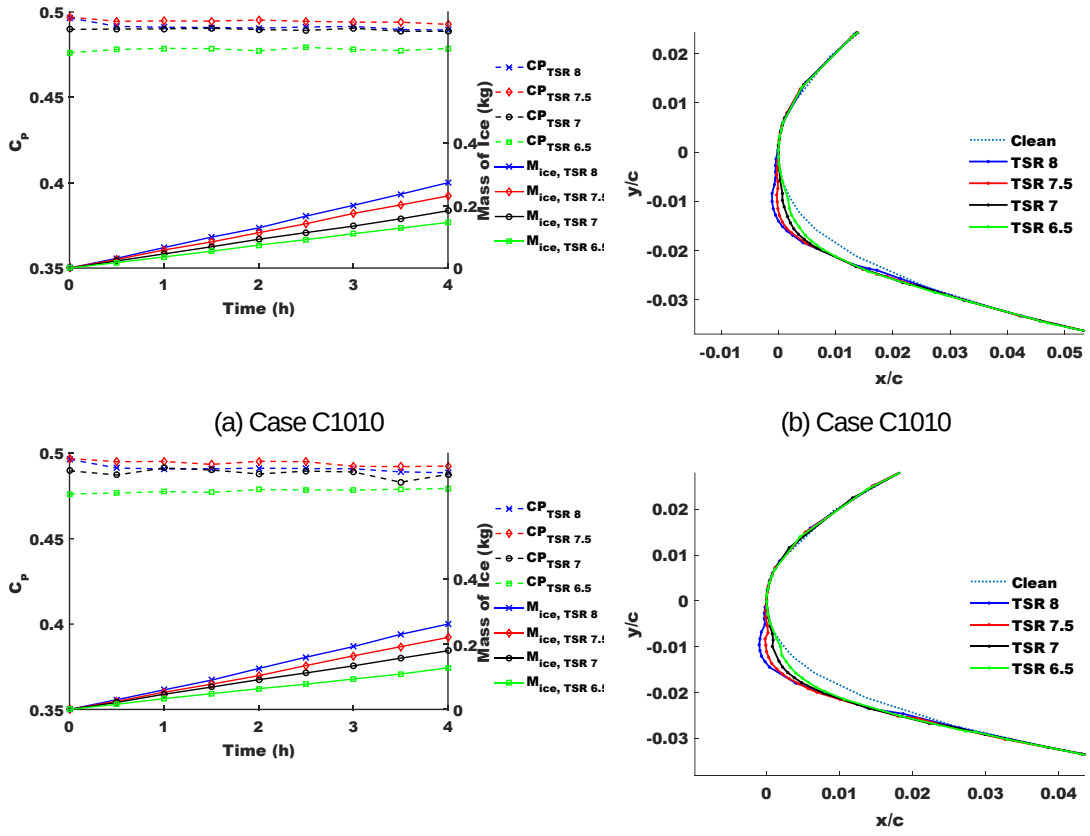

(a) Case C1010 (b) Case C1010

(c) Case C105 (d) Case C105

Figure 54a-d: Wind turbine Cp deteoration and ice accumulation per blade during events C1010 (a) and C105 (c) and ice shapes on section D at the end of events C1010 (b) and C710 (d).

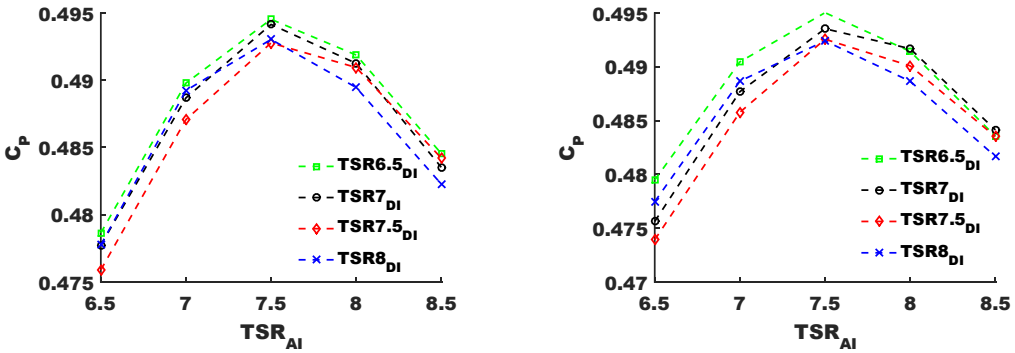

(a) Case C1010 (b) Case C105

Figure 55a-b: Power characteristics of modified tip-speed ratio values after icing events C1010 (a) and C105 (b).

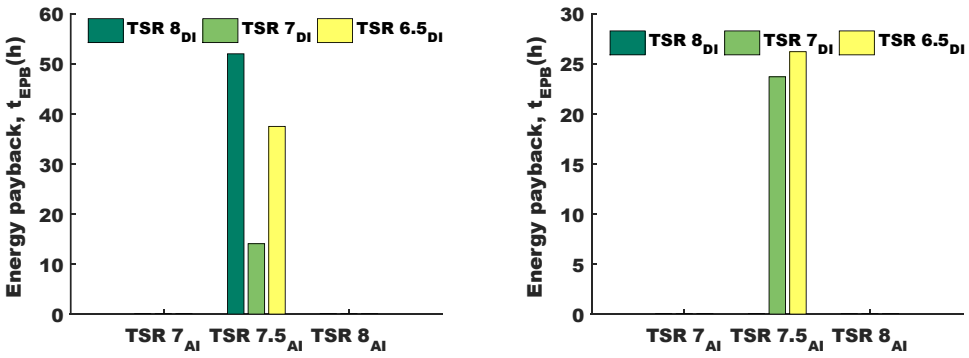

(a) Case C1010 (b) Case C105

Figure 56a-b: Energy payback time for different tip-speed ratio after icing (TSR_{AI}) values for events C1010 (a) and C105 (b).

5.3 Discussion and Further Work

The approach taken in this study of determining an energy payback time for different TSR operational strategies was found to be useful for both comparing the effectiveness of different strategies and indicating when normal operation can be maintained, or a different ice mitigation technique would be needed (e.g. an anti/de -icing system). It allows for the systematic design and evaluation of different derating scenarios, which was not the focus of precious research. The current energy payback time model could be extended do determine which strategy is the most effective when vibrational and structural analyses are incorporated. The viability of a TSR strategy would depend on the wind turbine type, local weather parameters and structural damage limitations. As rotational speed would actually decrease on variable-speed and variable-pitch wind turbines due to ice formation, a further improvement to the model could be achieved by modelling the transient behaviour of the TSR during ice build-up. This will be particularly beneficial when analysing longer severe icing events.

As there are many different icing events that can last for a few hours to several days, the viability of the different operational strategies proposed in this study still needs further investigation. The current analysis utilised XFoil, which enabled the aerodynamic performance of a large number of different ice shapes to be analysed with relatively low computational effort. However, the suggested ideal tip-speed ratio strategy for each event highly depends on the accuracy of the predicted aerodynamic penalties caused by ice build-up. In this study, the aerodynamic performance predictions are more reliable and accurate for the generated ice shapes without extreme irregularities and high curvature at the leading edge. Therefore, for the analysis of icing events leading to more irregular shapes, higher fidelity tools, such as Navier-Stokes equation-based solvers, are required.

5.4 Conclusion

This chapter examined the effectiveness of rotational speed modifications for the NREL 5 MW reference wind turbine during icing conditions. The turbine was simulated for three icing events, three wind speeds and two ambient temperatures, resulting in 12 different cases. To compare the effectiveness of each strategy, an energy payback time parameter was modelled to determine when slowing a wind turbine down during an icing event would provide overall more energy than a conventional strategy. The obtained results indicate that alternative strategies for mitigating ice losses, realised by tip-speed ratio modifications, are most effective for short and severe icing events similar to the event selected for the current analysis. For LWC of 5×10^{-4} $kg.m^{-3}$ and MVD of 25×10^{-6}m, the energy that is lost due to reducing the tip-speed ratio can be recovered within 0.5-2.5 hours post-icing event, thereby reducing the power losses from 7% to 23% and ice mass accreted on each blade from 20% to 30%. However, for longer and milder events, the energy recovery time is significantly longer (around 10-28h) suggesting the reference design strategy should be maintained. Additionally, the possibility for applying the TSR modification strategies should be considered carefully, as only limited ice mass would be acceptable due to structural constraints. Furthermore, the need for higher fidelity analysis tools is apparent for longer icing events, with XFoil being more effective for modelling short rime and glaze icing conditions, which do not result in severe horn-like shapes. Where previous wind turbine icing studies have tended to focus on just ice-induced power losses, this study has demonstrated the importance of considering a wind turbine blade's power characteristics and energy production throughout an icing event and performance once an icing event ends. The energy payback time method presented can identify which tip-speed ratio modifications can be used during and after an icing event, provided local meteorological conditions can be accurately predicted. Thus, this work will be of significant interest to wind turbine operators working in cold climate locations.

5.5 Summary

Advancements in derating ice mitigation operational strategy, realised with modifications of the rotational speed during icing conditions were proposed. The performance of the NREL 5 MW reference wind turbine was simulated for twelve icing events with varied wind speed, icing parameters and ambient temperature to test the developed design procedure for derating. By implementing estimated payback time model and systematic approach for choosing operational TSR during and after icing, the icing and operational conditions when derating would be a viable operational strategy for ice mitigation were identified. For extreme icing events with duration up to 1 hour, derating could reduce power losses up to 20% and ice mass up to 30%. The lost energy due to intentional reduction of the operational rotational speed with the reduction of the TSR would be recovered in 0.5 to 2.5 hours. The presented method aids the identification of cases where derating would be inadequate for ice mitigation and either the reference operational strategy should be maintained, or an alternative ice mitigation strategy should be

considered. Derating would be cost competitive operational strategy against currently available ice mitigation strategies, as it does not require the installation of additional systems and can be implemented by programming or developing advanced wind turbine controllers.

6 Wind Turbine Adaptation to Icing

The aim of this chapter is to establish a method for evaluating and selecting electrothermal anti-icing and tip-speed ratio derating strategies for wind turbines operating in cold climates. This is to enable wind turbine operators to determine how effective a selected icing mitigation strategy is under different conditions and choose the most effective strategy for a particular wind turbine and location. This is timely as electrothermal anti-icing systems for wind turbines are being actively tested and implemented, while tip-speed ratio derating is an untested ice mitigation strategy, but inexpensive and easily realisable (Homola, Matthew C. *et al.* 2012). The study further sets out to investigate how the preferred choice of strategy can change based on financial costs and icing condition variations.

6.1 Methodology

To demonstrate the method for evaluation and selection of ice mitigation operational strategies, it was assumed that two approaches for ice mitigation could be applied to a utility scale wind turbine during an extreme in-cloud icing event: derating scenarios realised by modifying the operational TSR and electrothermal anti-icing. In addition, operational shutdown was considered, as often it has been used to mitigate the accretion of ice on wind turbines, though it leads to prolonged periods of zero power output. The performance of the wind turbine for each ice mitigation technique was analysed by modelling the energy yield for a 24-hour period, with a 1-hour icing event occurring at the start of the analysis period. The length of the icing event was assumed to be one hour, as extreme events are typically short (Cober, Isaac and Strapp 1994, Lamraoui *et al.* 2014, Shu *et al.* 2018). The anti-icing energy requirements were modelled using LewINT, which models the needed heat flux to keep an aerofoil surface at a prescribed temperature. Two surface temperatures (5 °C and 15 °C) and two variations of the protected aerofoil surface (full protection and water impingement zone protection) were chosen for the anti-icing analysis. The viability of the anti-icing operational approach was estimated by using a return investment cost model introduced in (Peltola *et al.* 1999), which is based on the difference between the energy lost due to ice accumulation and the energy required to operate the anti-icing system. To investigate how the suitability of the operational strategies might change according to the weather conditions, two additional scenarios were introduced to consider a lower wind speed and a longer mild icing condition.

6.1.1 Icing conditions and ice mass calculation

The current approach was demonstrated for the 1-hour icing event, with wind speed of 10 ms^{-1}, liquid water content (LWC) of 5×10^{-4} kgm^{-3} and droplet median volume diameter (MVD) of 25×10^{-6} m, as defined in Table 1; this is representative of extreme icing severity (Lamraoui *et al.* 2013). The relative speed to the outermost blade section was calculated to be 71.4 ms^{-1} for a

reference TSR of 7.5 (TSR_R), which results in an ice accumulation rate of approximately 0.053 m/hour at the stagnation region. As anti-icing power requirements and ice shapes vary with ambient conditions, a wider range of ambient temperatures (T_{AMB}) from -30 °C and -5 °C were studied for this chapter. Two additional icing scenarios were selected to investigate how the wind turbine performance would vary if operational and weather conditions change. The first additional scenario included lowering the wind speed to 7 ms^{-1} and keeping the weather conditions unchanged. In the second scenario, the icing duration was increased to 4 hours and the LWC and MVD were selected to 3.5×10^{-4} kgm^{-3} and 20×10^{-6} m, respectively. The icing events were defined in Table 1.

6.1.2 Anti-icing power estimation

One-dimensional anti-icing analyses using LewINT® ice accretion software have been reported to provide satisfactory results for heat flux estimation (Al-Khalil *et al.* 1997, Wright, William 2008). The composition of the blade sections and the material thermal properties are as pre-defined in LewINT (Reid *et al.* 2013). For the analysis, it is assumed that the anti-icing will be operated in a running-wet state. This ensures that the impinged water on the surface of the aerofoil will be in liquid phase rather than being evaporated upon impact. The target surface temperate (T_{SURF}) was chosen to be either 5 or 15 °C, as these surface temperatures are typically considered for an AIS design (Battisti *et al.* 2007, Suke 2014).

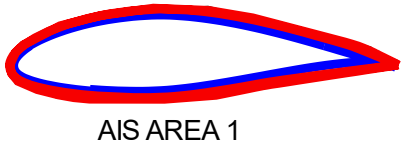

a)

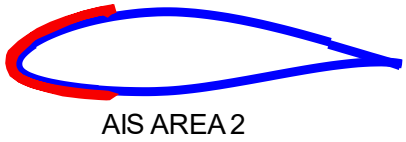

b)

Figure 57: a-b AIS for full surface (a) and impingement zone (b) protection.

To investigate how the protected area affects the power demand for the chosen icing conditions, two simplified protected surface areas are considered, as shown on Figure 57a-b. AIS Area 1 covers the whole area of the aerofoil blade section (Figure 57a) while AIS Area 2 protects only the water impingement zone (Figure 57b). While full protection of the surface would require the highest possible power requirement, it indicates the upper limit of needed power, which can be used to establish the maximum energy required for an AIS. The impingement area protection would require the least power as normally the water impingement zone is narrower than the ice formation zone on the aerofoil surface. However, it can be used to establish lower idealised limits of the needed power for operating an AIS. When impingement

area anti-icing is chosen, resultant ice shapes are expected if the supplied heat flux to the surface of the blade is insufficient to keep the impinged water in a liquid phase. For this study, a conservative assumption is made that no residual ice shapes will form as this would require an AIS system design layout to be modelled and sized.

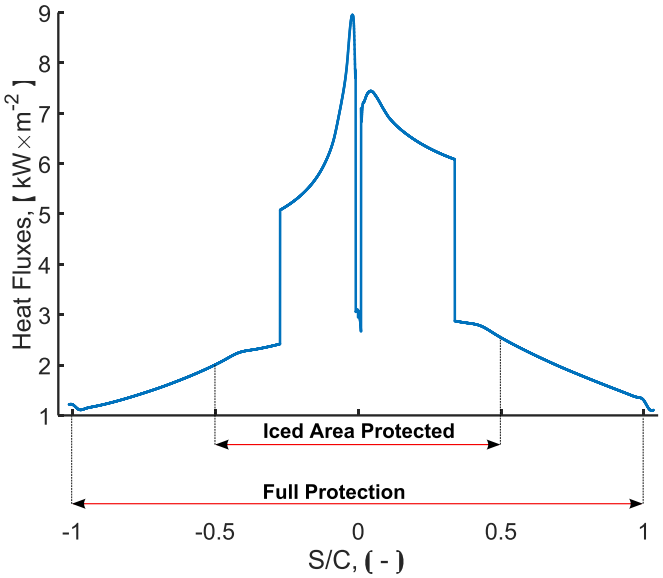

Figure 58: An example integration limit for estimating the required power for supplying the needed heat flux for anti-icing, when different protection areas are considered.

The required power, P_{Req}, to run an AIS is calculated by integrating the elemental heat flux, q_i, along the aerofoil surface (Figure 58) and the blade section width, ΔR_i (see Eq. 26). The needed heat flux for each blade section is estimated at the mid-section location (*i.e.* locations A, B, C and D in Fig. 1) and P_{Req} is calculated assuming constant distribution of q_i along ΔR_i. The protected area type (Figure 57a-b) defines the limits of integration and the needed power. Figure 58 shows the distribution of the needed heat flux along the unwrapped distance, *s*, (*i.e.* the coordinate system fixed to the blade surface), normalised by the blade section chord length, *c*. Thus, for different protected areas the limits of integration would differ and can be defined as -/+*s′*, which in the case of full area protection (Figure 57a) become -/+ s/c.

$$P_{Req} = \Delta \mathrm{R_i} \int_{-s'}^{s'} q_i ds \tag{26}$$

6.1.3 Evaluation of ice mitigation strategies

Operating according to different operational strategies results in variable wind turbine performance. Figure 59 shows how the instantaneous power output of a 5 MW wind turbine varies for different strategies during a 1-hour icing event at the start of a 24-hour period. For this study, there are four types of sustained power losses: losses due to operation according to the reference tip-speed ratio (TSR_R) strategy; losses from intentional power drop from derating

(TSR_M) and ice accumulation; net power loss from running AIS; and no power output during complete shutdown (standstill).

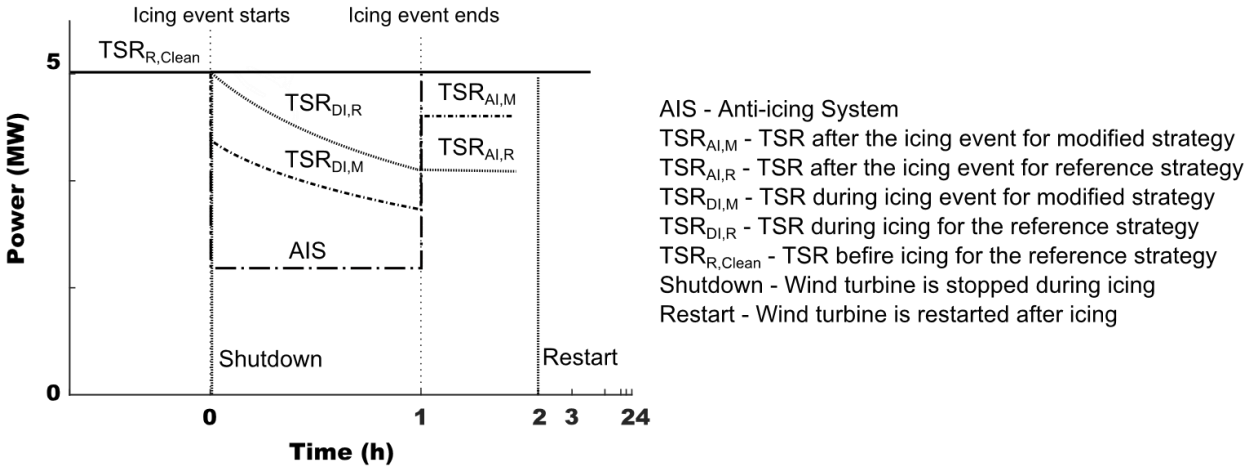

Figure 59: Instantaneous power output for a 5 MW wind turbine before, during and after a 1-hour icing event for different operational strategies in a 24-hour operational period.

The net power drop due to AIS operation – and the subsequent daily net energy loss – is limited by the duration of the icing event, as the blade surface should be clean once the icing event ends and assuming that there are no ice residues. The assumption is made that for anti-icing the blade would be clean at the end of the icing event and net power output would be restored to the reference TSR ($TSR_{R,clean}$). It should be noted that in reality ice residue is possible even with an ice protection system due to uneven heating and heating element layout design. Thus, additional losses can be incurred, which can affect the evaluation of ice mitigation strategies.

Operating without an AIS leads to ice accumulation. Instantaneous power output is therefore decreased for the reference strategy and derating both during ($TSR_{DI,R}$ and $TSR_{DI,M}$) and after ($TSR_{AI,R}$ and $TSR_{AI,M}$) an icing event. Figure 59 represents how deliberately slowing down the TSR to reduce ice build-up could result in a higher energy yield over a given reference period. As natural mechanisms of ice removal (melting, shedding and wind erosion) are not modelled in this study, lower and upper limits for the expected power losses were considered. The lower limit assumes that all ice formation is removed immediately after the end of the active icing event (*i.e.* the power output at the end of the event recovers to the clean rotor state, $TSR_{R,\ Clean}$). The upper limit is defined considering no ice shape changes after the icing event for the next 23 hours, which leads to constant reduced power after the active icing event, providing the wind speed remains unchanged. The actual performance post icing will depend on the rate of the ice removal for steady state analysis.

Operational shutdown is modelled as instantaneous power output recovery after the icing event, with no power output during the icing event (i.e. the wind turbine is stopped). However, in reality, melting time of up to 6 hours have been reported for wind turbines using operational shutdown (Dierer, Oechslin and Cattin 2011). Long recovery times lead to extreme energy

losses (e.g. 2 hours of stoppage for a 5 MW wind turbine results in an 8.3% daily energy loss). Therefore, operational shutdown only during the event and instantaneous power recovery post-icing event is an idealised scenario and it indicates if shutdown can become a viable solution in comparison to other operational strategies. If operational shutdown is found viable during this idealised case, a maximum viable stoppage time for melting would be established.

Total energy loss (E_{Loss}) estimations for the 24-hour period have been calculated for each strategy in relation to the energy that could have been achieved for non-icing conditions (E_{CLEAN}), *Eq.* 27, with E_{AIS}, $E_{TSR,M}$, $E_{TSR,R}$ and E_S representing the daily energy generated for the different potential modes of operation. The subscripts denote operation with anti-icing (AIS), derating via a modified tip-speed ratio (TSR,M), a reference tip-speed-ratio (TSR,R) and operation shutdown (S), respectively.

$$E_{Loss} = \left|E_{CLEAN} - E_{AIS/TSR,M/TSR,R/S}\right|/E_{CLEAN} \tag{27}$$

A break-even scheme, outlined in (Battisti 2015b, Peltola *et al.* 1999), is used to determine when an AIS operational strategy is a viable solution for ice mitigation. The scheme is based on the price of electricity, c_e, the yearly investment for implementing the system *I*, Eq. 28, an annuity factor, *a*, and the difference in lost energy from ice deposition and net energy reduction due to operating AIS ($E_{LOSS} - E_{REQ}$). The estimation is performed by limiting the cost of operation *A1, Eq.* 29*,* to be less or equal to the loss from icing *B1, Eq.* 30. When solving Eq. 29 and Eq. 30 simultaneously for the number of icing days, *N*, for an AIS to break-even in a year, Eq. 31 is obtained. The calculations are performed considering an initial investment cost of £ 3.9 M for the reference wind turbine (IRENA 2012, IRENA 2019), electricity price of 5 p/kWh, annuity factor of 12.5 and annual operations and maintenance expenditure, $AIS_{O\&M}$, of 2% from the initial investment for the anti-icing system. The initial cost of an anti-icing system, AIS_{CAPEX}, can be up to 5% of the wind turbine capital cost (Laakso and Peltola 2005) and in this study a range between 2-5% is investigated.

$$I = \frac{\overline{AIS_{CAPEX}}}{a} + AIS_{O\&M}AIS_{CAPEX} \tag{28}$$

$$A1 = I + c_e E_{REQ} N \tag{29}$$

$$B1 = c_e E_{LOSS} N \tag{30}$$

$$N \leq I/(E_{LOSS} - E_{REQ})c_e \tag{31}$$

6.2 Results and discussion

In this section, the ideal derating scenario (TSR_M) for the defined icing event in 2.1 is initially established using the energy payback time method as detailed in Chapter 5. By considering the daily net energy losses, an AIS strategy is compared with the selected derating scenario, reference TSR and shutdown strategies.

To identify the most suitable TSR_M for the defined icing condition in 2.1, energy payback times and ice mass accumulation are modelled. The operational TSR during icing (TSR_{DI}) for TSR_M was chosen to achieve the shortest energy payback time (t_{EPB}). The minimum operational TSR for the NREL 5 MW wind turbine, at a wind speed of 10 ms^{-1}, is 5 as shown in Chapter 5; this is based on the original definition of the wind turbine and the chosen electrical generator (Jonkman *et al.* 2009). Thus, t_{EPB} was calculated considering a TSR range between 5 and 7.5.

Energy payback time estimations for the extreme icing event are shown in Fig. 5a-d. The results indicate that for most cases either a TSR_{DI} of 6.5 or 7 should be chosen, as they provided the shortest energy payback time. The energy payback time for a TSR_{DI} of 6.5 was predicted to be more than double in comparison to a TSR_{DI} of 7. However, the latter was not found to be a possible option for operation at T_{AMB} of -5 °C. Thus, a TSR_{DI} of 6.5 was chosen as it outperformed the TSR_{DI} of 5 for T_{AMB} of -30 °C, -20 °C and -5 °C, while for T_{AMB} of -10 °C the difference in the resultant t_{EPB} was less than 1 hour (Fig. 5c). The expected energy payback time for operating the wind turbine at a TSR_{DI} of 6.5 and a TSR_{AI} of 7.5 was estimated to be 6.3 hours, 4.8 hours, 4.6 hours and 1.9 hours for T_{AMB} of -30 °C, -20 °C, -10 °C and -5 °C, respectively.

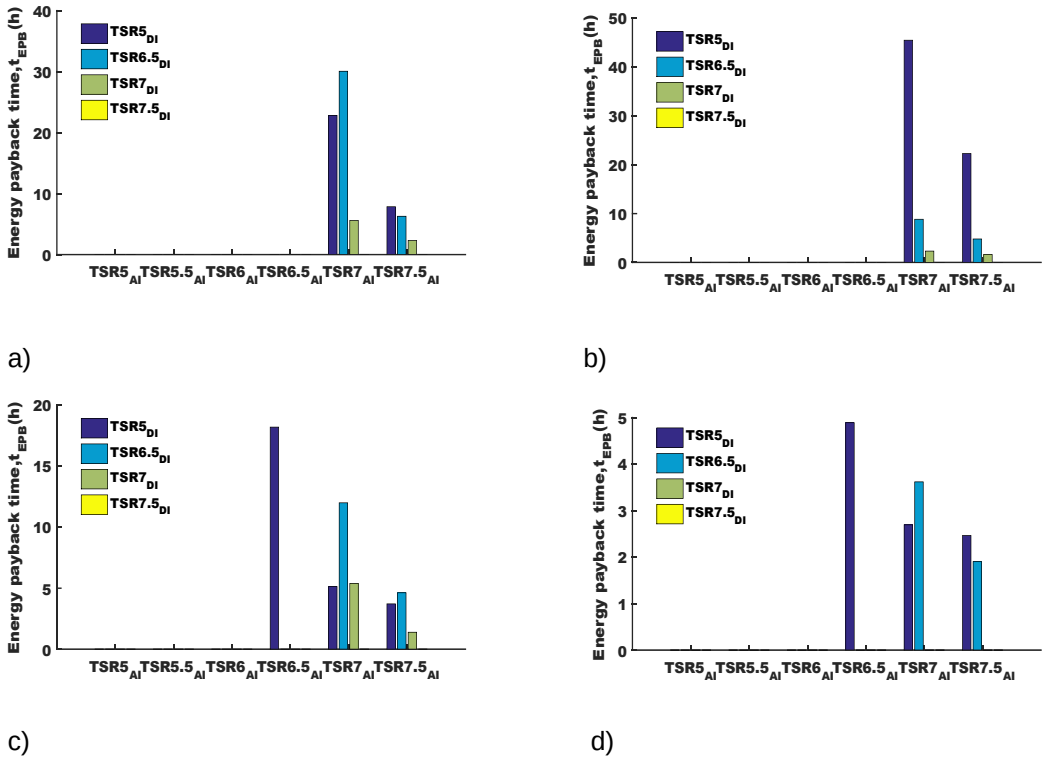

Figure 60a-d: Energy payback time (t_{EPB}) for ambient temperatures (T_{AMB}) of -30 °C (a), -20 °C (b), -10 °C (c) and -5 °C (d)

When selecting derating, both ice mass reduction and energy payback time should be considered. Fig. 61 depicts how the accumulated ice on the wind turbine rotor varies with TSR_{DI}. Operating at a TSR_{DI} of 5 resulted in the slowest rotational speed of the rotor, which led to the lowest ice deposition rate and the least accumulated ice mass over the range of ambient temperatures. When TSR_{DI} was increased to 6.5, the total ice mass on the rotor increased to 63 - 78 kg: roughly 70 – 80 % more ice. Operating at a TSR_{DI} of 6.5 led to approximately 23 % less ice mass in comparison to a TSR_{DI} of 7.5 (TSR_R). Based on the t_{EPB} and ice mass results, a TSR_{DI} of 6.5 and TSR_{AI} of 7.5 has been chosen as the most suitable TSR_M option for comparison with the other ice mitigation strategies.

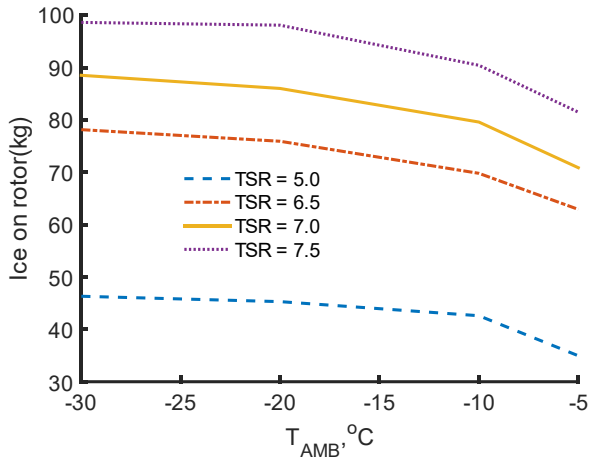

Figure 61: Ice mass accumulation on the wind turbine rotor during an extreme icing event and its variation for TSR_{DI} 5 to 7.5 (b)

The performance of the wind turbine was analysed by modelling the daily net energy losses (E_{24}) for every operational strategy. Each strategy would lead to different power losses, as described in Section 2.3. Figure 62 depicts how these losses vary over a range of considered temperatures for the alternative operational strategies. For the reference operational strategy and derating (*i.e.* TSR_R and TSR_M, respectively), the daily net energy reduction is shown as an area with lower and upper limits. The lower limit corresponds to the idealised case with deposited ice removed immediately after icing, while the upper limit shows the incurred losses if ice stayed during the 23 hours of operation after the 1-hour icing event. The operational strategy that ensured the lowest E_{24} indicated the best approach for operation during the considered conditions.

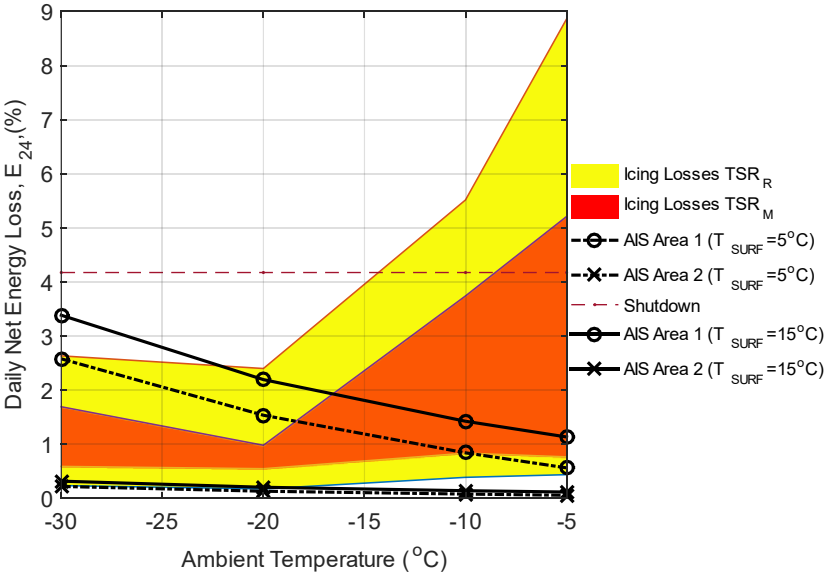

Figure 62: Performance graph indicating the variation in net daily energy loss for ambient temperatures ranging from -30 to -5 °C when derating, AIS and shutdown ice mitigation strategies are utilised.

The reference operational strategy and derating allow for ice to form on the blades, leading to deteriorated performance. Figure 62 shows that between 0.2 and 8.7% less energy would be generated if the wind turbine's reference operational strategy, TSR_R (*i.e.* is 7.5), was followed. However, when operated at TSR_M (*i.e.* TSR_{DI} of 6.5 and TSR_{AI} of 7.5), the maximum incurred losses reduced to 5.2 %, which is a 37% decrease. The highest energy reduction was found at T_{AMB} of -5 ºC, as typically more abrupt ice shapes form in such conditions. In comparison to TSR_R, the overall improvement in the wind turbine performance for TSR_M is identifiable by the smaller area depicting E_{24}.

Figure 62 shows when anti-icing will be the preferred operational strategy to minimise daily net energy losses. Considering an average of E_{24}, based on the upper and lower limits for derating and the reference strategy, AIS Area 1, at a surface temperature of 15 ºC, would be the preferred strategy for ambient temperatures above -10 ºC. This would change to -15 °C, if T_{SURF} was 5 ºC. The energy to operate the AIS Area 1 strategy is higher for lower T_{AMB} because the increased convective cooling needs to be balanced from the supplied heat flux. It is interesting to note that for T_{AMB} lower than -15 °C, the TSR_M was estimated to provide the best ice mitigation effect, which infers that derating for some icing conditions can be a more effective ice mitigation technique than AIS based on entire blade surface heating.

Water impingement zone protection (AIS Area 2) would ensure the lowest E_{24}. However, this result corresponds to the minimum E_{24} that would be sustained when AIS is used, as the water impingement area is generally smaller than the ice build-up area, especially in glaze icing conditions (*i.e.* T_{AMB} higher than -10 ºC and high LWC and MVD values). The margins in predicted daily net energy losses between the other strategies and AIS Area 2 can be used for optimisation purposes of AIS Area 2, which might include wider protection area and higher T_{SURF}. Figure 62 highlights how the importance of having a well-designed AIS protection area increases at lower ambient temperatures.

The operational shutdown strategy led to constant daily net energy losses of approximately 4%. The results showed that complete shutdown might be preferred for temperatures between -10 and -5 °C, if ice was to remain on the turbine blades for more than 23 hours after the active icing event and it was not possible to implement TSR_M and/or AIS strategies. These results were obtained with the assumption that the recovery time to ice- free blades for this operational strategy is 1-hour. However, in reality, ice might need more time to melt or could accrete during the shutdown, if the wind turbine is set to idle conditions. It is concluded that operational shutdown is not a viable solution for ice-induced energy loss mitigation.

The number of average icing days for AIS Area 1 and AIS Area 2 to break-even in comparison to the other strategies is shown in Figure 63a-b. This was modelled by comparing the differences in the expected daily net energy losses. The break-even period for incorporating AIS was obtained using the scheme outlined in Section 2.3 and the average from the E_{24} areas for both TSR_R and TSR_M (see Figure 62). The calculations were made by choosing AIS_{CAPEX} to be

3.5%, while error bars indicate how the break-even period would change if the cost of the system was as low as 2% or as high as 5% of the wind turbine's capital cost. For ambient temperatures above -5 °C and T_{SURF} of 5 °C, AIS Area 1 would be preferred to TSR_R, if there were between 42 to 104 days of extreme icing. In comparison to a TSR_M and shutdown, this increased to 70 – 175 days and 47 – 118 days. The number of icing days per year to reach viability decreased by 11, 17 and 12%, when AIS Area 2 was compared to TSR_R, TSR_M and shutdown, respectively. However, for AIS Area 2 to be viable for ambient temperatures above -10 ºC in comparison to the other operational strategies, at least 77 days of extreme icing would be required. When the surface protection was changed to 15 ºC, for the same T_{AMB}, the needed icing days for AIS Area 1 increased by 16 – 31 %. For lower ambient temperatures, the results highlight the importance of having an optimised anti-icing system from both a cost and performance perspective as the potential range in number of icing days required per year for viability is significant.

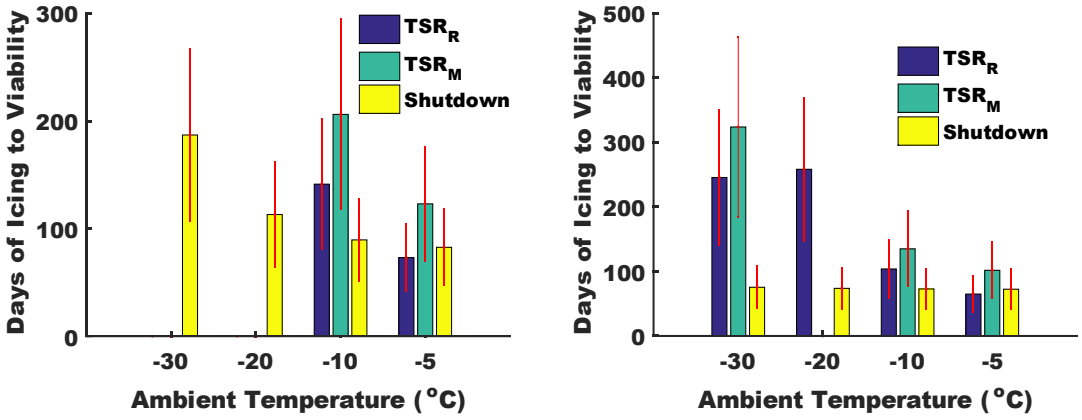

a) b)

Figure 63a-b: Number of icing days per year, which are required for the AIS Area 1 (a) and AIS Area 2 (b), at surface temperatures of 5°C, to be a viable solution, given the expected daily energy losses for other ice mitigation operational strategies

6.2.1 Variation in wind speed and meteorological conditions

At a wind speed of 7 ms^{-1}, it was found that derating could not provide improved performance as it led to higher or comparable energy losses, which is identifiable from the overlapping of E_{24} regions for TSR_M and TSR_R on Figure 64a. Thus, the TSR_M analysis showed how it is better to operate the wind turbine following TSR_R or using an alternative operational strategy. The results suggested operating at TSR_R was preferable because, for T_{AMB} between -30 and -15 °C, the daily energy losses would be no higher than 1% and the additional ice mass would be only 54 kg (Figure 64b), which is small in comparison to the weight of the blades (*i.e.* approx. 110 tons). Because of the relatively small daily energy losses (less than 10%), anti-icing would not be a

viable option for these operational conditions as shown in Figure 65a-b, unless the cost of the system and its power demand could be reduced.

For a long event with smaller LWC and MVD values, higher daily energy losses could be expected as shown on Figure 64c. The TSR_M strategy was found effective for T_{AMB} between -10 and -5 °C, with higher losses predicted for TSR_R. For a TSR_{DI} of 7 and a TSR_{AI} of 7.5, the estimated payback time would range between 0.8 and 14.5 hours and the ice accumulation mass would reduce by around 11% (see Figure 64d). However, TSR_R should be considered for temperatures lower than -10 °C (Figure 64c).

Figure 66a-b shows that if AIS Area 1 cost could be brought down to 2% of the wind turbine capital investment, the system would be viable for ambient temperatures above -5 °C and a T_{SURF} of 5 °. In comparison, the icing days to reach viability for AIS Area 2 reduced by 22, 42 and 10% against TSR_R, TSR_M and shutdown, respectively. From Figure 65b can be seen that an optimised AIS could be found effective for longer icing events even at T_{AMB} of -30 ºC, providing there were more than 50 icing days annually. The main difference for the results was the amount of maximum sustained daily energy losses (16%), which is high because of the prolonged icing event duration.

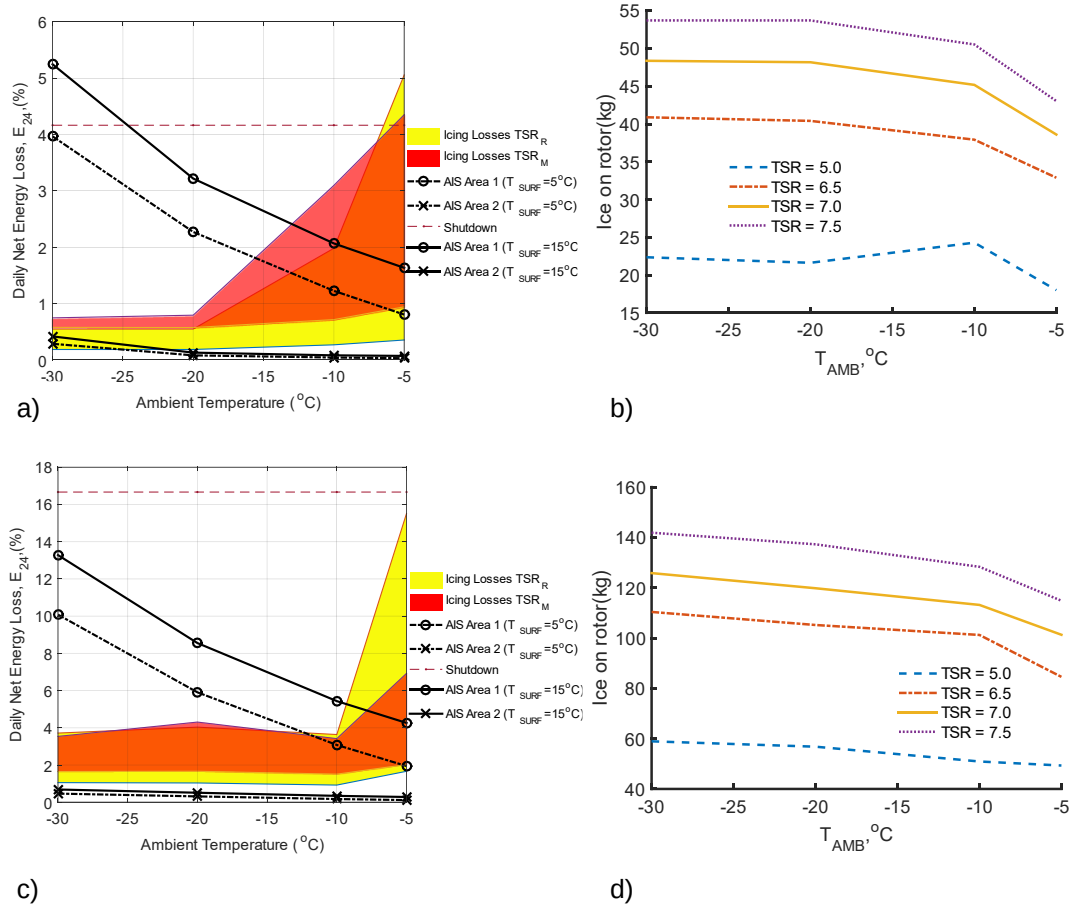

Figure 64 a-d: Daily energy loss (a and c) and total ice mass (b and d) for a 1-hour long icing event at a wind speed of 7 ms^{-1} (a-b) and a milder 4-hour long icing event at a wind speed of 10 ms $^{-1}$ (c-d).

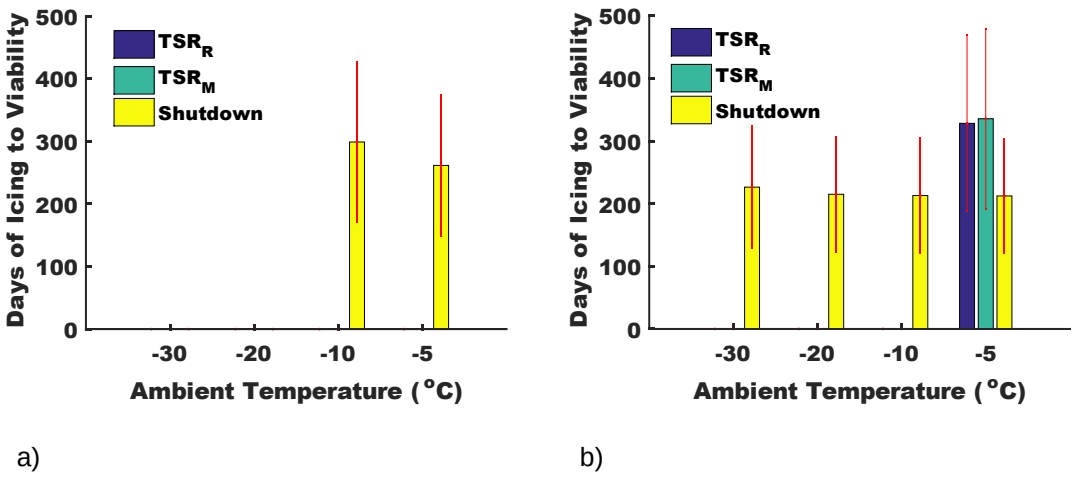

Figure 65a-b: Number of icing days per year, which are required for the AIS Area 1 (a) and AIS Area 2 (b), at a surface temperature of 5 °C, to be a viable solution, given the expected daily energy losses for other operational strategies; the wind speed is 7 ms-1

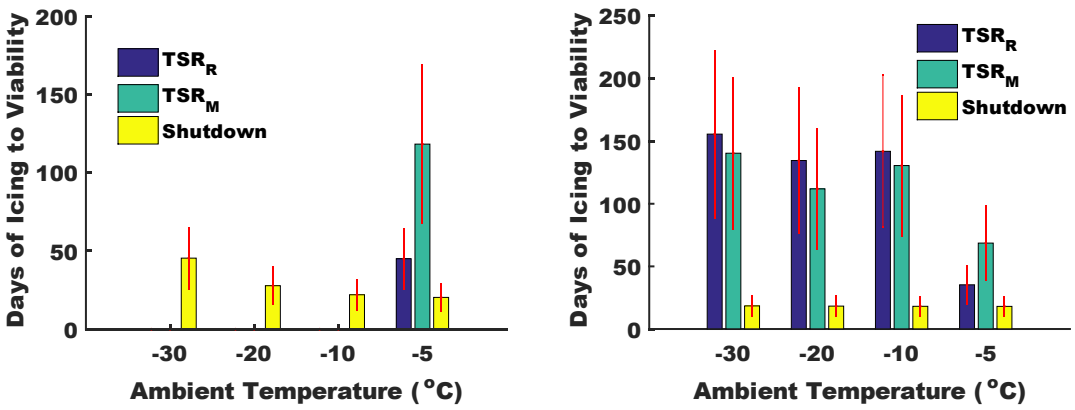

a) b)

Figure 66a-b: Number of icing days per year, which are required for the AIS Area 1 (a) and AIS Area 2 (b), at a surface temperature of 5 °C, to be a viable solution, given the expected daily energy losses for the other operational strategies; the wind speed is 10 ms^{-1}

6.3 Discussion and Further Work

The present work is aligned with the motivation of wind turbine manufacturers and operators to develop robust methods, systems and standards to operate wind turbines more efficiently in cold climates. The method outlined in this study enabled electrothermal anti-icing and tip-speed ratio derating strategies to be evaluated and compared for ice mitigation. It allows for the comparison of other ice mitigation strategies providing their cost for implementation and operation can be incorporated into the viability and performance analysis.

The energy yield assessment for the chosen strategies was conducted for a 24-hour period of operation with icing events of either 1 or 4 hours duration. The viability results for AIS – based on the number of icing days – and derating therefore do not take into account the possibility of multiple icing events occurring in a single day. Seasonal, yearly and event-based analysis should be developed by including various scenarios, which will be especially valuable for the day ahead estimation of energy prices. Future work should focus on the consideration of various scenarios for which a set of operational strategies are implemented and how the performance of the wind turbine can change if the best operational strategy fails. Thus, advanced and complex ice mitigation strategies can be developed to ensure the optimal operation of future wind turbines.

In further work, the sensitivity of the anti-icing viability result could be studied to investigate the impact of the financial assumptions made for electricity price and investment cost in conjunction with anti-icing system layout design and control algorithms. In addition, the viability analysis can be improved by accounting for the efficiency of anti-icing systems as suggested in (Battisti 2015b). The financial viability analysis could also be improved to account for the additional cost of implementing derating. Structural and dynamic analysis, by using the total ice mass, could show that due to fatigue loads the wind turbine structural integrity might need additional

reinforcement leading to additional cost for implementation, which should be accounted during comparison with other ice mitigation strategies.

The method presented in this study can be adopted for evaluating other wind turbines, locations, icing events and operational approaches for ice mitigation. . ; however, this will require:

- Improved ice climate mapping, information on the expected icing intensity and icing event distribution in local regions
- Higher accuracy aerodynamic analysis tools for modelling aerofoils with abrupt shapes on the leading edge; in this study it was found that lift reduction varied between 3.9% and 26% depending on the aerodynamic analysis tool used
- More data on ice mitigation strategy performance over long-term periods and details on cost and maintenance
- Incorporation of dynamic analyses to inform wind turbine operations in real-time, as the current method proposed in this research is limited to event-based modelling

6.4 Conclusion

This study found that a combination of derating, anti-icing and maintaining reference operating procedures can be used to maximise wind turbine power production during icing conditions; however, strategy selection needs to consider daily net energy losses, ice mass accumulation, icing event frequency and financial payback times. Derating outperformed anti-icing solutions for short extreme icing events at ambient temperatures below -10 °C. At lower wind speeds or for long mild icing conditions below -10 ºC, the wind turbine's reference operational mode should be maintained. Anti-icing was preferred for ambient temperatures above -5 °C for short extreme and long mild conditions providing the cost of the system was no higher than 2% of the wind turbine's capital cost and there were more than 43 short extreme or 26 long mild icing event occurrences per year. Anti-icing system viability was highly sensitive to the cost of implementation and surface protection area, which will require further advancements to be made in anti-icing system designs. Derating reduced the accumulated ice mass by up to 23% and anti-icing would still be required for complete ice accretion prevention. From an energy savings perspective, our findings indicated that an operational shutdown strategy was not a viable option. Further work should research how the current findings change for different wind turbine designs and site locations.

Our findings highlight the importance of having a combination of alternative ice mitigation strategies embedded into installed wind turbines in cold climates, and operational procedures in

place for strategy selection, where strategy selection considers carefully daily net energy losses, ice mass accumulation, icing event frequency and financial payback times.

6.5 Summary

A method to compare and evaluate different ice mitigation operational strategies was presented in this chapter. It was realised by taking into account accumulated ice mass, net energy losses both during and after an icing event and financial breakeven points. It was demonstrated for the assessment of the NREL 5 MW reference wind turbine during different icing events. Our results showed how derating can be preferred over electrothermal anti-icing and how this changed for different wind speeds, icing conditions, ambient temperatures and system costs. For a 1-hour extreme icing event, derating reduces accumulated ice mass and daily power loss by up to 23% and 37%, respectively. Anti-icing was identified to be the preferred strategy provided there were 42 extreme icing event occurrences per year at ambient temperatures above -5 ºC and the system only costs 2% of the turbine's capital cost.

7 Conclusion

This chapter summarises the work that has been done to address the research questions posted in the beginning of the thesis and the defined aim. The research questions are restated and the research, which was conducted to address each one is summarised. In response to each research question, the original contributions to knowledge in the field of wind turbine operation in cold climates are highlighted. The chapter ends with an assessment of the extent to which the overall aim was achieved and provides recommendations for further research.

7.1 Research questions

7.1.1 What is the uncertainty in predicting aerodynamic degradation due to icing when using low computationally intensive tools?

This research question was addressed in Chapter 4, where experimental and numerical methods were used to evaluate the aerodynamic degradation of eight ice shapes, which were simulated with LewINT for a 1-hour extreme icing event and two different wind turbine operational strategies. As the capabilities of the experimental setup did not allow for operational condition Reynold numbers to be achieved, numerical simulations with both XFoil and Fluent were conducted. The aerodynamic characteristics of the modelled ice shapes were tested over a range of angles of attack and the changes in the overall performance were analysed. The simulation results were obtained for Re that could be achieved both in the wind tunnel and during operational conditions of the NREL 5 MW reference wind turbine blade.

The overall icing losses for all cases were quantified by studying the changes in the lift curve slope, the maximum lift coefficient and the aerodynamic coefficients at an operational angle of attack for the wind turbine blade of 4.5 º. It was found that using 3D printed models to quantify

aerodynamic degradation can significantly underestimate the icing losses. In comparison to ice shapes produced in icing research wind tunnel, the aerodynamic lift and drag degradation was measured to be underestimated by more than 5 and 10 times, respectively. Similar results were obtained with Fluent for the low Re simulations, whereas XFoil predicted much higher degradation, but comparable with the results that could be found in the literature. It was concluded that using 3D printed ice shapes with aspect ratio of 3 cannot sufficiently determine the magnitude of the icing losses of the studied ice shapes; however, it enables the overall evaluation of their aerodynamic behaviour.

While low Re data on ice shapes has a more research-based focus and could be used to develop tailored simulation tools and measuring techniques, only high Re results are relevant for modelling wind turbine performance. Fluent and XFoil both showed reduction in the aerodynamic performance for the investigated ice event and overall performance improvement for the alternative ice shapes. The overall agreement in the predicted values of Cl and Cd for XFoil and Fluent was found to be between 0.6% and 30% with the exception for 0 º angle of attack for an ice-free aerofoil, which was attributed to the CFD simulation setup. Although for some ice shapes XFoil was found to have convergence issues, it was concluded that due to its simplicity and fast computational capabilities, it was a suitable tool for preliminary studies on wind turbine performance for relatively short icing events, which do not lead to abrupt ice shape geometries. Its application would be particularly useful when considering and designing operational strategies for ice mitigation, which rely on the regulation of control parameters (*i.e.* angle of attack, rotational speed and pitch angle).

The research question helped identifying the possible uncertainties, which can be expected when using XFoil and Fluent to estimate or predict aerodynamic degradation due to icing. As most likely both tools will still be actively used for wind turbine performance modelling, the estimated agreement in their predictive capabilities will be valuable for future research. The contribution to knowledge in this chapter are:

- Experimental data, which supports previous numerical findings that intentional reduction of the rotational speed during icing could be used to mitigate ice-induced power losses.
- Definition of the expected uncertainty when low computationally intensive tools such as XFoil are being used for the evaluation of the aerodynamic characteristics of iced aerofoils.

7.1.2 How can a wind turbine operational strategy be designed to improve wind turbine output during icing conditions without the installation of additional systems?

Following the experimental results from Chapter 4, which indicated that wind turbine performance can be improved by modifying the operational TSR during an icing event, in Chapter 5 the project went on with the development of a systematic approach to implement a

derating strategy and evaluate its viability for different operational and icing conditions. A method for the systematic choice of operational TSR during and after an icing event was developed, which was a limitation of previous studies investigating the benefits of using derating during icing for power optimisation. In addition, estimated payback time parameter was modelled to determine when the chosen derating strategy would be effective in reducing the incurred icing losses and increasing power output. XFoil, BEMT, LewINT and Qblade were used to obtain the needed wind turbine characteristics to design the ice mitigation derating strategies.

The performance of the NREL 5 MW reference wind turbine was modelled for 12 typical in-cloud icing events with varying operational and environmental conditions. The proposed design procedure provided a set range of possible operational TSR settings to be used for rotational speed modifications, while the energy payback time parameter indicated when the chosen derating scenario was a viable option and it could effectively reduce the ice-induced power losses and accumulated ice mass. For short and extreme icing events reducing the operational TSR from 7.5 to 6.5 during the event and recovering it to 7.5 after the event was found to reduce the incurred power losses and accumulated ice mass on each blade up to 23% and 30%, respectively. The energy, which was lost from intentional reduction of the operational TSR was estimated to be recovered within 2.5 hours after the icing event finished and the design TSR recovered. The presented method for implementation and design of derating operational strategies for ice mitigation aids in the identification of cases when alternative ice mitigation strategies would be needed.

In response to this research question, the development of a design procedure for derating ice mitigation strategy realised by operational tip-speed ratio modifications was achieved. In comparison to the other ice mitigation strategies, derating is advantageous, as its implementation is believed to not require the installation of additional systems. However, this would need further investigation and a direct collaboration with wind turbine manufacturers. The contribution to knowledge in Chapter 5 was accomplished by:

- Numerical results for a wider range of icing events, which showed how derating ice mitigation strategy can improve the performance of a utility-scale horizontal-axis wind turbine.
- Systematic methods for determining the range of possible operational tip-speed ratios for realising derating ice mitigation strategy.
- A design procedure based on an energy payback time method, which accounts for the lost energy from utilising the strategy and indicates what the best derating scenario is for a given wind turbine, icing event and operational condition; and when an alternative ice mitigation strategy would be required.

The work contained in Chapter 5 was published in the journal Renewable Energy:

- Stoyanov DB, Nixon JD. Alternative operational strategies for wind turbines in cold climates. *Renewable Energy*. 2020; 145:2694-2706; IF6.3

7.1.3 How can alternative ice mitigation strategies be evaluated and selected to improve wind turbine adaptation to cold climates?

This research question, and sub question, was answered in Chapter 6, where a method to compare and evaluate different ice mitigation strategies was developed based on modelling accumulated ice mass, net energy losses and financial breakeven points. It was demonstrated for three icing events with either 1 hour or 4 hours duration, which occurred in the beginning of a 24-hour period of operation of the reference wind turbine. It was assumed that the reference operational strategy, derating, anti-icing and operational shutdown could be set by the wind turbine controller for adapting the wind turbine to the icing events. By investigating how the ice induced daily energy losses vary with the choice of operation, it was determined when each operational strategy would be preferred for ice mitigation.

The results showed how depending on the expected icing events the choice of preferred operational strategy for ice mitigation could change. Derating was found to be more effective for reducing the daily energy losses in comparison to anti-icing for short extreme icing events with ambient temperatures less than -10 °C. However, for higher temperatures anti-icing was found a possible and effective ice mitigation strategy; this would depend on the design parameters of the system, its cost and the frequency of the icing events per year. It was found that for ambient temperatures above -5 °C, anti-icing of the whole surface of the protected blade sections would be a viable ice mitigation strategy if the cost of the system did not exceed 2 % of the wind turbine's capital cost and there were more than 43 short extreme or 26 long mild icing events occurrences per year. The main advantage of the developed method is that it allows for the comparison of other ice mitigation strategies providing their cost for implementation and operation can be incorporated into the viability and performance analysis.

For the final research question, the contributions to knowledge are:

- A method to evaluate and select different operational strategies for ice mitigation, which can be used to select a set of operational strategies for future wind sites in cold climates
- Evaluation of derating strategy and demonstrating the operational and environmental conditions when it would be an effective ice mitigation strategy and could outperform conventional solutions.
- Definition of limits for viable design layouts of anti-icing systems for relatively short mild and extreme icing events.

Initial studies related to this work were presented at the Wind energy conference in London, UK in 2017. Partial findings were presented at the Winterwind conference in Are, Sweden in 2020. Published materials related to the findings in this chapter are:

- Stoyanov, D. B., Sarlak, H., and Nixon, J. D. (2020) 'Operational Strategies for a Large-Scale Horizontal-Axis Wind Turbine during Icing Conditions'. in *Renewable Energy and*

Sustainable Buildings, Innovative Renewable Energy. ed. by Sayigh, A. Switzerland: Springer Nature, 839

- Stoyanov, D. B., Nixon, J. D., and Sarlak, H. (eds.) (2020) Proceedings from Winterwind 2020. 'Performance Maps for Ice Mitigation Operational Strategies'. held 3-5 February at Åre. Sweden: Winterwind
- Stoyanov, D. B., Nixon, J. D., and Sarlak, H (2020) Analysis of derating and anti-icing strategies, for wind turbines in cold climates, Applied Energy, Volume 288, 2021, 116610, ISSN 0306-2619.

7.2 Aim of the project: To improve wind turbine performance in cold climates through advancements in implementation, comparison and selection of ice mitigation operational strategies.

It is considered that the aim of the thesis was successfully achieved through the research outcomes, which resulted from answering the posed research questions. New knowledge has been gained in modelling wind turbine performance in icing conditions with a focus on the uncertainties, which can be expected when using different tools for determining aerodynamic degradation. It was demonstrated how derating operational strategy realised by modifications of the operational tip-speed ratio during icing can be designed and for what conditions it is effective for ice mitigation, which directly makes it suitable for high fidelity analysis and protype testing. The developed approach for comparison and evaluation of ice mitigation strategies can be used for any wind turbine, icing event and operational icing conditions. Its advantage is that the used parameters to evaluate and compare different strategies are typically modelled when wind turbine performance in icing conditions is being analysed. The evaluation of the ice mitigations techniques using the proposed method promotes a more holistic approach of studying ice mitigation strategies, as current research tends to analyse each strategy separately. The work covered in this thesis was based on the philosophy of applying engineering analysis for the development of potentially effective and simple approach for ice mitigation and promote the development of evaluation tools for ice mitigation strategies, which would aid the process of adapting wind turbines to cold climates and effectively harvesting the abundant wind kinetic energy. Thus, contribute and ensure the expenditure of renewables to ensure sustainable and green future energy generation.

7.3 Future Work

Some of the aspects of this work that can be a subject of future research were highlighted in the end of Chapter 5 and Chapter 6. They include the utilisation of higher fidelity tools for the aerodynamic analysis and scenario-based analysis for the developed design procedure for derating and the comparison and evaluation methods. This will build on the current findings and will help to generate a useful database, which can be used to model and design better control strategies. Any future experimental or field tests will be extremely beneficial in supporting the

current findings and identifying areas of future research, as the work covered in this thesis on operational strategies was predominately simulation-based.

In this thesis the uncertainties that could be expected when using low computationally intensive tools for the evaluation of aerodynamic degradation were analysed. The experimental data showed that 3D printed ice shapes in some cases might not be sufficient to represent the actual degradation that will be registered for real ice shape. Future work should be directed to identify the ice shapes that can be studied using 3D printing to analyse their characteristics and their effect on the aerodynamics. Pressure readings and visualisation techniques should be used to obtain, as much data as possible, which will also be beneficial for identifying the limitation of the computational tools that are usually utilised for aerodynamic analysis. Panel- and mesh- based models have been developed for other applications than icing, which should be accounted during analysis. This data will aid the development of new models and methods that can be effectively used for wind turbine performance analysis and improvement in cold climates.

Future research should focus on the Re effect on the aerodynamic degradation for different ice shapes. Previous research identified that the aerodynamic characteristics of some ice shapes are insensitive to changes in the Re. In addition, Lynch and Khodadoust (2010) suggested that the aerodynamic degradation measured for low Re is unrelatable for high Re. However, the authors also reported that for some ice shapes the aerodynamic degradation does not change after a certain Re. Thus, it will be of interest to quantify the performance of different ice shapes for a wide range of Re (from 500 000 to 9 000 000) and determine how the ice induced aerodynamic degradation vary and what generalisation of the characteristics can be made. As at high Re aerofoils usually have high lift generating capabilities, the degradation for high Re will be higher than the degradation for low Re, given there is Re after which the aerodynamic characteristics of ice shapes do not change. This analysis might help developing a method for relating low Re degradation measurement to high Re applications, which will be extremely beneficial for future studies.

The design procedure, which was developed in this thesis for derating should be tested further so that it can be implemented in a prototype control system. Tests in a research icing wind tunnel should be considered so that the detailed changes in the ice shapes and the variation of their aerodynamic characteristics can be studied. Additionally, the control algorithms should be connected to a reliable ice sensing system. Further research will be needed to study the effects that the response of the system can have on the effectiveness of the derating strategy. Ultimately, field testing of derating will be needed, which will be used to quantify with great accuracy the possible benefits that the strategy can have during operation in icing conditions.

Another important aspect for the utilisation of the derating ice mitigation strategy is that in order to implement it and use it effectively, a guarantee should be provided for manufacturers and operators covering the balance between intentionally lost energy from derating and the mitigated ice induced power losses. As a financial loss will be registered in the expectation of

financial gain post icing event, the vitality of developed systems ensuring reliable ice detection and power loss forecasting is apparent. The acceptance of the philosophy of the strategy might require specific discussions supported with modelling and simulation data. Thus, it is of practical importance to ensure that the aforementioned points for further research and development are covered so that an informed decision can be made for the deployment of such mitigating actions.

Future research on ice mitigation strategies should include tools and approaches that can be used to compare and select optimal operational strategies for icing conditions. Currently, this is the only study, which attempts to advance the decision-making process for ice mitigation strategy selection. The next step in the development of the presented method is not only to include more ice mitigation strategies but also provide a modular software environment so that the comparison and the valuation can be made seamlessly. This will greatly support wind turbine manufacturers and operators for both findings an optimal design for ice mitigation strategy and ensuring an optimal exploitation of wind turbine sites.

To realise the full benefit of combining alternative ice-mitigation operational strategies, a number of advancements will be needed in:

- Sensing equipment to i) monitor icing-event, post-icing and environmental parameters, and ii) detect and characterise ice accretion along the length of turbine blades
- Dynamic control algorithms with artificial intelligence for selecting different operational regimes.
- Prototyping and testing of emerging ice-mitigation strategies in collaboration with operators and manufacturers
- Anti-icing system design to optimise blade surface protection area, accurately control surface temperatures, prevent material damage and reduce installation, operating and maintenance costs.

Appendices

Appendix 1

The transition between the inflation region and the global mesh on the leading and trailing edges are displayed in Figure A1. 1 and Figure A1. 2 , respectively. To improve the mesh in future research specific treatments would be needed to reduce the elements with high aspect ratios in the wake region of the aerofoil. In addition, when ice is being included in the simulations specific automated procedures should be incorporated so that the mesh quality and conformity to the iced shape can be ensured during automation procedures such as the one needed in modular-type analysis systems.

The obtained y+ from the mesh setup in section 3.3.5 can be examined in Figure A1.3, where its distribution along the aerofoil's surface is shown. Additionally, in Figure A1.4 the complete residuals for a representative simulation are shown. The current setup can be improved by improving the mesh in the wake region so that lower residuals for the continuity equation can be obtained.

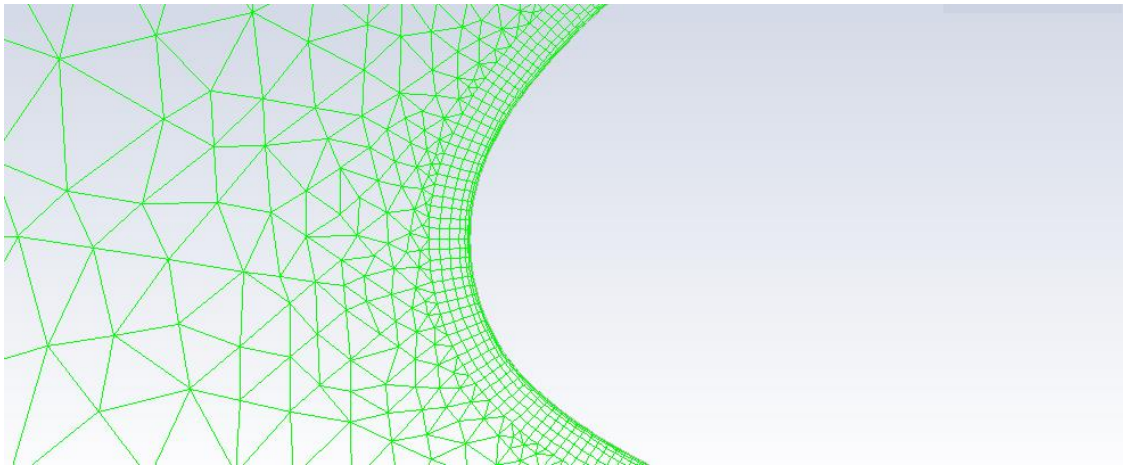

Figure A1. 1: The wall treatment of the aerofoil at the leading edge with prism layers transitioning to the triangles

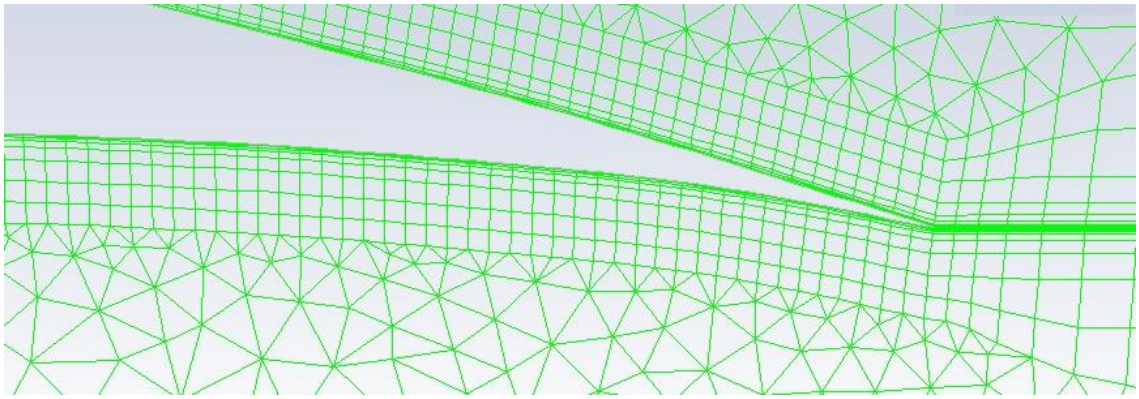

Figure A1. 2: The wall treatment of the aerofoil at the trailing edge with prism layers transitioning to the triangular main mesh

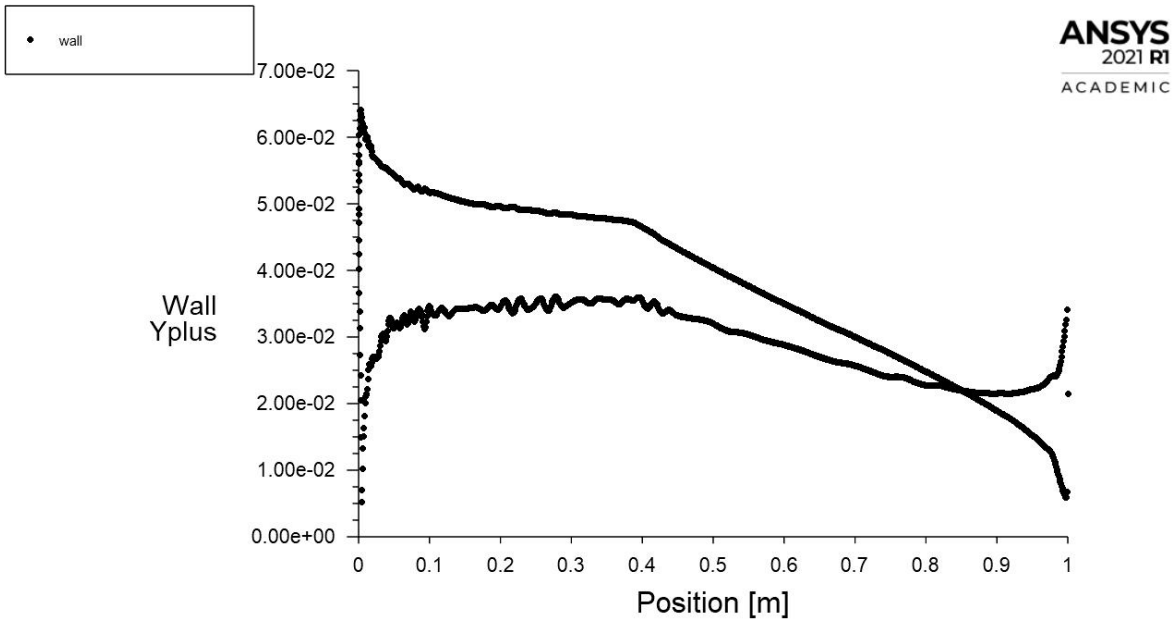

Figure A1. 3: Y+ value for distribution resulting from setting the first prism layer height to 3×10^{-7}, the growth rate to 2 and the total number of layers to 15.

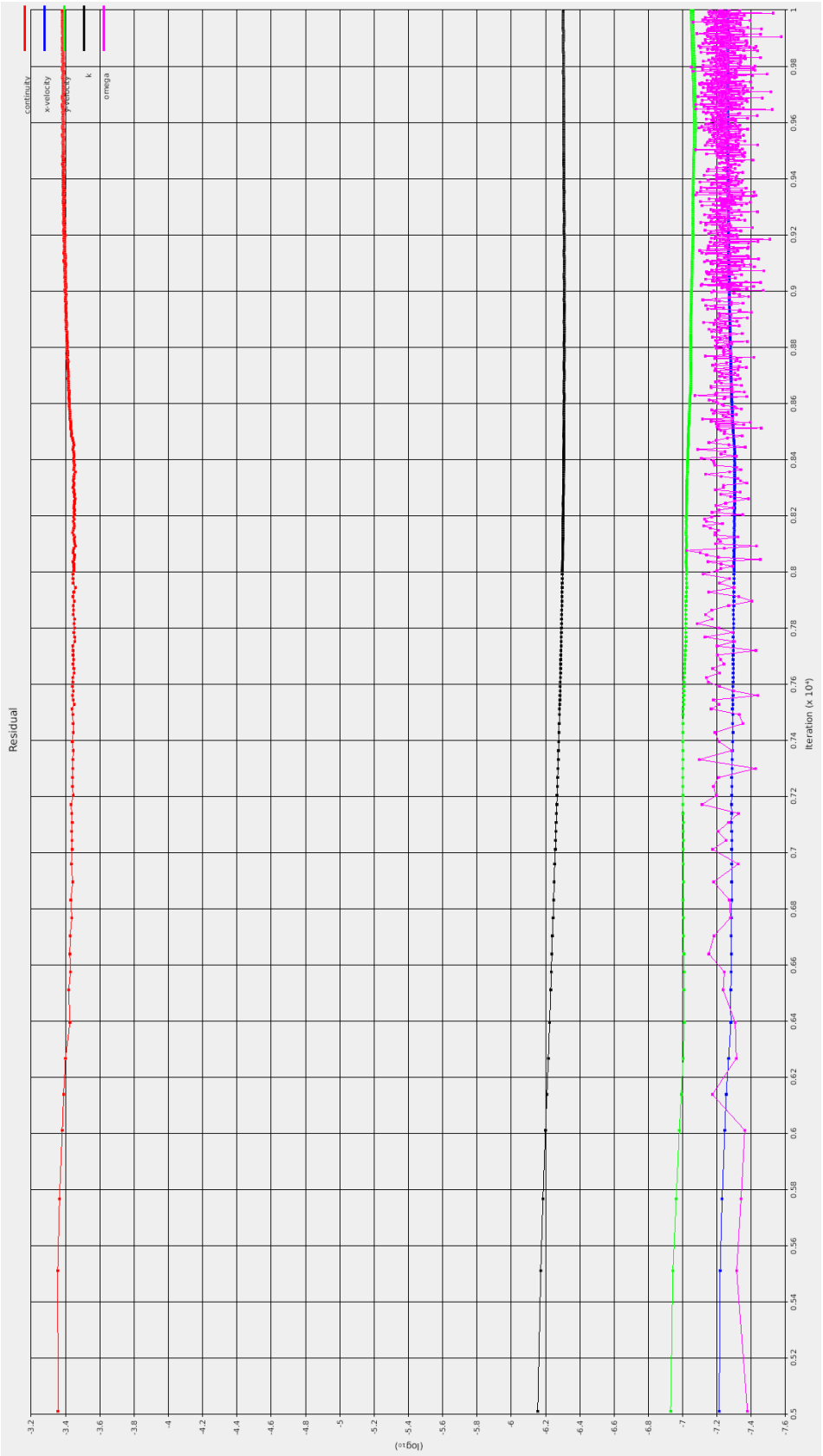

Figure A1. 4: Representative convergence criteria graph for the current CFD numerical setup, showing the absolute residuals after solving the continuity equation (continuity), the velocity in x (x-velocity) and y (y-velocity) direction, the turbulence kinetic energy (k) and the specific turbulent dissipation rate (omega); which are all outputs from the k-w STT model.

Appendix 2

Wind tunnel wall effect corrections are required to account for the finite distance of the lateral flow boundaries to the tested article. For closed-section low-speed wind tunnel, two-dimensional analysis and test article spanning through the wind tunnel work section, buoyancy, solid blockage, wake blockage and streamline curvature alteration correction need to be applied, [Barlow: pp.350].

Allen and Vincenti. The c/h value should be kept up to 0.4 for low Mach numbers and tests, which are meant to obtain the performance coefficients of the aerofoil up to and beyond the point of maximum lift. For the current tests it is 0.409 (chord length of 0.125m and working section height of 0.305m). This means that some inaccuracies can be contributed to the drawbacks of the theory for the correction or just mentioned that higher uncertainties can be expected.

To get a ratio of 0.39, the maximum chord length should be 0.120m

Buoyancy

Solid blockage

To a first order approximation solid blockage can be assumed to result in changed flow speed or dynamic pressure at the tested article for aerofoil frontal area to wind tunnel cross section area ratio in the range of 0.01-10. The effect is caused of having tunnel walls, which constrain the wind flow and lead to increased stresses on the aerofoil surface. It depends on the aerofoil thickness, thickness distribution and model size. The correction factor due to solid blockage is as given in Eq. A2.1, where K_1 is 0.7 and C is wind tunnel cross-section area.

$$\epsilon^{sb} = K_1 \times (0.7 \times thickness \times chord \times span)/C^{\frac{3}{2}} \quad \text{(A2.1)}$$

Wake blockage

Wake blockage leads to increased drag and velocity increment due to induced pressure gradient at the body due to the presence of a wake. The magnitude of the correction increases when wake size increases, which is a function of the tested body shape and the ratio of wake area to the tunnel area. The effect leads to a velocity increment at the model. The wake blockage correction factor, Eq. A2.2, is a function of the chord length, height of the tunnel, h, section and the uncorrected drag measurement, c_{du}.

$$\epsilon_{wb} = 0.5 \times \frac{c}{h} \times c_{du} \quad \text{(A2.2)}$$

Streamline curvature alteration

Due to the inability of the flow passed the tested body to expand, the curvature of the streamlines are altered in comparison to flow in an infinite stream. The effect leads to increased lift, moment coefficient and angle of attack. The performance of the body during wind tunnel tests is changed as it has 1% higher camber. The correction for altered streamline curvatures is presented by Eq. A2.3), where it can be seen that the correction depends on the magnitude of lift and moment coefficients and a constant σ, given by Eq. 2.4.

$$\Delta\alpha_{sc} = \frac{57.3 \times \sigma}{2 \times \pi} \times (c_{lu} + 4 \times c_{m0.25u}) \quad \text{(A2.3)}$$

$$\sigma = \frac{\pi^2}{48} \times \left(\frac{c}{h}\right)^2 \quad \text{(A2.4)}$$

Two-dimensional corrections

In the given formulae subscript *u* denotes uncorrected data, while *q* corresponds to clear stream values. The corrected values of velocity, Re, angle of attack, lift, pitching moment and drag coefficients are given by Eq. A2.5 to Eq. A2.11. However, the drag should be corrected for the buoyancy effects before using Eq. 2.11 by subtracting the longitudinal static pressure gradient.

$$V = V_u \times (1 + \epsilon) \quad \text{(A2.5)}$$

$$\epsilon = \epsilon_{sb} + \epsilon_{wb} \quad \text{(A2.6)}$$

$$Re = Re_u \times (1 + \epsilon) \quad \text{(A2.7)}$$

$$\alpha = \alpha_u + \Delta\alpha_{sc} \quad \text{(A2.8)}$$

$$cl = cl_u \times (1 - \sigma - 2 \times \epsilon) \quad \text{(A2.9)}$$

$$c_{m0.25} = c_{m0.25u} \times (1 - 2 \times \epsilon) + 0.25 \times \sigma \times cl \quad \text{(A2.10)}$$

$$c_{d0} = c_{d0u} \times (1 - 3 \times \epsilon_{sb} - 2 \times \epsilon_{wb}) \quad \text{(A2.11)}$$

Appendix 3

The surface roughness analysis was conducted a surface roughness/contour measuring system FORMTRACER SV-C3100/4100. A conical stylus was used with cone angle of 60 ° and tip radius of 0.002 m as illustrated in Figure A3.1. The analysis was done on a patch of the printed aerofoil. The measurement conditions such as measured length and measuring speed are listed in Table A3.1, while the measured profile is shown in **Error! Reference source not found.**. The r esults of the measurement are listed In Table A3.2; The arithmetic mean height, R_a, maximum profile peak height, R_p, maximum profile valley depth, R_v, maximum height of profile, R_z, and total height profile, R_t, were sampled to be 0.0128, 0.0326, 0.0388, 0.0714 and 0.0792, respectively.

The arithmetic mean height was used to obtain an equivalent sand grain roughness height as suggested in [ref]. However, for large values of Ra, the author showed that increased uncertainty can be expected when using the developed scheme. In this case, the actual values from the paper were taken, which are based on a 1.57 cm galvanized steel pipe and Ra being 12.8×10^6 m, instead of using the proposed correlation.

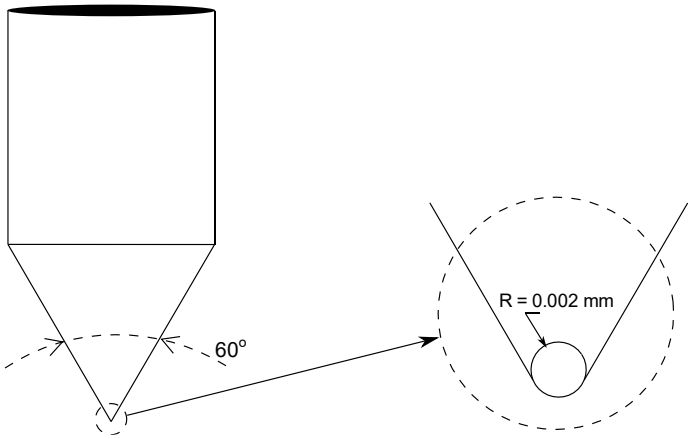

Figure A3. 1: The conical stylus used to perform the measurements with cone radius of 60 ° and tip radius of 0.002 mm

Table A3. 1: Measured parameters

Instrument	SV-C3100
Measured Length (in X), mm	12.5
Measured Pitch, mm	0.0010
Measured Speed, mm/sec	2
Z1-axis Range, mm	0.8
Sampling Method	X-axis Pitch
Z Gain Adj. Ratio	0.994837
Symmetric Compensation	Non
Straightness Compensation	Non
Straightness Compensation (X-axis)	Non
Stylus Radius Compensation	Non
Polar Reversal	Non

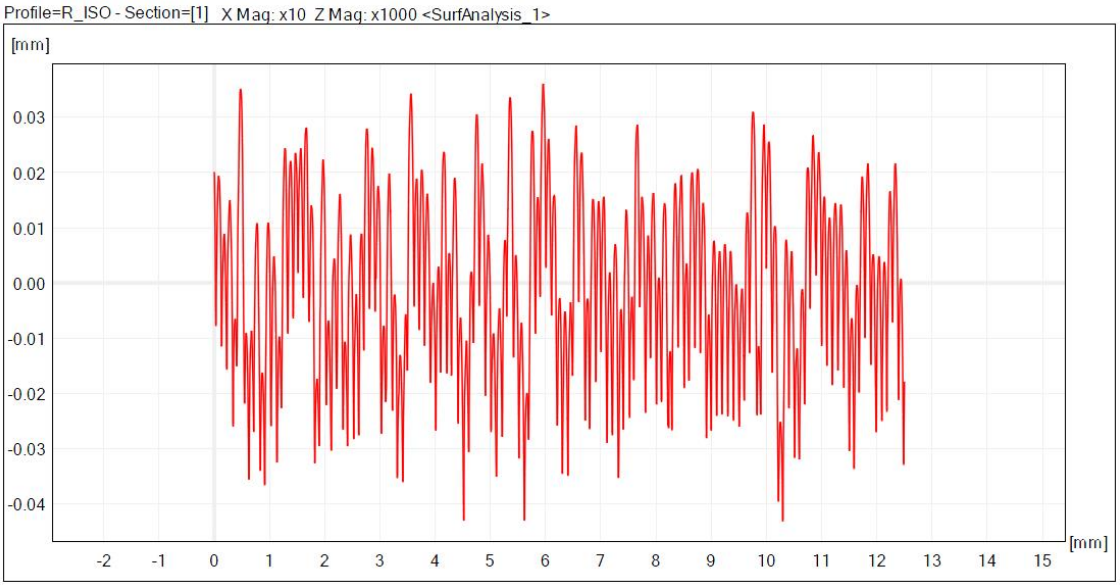

Figure A3. 2: Surface roughness profile on the chosen patch from the leading edge of the printed aerofoil

Table A3. 2: Surface roughness analysis parameters

Measured Results	
Ra, mm	0.0128 0.0714
Rp, mm	0.0326
Rv, mm	0.0388
Rz, mm	0.0714
Rt, mm	0.0792

Appendix 4

The pressure distribution obtained with XFoil and Fluent for the operational angle of attack at TSR of 7.5 (4.5 °), for the analysed cases in sub-section 4.1.2.3, are shown in Figure A4.1 and Figure A4.2. The graphs illustrate the good agreement (*i.e.* within 10 %) between the two pieces of software for Re of 6×10^6 at the operational angle of attack of blade section D.

As stated, the greatest difference between XFoil and Fluent is for the clean aerofoil surface, Figure A4.1a. The disagreement in the prediction of the C_P magnitude on the suction side can be attributed to the quality of the mesh that has been used to obtain the results with Fluent k-w SST turbulence model. However, it can be improved with further refinement, which would require either different mesh topology or more advanced meshing technique. However, for the purpose of this study, the quality of the mesh was considered to be sufficient.

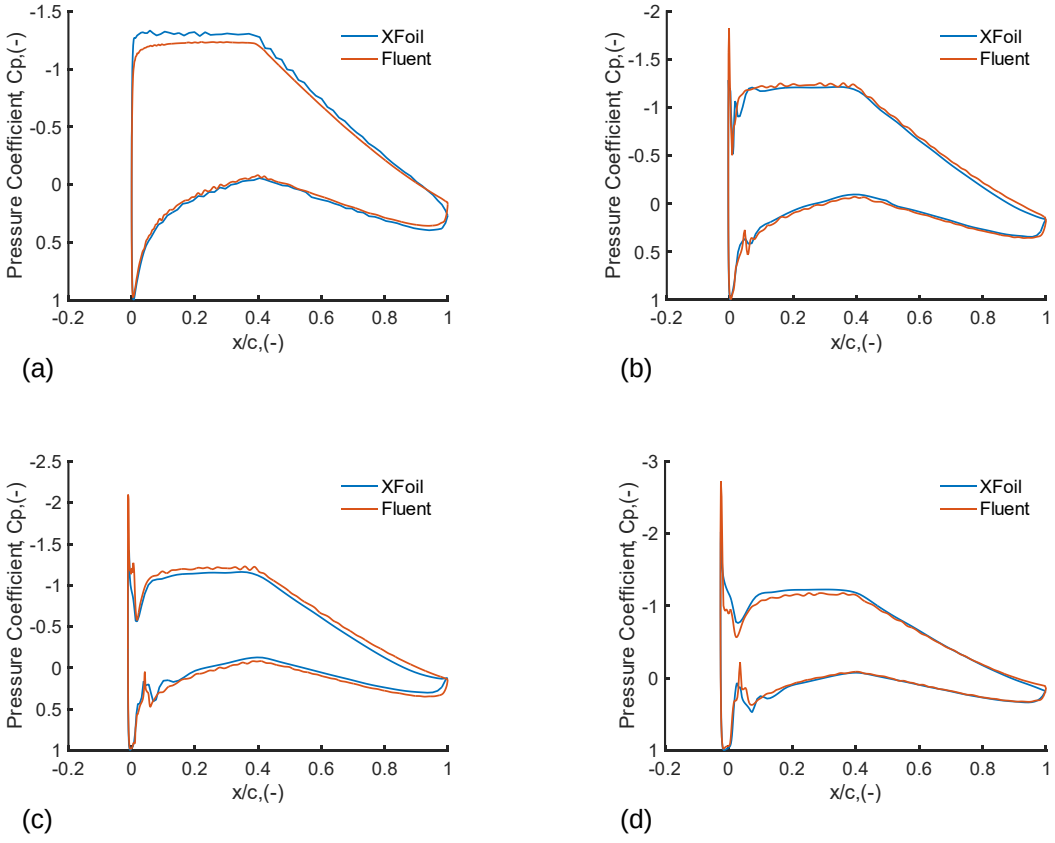

Figure A4. 1a-d: Pressure coefficient distribution at time intervals of 0 (a), 0.25 (b), 0.50 (b) and 1.0 (d) hours during one-hour extreme icing event for NACA 64-618 aerofoil, simulated at Re of 6×10^6 with XFoil and Fluent k-w SST turbulence model for angle of attack of 4.5 °

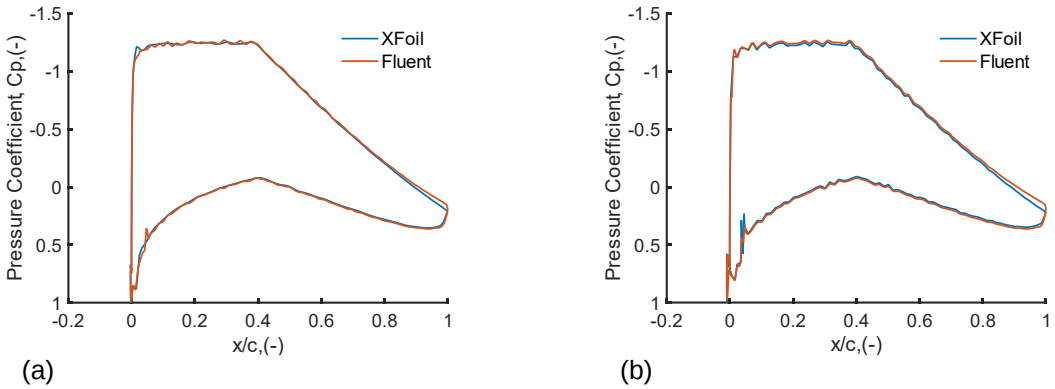

Figure A4. 2a-b: Pressure coefficients for the iced NACA 64-618 aerofoil at section D, for angle of attack of 4.5°, after 0.5 (a) and 1.0 (b) hours of icing at reduced tip speed ratio of 5.0 and Re of 6×10^6

Appendix 5

The appendix provides an overview of the ice shapes that have formed at the end of an icing event for the modelled 2D sections of the NREL wind turbine blade: sections A (33m), B (41m), C (50.5m) and D (59.5m). Figures A5.1-A5.12 show a total of 180 ice shapes that have been used to calculate the performance of the wind turbine after an icing event the energy payback time parameter. For brevity, all 1176 ice shapes – that have been generated to calculate the Cp and ice mass values throughout the icing events – are not shown.

Figures A5.1 - 5.12 show how ice thickness and mass increases with radial position, lower ambient temperatures and higher TSR setting. In addition, it can be noticed how the ices shapes become more irregular for lower ambient temperatures with horn-like protrusions on the aerofoil surface.

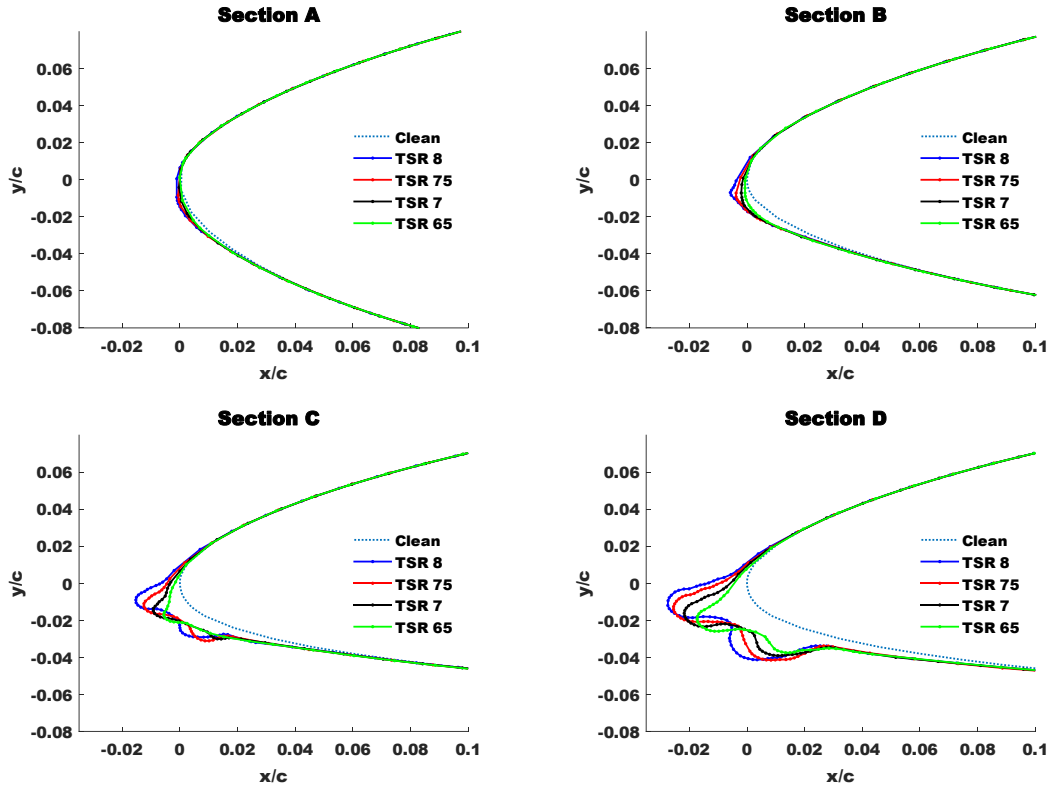

Figure A5. 1: Ice shapes formed at four different sections along the NREL 5 MW wind turbine blade at the end of icing event A1010.

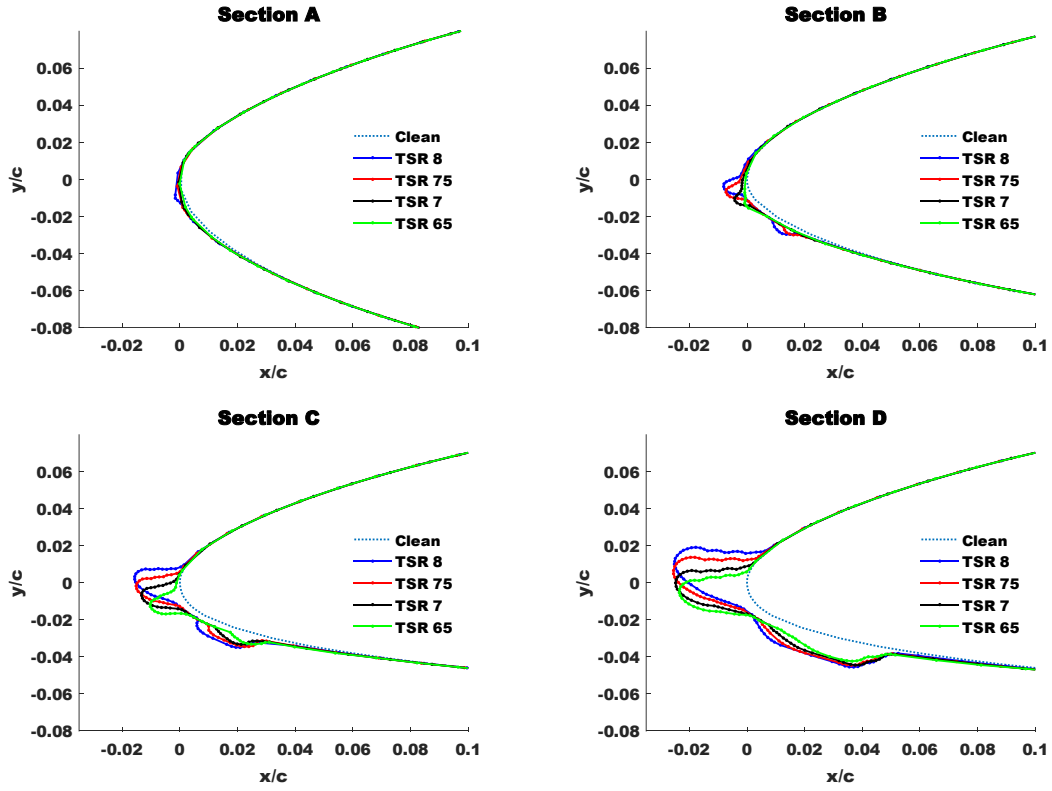

Figure A5. 2: Ice shapes formed at four different sections along the NREL 5 MW wind turbine blade at the end of icing event A105

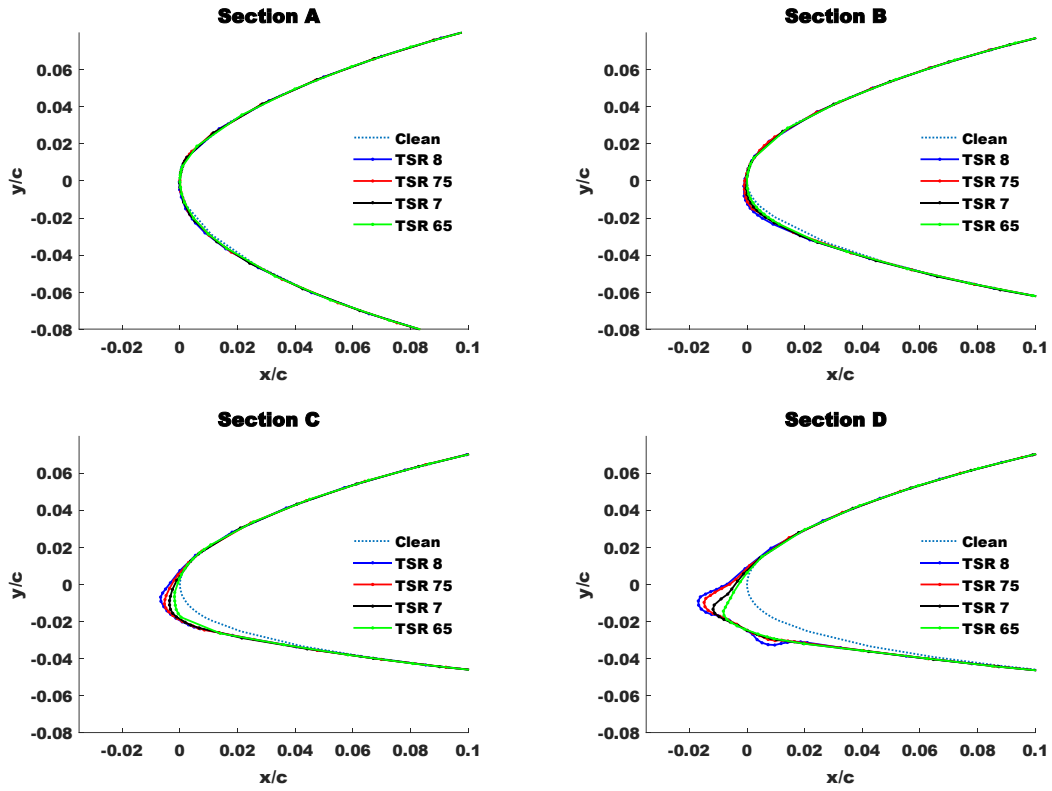

Figure A5. 3: Ice shapes formed at four different sections along the NREL 5 MW wind turbine blade at the end of icing event A710

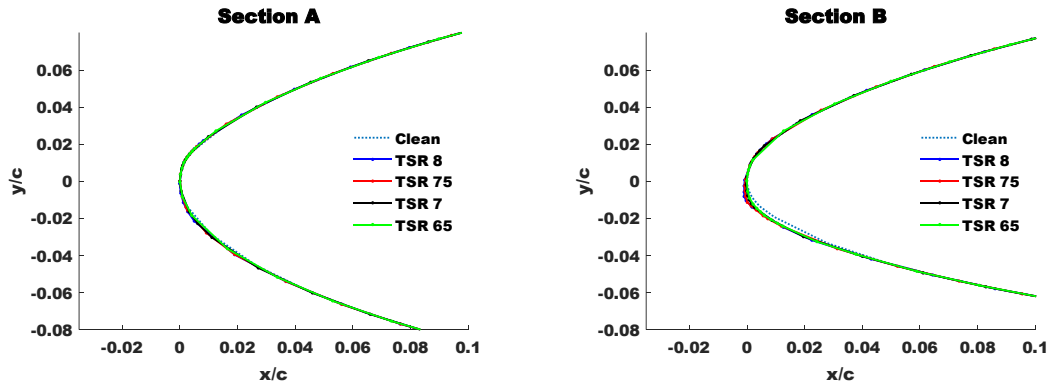

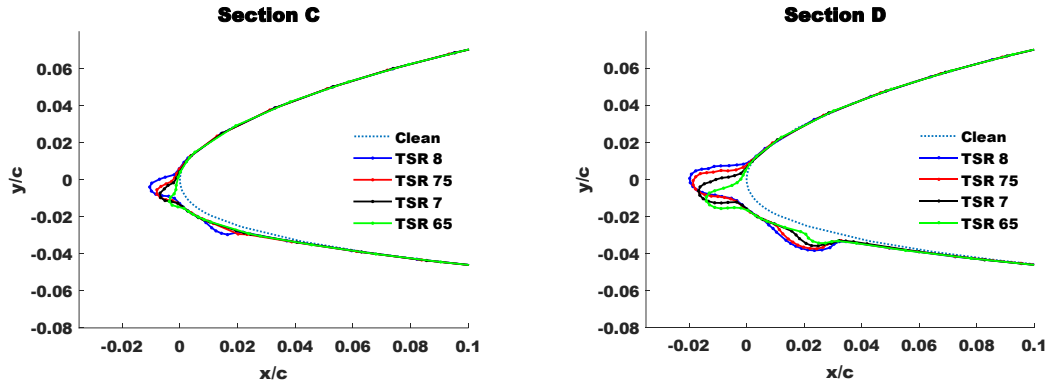

Figure A5. 4: Ice shapes formed at four different sections along the NREL 5 MW wind turbine blade at the end of icing event A75

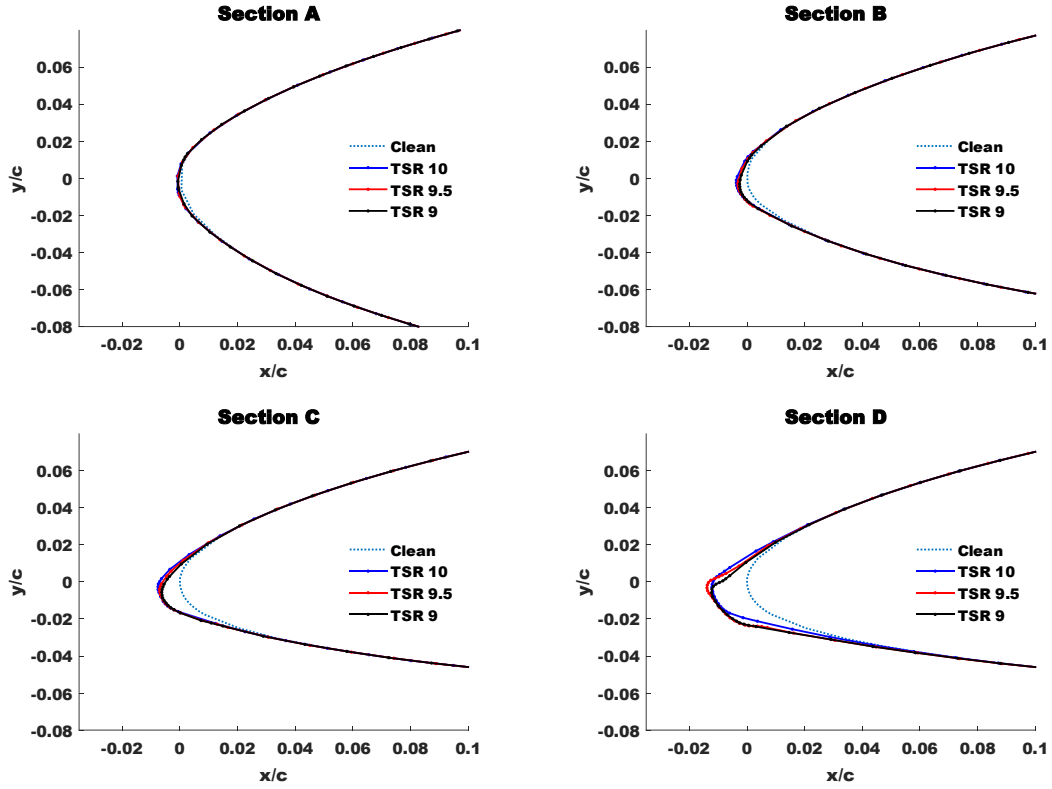

Figure A5. 5: Ice shapes formed at four different sections along the NREL 5 MW wind turbine blade at the end of icing event A510

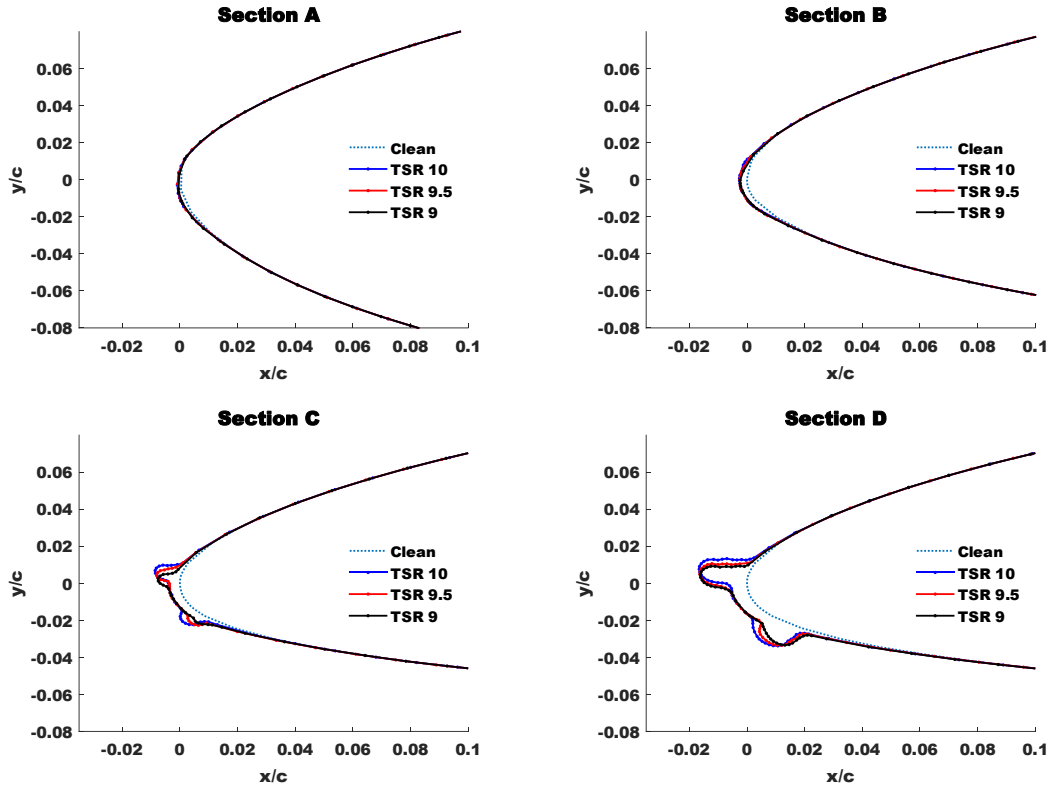

Figure A5. 6: Ice shapes formed at four different sections along the NREL 5 MW wind turbine blade at the end of icing event A55

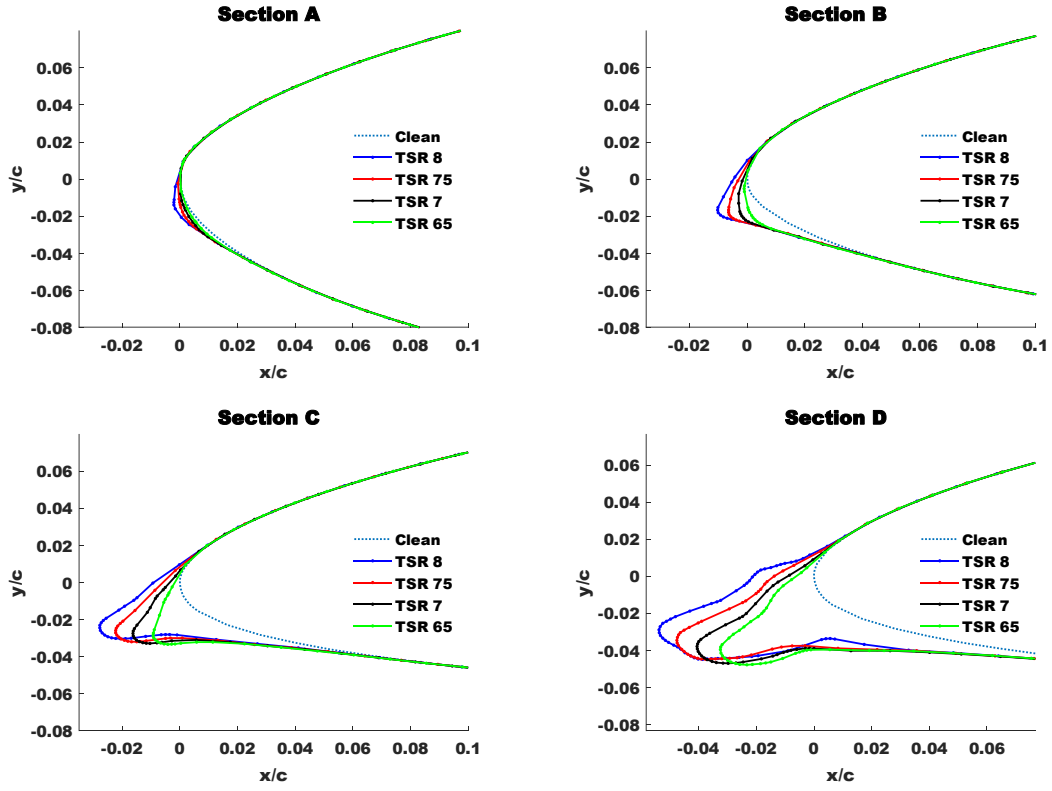

Figure A5. 7: Ice shapes formed at four different sections along the NREL 5 MW wind turbine blade at the end of icing event B1010

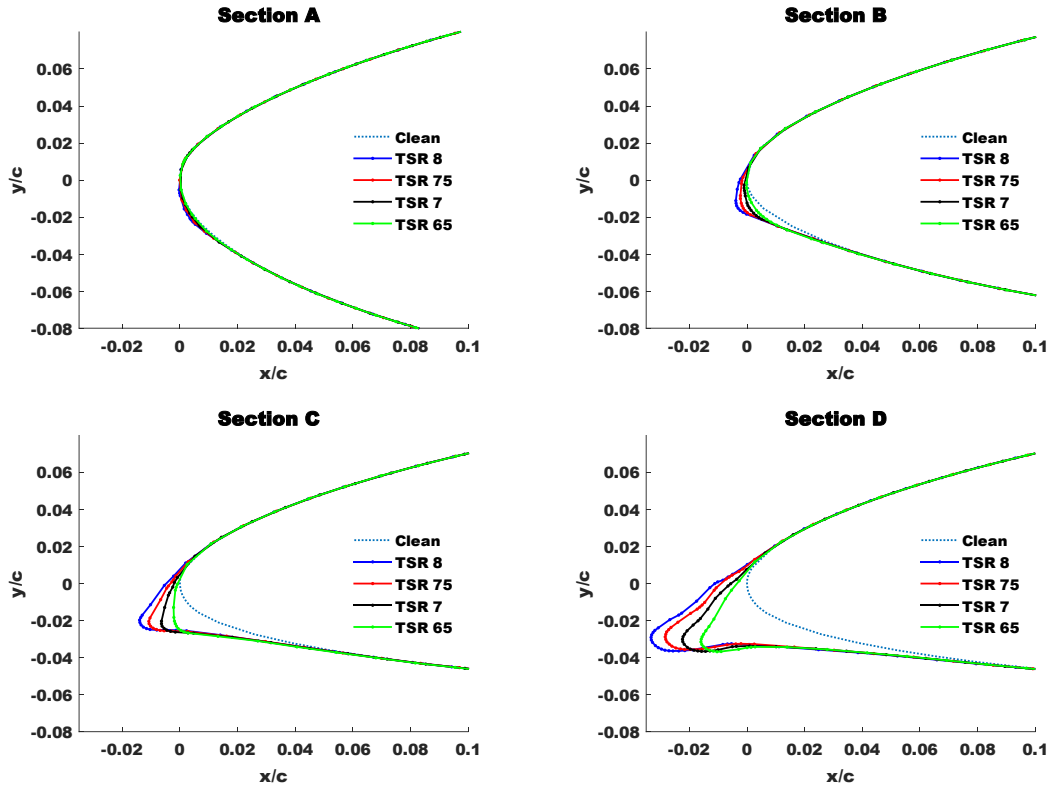

Figure A5. 8: Ice shapes formed at four different sections along the NREL 5 MW wind turbine blade at the end of icing event B710

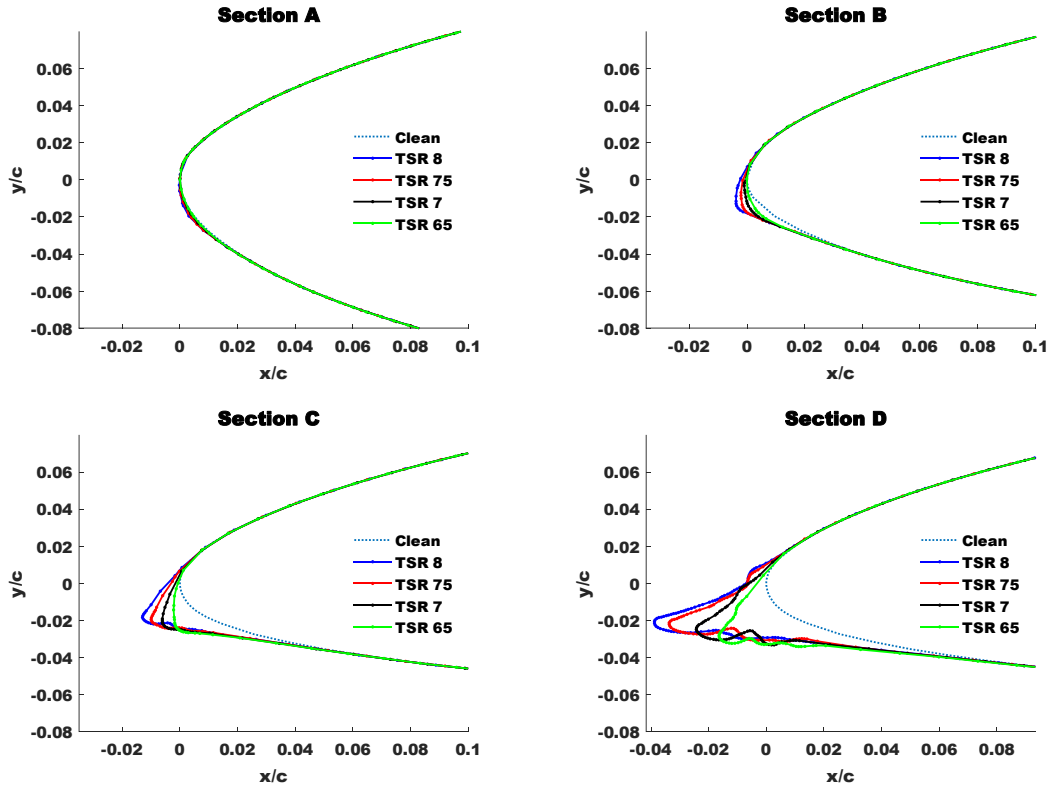

Figure A5. 9: Ice shapes formed at four different sections along the NREL 5 MW wind turbine blade at the end of icing event B75

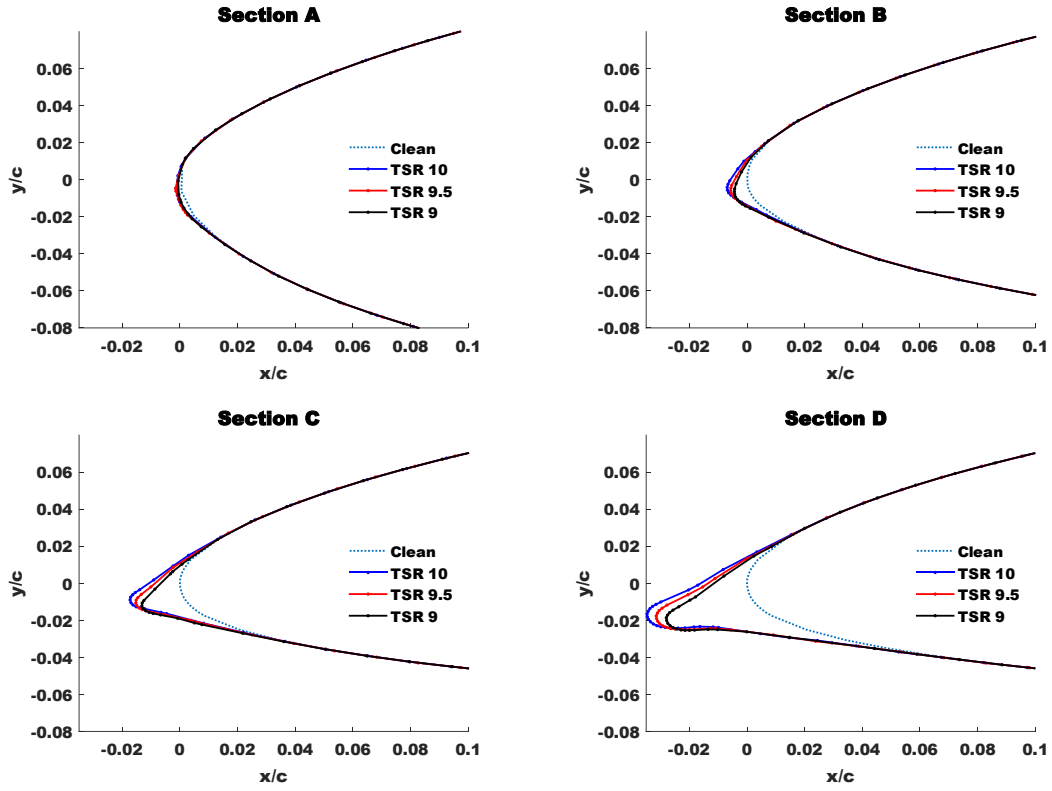

Figure A5. 10: Ice shapes formed at four different sections along the NREL 5 MW wind turbine blade at the end of icing event B510

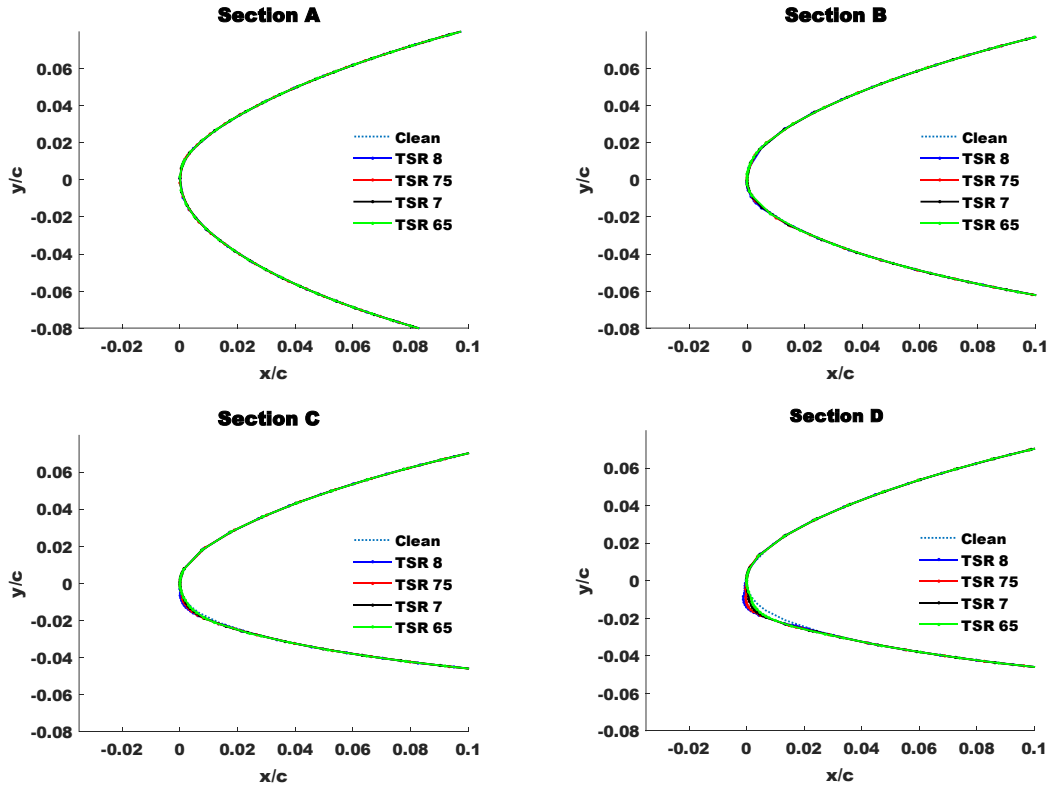

Figure A5. 11: Ice shapes formed at four different sections along the NREL 5 MW wind turbine blade at the end of icing event C1010

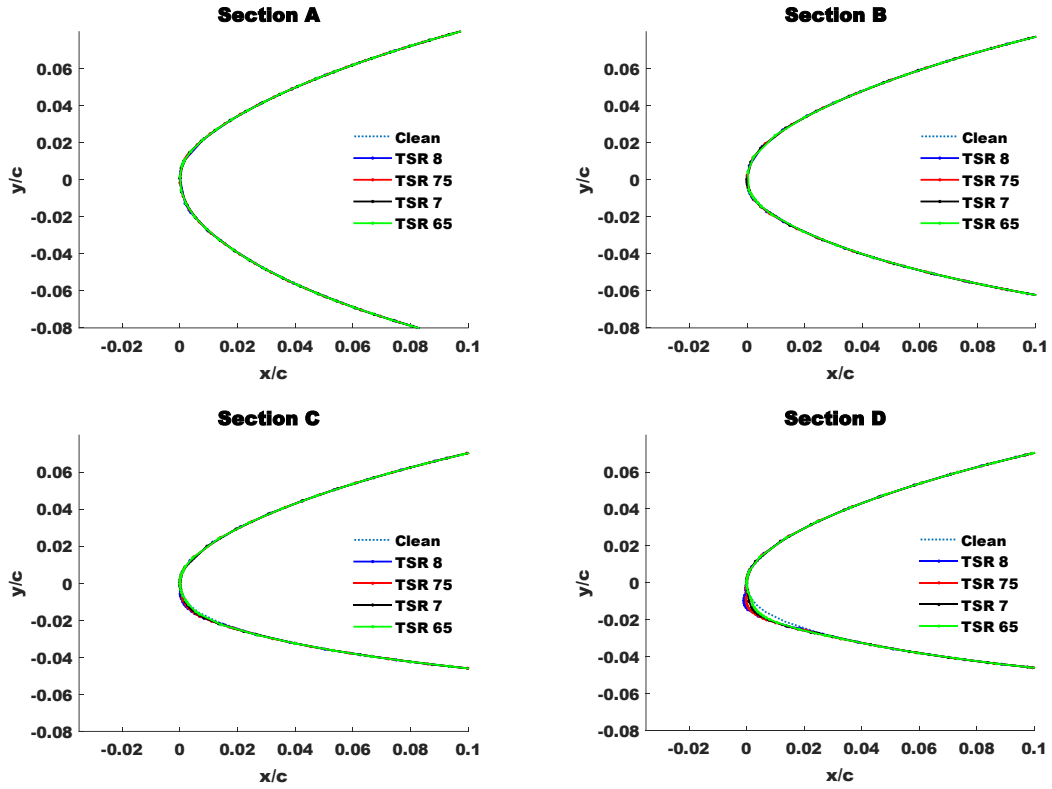

Figure A5. 12: Ice shapes formed at four different sections along the NREL 5 MW wind turbine blade at the end of icing event C105

References:

1. ABBOT, I. H. and VON DOENHOFF, A., E. (1959) *Theory of Wind Section*. 2nd edn. Canada: General Publishing Company

2. Adams, T., Grant, C., and Watson, H. (2012) 'A Simple Algorithm to Relate Measured Surface Roughness to Equivalent Sand-Grain Roughness'. *International Journal of Mechanical Engineering and Mechatronics* 1

3. Agrawal, B. N. and Platzer, M. F. (2018) *Standard Handbook for Aerospace Engineers / Brij N. Agrawal [and] Max F. Platzer, Editors*. New York: McGraw-Hill Education

4. Al-Khalil, K. M., Horvarth, C., Miller, D. R., and Wright, W., B. (1997) *Validation of NASA Therma Ice Protection Computer Codes*

5. Andy, P. B., Addy, H., Jr., Bragg, M., B., Busch, G. T., and Montreuli, E. (2011) *Aerodynamic Simulation of Ice Accretion on Airfoils* [online] available from <https://ntrs.nasa.gov/search.jsp?R=20110013362>

6. Barber, S., Chokani, N., and Abhari, R. (2011) 'Assessment of Wind Turbine Performance in Alpine Environments'. *Wind Engineering* 35 (3), 313-328

7. Baring-Gould, I., Tallhaug, L., Vindteknikk, K., Ronsten, G., Horbaty, R., Cattin, R., Laakso, T., Durstewitz, M., Lacroix, A., Peltola, E., and Wadham-Gagnon, M. (2010) *Expert Group Study on Recommendations for Wind Energy Projects in Cold Climates*. Finland: VTT

8. Battisti, L. (2015a) 'Chapter 4 Icing Process'. in *Wind Turbines in Cold Climates*. ed. by AnonSwitzerland: Springer, 177-248

9. Battisti, L. (2015b) *Wind Turbines in Cold Climates*. 1st edn: Springer International Publishing

10. Battisti, L., Fedrizzi, R., Dal Salvio, S., and Giovannelli, A. (eds.) (2007) . 'Influence of the Type and Size on Wind Turbines on Anti-Icing Thermal Power Requirements for Blades'. held January 2007

11. Begin-Drolet, A., Roberge, P., Ruel, J., and Lemay, J. (eds.) (2020) *Proceedings from Winterwind 2020*. 'How Efficient is Your Blade Heating'. held 3-5 February at Åre. Sweden: Winterwind

12. Blasco, P., Palacios, J., and Schmitz, S. (2016) 'Effect of Icing Roughness on Wind Turbine Power Production'. *Wind Energy* 20 (4), 601-617

13. Bragg, M., B., Broeren, A., P., and Blumenthal, L., A. (2005) 'Iced-Airfoil Aerodynamics'. *Progress in Aerospace Sciences* (41), 323-362

14. Brahimi, M. T., Chocron, D., and Paraschivoiu, I. (1998) 'Prediction of Ice Accretion and Performance Degradation of HAWT in Colc Climates'. *American Institute of Aeronautics and Astronautics* (A98), 60-69

15. Bredesen, R. E., Cattin, R., Clausen, N., Davis, N., Jordaens, P. J., Khadri-Yazami, Z., Klinstrom, R., Krenn, A., Lehtomaki, V., Ronsten, G., Wadham-Gagnon, M., and Wickman, H. (2017) *Wind Energy Projects in Cold Climates*: iea wind

16. Brillembourg, D. (2013) *Turbines Under Atmospheric Icing Conditions - Ice Accretion Modelling, Aerodynamics, and Control Strategies for Mitigating Performance Degradation*. Unpublished Master of Science thesis or dissertation: Pennsylvania State University

17. Byrkjedal, Ø (ed.) (2009) *IWAIS Proceedings*. 'Estimating Wind Power Production Loss due to Icing'. held 8-11/09/2009 at Andermatt: IWAIS

18. Cattin, R. (2012) *Icing of Wind Turbines*: ELFORSK

19. Chen, L., Tan, B., Kvamsto, G., Nils, and Johannessen, M., Ola (2014) 'Winter Cyclone/Anticyclone Activity Over China and its Relation to Upper Tropospheric Jets' 66

20. Chocron, D., Brahimi, M. T., and Paraschivoiu, I. (eds.) (1996) *1996 European Union Wind Energy Conference*. 'Numerical Simulation of Ice Accretion on Wind Turbine Blades'. held 20-24 May at Goteborg, Sweden

21. Cober, S., G., Isaac, G., A., and Strapp, J., W. (1994) 'Aircraft Icing Measurement in East Coast Winter Storms'*. Journal of Applied Meteorology* 34, 88

22. Coder, J. G. and Maughmer, M. D. (2014) 'Comparisons of Theoretical Methods for Predicting Airfoil Aerodynamic Characteristics'*. Journal of Aircraft* 51 (1), 183-191

23. Dalili, N., Edrisy, A., and Carriveau, R. (2007) 'A Review of Surface Engineering Issues Critical to Wind Turbine Performance'*. Renewable & Sustainable Energy Reviews* 13 (2009), 428-438

24. Davis, N., Hahmann, A. N., Clausen, N., and Zagar, M. (2014) *Icing Impacts on Wind Energy Production*. [online] Doctor of Philosophy thesis or dissertation. DTU: Technical University of Denmartk

25. Dierer, S., Oechslin, R., and Cattin, R. (2011) 'Wind Turbines in Icing Conditions: Performance and Prediction' 6, 245-250

26. Dimitrova, M., Ibrahim, H., Fortin, G., Ilinca, A., and Perron, J. (2011) 'Software Tool to Predict the Wind Energy Production Losses due to Icing'*. IEEE Electrical Power and Energy Conference*, 462

27. Dimitrova, M., Ramdenee, D., and Ilinca, A. (eds.) (2011) *World Renewable Energy Congress 2011*. 'Evaluation and Mitigation of Ice Accretion Effects on Wind Turbine Blades'. held 8-11 May 2011 at Sweden: Bioenergy Technology (BE)

28. Drela, M. (1989) *XFOIL: An Analysis and Design System for Low Reynolds Number Airfoils*.

29. ESA (2001) *Atmospheric Icing of Structures*. Ethiopia: Ethiopian Standards Agency

30. Etemaddar, M., Hansen, M., and Mo, T. (2012) 'Wind Turbine Aerodynamic Response Under Atmospheric Icing Conditions'*. Wind Energy* 17 (2), 241-265

31. Eurostat (2020) *Renewable Energy Statistics*. Online article edn: eurostat

32. Fakorede, O., Feger, Z., Ibrahim, H., Ilinca, A., Perron, J., and Masson, C. (2016) 'Ice Protection Systems for Wind Turbines in Cold Climate: Characteristics, Comparison and Analysis' 65, 662

33. Fakorede, O., Ibrahim, H., Ilinca, A., and Perron, J. (2016) 'Experimental Investigation of Power Requirements for Wind Turbines Electrothermal Anti-Icing Systems'. in *Wind Turbines - Design, Control and Applications*. ed. by Anon

34. Finstad, K., J., Lozowski, E., P., and Gates, E., M. (1986) 'A Computational Investigation of Water Droplet Trajectories'*. Journal of Atmospheric and Oceanic Technology* 5, 160

35. Fortin, G. and Perron, J. (2009) 'Wind Turbine Icing and De-Icing'*. American Institute of Aeronautics and Astronautics Journal*, 1-21

36. Fortin, G., Perron, J., and Ilinca, A. (2007) 'Icing Simulation on Wind Turbine Blades'*. American Institute of Aeronautics and Astronautics Journal*, 1-10

37. Gao, L., et al (2019) *A Hybrid Strategy Combining Minimized Leading-Edge Electric-Heating and Superhydro-/Ice-Phobic Surface Coating for Wind Turbine Icing Mitigation* [online] . available from <http://www.sciencedirect.com/science/article/pii/S0960148119304240>

38. GE Renewable Energy (2013) *Tech Tales: Using WIOM Controls to Mitifate Stalls during Blade Icing Events*. Video edn: Youtube

39. Glauert, H. (1983) *The Elements of Aerofoil and Airscrew Theory* [online] . Cambridge: Cambridge University Press. available from <https://www.cambridge.org/core/books/elements-of-aerofoil-and-airscrew-theory/0C4C47E23791589BD720E53695477784> [2020/04/13]

40. Gouttebroze, E., et al (2000) *Canice-Capabilities and Current Status*. Workshop article edn: NATO/RTO

41. Gray, V., H. (1964) *Prediction of Aerodynamic Penalties Caused by Ice Formation on various Airfoils*. Ohio: National Aeronautics and Space Administration

42. Habashi, W. G., Morency, F., and Beaugendre, H. (eds.) (2001) *7th Internation COngress of Fluid Dynamics and Propulsion*. 'FENSAP-ICE: A Comprehensive 3D Simulation Tool for in-Flight Icing'. held December at Egypt

43. Han, Y. and Palacios, J. (eds.) (2012) . 'Analytical and Experimental Determination of Airfoil Performance Degradation due to Ice Accretion'. held 25-28 June at NewOrleans, Louisiana: AIAA

44. Han, W., Kim, J., and Kim, B. (2018) 'Study on Correlation between Wind Turbine Performance and Ice Accretion Along a Blade Tip Airfoil using CFD'*. Journal of Renewable and Sustainable Energy* 10 (2), 023306

45. Hansen, M. O. L. (2008) *Aerodynamics of Wind Turbines*.: Earthscan

46. Hau, E. (2013) *Wind Turbines Fundamental, Technologies, Applications, Economics*. Third edn. trans. by Renourad, H. v. London: Springer

47. Herbert-Acero, J., Probst, O., Rivera-Solorio, C., Castillo-Villar, K., and Mendez-Diaz, S. (2015) 'An Extended Assessment of Fluid Flow Models for the Prediction of Two-Dinesional Steady-State Airfoil Aerodynamics'*. Computational Methods for Engineering Science* 2015

48. Hochart, C., Fortin, G., and Perron, J. (2007) 'Wind Turbine Performance Under Icing Conditions'

49. Homola, M. (2005) *Impacts and Causes of Icing on Wind Turbines*: INTERREG III B PROJECT

50. Homola, M., Wallenius, T., Makkonen, L., Nicklasson, P., and Sundsbo, P. (2010) 'Turbine Size and Temperature Dependence of Icing on Wind Turbine Blades'. *Wind Engineering* 34

51. Homola, M. C., Virk, M. S., Nicklasson, P. J., and Sundsbø, P. A. (2012) 'Performance Losses due to Ice Accretion for a 5 MW Wind Turbine'. *Wind Energy* 15 (3), 379-389

52. Hu, L., Zhu, X., Hu, C., Chen, J., and Du, Z. (2017) 'Wind Turbine Ice Distribution and Load Response Under Icing Condition'. *Renewable Energy* 113, 608-619

53. Hudecz, A. (2014) 'Icing Problems of Wind Turbine Blades in Cold Climates'

54. IRENA (2019) *Renewable Power Generation Const in 2018*

55. IRENA (2012) *Renewable Energy Technologies: Cost Analysis Series, Wind Power* [online]

56. Jasinski, W., J., Noe, S., C., Selig, M., S., and Bragg, M., B. (eds.) (1998) . 'Wund Turbine Performance Under Icing Conditions'

57. Jha, K., Pankaj, Brillembourg, D., and Schmitz, S. (eds.) (2012) *AIAA Aerospace Sciences Meeting Including the New Horizons Forum and Aerospace Exposition*. 'Wind Turbines Under Atmospheric Icing Conditions - Ice Accretion Modelling, Aerodynamics, and Control Strategies for Mitigating Performance Degradation'. held 09-12 January at Nashville, Tennessee: AIAA

58. Jha, A. R., Jha, P. D., and Jha, P. D.,A.R. (2010) *Wind Turbine Technology* [online] . Baton Rouge: CRC Press LLC. available from <http://ebookcentral.proquest.com/lib/coventry/detail.action?docID=565933>

59. Jin, J., Yi and Virk, M., S. (eds.) (2019) . 'Ice Accretion on Wind Turbine Blade - an Experimental Study of S819'. held June 23-28

60. Jonkman, J., Butterfield, S., Musial, W., and Scott, G. (2009) *Definition of a 5-MW Reference Wind Turbine of Offshore System Development*. USS: National Renewable Energy Laboratory

61. Karlsson, T., Turkia, V., and Wallenius, T. (2013) *Icing Production Loss Module for Wind Power Forecasting System*. Finland: JULKAISIJA – UTGIVARE

62. Kinzel, M., Sarofeen, C., and Noack, R. (eds.) (2010) *AIAA Applied Aerodynamics Conference*. 'A Finite-Volume Approach to Modeling Ice Accretion'. held 28 June at Chicago, Illinois: AIAA

63. Krenn, A., Jordaens, P. J., Wadham-Gagnon, M., Davis, N., Clausen, N., Lehtomaki, V., Jokela, T., Kaija, S., Khadri-Yazami, Z., Ronsten, G., Wickman, H., Klinstrom, R., and Cattin, R. (2016) *Wind Energy in Cold Climates Available Technologies - Report*. n.p.: iea Wind

64. Laakso, T., Baring-Gould, I., Durstewitz, M., Horbaty, R., Lacroix, A., Peltola, E., Ronsten, G., Tallhaug, L., and Wallenius, T. (2010) *State-of-the-Art of Wind Energy in Cold Climates*. Finland: VTT Technical Research Centre of Finland

65. Laakso, T. and Peltola, E. (eds.) (2005) . 'Review on Blade Heating Technology and Future Prospects'

66. Lamraoui, F., Fortin, G., Benoit, R., Perron, J., and Masson, C. (2014) 'Atmospheric Icing Impact on Wind Turbine Production'. *Cold Regions Science and Technologies* 100, 36-49

67. Lamraoui, F., Fortin, G., Benoit, R., Perron, J., and Masson, C. (2013) 'Atmospheric Icing Severity: Quantification and Mapping'. *Atmospheric Research* 128, 57-75

68. Lee, S. and Bragg, M., B. (2003) 'Investigation of Factors Affecting Iced-Airfoil Aerodynamics' [online] 40, 499-508. available from <http://icing.ae.illinois.edu/papers/03/AIAA-3123-273.pdf>

69. Lehtomaki, V., Krenn, A., Jordaens, P. J., Godreau, C., Davis, N., Khadiri-Yazami, Z., Bredesen, R. E., Ronsten, G., Wickman, H., Bourgeois, S., and Beckford, T. (2018) *Available Technologies for Wind Energy in Cold Climates*: IEA Wind Task 19

70. Lewis, W. (1947) *A Flight Investigation of the Meteorological Conditions Conducive to the Formation of Ice on Airplanes*. Calif: National Advisory Committee for Aeronautics

71. Lynch, F. T. and Khodadoust, A. (2001) *Effects of Ice Accretions on Aircraft Aerodynamics* [online] . available from <http://www.sciencedirect.com/science/article/pii/S0376042101000185>

72. Madi, E., et al (2019) *A Review of Integrating Ice Detection and Mitigation for Wind Turbine Blades* [online] . available from <http://www.sciencedirect.com/science/article/pii/S1364032118308141>

73. Makkonen, L., Laakso, T., Marjaniemi, M., and Finstad, K., J. (2001) 'Modelling and Prevention of Ice Accretion on Wind Turbines'. *Wind Engineering* 25 (1), 3-3-21

74. Makkonen, L. (2000) 'Models for the Growth of Rime, Glaze, Iciles and Wet Snow on Structures'. *The Royal Society* 358, 2913-2939

75. Makkonen, L. and AUTTI, M. (1991) 'The Effects of Icing on Wind Turbines'. *American Society of Mechanical Engineers*, 575-575-580

76. Manshadi, M. D. and Esfeh, M. K. (2016) 'Experimental Investigation of Flowfield Over an Iced Aerofoil'. *The Aeronautical Journal* [online] 120 (1227), 735-756. available from <https://www.cambridge.org/core/article/experimental-investigation-of-flowfield-over-an-iced-aerofoil/34156148C1C08DD31B47554571E711CB> [2019/11/15]

77. Marten, D. and Wendler, J. (2013) *Qblade Guidelines*. Berlin: TU Berlin

78. Menter, F. R. (1994) 'Two-Equation Eddy-Viscosity Turbulence Models for Engineering Applications'. *AIAA Journal* 32 (8), 1598-1605

79. Messinger, B. (1953) 'Equilibrium Temperature of an Unheated Icing Surface as a Function of Air Speed'. *Journal of the Aeronautical Science* 20, 29-42

80. Morgado, J., et al (2016) *XFOIL Vs CFD Performance Predictions for High Lift Low Reynolds Number Airfoils* [online] . available from <http://www.sciencedirect.com/science/article/pii/S1270963816300839>

81. Munduate, X. and Ferrer, E. (2009) *CFD Predictions of Transition and Distributed Roughness Over a Wind Turbine Airfoil*.

82. Myers, T. (2001) 'Extension to the Messinger Model for Aircraft Icing'. *AIAA Journal* 36 (2), 211-218

83. O. Günel, et al (2016) *CFD Vs. XFOIL of Airfoil Analysis at Low Reynolds Numbers*.

84. Parent, O. and Ilinca, A. (2011) 'Anti-Icing and De-Icing Techniques for Wind Turbines: Critical Review'. *Cold Regions Science and Technologies* 65 (1), 88-96

85. Pederson, M. C., Sorenson, H., Swytink-Binnema, N., Martinez, B., and Condra, T. (2018) 'Measurements from a Cold Climate Site in Canada: Boundary Conditions and Verification Methods for CFD Icing Models for Wind Turbines'. *Cold Regions Science and Technologies* 147, 11-21

86. Peltola, E., Marjaniemi, M., Stiesdal, H., and Jarvela, J. (eds.) (1999) . 'An Ice Prevention System for the Wind Turbine Blades'. held 1-5 March 1999 at Nice, France: Earthscan

87. Poots, G. (1996) *Ice and Snow Accretion on Structures*. 1st edn. Exeter: Research Studies Press

88. Pouryoussefi, S. G., et al (2016) *Experimental Study of Ice Accretion Effects on Aerodynamic Performance of an NACA 23012 Airfoil* [online] . available from <http://www.sciencedirect.com/science/article/pii/S100093611630019X>

89. Raj, L. P. and Myong, R. S. (2016) 'Computational Analysis of an Electro-Thermal Ice Protection System in Atmospheric Icing Conditions' 21, 1

90. Reid, T., Baruzzi, G., Ozcer, I., Switchenko, D., and Habashi, W. G. (eds.) (2013) . 'FENSAP-ICE Simulation of Icing on Wind Turbine Blades, Part 2: Ice Protection System Design'. held 07-10 January 2013 at Grapevine, Texas: AIAA

91. Rong, J., Bose, N., Brothers, C., and Lodge, M. (1991) 'Icing Test on a Horizontal Axis Wind Turbine' 15, 109-113

92. Sachse, K. (ed.) (2020) *Proceedings from Windterwind 2020*. 'Nordex Advanced Anti-Icing System for N149/4.0-4.5'. held 3-5 February at Åre. Sweden: Winterwind

93. Sandstad, J. (2018) *Aerodynamics of Iced Wind Turbine Airfoils; A CFD an Wind Tunnel Study*. [online] thesis or dissertation

94. Seifert, H. and Richert, F. (eds.) (1997) *Ewec '97*. 'Aerodynamics of Iced Airfoils and their Influence on Loads and Power Production'. held 6-9 October at Dublin

95. Sheldahl, R. E. and Klimas, C. P. (1981) *Aerodynamic Characteristics of Seven Symmetrical Airfoil Sections through 180-Degree Angle of Attack for use in Aerodynamic Analysis of Vertical Axis Wind Turbines* [online]

96. Shu, L., Liang, J., Hu, Q., Jiang, X., Ren, X., and Qiu, G. (2017) 'Study on Small Wind Turbine Icing and its Performance'. *Cold Regions Science and Technologies* 134, 11-19

97. Shu, L., et al (2018) *Study of Ice Accretion Feature and Power Characteristics of Wind Turbines at Natural Icing Environment* [online] . available from <http://www.sciencedirect.com/science/article/pii/S0165232X17301751>

98. Soderberg, S., Beckford, T., Ribeiro, C., and Derrick, A. (eds.) (2020) *Winterwind Proceedings*. 'Validation of Turbine Specific Modelled Ice Losses'. held 03-05/02/20 at Åre. Sweden: Winterwind

99. Spera, D. A. (1994) *Wind Turbine Technology : Fundamental Concepts of Wind Turbine Engineering*. New York: New York : ASME Press

100. Stoyanov, D. B. and Nixon, J. D. (2020) *Alternative Operational Strategies for Wind Turbines in Cold Climates* [online] . available from <http://www.sciencedirect.com/science/article/pii/S0960148119312108>

101. Suke, P. (2014) *Analysis of Heating Systems to Mitigate Ice Accretion on Wind Turbine Blades*. Unpublished Master of Applied Science in Engineering thesis or dissertation. Hamilton, Ontario: McMaster University

102. Tammelin, B., Cavaliere, M., Holttinen, H., Morgan, C., Seifret, H., and Santti, K. (2000) *Wind Energy Production in Cold Climates (WECO)*. Helsinki: Finish Meteorological Institute

103. Tammelin, B. and Seifret, H. (eds.) (2001) *Ewec 2001*. 'Large Turbines Go into Cold Climate Regions'. held 02-06.07 at Copenhagen

104. TecQuipment (2013) *AFA3 User Guides*. User Guide edn: TecQuipment Ltd

105. Timmer, W. A. and van Rooij, R. P. J. O. M. (2003) 'Summary of the Delft University Wind Turbine Dedicated Airfoils'. *Journal of Solar Energy Engineering* 125 (4), 488-496

106. Villalpando, F., Reggio, M., and Ilinca, A. (2016) 'Prediction of Ice Accretion and Anti-Icing Heating Power on Wind Turbine Blades using Standard Commercial Software'. *Energy* 114, 1041-1052

107. Villalpando, F., Reggio, M., and Ilinca, A. (2012) 'Numerical Study of Flow Around Iced Wind Turbine Airfoil'. *Engineering Applications of Computational Fluid Mechanics* 6 (1), 39-45

108. Wilcox, D. C. (2006) *Turbulence Modeling for CFD*. 3rd ed.. edn. La Canada, Calif.: La Canada, Calif. : DCW Industries

109. Wright, W., B. (2005) *Validation Results for LEWICE 3.0*. Ohio: AIAA

110. Wright, W., B., Gent, R. W., and Guffond, D. (1997) *DRA/NASA/ONERA Collaboration on Icing Research*. USA: NASA

111. Wright, W. (2008) *User's Manual for LEWICE Version 3.2*. Ohio: NASA

112. Yirtici, O., Ozgen, S., and Tuncer, I. H. (2019) 'Predictions of Ice Formations on Wind Turbine Blades and Power Production Losses due to Icing'. *Wind Energy* 22 (7), 945-958

113. Zanon, A., Gennaro, M., De, and Kuhnelt, H. (2018) 'Wind Energy Harnessing of the NREL 5 MW Reference Wind Turbine in Icing Conditions Under Different Operational Strategies'. *Renewable Energy* 115, 760-772